INSTITUTO POLITÉCNICO DE BRAGANÇA
Escola Superior de Tecnologia e Gestão

Experimental Tests and Numerical Simulation of the Fire Effect on Non-Load-Bearing Double-Stud Light Steel Framing Walls

Matheus Henrique Alves

A thesis submitted to the

School of Technology and Management - ESTiG

Polytechnic Institute of Bragança - IPB

in Partial fulfilment of the requirements for the Degree of Master of

Construction Engineering

May 2020

Experimental Tests and Numerical Simulation of the Fire Effect on Non-Load-Bearing Double-Stud Light Steel Framing Walls

Matheus Henrique Alves

A thesis submitted to the

School of Technology and Management

Polytechnic Institute of Bragança - IPB

in partial fulfilment of the requirements for the Degree of

Master of Construction Engineering

in the scope of the double degree program with the

Federal University of Technology – Paraná – UTFPR

Supervised by:

Prof. Dr Paulo Alexandre Gonçalves Piloto

Prof. Dr Erica Fernanda Aiko Kimura

May 2020

This page intentionally left blank.

Acknowledgements

This incredible and enlightening experience would not be possible without the valuable support, empathy, kindness, and patience that I have received from my family and friends. I am so lucky to have you guys around, and I apologize for being distant now and then. Special thanks to Douglas Rodrigues and Bárbara Rech, my adored friends in Brazil, who even being an entire ocean apart, proved to be my rock. Also, living in another country is quite challenging, yet exciting, and such a journey is even greater when it is shared with remarkable people, with special regard to Lauren Obrzut, Juliana Mazzarolo dos Reis and my new acquaintances from IPB, whose companionship, assistance, efforts, and perseverance are more than appreciated. This thesis is also dedicated to my Portuguese friends, who even when quarantined were able to convey their sympathy and amity.

The opportunity that I had to participate in a double degree program is a result of the joint efforts of the UTFPR and IPB communities. In that matter, I am grateful for having received the best possible and public education, and for taking the chance of engaging in academic activities from the very first year of my under graduation at UTFPR, always with the backing of Prof. Arthur Medeiros, whom I hold in high regard. I should give the proper credit to the entire IPB team for all their support, professionalism, and care, especially Eng. Luísa Barreira and Mohamed Khetata, without whom much of this work would not be attained. Also, I would like to express my gratitude and utmost respect to Prof. Paulo Piloto and Prof. Erica Kimura, who eagerly agreed to share a tip of their knowledge and expertise. Thank you so much for your major contributions, professionalism, and endless patience.

Lastly, a big thanks to Falper and Mr Francisco Catalán for so kindly providing the materials employed in the experimental tests of this research. Your technical contributions and compromise with quality and science are inspiring and much appreciated. I hope this work will be somehow constructive and worthy of your investment.

Abstract

Partition double-stud light steel framing walls provide an enhanced insulation performance when exposed to fire conditions. However, the behaviour of different configurations of such assemblies at high temperatures is still not well understood. In this sense, this study aimed to assess the fire resistance in terms of insulation requirements of double-stud light steel framing walls clad with one or two Type F gypsum plasterboards on both sides and with or without ceramic fibre cavity insulation. A series of experimental tests were conducted by subjecting small-scale specimens to ISO 834 standard fire curve and the numerical validation of each numerical model was performed using the Finite Element Method with a hybrid approach. Also, a simplified approach was proposed based on the improved design model available in the literature.

The results obtained in the experimental tests revealed that a wider cavity slows the heat transfer through the wall's cross-section, delaying the temperature rise on the unexposed gypsum plasterboard. The use of ceramic fibre cavity insulation increases substantially the fire resistance of the wall, although the heating rate of the steel studs on the exposed side is faster if compared to the specimens without cavity insulation. Moreover, concerning the specimens with the cavity partially filled with ceramic fibre, if the insulation blanket is placed towards the exposed side, enhanced fire resistance is achieved.

A hybrid approach was used to carry out the numerical analysis to determine the thermal response of each model throughout fire exposure using ANSYS® Multiphysics. It was verified that using different experimental curves to represent the temperature evolution inside the cavities or insulation blankets was essential to attain improved numerical results. Also, the concept of an air thermal layer located at specific regions of the wall models led to better and more consistent results. Moreover, the modified improved design method showed consistent results when compared with the experimental values. Overall, the predicted insulation fire resistance of the model specimens agreed well with the experimental data and useful information was provided to support further numerical and experimental studies.

Keywords: double-stud light-steel framing walls; LSF walls, partition walls; fire resistance; thermal insulation; numerical analysis; simplified design method.

Resumen

Las paredes de partición en acero ligero con doble montante proporcionan un rendimiento de aislamiento mejorado cuando se exponen al fuego. Sin embargo, el comportamiento de diferentes configuraciones de tales conjuntos a altas temperaturas todavía no se comprende bien. En este sentido, este estudio tuvo como objetivo evaluar la resistencia al fuego en términos de los requisitos de aislamiento de las paredes de armazón de acero ligero con doble montante revestidas con una o dos placas de yeso Tipo F en ambos lados y con o sin aislamiento de fibra cerámica en la cavidad. Se realizaron una serie de pruebas experimentales sometiendo las muestras a la curva de fuego ISO 834 y la validación numérica de cada modelo numérico se realizó utilizando el Método de los Elementos Finitos con un enfoque híbrido. Además, se propuso un enfoque simplificado basado en un modelo simplificado disponible en la literatura.

Los resultados experimentales revelaron que una cavidad más ancha ralentiza la transferencia de calor a través de la sección transversal de la pared, retrasando el aumento de temperatura en el lado no expuesto. El uso del aislamiento de fibra cerámica aumenta la resistencia al fuego de la pared, aunque la velocidad de calentamiento de los montantes en el lado expuesto es más rápida en comparación con las muestras sin aislamiento en la cavidad. Además, con respecto a las muestras con la cavidad parcialmente llena de fibra cerámica, si la manta aislante se coloca hacia el lado expuesto, se logra una mayor resistencia al fuego.

Utilizando ANSYS® Multiphysics, se seleccionó un enfoque híbrido para determinar la respuesta térmica de cada modelo durante la exposición al fuego. Se identificó que el uso de diferentes curvas experimentales para representar la evolución de la temperatura dentro de las cavidades o mantas aislantes es esencial para lograr mejores resultados numéricos. Además, el concepto de una capa del aire situada en regiones específicas de los modelos conduce a mejores resultados y más consistentes. Además, el método simplificado mostró resultados consistentes en comparación con los valores experimentales. En general, la resistencia al fuego en términos de los requisitos de aislamiento de los modelos coincidió bien con los datos experimentales y se proporcionó información útil para respaldar más estudios numéricos y experimentales.

Palabras cave: pared en acero ligero con doble montante; paredes de partición; resistencia al fuego; aislamiento térmico; análisis numérico; modelo simplificado.

Résumé

Les murs doubles non porteurs en acier léger offrent une meilleure performance d'isolation thermale lorsqu'ils sont exposés aux conditions d'incendie. Cependant, le comportement de différentes configurations de tels ensembles à des températures élevées n'est pas encore bien compris. En ce sens, le but de cette étude était d'évaluer la résistance au feu en termes d´exigences d'isolation des murs doubles en acier léger recouverts d'une ou deux plaques de plâtre (Type F) des deux côtés et avec ou sans isolation de cavité en fibre céramique. Une série de tests expérimentaux a été menée en soumettant les murs à la courbe de feu ISO 834 et la validation numérique de chaque modèle numérique a été effectuée en utilisant la Méthode des Éléments Finis avec une approche hybride. En outre, une approche simplifiée a été proposée sur la base d'une méthode simplifiée disponible dans la littérature.

Les résultats obtenus lors des tests expérimentaux ont révélé que l'existence d'une cavité plus large ralentit le transfert thermique à travers de la section transversale du mur, retardant l'augmentation de la température sur la plaque de plâtre non exposée au feu. L'utilisation d'un isolant en fibre de céramique dans la cavité augmente considérablement la résistance au feu du mur, bien que le taux de chauffe des montants du côté exposé soit plus rapide par rapport aux murs sans isolation de cavité. De plus, en ce qui concerne les murs dont la cavité est partiellement remplie de fibre céramique, si l'isolation de la cavité est placée vers le côté exposée, une meilleure résistance au feu est obtenue.

En utilisant ANSYS® Multiphysics, une approche hybride a été choisie pour effectuer l'analyse numérique afin de déterminer la réponse thermique de chaque modèle tout au long de l'exposition au feu. Il a été identifié que l'utilisation de différentes courbes expérimentales pour représenter l'évolution de la température à l'intérieur des cavités ou des couvertures isolantes était essentielle pour obtenir de meilleurs résultats numériques. En outre, le concept d'une couche de l'air située à des régions spécifiques des modèles a conduit à des résultats plus cohérents. De plus, l'approche simplifiée développée a montré des meilleurs résultats et plus cohérents par rapport aux valeurs expérimentales. Dans l'ensemble, la résistance au feu prévue en termes d'isolation des spécimens correspondait bien aux données expérimentales et des informations utiles ont été fournies pour étayer d'autres études numériques et expérimentales.

Mots clés : murs doubles en acier léger ; murs intérieurs ; résistance au feu ; isolation thermique ; simulation numérique ; modèle de conception simplifié.

Resumo

Paredes duplas não estruturais em aço leve possuem uma performance aperfeiçoada quando expostas a situações de incêndio se comparadas as paredes simples. No entanto, o comportamento em termos de isolamento térmico de diferentes configurações de paredes duplas ainda não é amplamente conhecido na literatura. Assim, o objetivo deste trabalho foi avaliar a resistência ao fogo em termos de isolamento térmico de paredes duplas revestidas com uma ou duas placas de gesso do Tipo F em ambos os lados e com ou sem isolamento de fibra cerâmica na cavidade. Foi realizada uma série de ensaios experimentais onde submeteram-se as paredes à curva padrão de incêndio ISO 834. A validação dos modelos numéricos foi realizada utilizando o Método dos Elementos Finitos com um enfoque híbrido. Adicionalmente, um modelo simplificado foi proposto baseado em um modelo simplificado existente na literatura.

Os resultados obtidos nos ensaios experimentais permitiram concluir que uma cavidade de maior profundidade reduz a transferência de calor ao longo da seção transversal da parede, diminuindo a taxa de aumento de temperatura na face não exposta. O uso de fibra cerâmica como isolamento aumenta significativamente a resistência ao fogo da parede, embora a taxa de aquecimento da flange dos montantes em contato com a face exposta seja expressivamente maior se comparada com os modelos sem isolamento na cavidade. Relativamente aos modelos com isolamento parcial, quando o isolamento é colocado em contato com o lado exposto, foi observado um melhor desempenho.

Para estimar a resposta térmica dos modelos, foi realizada uma análise térmica utilizando-se uma abordagem de elementos finitos híbrida em conjunto com ANSYS® Multiphysics. Observou-se que ao serem utilizadas curvas experimentais distintas para representar a evolução da temperatura na cavidade ou isolamento, melhores resultados foram obtidos. Ainda, para os modelos sem isolamento ou com isolamento parcial, considerou-se a existência de uma camada de ar limite localizada em regiões específicas dos mesmos, o que foi fundamental para garantir melhores resultados e mais consistentes. A resistência ao fogo quanto ao isolamento prevista para as paredes foi relativamente bem representada pelos resultados numéricos e simplificados e informações relevantes acerca do comportamento térmico de paredes duplas foram adquiridos nos testes experimentais e análise numérica.

Palavras-chave: paredes duplas em aço leve; paredes LSF; paredes de divisão; resistência ao fogo; isolamento térmico; análise numérica; modelo simplificado

This page intentionally left blank.

Contents

List of Tables

List of Figures

Nomenclature

Latin letters

A_i	Area of surface i
A_j	Area of surface j
c	Specific heat
C	Volumetric heat capacity
CFS	Cold-formed Steel
E	Integrity fire resistance criterion
FEM	Finite Element Method
FRR	Fire Resistance Rating
$\dot{g}$	Rate of heat generation or absorption per unit volume
h_i	The thickness of the layer being considered
$\dot{h}_{c,n}$	Net conduction heat flux along n direction at the surface boundary
$\dot{h}_{c,x}$	One-dimensional conduction heat flux
$\dot{h}_{net,cv}$	Net convection heat flux
$\dot{h}_{net,r}$	Net radiation heat flux between any two grey surfaces
$\dot{h}_r$	Radiation heat flux emitted by a real surface
I	Insulation fire resistance criterion
$k_{pos,exp,i}$	Position coefficient related to the layer (s) preceding layer i
$k_{pos,unexp,i}$	Position coefficient related to the layer backing layer i
$k_{pos,exp,n}$	Position coefficient related with the layer (s) preceding layer n
LSF	Light Steel Framing
LME	Liquid Metal Embrittlement
PID	Proportional Integral Derivative
R	Load-bearing fire resistance criterion
t	Time
t_{ins}	Insulation fire resistance of the assembly
$t_{prot,0,i}$	Basic protection value of layer i
$t_{prot,i}$	Protection value of layer i with protection function

$t_{prot,i-1}$	Protection value of the layer preceding layer i
$t_{ins,0,i}$	Basic protaction value of layer n with insulation function
$t_{ins,n}$	Insulation value of layer n with insulation function
T	Temperature
$\dot{T}$	First temperature derivative with respect to time
T_0	Ambient temperature
T_g	Gas temperature
T_m	Material surface temperature
U	Internal energy
$\vec{n}$	Normal unit vector

Greek letters

α_{cv}	Heat transfer coefficient or film coefficient
ρ	Density
ρ_i	Desnity of the layer being considered
σ	Steffan-Boltzmann constant
λ	Thermal conductivity
ε_f	Fire emissivity
ε_i	Emissivity of surface i
ε_j	Emissivity of surface j
Δ	Variation
Δt_i	Correction time for layer I with protective function
Δt_n	Correction time for layer n with insulation function
ε_m	Surface emissivity for a given material
ϕ	View factor
ϕ_{ij}	View factor between surfaces i and j
Ω	Dominium
Ω^e	Dominium of an element
ψ_k	Weighing function

Special notations

∇	Gradient operator
∂	Del operator
$\forall$	For all

This page intentionally left blank.

Chapter 1

1 Introduction

The Light Steel Framing (LSF) system is widely acknowledged as one of the most efficient methods available for residential, commercial, and industrial construction. Its constituent elements are assembled into both load-bearing and non-load-bearing building structures, suchlike walls, floors, ceilings, and roofs and, since the steel frame consists primarily of lightweight, high strength to weight ratio and dimensionally stable galvanized Cold-formed Steel (CFS) members, LSF offers multiple advantages over traditional building techniques such as timber and masonry, including a significant increase in the speed of construction, higher durability and a substantial improvement in the environmental and physical performance of a building, as well as an enhanced aesthetic appeal and reduced costs with maintenance [1,2].

As the demand and popularity of LSF assemblies increase, special attention has been brought to their safety requirements, particularly those concerning fire behaviour. Hence, an adequate assessment of the performance of lightweight steel-framed building structures under fire conditions is essential to assure a proper fire safety design and compliance with the requirements recommended by standards and codes of practice, which are fundamental to prevent and mitigate hazards due to fire events [2–4].

In this sense, the non-load-bearing walls framed with thin-walled CFS sections are one of the major components of the LSF system and, as such walls are mainly used as partitioning, they play a vital role as fire barriers, controlling the fire spread throughout the compartments and sustaining the overall integrity of a building for longer [3-5]. Thus, unloaded LSF walls should be carefully assessed in terms of fire safety requirements, namely their fire resistance, expressed by means of *Fire Resistance Rating* (FRR), i.e. the rating period in which a building component, when exposed to a standard fire scenario, fails in one or more of the specified criteria [2,4]. On this subject, improved fire resistance of LSF walls relies mostly on diverse assemblage methods and fire protective materials, including assorted types of sheathing boards

and cavity wall insulation materials, which noticeably influence the time-temperature profiles developed over the surfaces of the wall elements and their failure modes under fire.

Thus, although the behaviour of conventional LSF walls in standard fire scenarios is broadly known, there is still a need to conduct experimental tests and validate analytical models to assess the insulation performance under fire of different assemblies of partition LSF walls with increased FRR (e.g. fire-rated, double-stud and separation walls), which may contribute to improving performance-based and prescriptive fire design rules for LSF construction, therefore assuring its safety at elevated temperatures.

1.1 Single and Double-Stud Non-Load-Bearing LSF Walls

Non-structural LSF is mainly employed in the construction of internal *partition walls* that do not carry axial or lateral external loads from adjacent structures. They can be assembled in various ways to provide proper acoustic and thermal insulation. Their typical frame consists essentially of vertically arranged CFS *studs* and horizontal *tracks* that are connected by welding, riveting, screwing, clinching or powder-actuated fastening [6]. The frame is lined with sheathing boards or composite panels attached to the framework by self-drilling screws. When applicable, the insulation can be placed internally (wall cavity) or, externally, such as in a composite panel, as illustrated in Figure 1.1 and Figure 1.2.

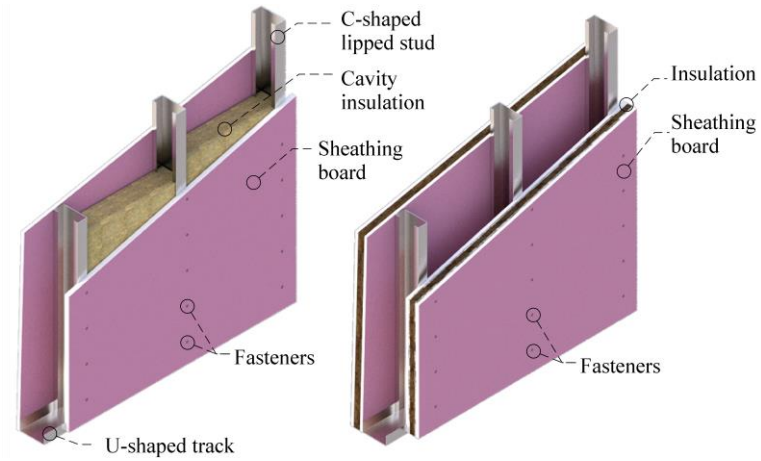

Figure 1.1- Typical single-stud LSF wall assemblies.

Depending on the floor-to-ceiling height, framing method, lateral restraints, and assorted design specifications, additional strengthening using intermediate horizontal tracks may be required to provide stiffness and lateral stability to the framework. Such tracks are usually referred to as *noggin* or *blocking tracks*. Bracing systems and resilient channels also deliver improved overall stability to the steel frame, especially in regards to load-bearing frames.

In construction engineering, single-stud walls are normally used as partitioning. However, when an enhanced thermal performance and soundproofing, as well as a higher durability are required, double-stud LSF walls are efficient alternatives that adjust more adequately to the energy and cost-saving requirements of buildings. Thus, such walls can be successfully used in extreme climates and other special applications (e.g. corridor walls, meeting rooms, etc.). Figure 1.2 displays a set of different cross-sectional configurations of double-stud LSF walls, where the steel frame arrangement is comprised by two stud rows that can be either staggered or aligned. Also, a void or insulated gap between the stud rows may exist. It is noteworthy that the buildability and components that are used as sheathing and cavity insulation in double-stud assemblies are comparable to single-stud walls, although the initial construction cost differs significantly.

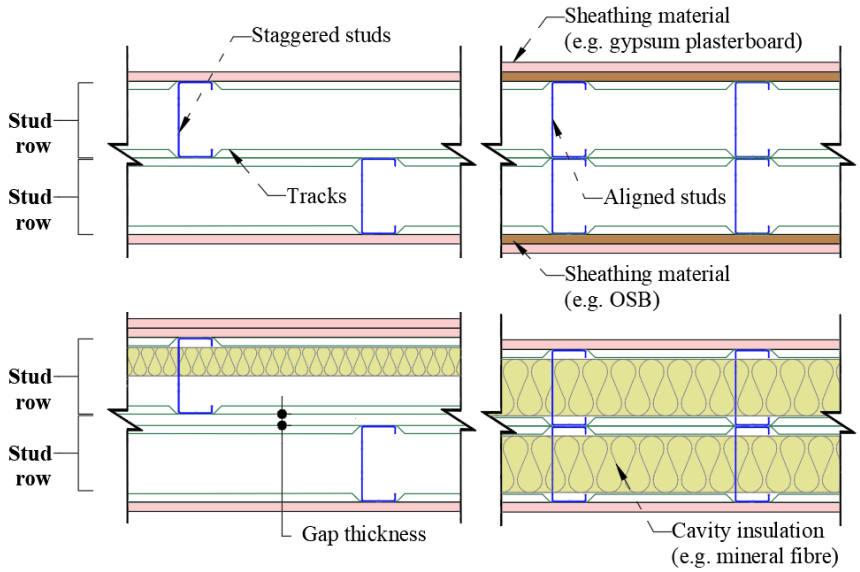

Figure 1.2- Different configurations of double-stud LSF wall assemblies.

1.1.1 Thin-Walled Cold-formed Steel

The steel frame is commonly composed of *galvanized thin-walled* C, U or Z-shaped CFS sections ranging from 0.4 to 6.4 mm thick, depending on the application [4]. The profiles can be configurated in several forms to fulfil design conditions. Regarding partition walls, the most widely used steel sections are C and U-shaped profiles, and for non-structural purposes, their thickness can be as low as 0.46 mm [7]. Figure 1.3 illustrates the main geometry parameters of C and U-shaped sections that are often used as studs and tracks of partition walls. Moreover, CFS members can be unstiffened or stiffened, using stiffeners in their webs and/or flanges. As depicted in Figure 1.3, stud profiles normally have lipped flanges to increase their strength and stiffness, whereas tracks are generally made with unstiffened flanges angled inwards to properly accommodate studs [1], although lipped tracks are currently being employed in construction practice.

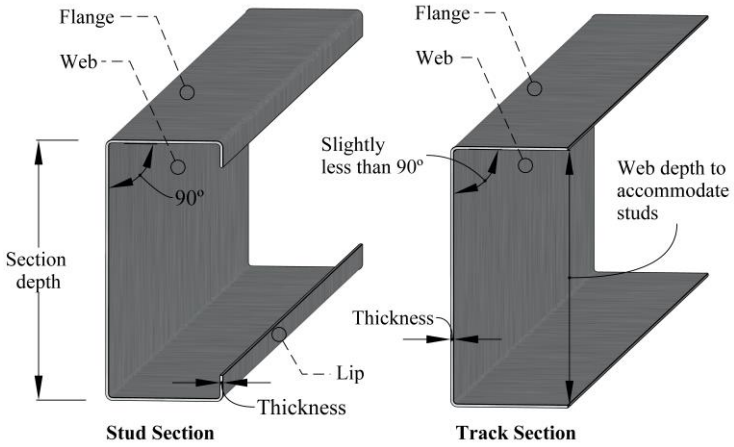

Figure 1.3 – Geometry of C-shaped studs and tracks for partition walls. Adapted from CSSBI [1].

1.1.2 Sheathing and Cavity Insulation

Sheathing and *cavity insulation* materials are significant elements of LSF walls due to their critical influence in the thermal, structural, and acoustic performance of the assembly. Apart from its sealing function, *gypsum-based sheathing* supplies fire protection for either load or non-load-bearing walls, due to its insulating properties, moisture content and chemically-bonded water, working as thermal rated fire barriers for the steel frame and other structural and non-structural wall components [8]. Gypsum lining may be assembled into single or multi-

layered arrangements, where each board may have a thickness of 6 to 25 mm and a density ranging from 550 to 850 kg/m³ [9]. The boards are typically composed of gypsum plaster, gypsum fibre or gypsum glass fibre covered with a paper-facing. Cement-based and wood composites can also be employed as fire protection layers in partition walls.

As for the cavity insulation, *mineral fibrous materials* (e.g. rock wool, glass fibre and ceramic fibre), in addition to offering improved acoustic behaviour, because of their high melting point, high porosity and low thermal conductivity, prove outstanding integrity and insulation performance at elevated temperatures, preventing the fire propagation along the wall cavity for a certain temperature range, depending on the insulation type. Moreover, cellulose-based insulation is also available for LSF wall panels.

1.1.3 Fire Resistance

The Fire Resistance Rating (FRR) of composite LSF walls depends on the *thermal*, *structural* and *integrity* behaviour of all their constituent elements when exposed to a fire event. Consequently, to accurately evaluate the fire resistance of such walls, the following aspects must be considered:

- Mechanical and thermal properties of the constituent materials at elevated temperatures;
- Assembly, fastening details and geometry of the wall elements;
- Fire load and severity;
- Integrity behaviour, shrinkage resistance and type of sheathing;
- Restraints, support, and load conditions.

Sheathing and cavity insulation enhance the insulation performance of partition walls, delaying the temperature rise on the unexposed surfaces and reducing the risk of fire propagation through the cavity [10]. Furthermore, at ambient temperatures and up to a certain degradation level under fire, gypsum panels also act as lateral restraints to the steel studs, preventing global buckling about the minor axis and flexural-torsional buckling failure [11,12]. However, at extreme temperatures, gypsum plasterboards suffer from *ablation, cracking* and *fall-off*, which leads to an intensification of the heat flux across the cross-section of the wall.

Additionally, the weakening of the *plasterboard joints* and the presence of cavity insulation increases the thermal gradient in a wall subjected to fire on one side, intensifying *thermal bowing* of the steel frame, and ablation and fall-off of the gypsum boards, thus reducing the fire resistance of the LSF wall [13,14].

Moreover, since thin-walled CFS heats up rapidly under fire, expanding and modifying its properties, the steel frame behaviour is particularly important for load-bearing structures. At critical temperature levels, when the steel reaches temperatures higher than 300-400 °C, sheathing and insulation reduce the contribution to the overall strength and stiffness of the wall and elevated non-uniform temperatures induce a complex strain field in the steel, especially when the frame is directly exposed to fire and cavity insulation is employed. Thus, premature structural failure of the studs, namely yielding, local, distortional, flexural, distortional-flexural buckling and web buckling are likely to occur [15].

In terms of experimental analysis and according to EN 1363-1 [16], the fire resistance of LSF walls can be determined by submitting one side of the wall specimen to a standard fire load that behaves according to the heating curve specified by ISO 834 [17]. Under a standard fire test, the FRR of a building component is then defined according to the following failure criteria:

- *Load-bearing capacity* (R)*:* the rating period in which the specimen sustains its load-bearing ability until failure when both specified deflection and rate of deflection are exceeded or collapse occurs;
- *Integrity* (E)*:* the rating period in which the specimen prevents the passage of flames, smoke or hot gases from the exposed to the unexposed side, which can be evaluated by the penetration of a gap gauge through surface openings or the ignition of a cotton wool pad or the incidence of flames on the unexposed side, measured in terms of their time of occurrence, duration and location.
- *Insulation* (I)*:* the rating period in which the specimen sustains its capability to resist the average temperature variation on the unexposed side up to 140 ºC (T_{ave}) or temperature variation at any location on the unexposed side up to 180 ºC (T_{max}), above the ambient temperature.

The assessment of the fire resistance of LSF walls in terms of insulation, integrity and load-bearing endurance should be based on *full-scale* testing, given that the heat distribution in the assembly, occurrence of cracks in the gypsum lining and its shrinkage resistance will vary considerably with the dimensions of the wall, and the structural behaviour of the steel frame depends on its geometric features, restraints and support conditions. However, *small-scale* specimens can be employed in standard fire tests, as they still provide useful data regarding thermal transmission effects.

Fire-resistant LSF walls with increased FRR should supply enough time for safe evacuation and minimize property loss. There are several types of partition walls with different FRR and functionalities. More details can be seen in CSSBI, (2005; 2012) [1,18], LSK, (2005) [7] and Yandzio et al. (2015) [8].

1.2 Standard Building Fires

Standard building fires are characterized by conventional curves that relate to the post-flashover propagation and development phases of realistic natural fires, without considering the characteristics of the compartment. Such phases characterise the period where a *continuous combustion* process starts to progress rapidly in which higher temperatures are achieved and therefore, they are of utmost relevance to the fire behaviour of building structures. Natural fires allow to incorporate different fire severities, realistic fire loads and construction features of various building compartments, and although real building fires predict more accurately the fire resistance of construction components, standard fire curves give relevant comparative results and can be successfully used to validate small and full-scale thermal models.

In this context, the assessment of the fire resistance of LSF walls is frequently based on the nominal standard time-temperature fire curve given by ISO 834 [17], as shown in Figure 1.4, which is currently based on gas-fired furnaces.

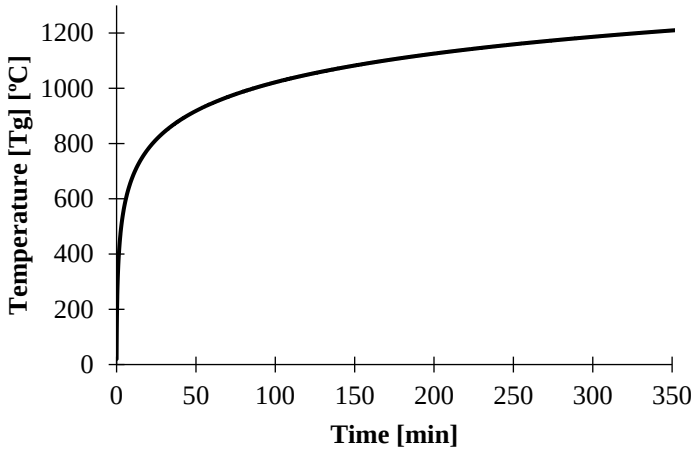

Figure 1.4 – Standard fire curve.
ISO 834 [17].

Eq. 1.1 provides the analytic expression that represents the development of the furnace temperature T_g [ºC] over time, where T_0 is the ambient temperature [°C] and t is the time elapsed [minutes]. Moreover, EN 1363-1 [16] requires that $T_0 = 20\ °C$.

$$T_g = T_0 + 345 \times \log_{10}(8t + 1) \quad \textbf{1.1}$$

1.3 Research Objectives

This research aims to include experimental tests, numerical validation, and propose a simplified method to improve the knowledge about the fire resistance of small-scale double-stud non-load-bearing LSF walls with different configurations when exposed to standard fire conditions.

Experimental tests were performed to validate the numerical models and verify compliance with the requirements of EN 1363-1 [16] and EN 1364-1 [19]. The fire resistance of small-scale specimens will be evaluated in terms of their Fire Resistance Rating based on the *insulation* criteria and overall thermal performance. A single double-stud asymmetrical frame arrangement is used for all specimens, varying only the sheathing and insulation configurations. Type F fire-resistant gypsum boards are employed as sheathing and ceramic fibre as wall cavity insulation.

Special numerical tasks were applied to develop an accurate transient model to predict the temperature field and the fire resistance of the walls using ANSYS® Multiphysics. The validation of the 3D finite-element models without fluid interaction is performed by determining the temperature field of the cross-section after 60, 90, 120 and 180 minutes of fire exposure, with a further comparison with the experimental results (*Advanced Calculation Method)*.

A *simplified calculation method* based on the modified improved design method was also developed to determine the fire resistance of the simplified models after 60, 90, 120 and 180 minutes of fire exposure and the results obtained are compared with both experimental and numerical data.

1.4 Thesis Outline

Chapter 1 introduces the main advantages of using LSF structures and concerns with their fire safety and behaviour under elevated temperatures. An overview of the assembly and construction of typical partition walls is presented. The definition and assessment criteria to determine the fire resistance rating of LSF structures subjected to standard fire are explained.

Chapter 2 explores the heat transfer mechanisms and thermal behaviour of LSF walls under fire conditions and main parameters affecting their fire resistance. It also presents previous numerical and experimental studies and the main findings related to both load-bearing and non-load-bearing single and double-stud LSF walls.

Chapter 3 presents the details of the experimental tests conducted to assess the thermal performance of different configurations of double-stud LSF walls. Details about the construction of the specimens, observations and the results obtained from standard fire tests are compared and discussed, and the FRR regarding thermal transmission effects of the specimens is determined.

Chapter 4 describes the basics of the Finite Element Method for heat transfer analysis in advanced calculation methods to determine the thermal response of LSF walls under standard fire conditions. Details on the development process of the numerical models are provided and the predicted results for the insulation fire resistance of each wall configuration are compared and validated according to the experimental tests.

Chapter 5 assesses the development of a simplified method to determine the fire resistance of the specimens tried, based on the improved design method available in the literature. To determine its applicability, the simplified results are compared with the experimental and numerical figures.

Chapter 6 summarises the main conclusions and observations relating to the experimental, numerical, and simplified studies carried out to assess the thermal performance of different configurations of double-stud LSF walls. Recommendations for further studies are provided.

Chapter 2

2 Fire Behaviour of LSF Walls

Composite structures are largely employed in construction engineering given that enhanced performance is usually achieved when the properties of each constituent material are combined. However, under fire conditions, composite structures may experience complex modes of heat transfer and thermal behaviour, which can difficult the modelling process to obtain the overall thermal response of the composite, especially because of the nonlinear time-temperature dependence of the governing equations and material thermal properties, as well as irregular boundary conditions. Yet, in addition to defining appropriate boundary values, simplified hypotheses can be inferred by identifying the relevant modes of heat transfer and their assumptions. For that purpose, a proper understanding of the basic heat transfer mechanisms and thermal actions on LSF walls under fire is required.

This section provides the necessary background to conduct the experimental and numerical studies on the thermal performance of double-stud LSF walls relating to the objectives of this research, including a brief study of the heat transfer mechanisms and thermal actions pertaining LSF wall panels and the behaviour of their elements under fire conditions. Furthermore, it explores the current state of knowledge, recent findings, and contributions on the field of both load and non-load-bearing LSF walls exposed to standard fire scenarios, considering experimental and numerical aspects. A detailed literature review is presented regarding the fire performance of double-stud assemblies.

2.1 Heat Transfer and Thermal Actions

Heat transfer can be defined as the thermal energy being transported within a medium, through a vacuum or between media due to a spatial thermal gradient. Such phenomenon occurs through one or more of its three different modes: conduction, convection, and radiation, normally quantified in terms of *heat flux*, i.e. the thermal energy rate per unit area [20,21].

2.1.1 Conduction

Conduction takes place in solids, liquids, and gases, wherein heat is exchanged from molecules with a higher energy state to those with a lower energy state because of interactions between them, such as diffusion, collusion, and free movement [20,22]. According to *Fourier's Law*, the one-dimensional conduction heat flux $\dot{h}_x$ [W/m²] through a stationary medium along an infinitesimal direction dx [m] is proportional to an existing temperature gradient dT [K] across that medium, as given by

$$\dot{h}_{c,x} = -\lambda \frac{dT}{dx} \qquad \textbf{2.1}$$

In Eq. 2.1, the *thermal conductivity* of the material, λ [W/mK], is a physical property that measures the capacity of a substance to conduct heat and depends mostly on the constitution of the media, temperature, and pressure conditions. Metals tend to have high thermal conductivities because of the motion of free electrons, whereas insulators and most non-metal construction materials exhibit low thermal conductivities, as heat is conducted via molecular vibrations only. Additionally, for non-metals, density, lattice structure, porosity, and moisture content will affect their thermal conductivity significantly. It should be pointed out that the *heat transfer area* should be *always perpendicular* to the direction of the heat flux, which flows towards the lowest temperature [21].

Regarding the modelling of composite building structures subjected to fire, as the fire gas temperature changes over time, a *transient state* approach is essential, in which the transient conduction heat flux can be approximated by means of a model and time discretization and suitable initial and boundary conditions, considering the domain and the effective thermal properties of the composite materials and their surface interactions with the fire, ambient, adjacent surfaces and voids. The numerical assessment of transient heat conduction is discussed in Chapter 4.

2.1.2 Convection

Convection encompasses conduction too, but heat is also affected by the bulk motion of a fluid. An example would be the heat transfer between gas in motion and a bounding surface

at different temperatures. Additionally, in some cases, convection occurs due to latent heat exchange, generally associated with the phase change of a material, such as in evaporation and condensation of fluids [20,23]. Regardless of the mechanism, the convective heat flux is proportional to a temperature difference. Hence, following *Newton's Law of Cooling* and as per EN 1991-1-2 [24], the net convective heat flux $\dot{h}_{net,conv}$ [W/m²] between a surrounding gas at temperature T_g [K] and a surface area at temperature T_m [K] is expressed as

$$\dot{h}_{net,cv} = \alpha_{cv} \, (T_g - T_m) \qquad \textbf{2.2}$$

In Eq. 2.2, referring to standard fire scenarios in buildings, T_g is the gas temperature nearby the surfaces of the fire exposed element, consistent with the respective environment temperature, and α_{cv} is the heat transfer coefficient or film coefficient [W/m²K], whose values tend to be directly proportional to the thermal conductivity of the surrounding fluid and are influenced by temperature, surface geometry, and fluid thermophysical properties and especially the motion behaviour. For the fire exposed surface, T_g varies according to the nominal standard time-temperature fire curve specified by ISO 834 [17].

Determining the appropriate film coefficient (convection coefficient) at the fluid-solid interface is quite a complex procedure. Nonetheless, under fire conditions, as radiation tends to be the most relevant heat transfer mechanism, the temperature distribution in a fire exposed element will not be overly sensitive even to large variations in the heat transfer coefficient [12].

2.1.3 Radiation

Radiation is the heat emitted from solids, liquids, and gases via electromagnetic waves and unlike conduction and convection, it does not require a material medium to occur [20,21]. The thermal radiation flux $\dot{h}_r$ [W/m²] emitted by a real surface area at temperature T_m [K] is given by

$$\dot{h}_r = \sigma \, \varepsilon_m \, T_m^{\,4} \qquad \textbf{2.3}$$

where the Stefan-Boltzmann constant σ equals 5.67×10^{-8} [W/m²K⁴] and ε_m is the *emissivity* of the surface. The emissivity is a property with values in the range $0 \leq \varepsilon_m \leq 1$ that indicates the capacity of a surface to emit radiant energy relative to a black body ($\varepsilon_m = 1$) when they are both at the same temperature, and depends on the emitting surface material, finishing and temperature, as well as radiation wavelength and direction [20,21].

When the electromagnetic waves reach a surrounding surface, the receiving irradiated energy is partly reflected and transmitted, whereas the remaining is absorbed. In a fire event, the surfaces of a construction element are enclosed by the flames and hot gases, and for practical reasons, the radiant energy exchange between any two surfaces within an enclosure may be approximated by heat transfer between *opaque*, *diffuse*, *grey surfaces*, in which multiple reflections and partial absorptions occur [12,22]. This is called *grey body radiation*. That means that the surfaces are nontransparent and their emissivity is considered independent of temperature, and radiation wavelength and direction, and the average surface emissivity equals its average absorptivity (*Kirchhoff's Law*) [12,20]. In such circumstances, the resulting radiation heat from an emitting surface at temperature θ_g [K] towards the receiving surface at temperature T_m [K], without considering transmission effects, is called the net rate of radiation heat transfer, $\dot{h}_{net,r}$ [W/m²], as given by the following Eq. 2.4.

$$\dot{h}_{net,r} = \frac{1}{\frac{1-\varepsilon_i}{\varepsilon_i} + \frac{1}{\phi_{ij}} + \frac{A_i}{A_j}\left(\frac{1-\varepsilon_j}{\varepsilon_j}\right)} \sigma\left(T_g^{\,4} - T_m^{\,4}\right) \qquad \textbf{2.4}$$

Where A_i, A_j are the surface areas, ε_i, ε_j are the emissivity of the two surfaces, and ϕ_{ij} is the view or shape factor (dimensionless), which means a parameter that accounts for the surface orientation and shadow effects on the radiation heat exchange between two relative surfaces, defined as the rate of radiation leaving a surface i that reaches directly another surface j, with $0 \leq \phi_{ij} \leq 1$ [12,22]. Eq. 2.4 is valid when the radiation coming from the source is *uniform* throughout its surface in all directions and the medium between the surfaces is considered to be *transparent* to radiation, that is, it does not contribute to radiation effects within the enclosure.

Moreover, Eq. 2.4 can be adapted to quantify the net radiation heat affecting a building element when subjected to fire, as shown in the following Eq. 2.5. In this case, the fire and exposed surfaces are considered as two distant grey bodies, in a way that the radiation reflected

by the exposed surface is lost to the surroundings and not absorbed back by the fire [21]. According to EN 1991-1 [24], Eq. 2.4 becomes

$$\dot{h}_{net,r} = \phi\, \varepsilon_f\, \varepsilon_m\, \sigma \left(T_g^{\,4} - T_m^{\,4}\right) \qquad \textbf{2.5}$$

in which ε_f and ε_m are the emissivity of the fire and exposed surfaces, respectively, T_g [K] is the gas temperature and T_m [K] is the surface temperature of the fire exposed surface.

2.1.4 Thermal Actions on Partition LSF Walls

In a typical non-insulated LSF wall clad with gypsum plasterboard and subjected to fire on one side, the heat generated by the fire is first transferred to the exposed surface by radiation and convection, being radiation the dominant mode. Then, conduction takes place along the thickness of the unexposed protection layers and steel sections, and the heat is dispersed around the cavity by way of radiation and convection, as illustrated in Figure 2.1. Lastly, conduction occurs through the unexposed layers and heat is released into the ambient via radiation and convection, with convection being predominant at lower temperatures.

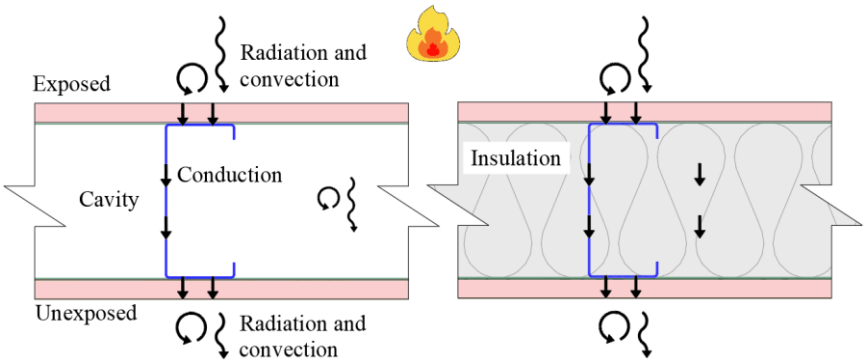

Figure 2.1- Typical thermal actions on uninsulated and cavity insulated single stud LSF walls.

Internal convection also ensues in the gypsum boards due to water evaporation at temperatures up to 120 ºC, along with radiation effects in its porous structure over temperature rise. Nevertheless, internal convection is a phenomenon that can be reasonably simulated by using appropriate effective specific heat values. Additionally, a common construction practise is to insert a porous media in the wall cavity (e.g. mineral insulation), wherein conduction,

convection and radiation take place. However, in the case of porous media, such as gypsum and insulation, their effective thermal conductivities account for the radiation and convection effects in their voids, and the heat transfer is then dominated by conduction. Moreover, integrity complications, such as lining fall-off, weakening of the plasterboard joints, and ablation of the cavity insulation will affect the heat transfer modes throughout the wall and hence its temperature distribution. Such effects are greatly simplified if user-input data are provided.

From the previous analysis, the net heat flux onwards the exposed or outwards the unexposed surface of a partition LSF wall is due to a combination of convection and radiation. Thus, combining Eqs. 2.2 and 2.5, EN 1991-1-2 [24] states that the net heat flux $\dot{h}_{net}$ [W/m²] on the exposed or unexposed surface of a building component is

$$\dot{h}_{net} = \dot{h}_{net,cv} + \dot{h}_{net,r} \quad \textbf{2.6a}$$

$$\dot{h}_{net} = \alpha_{cv} \left(T_g - T_m\right) + \phi\, \varepsilon_f\, \varepsilon_m\, \sigma \left(T_g{}^4 - T_m{}^4\right) \quad \textbf{2.6b}$$

2.2 Thermal Behaviour of LSF Wall Elements in Fire

The behaviour of LSF walls at elevated temperatures is determined by their thermal and structural performance, which are evaluated by exposing the wall to a fire load and assessing its time-temperature profiles, integrity, and load-bearing endurance. Kesawan and Mahendran (2018) [11], based on extensive research review, concluded that the main parameters influencing the thermal behaviour of LSF walls are: composition, thermal properties, fall-off and joint effect of the gypsum plasterboards and; cavity insulation, CFS and their thermal properties. Such factors will impact the heat transfer mechanisms, therefore determining the suitable experimental and modelling approaches.

2.2.1 Gypsum Plasterboard

2.2.1.1 Calcination Reactions and Thermal Properties

Gypsum plasterboard is the most common board for sheathing in LSF construction. Its main component is calcium sulphate dihydrate ($CaSO_4.2H_2O$) with about 3% of free water and

approximately 20% of chemically-bonded water [25] and may contain calcium carbonate ($CaCO_3$) and magnesium carbonate ($MgCO_3$). The composition proportioning and the usage of additives to hone shrinkage resistance (e.g. glass fibre and vermiculite) produce different types of gypsum panels, including fire-rated ones with increased FRR.

The content of water is a central factor regarding the fire endurance of gypsum-based sheathing. When exposed to elevated temperatures, gypsum dehydrates in two main phases through calcination, which takes place at 80-250 ºC. During the dehydration process, the water content within the gypsum boards is gradually released, leading to a temperature plateau in their unexposed surface time-temperature curve. The length of this plateau depends on the heating rate, the thickness of the board, density, and gypsum composition and occurs until $CaSO_4.2H_2O$ turns into anhydrous forms. The temperature range and period in which the dehydration process occurs diverges to a great extent according to the type of gypsum panel, the content of impurities, heating rate and partial water vapour pressure [26,27]. Besides that, since the dehydration process is an endothermal reaction, it is responsible for partially absorbing the heat generated in a fire event, avoiding early overheating of the unexposed board's surface and contributing to the insulation and integrity performance of LSF walls [25,28]. Additionally, through late endothermal reactions, calcium carbonate and magnesium carbonate decompose at 600-800 ºC.

In an LSF wall, because of the variability of the gypsum plasterboard composition and the different types of heat transfer that occurs during a fire, the behaviour at elevated temperatures of their thermophysical properties such as specific heat, density, emissivity, thermal conductivity, and convection coefficient should be accurately determined or cautiously calibrated for modelling purposes in order to include the effects of gypsum plasterboard calcination, cracking behaviour, ablation and fall-off under standard fire conditions.

Concerning the emissivity and convective coefficient, there are no large differences encountered amongst the literature. The exposed and unexposed side emissivity is set around 0.8-1.0 at all temperatures and fire and unexposed side convective coefficients are about 25 W/m²/K and 9.0-10 W/m²/K, respectively, at all temperatures. As for the specific heat, density and thermal conductivity, the values tend to vary slightly depending on the test conditions in which they were determined, gypsum manufacturing process, composition, and partial water vapour pressure. Gunawan (2011) [29] and Keerthan and Mahendran (2012) [9] investigated variations encountered in the literature for thermal properties of gypsum plasterboards and according to their findings, specific heat values tend to agree for the first dehydration peak

(~125 ºC), but inconsistencies were found regarding the temperature in which the second dehydration ensues. It should be noted that, if water vapour pressure is negligible, the second dehydration peak will likely not occur and vice-versa [26]. As per Keerthan and Mahendran's (2012) [9] findings, no large differences can be seen for the temperature in which calcium carbonate or magnesium carbonate decomposes, and for gypsum boards with $CaCO_3$, that temperature tends to remain at ~670 ºC. Regarding thermal conductivity, the values found agree up to 400 ºC and differences after that point are due to plasterboard's shrinking behaviour and whether ablation and fall-off effect were properly accounted for or not. In terms of density, different types of plasterboards have varied densities, but overall, an expressive drop in density values is found at the temperature in which the first dehydration reaction takes place, remaining approximately constant after that point.

2.2.1.2 Fall-off and Joint Effect

As the calcination progresses, after most of the dehydration process occurred, gypsum turns into weaker forms, which drastically reduces its strength and shrinkage resistance, eventually leading to ablation and further partial or full plasterboard fall-off. Such integrity problems are also aggravated by board tearing due to shear forces at the fasteners and screw pull out. The fall-off of the gypsum plasterboard, on the fire-exposed side, quickly increases the temperature of the steel elements and the heat flux through the wall and thereby is of greatest importance in terms of fire resistance. For thermal modelling purposes of LSF walls under standard fire conditions, fall-off effect can be evaluated by using adequate effective thermal conductivity values, experimental data input or in some cases the gypsum plasterboard is removed from the model at an appropriate time (killing elements, for example).

As concluded by Mahendran and Kesawan (2015) [30], who conducted standard fire tests on insulated and non-insulated load-bearing LSF walls made of CFS frame covered with dual gypsum sheets, fall-off endurance seems to decrease when cavity insulation is employed, which according to Sultan and Kodur (2006) [14] and Kolarkar and Mahendran (2012) [31], this can be attributed to the fact that the insulation delays the heat transmission, keeping the fire-exposed plasterboard hotter and supported. Analogous remarks were observed by Kolarkar and Mahendran (2012) [31] for non-load-bearing walls with similar configurations and additionally, in their experimental tests, plasterboard fall-off did not occur in uninsulated assemblies with single plasterboard. Furthermore, Chen et al. (2013) [32], in their study of the fire resistance of full-scale load-bearing stud walls externally insulated on the fire-side with

aluminium silicate wool sandwiched between two gypsum sheets, found that a higher screw-to-panel edge distance can help avoid complete fall-off of the outer gypsum board on the fire-side. Also, the fall-off of the plasterboards can be prevented by screw fastening until a certain point. Nonetheless, at high temperatures board tearing and screw pull out may reduce significantly the ability of the fasteners to retain the board in place [11].

Another detrimental effect of fire exposure is the intensive heat flux through the joints of plasterboards, which causes a localized temperature rise on steel members, increasing thermal bowing deflection, i.e. as a result of differential thermal expansion, the steel stud tends to bow towards the furnace or ambient side, thus reducing its load-bearing capacity, especially in assemblies with a single protection layer. Overall, as concluded by Kodur and Sultan (2006) [14] double plasterboards with staggered joints improve the thermo-structural performance of loaded LSF walls, reducing the damaging consequences of plasterboard joints and early overheating of the wall's surfaces. Also, despite leading to higher steel thermal gradients and intensifying fall-off of gypsum boards, cavity insulation is beneficial in assuaging the joint effect [30].

Moreover, Kolarkar and Mahendran (2012) [31], based on a series of full-scale unloaded LSF wall panels, stated that joints do not affect significantly the insulation performance of non-insulated assemblies protected with one fire-resistant gypsum board on both sides. Additionally, Ariyanayagam et al. (2016) [33], also confirmed that such joints have little importance in the temperature profile of the unexposed side plasterboard of non-load-bearing single-lined uninsulated stud wall configurations. Thus, it can be inferred that, in terms of insulation, plasterboard joints may not affect significantly the fire resistance of non-load-bearing walls [33].

Gunalan and Mahendran (2013) [34] were able to include the joint effect in their numerical simulations by using stud average temperatures from experimental results of load-bearing walls, but predicting the behaviour of plasterboard joints is complicated since it depends on the level of workmanship and characteristics of the joint sealants and tapes, then further research is necessary to include the joint effect directly in numerical simulations. In addition, the construction of small-scale specimens usually does not include any joints, given the standard size of most commercial plasterboards available.

2.2.2 Thin-Walled Cold-formed Steel

Cold-formed Steel sections are usually thinner than the hot-rolled ones. In real fires with varying temperatures, the structural behaviour and strain distribution of thin-walled CFS is quite complex and non-uniform, which results in a severe reduction of its bearing capacity with stresses below the yield strength. Thus, studs will likely fail in distinct types of instability modes, such as local, distortional, flexural, and flexural-distortional buckling (Figure 2.2b). Even in non-load-bearing walls, because of thermal actions and support restraints, axial compressive efforts and bending stresses will be developed over the steel profiles and potential buckling modes may be observed when performing standard fire tests. Additionally, thermal bowing of the steel parts due to thermal gradients (Figure 2.2a) may become a huge concern in terms of load-bearing endurance and integrity performance of LSF walls.

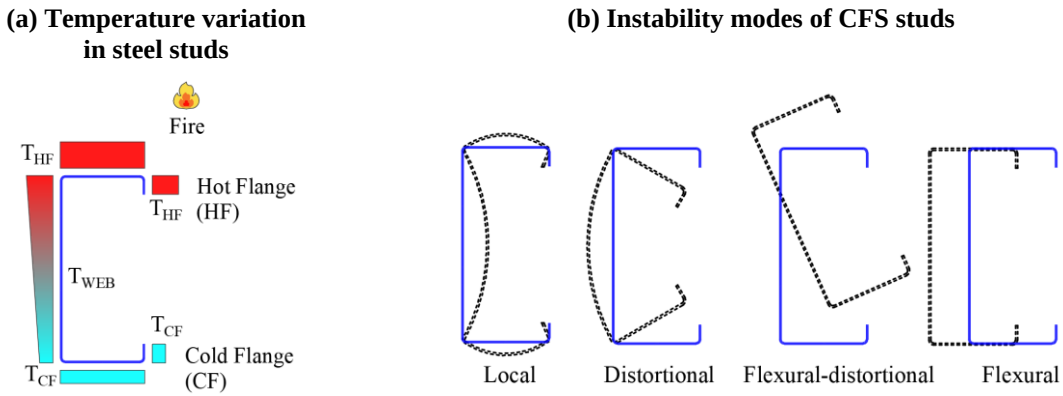

Figure 2.2 – Temperature distribution in a CFS stud profile and stud potential failure modes under fire.

Figure 2.2a shows a typical simplified temperature distribution along the cross-section of a CFS lipped stud in a fire event. For non-insulated cavities, if the joint effect is negligible and measurements are taken before plasterboard fall-off, then it can be assumed that there is a linear temperature variation over the depth, width and thickness of the steel, thus the stud size usually does not influence in the early stages of the temperature evolution along the cross-section of a wall under fire [11,35]. However, plasterboard fall-off, joint and insulation effects increase the steel temperature gradient along its cross-section, and in the case of cavity-insulated walls, steel may act as a thermal bridge and impact the wall's overall thermo-structural behaviour. For modelling purposes, Feng et al. (2003) [35], Gunalan and Mahendran (2013) [34] and Ariyanayagam and Mahendran (2014) [36] have demonstrated that the steel

temperature distribution shown in Figure 2.2a can be successfully used for structural and thermal modelling of several configurations of LSF walls, as long as localised temperature rises in the steel are properly accounted for. The size and shape of CFS parts tend to affect more significantly the structural performance of LSF walls, given that slenderness, thickness and stiffness of different profiles and changes in their thermomechanical properties at elevated temperatures are directly linked to their bearing capacity and structural failure modes.

Regarding thermal properties, carbon steels present a typical evolution in the specific heat with a maximum value that corresponds to allotropic transformation at around 700-800 °C. The thermal conductivity decreases up to 800 ºC because of the intensification of electron scattering as the temperature rises, remaining constant after that point. The density remains constant at 7850 kg/m³. The thermal properties may vary amongst carbon steels on account of different chemical compositions, but as concluded by Craveiro et al. (2016) [37], who assessed the transient state thermal and mechanical properties of low-strength CFS S280GD at temperatures ranging from 20 to 800 °C, the values for thermal conductivity preconized by EN 1993-1-2 [38] are over-conservative, whereas the experimental values obtained by the authors for the specific heat tends to agree reasonably with the Eurocode. Moreover, EN 1993-1-2 [38] establishes that, when no experimental data are available, the emissivity of carbon steels should be taken as 0.7 constant.

2.2.3 Ceramic Fibre Insulation

In terms of fire behaviour, insulation materials are used to avert extreme temperature rise of the unexposed side of LSF walls, providing enhanced insulation performance. Nevertheless, cavity insulation tends to increase the thermal gradient along the cross-section of the steel frame as the hot-flange will heat faster than the cold-flange due to the small thermal conductivity of the insulation, thus inducing thermal bowing deflections and higher thermal stresses, which decreases the fire resistance of the wall regarding structural performance. Apart from load-bearing adequacy, according to Ariyanayagam and Mahendran (2019) [39] tests, the fire resistance of full-scale unloaded LSF walls was enhanced by 12 min when glass fibre cavity insulation was employed, but the insulation started to melt after 45 minutes at 650 ºC, which suggests that insulation with a higher melting point should be used for better insulation behaviour (e.g. rock wool and ceramic fibre).

Ceramic fibre is employed as insulation in applications that demand or generate high temperatures and it is available in several shapes, such as blankets, ropes, additives, boards, and papers and its main components are silica-alumina arrangements. For LSF walls, blankets are frequently used. Lightweight, low density, high melting point (>1000 ºC) and low thermal conductivity are features that make ceramic fibre quite attractive in terms of the energy performance of LSF walls. Furthermore, ceramic fibre's recyclability and fire-retardant properties contribute to energy saving and enhanced fire performance in buildings.

The thermophysical properties of the ceramic fibre depend mainly on its composition and manufacturing process in which the fibres are pressed to achieve different densities, being blankets the lightest ones. Overall, thermal conductivity tends to increase with temperature and density because of changes in the porosity of the ceramic fibre, which can reach up to 90%, and increased radiation effects over temperature rise due to ablation and voids in the insulation. As for the specific heat, it remains approximately constant, since the melting point of most ceramic fibres are usually higher than 1100 ºC and their moisture content is negligible.

2.3 Literature Review Findings

2.3.1 Single Stud LSF Walls

Gerlich et al. (1996) [15] conducted fire tests on conventional uninsulated load-bearing LSF walls single-layered with glass fibre-reinforced gypsum boards. They modelled the temperature distribution of the specimens under standard and real compartment fire scenarios to predict CFS stud failure. The authors were not able to include mass transfer mechanisms and cracking behaviour of gypsum panels, thereby inaccuracies were shown in the unexposed side plasterboard surface temperature below 120 ºC and the model did not seem to work properly for very high temperatures, owing to integrity failure of the gypsum plasterboards and high steel thermal deflections, which led to an extreme temperature rise in the wall. Overall, modelled temperatures for the steel elements were higher than those obtained experimentally, indicating higher thermal gradients in the model and overpredicting the stud mid-span deflection related to thermal expansion and second-order effects.

Sultan (1996) [40] proposed a one-dimensional model to simulate the surface temperature of unloaded non-insulated CFS stud wall assemblies protected with Type X gypsum plasterboards on the exposed and unexposed side. The thermal properties of the gypsum boards were determined experimentally. In the thermal model developed, conduction in the steel was considered insignificant by reason of its small thickness (0.46 mm) and the radiation contribution from the steel surfaces was neglected. Also, the heat absorbed by the dehydration of gypsum boards was included, but fall-off and ablation were disregarded, as well as the heat lost to the air cavity. The proposed model, based on the finite difference method, was validated according to experimental tests and the obtained results represented reasonably the surface time-temperature curves up to 600 ºC when the gypsum board on the fire-exposed side started to present integrity issues, such as cracking, ablation and spalling. Additionally, it was identified that in the first 10-15 minutes of the experimental fire tests, the measured temperatures on the surfaces of the gypsum plasterboards facing the cavity were higher than the predicted ones because of the forced convection and radiation mechanisms induced by the furnace flames, which tends to be more intensive at the commencement of the test so as to represent the post flashover phase of a standard fire.

Sultan and Kodur (2000) [41] analysed the parameters influencing the fire resistance of conventional full-scale unloaded drywall assemblies under standard fire conditions. Tests 1 through 4 were clad with one Type X plasterboard on the fire-side and two on the unexposed side. Glass fibre, rock fibre and cellulose fibre insulation (wet-sprayed), all 90 mm thick, were employed in Tests 2, 3 and 4, respectively. Test 1 was non-insulated. The results showed that Test 3 performed better than Test 1 (54 % higher fire resistance) because the insulation delayed the average temperature rise on the unexposed side of the cavity side plasterboard, remaining integral even after spalling of the fire-side plasterboard. However, Test 2's thermal behaviour was the same of Test 1's, that is, glass fibre insulation seems to have little effect on the thermal behaviour of LSF walls at high temperatures, probably due to the loss of its integrity. In the standard tests realized by Keerthan and Mahendran (2013) [42], the glass fibre insulation sandwiched between two fire-resistant gypsum plasterboards, melted when the cavity insulation interface temperature approached 700 ºC, regardless of the insulation thickness and density. Test 4's thermal behaviour was similar to that of Test 1's because since the cellulose fibre was wet-sprayed when the fire-side plasterboard fell off, insulation was no longer provided to the cavity. The authors also stressed the importance of fixing the insulation tightly in the cavity between the studs, preventing it from falling off at high temperatures.

Alfawakhiri and Sultan (2000) [43] proposed an analytical fire resistance model for load-bearing LSF walls based on experimental data from six standard fire tests. Each wall consisted of 8 central C-shaped CFS lipped studs. The stud frame was protected with double 12.7 mm thick Type X fire-resistant gypsum sheets on each side. The assemblies were either non-insulated and insulated with glass fibre blankets, rock fibre blankets and dry blown cellulose. All specimens failed under the load applied and no insulation failure was observed for all tests at structural failure, which indicates that non-load-bearing similar assemblies could achieve additional FRR in terms of insulation. The authors also noted that cavity insulation increases the steel thermal gradient, especially in the central studs where the temperature raised significantly faster when compared to the studs at the wall ends, thus leading to higher thermal deflections in the cavity-insulated assemblies, whereas non-insulated cavities present a more uniform steel temperature distribution. Moreover, in their one-dimensional thermal model, the authors ignored the presence of the steel frame because steel thermal properties and lightweight features have negligible influence in the heat transfer mechanisms. The thermal properties of the gypsum plasterboard were adapted to include its moisture content and phase change, and to consider the issues encountered by Sultan (1996) [40], the fall-off was modelled by removing the gypsum plasterboard from the simulation at a time determined based on the fall-off occurrence observed in the experimental tests. The modelled temperatures were used to predict the structural failure of the steel studs and the results showed a reasonable agreement with the experimental findings, although predicted and experimental failure times diverged for cavity-insulated assemblies.

Feng et al. (2003) [35] studied the experimental and numerical behaviour of small-scale LSF wall panels under standard fire. The symmetrical assemblies were either non-insulated or insulated with 100 mm thick mineral wool and clad with 1 or 2 layers of 12.5 mm thick fire-rated plasterboards. The steel frame was comprised by lipped and unlipped CFS stud sections. Overall, assemblies with two plasterboards, with and without cavity insulation, did not present insulation and integrity failure even after 2 hours of fire exposure. Assemblies with one gypsum sheet and with mineral wool insulation also performed well at temperatures up to 1 hour. As predicted, cavity insulation increased the thermal gradient across the steel sections due to insulation effect. Concerning the numerical simulation conducted, the thermal properties of the gypsum board were validated using ABAQUS and steel and mineral wool properties were taken from Eurocode 3 Part 1-2 [38] and manufacture's specification, respectively. The comparison between the results obtained experimentally and those simulated for the surface temperature

and steel thermal gradient showed a good agreement for non-insulated specimens. However, cavity-insulated tests displayed higher simulated steel thermal gradients, which is possibly due to the assumed perfect contact between the insulation and the steel interface and uncertainties about the insulation's thermal properties. In real assemblies, voids between the insulation and the steel interface, as well as the ablation of the insulation, increase the radiation effects in the cavity, thereby contributing to a more uniform temperature variation in the steel. Also, for all cavity-insulated specimens, mineral wool remained intact throughout the test. Furthermore, it was found by way of parametric analysis that the high thermal conductivity of the steel affects significantly the heating rate of the unexposed board, decreasing the time to reach insulation failure, which contradicts the assumptions made by Sultan (1996) [40] and Alfawakhiri and Sultan (2000) [43] in their thermal models. That hypothesis is later corroborated by Dias et al. (2018) [44] whose studies indicated that for unloaded cavity-insulated walls, insulation failure time should be determined based on the temperatures of the unexposed plasterboard at the stud locations, rather than at its overall surface. The parametric analysis developed by Feng et al. (2003) [35] allowed the authors to conclude that the section thickness and short lip widths hardly affect the temperature development on the unexposed side of LSF wall panels. Thus, the steel temperatures tend to be more expressively influenced by the presence of insulation material in the wall's cavity rather than their shape and thickness.

Later on, Kolarkar and Mahendran (2012) [31] carried out extensive research on the thermal performance under standard fire of small-scale partition LSF walls with the same steel configuration, comprised by high-strength CFS lipped studs. The assemblies had 1 or 2 layers of fire-resistant gypsum panels on each side and were either non-insulated or cavity-insulated with rock fibre, glass fibre and wet-sprayed cellulose. Non-insulated assemblies with one and two gypsum layers failed as per insulation criterion but did not exhibit gypsum plasterboard fall-off in the fire-side and the studs remained in a good condition after the test. Additionally, for the specimen with one gypsum plasterboard, the joint effect was considered negligible to the insulation performance of the wall, although it pointedly affected the temperature profile of the stud in direct contact with it. On the contrary, assemblies with cavity insulation and double plasterboards did not show insulation failure but fall-off of the gypsum plasterboard in the fire-side was noticed for all specimens after the average temperature between the plasterboards on the exposed side reached 950-1000 ºC, attributable to the reduced heat flow in the insulation. Moreover, insulation amplified the heating rate of the stud's hot flange, thus stud thermal bowing was significant and local buckling of the hot flange was observed in the central stud.

Rock fibre, despite inducing the highest thermal gradients in the steel, provided improved insulation performance when compared to cellulose and glass fibre. Overall, due to the prolonged dehydration mechanisms in the gypsum, the use of two plasterboards supplied around 60 minutes of initial fire protection, whereas for single plasterboards it was only 20 minutes.

Poologanathan and Mahendran (2012) [45], through experimental and numerical studies using SAFIR, assessed the influence of various parameters on the thermal performance of assorted full-scale load-bearing CFS stud walls configurations subjected to AS 1530.4 [46] standard fire curve. Their proposed model predicted the average temperature profile of the walls with sensible accuracy when compared to the experimental results, even at higher temperatures, when insulation and lining materials experience integrity issues, which affect negatively thermal models, as seen in the studies led by Sultan and Kodur (2000) [41] and Feng et al. (2003) [35]. The integrity loss of gypsum plasterboard and insulation were modelled by using suitable effective thermal properties based on a series of experimental results and past research, which contributed to achieving enhanced modelled results. Further, their finite element analysis also allowed to confirm the damaging effect of cavity insulation on the structural performance of LSF walls. By means of parametric analysis, it was verified that the shape and depth of the CFS elements do not influence their temperature profile and has little significance on the overall thermal performance of non-insulated LSF wall panels.

Nassif et al. (2014) [47] modelled the temperature distribution of a full-scale unloaded CFS stud wall, cavity-insulated with rock wool and clad with double gypsum plasterboards on both sides. The gypsum specific heat values were taken from Sultan (1996) [40], which considered the dehydration reactions. Nevertheless, in contrast with the remarks made by Poologanathan and Mahendran (2012) [45], thermal conductivity was assumed constant after 800 ºC, thus inaccuracies are found in the temperature distribution of the steel and gypsum elements after 700 ºC because of plasterboard fall-off on the fire-side. Cavity insulation was assumed to fill the wall's cavity and good agreement was obtained between the calculated and measured temperatures for the stud hot and cold-flanges, with a reasonable prediction of its thermal bowing displacements.

Thanasoulas et al. (2016) [48] simulated the thermomechanical behaviour of CFS drywall systems protected with 1 or 2 layers of fire-resistant gypsum sheets with an air cavity or mineral wool cavity insulation. The cavity behaviour was modelled assuming the "air conducting body" hypothesis, considering the thermophysical properties of the air. Therefore,

slight differences between the experimental and modelled temperatures for the cavity-side of both exposed and unexposed plasterboards were encountered, suggesting that supplementary appropriate boundary conditions should be considered to simulate the thermal behaviour of the air cavity. Ariyanayagam and Mahendran (2017)'s [49] work and various past researches demonstrated that the air cavity can be successfully modelled by defining convection and radiation at its boundaries. Unexpectedly, the use of mineral wool insulation did not affect the structural response of the LSF models tried, as the temperature gradients found for insulated and non-insulated assemblies were comparable, whereas the use of a single or double plasterboard affected expressively the time to reach structural failure.

Rusthi et al. (2017) [50] developed 3D finite element models to better evaluate the fire performance of LSF walls exposed to ISO 834 [17] standard fire curve. According to the authors, a 3D model would contribute to fully comprehend parameters that are not regularly accounted for in 1D and 2D simulations, such as the influence of noggin tracks, diverse steel and cavity shapes, service holes and mixed boundary conditions. The thermal properties used included the thermophysical behaviour of gypsum plasterboards and insulation at high temperatures, i.e. integrity loss, dehydration, ablation and fall-off. Steel thermal properties were taken from Eurocode 3 Part 1-2 [38]. Conduction was defined using the thermal properties of the materials. The emissivity was 0.9 constant for all enclosures throughout the simulation and as for convection, film coefficients of 10 and 25 W/m²/K were assigned for the unexposed and exposed sides, respectively. Perfect contact between the plasterboards and the steel elements was assumed. For non-insulated assemblies, as radiation tends to be the major heat transfer mechanism in air cavities, conduction and convection were negligible in that region. The plasterboard transient time-temperature history showed a remarkedly good agreement with experimental tests, even for cavity-insulated assemblies. The model also provided accurate steel temperatures, allowing the prediction of failure modes and the critical temperature of the hot-flange. The thermal model was effectively implemented in a coupled thermo-mechanical parametric analysis, yielding adequate results for various load and non-load-bearing models.

More recently, Chen et al. (2018) [51] proposed an alternative methodology to address the integrity behaviour of fire-resistant gypsum plasterboards in LSF walls and composite panels. In their analysis, instead of using the direct thermal conductivity measured using the heated approach, which is the common practice, the plasterboard is heated beforehand and then a transient-state thermal conductivity measurement is carried out. Experimental tests were conducted and for the steel stud assemblies clad with 2 gypsum plasterboards on both sides

with a cavity partially insulated with 35 mm thick rock wool in contact with the fire-exposed side, local buckling of the stud web and fall-off of the fire-exposed plasterboard were observed, owing to insulation effect. A 2D model using ABAQUS was developed using similar boundary conditions presented by Rusthi et al. (2017) [50], except emissivity, taken as 0.8 for all enclosures. To simulate plasterboard fall-off the authors employed the birth-death element technique, which consisted of removing the fire-side exposed plasterboard when its surface temperature reached 690-750 ºC (critical temperature). Except for the temperatures around the cavity, the simulated results presented a good agreement with the fire tests and showed the measured post-heated thermal conductivity of plasterboards can be used adequately in numerical simulations. Furthermore, Chen et al. (2018; 2019) [51,52] also stated the improved insulation performance of aluminium silicate-based mineral wool when compared to rock wool under the same fire conditions and assembly configurations.

Ariyanayagam and Mahendran (2018) [53,54] developed standard fire tests on full-scale loaded and unloaded LSF walls to inspect the effects of cavity insulation (glass fibre), noggins and number of gypsum plasterboards on their structural and thermal performance. It was verified that cavity insulation decreased the FRR of load-bearing LSF assemblies, whereas the employment of horizontal noggins increased the FRR due to the reduction in studs' lateral deflections. Moreover, for unloaded assemblies, the noggin proved to be negligible to their insulation performance, but it was found that an increase in the gypsum board thickness by 3 mm (13 to 16 mm) led to a rise of 30 minutes in the insulation fire resistance of uninsulated walls with one gypsum plasterboard. Furthermore, using two layers of gypsum sheet on each side of the uninsulated walls increased their insulation resistance by 100 minutes when compared to single-layered similar assemblies. Also, glass fibre insulation provided only 12 minutes rise in the insulation failure of the walls. Consequently, insulation materials with enhanced integrity behaviour, such as ceramic wool and rock wool should be employed in LSF walls for better insulation performance.

Thanasoulas et al. (2018) [55] used parametric studies to assess the effect of the mineral wool insulation in the fire resistance of loaded LSF walls. All assemblies were covered with double fire-resistant gypsum panels on each side. Surprisingly, the assembly that was fully cavity-insulated with mineral wool presented the highest load-bearing endurance when compared to specimens partially insulated and uninsulated. Additionally, concerning the partially insulated assemblies, when the insulation was placed towards the fire-exposed plasterboards, an improved fire resistance rating was observed, which was attributed to the high

heat absorptivity of the mineral wool and heat dissipation to the remaining air cavity. Conversely, if the insulation is placed facing the unexposed side, a quick temperature build-up will be developed on the exposed side. However, in more recent experimental and numerical studies, Dias et al. (2018) [44] and Ariyanayagam and Mahendran (2019) [13] concluded that fully cavity-insulated assemblies, clad with single and double plasterboards, despite having enhanced insulation performance, display a lower load-bearing endurance when compared to uninsulated walls, although only glass fibre and rock wool were included in their analysis. The differences observed may be due to integrity behaviour of the insulation materials used. Therefore, the thermal and structural performance of LSF walls seems to be affected not only by the employment of cavity insulation, but by its type and whether the cavity is fully or partially insulated towards the exposed or unexposed side.

The fire performance on LSF walls is also being investigated at the Polytechnic Institute of Bragança (Portugal) with the aim of developing accurate numerical models based on the thermal analysis with fluid-structure interaction [56]; validate the numerical models with experimental tests developed elsewhere [57], and herein; analysing the fire performance of LSF structures using the simplified one-dimensional heat flow [58] and; presenting a sequential numerical model to study the fire resistance of LSF walls made with composite panels [59].

The last published work [60] presents seven small-scale specimens that were tested to define the fire resistance of non-load-bearing LSF walls made with different materials. All tests were validated using two-dimensional numerical models, based on the finite-element method, the finite-volume method and hybrid finite-element method. A good agreement was achieved between the numerical and the experimental results from fire tests. The fire resistance increased with the number of studs and with the thickness of the protection layers. The hybrid finite-element method solution method seems to be the best approximation model to predict fire resistance.

Regarding simplified approaches to estimate the structural and thermal behaviour of LSF walls at elevated temperatures, Wang and Shahbazian (2014) [61] conducted a finite-element 2D thermal analysis to predict the cross-section temperature of cavity-insulated LSF walls with different stud sections lined with gypsum plasterboards and subjected to diverse parametric fires. The study is based on the work of Wang and Shahbazian (2013) [62], who found that the temperature distribution in the steel varies roughly linearly between the hot and cold sides, allowing the authors to devise a simplified 1D thermal model based on the finite difference method and weighed averages of the thermal properties for a specific region of the

wall, which considered the presence of the steel studs. The simplified results differed in 6 % when compared to the finite-element analysis, with a standard deviation of 8.54 %. Similarly, in the work developed by Piloto et al. (2017) [58], a one-dimensional simplified approach founded on the finite-difference and lumped thermal analysis was proposed to predict the temperature field of cavity-insulated assemblies. The models were designed using effective material thermal properties and considered the influence of the steel sections on the temperature development of the unexposed surface of the gypsum plasterboard. The simplified results agreed well with the numerical data from ANSYS.

Gunalan and Mahendran (2014) [63] considered idealised time-temperature profiles of steel studs for several assemblies of LSF walls with and without insulation layers and lined with gypsum plasterboards. The idealised average time-temperature profiles of the steel sections were formulated based on the measured temperatures of the hot and cold flange from experimental tests, and were further employed to carry out numerical simulations and parametric studies to predict the critical temperature of LSF wall studs under standard fire condition. The comparison between the fire resistance (stud failure time) using numerical simulations and the proposed simplified method agreed well for the models tried under different load ratios.

The accuracy of simplified methods to predict the thermal and structural failure of LSF walls under fire conditions relies mostly on experimental data and whether the cavity of the walls is filled with insulation material or not. In this sense, a broader approach is necessary to investigate the effects of void cavities, the position of the layers in the assembly and common integrity issues related with LSF building structures.

2.3.2 Double-stud LSF Walls

As seen in section 2.3.1, several studies were conducted to assess the structural and thermal performance of conventional LSF walls under fire conditions, but just a few carried out extensive analysis on the performance of double row stud walls with diverse configurations.

Shoub and Son (1973) [64], analysed the fire resistance of full-scale load-bearing double-stud walls under a single load ratio (15 kN/m per wall module). The walls were 4.85 m long by 2.44 m high and specimen n°1 was comprised of two similar modular walls with an air gap between them. Both modules were made with CFS lipped studs and covered on their cavity

side and outer side with a single Type X fire-resistant gypsum plasterboard, respectively, and the cavity of each stud row was insulated, as shown in Figure 2.3.

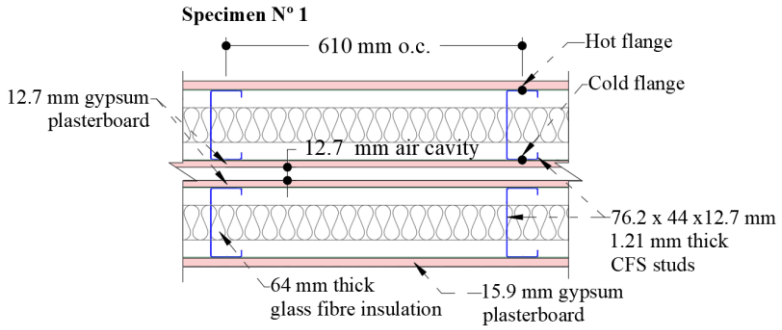

Figure 2.3- Double row stud wall tested by Shoub and Son (1973).

The specimen was subjected to a standard fire test according to ASTM E119 [65]. The fire-exposed module failed structurally at 42 minutes, shortly after fall-off of the fire-exposed plasterboard, and the fire-unexposed module lost its integrity after 1 hour and 13 minutes. The average temperature rise on the unexposed outer plasterboard was always smaller than 100 °C and did not reach the temperatures that characterize insulation failure. The early structural failure was due to the intensive heat flux through the joints on the fire-side plasterboard, exposing the steel studs and speeding up thermal bowing. Subsequently, crack openings, ablation and fall-off of the fire-exposed gypsum board were observed. The authors concluded that plasterboard joints are a significant weak spot and single plasterboard assemblies are not good enough to prevent early structural failure of the studs for a 1-hour FRR and that additional layers of staggered gypsum plasterboards would delay the intensive heat flux through the sheathing joints. Moreover, the space between the two modules proved to be irrelevant to the wall's overall thermal resistance. The effect of cavity insulation was not examined by the authors, but the results for the temperature profile across the steel cross-section of the exposed wall module shows that the average hot flange temperature after the first 20 minutes differs significantly from the cold flange temperature, representing a high thermal gradient and increased heating rate of the hot flange. At 40 minutes and further, thermal gradients decreased and the hot and cold flange temperatures rose substantially, matching at 45 minutes (750 ºC), indicating integrity loss of the glass fibre insulation. Structural failure of the unexposed wall module occurred at 42 minutes, right after the high thermal gradient observations (20-40 minutes) and exposed plasterboard fall-off. After 750 ºC, the thermal gradient decreased, since

the insulation had probably partially disintegrated, allowing for a more uniform heat transfer in the cavity. For the fire-unexposed wall module, the insulation possibly remained integral and the highest thermal gradients are seen only after 55 minutes, 18 minutes prior to buckling failure of the studs towards the fire.

Later on, Kodur and Sultan (2006) [14] carried out full-scale fire tests on load-bearing walls with double-stud rows made of CFS lipped studs with 92 x 41 x 12.7 mm and 0.912 mm thick set apart by a 7 mm gap. The walls were covered with both one and two layers of fire-resistant gypsum plasterboards on each side and the cavity was either non-insulated or insulated, as shown in Figure 2.4. The specimens had diagonal cross-bracing to provide better lateral stability and were under the same loading conditions.

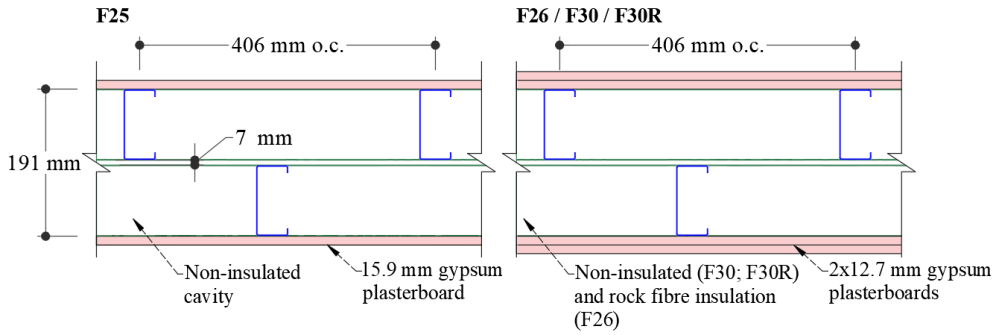

Figure 2.4- Double row stud walls specimens tested by Kodur and Sultan (2006).

For the whole testing-length, insulation failure was not detected for all test specimens, whilst structural failure occurred via local buckling. The specimens F30 and F30R lost their load-bearing capacity at 100 and 102 minutes, respectively, and specimens F26 and F25 failed at 84 minutes and 35 minutes, respectively. Thus, as observed for single stud LSF walls, the employment of rock fibre insulation and the use of a single layer of gypsum plasterboard proved to be detrimental to the structural behaviour of double-stud walls. It is noteworthy that the joint effect was minimized in double-layered assemblies by staggered joints. Additionally, it was observed that for the specimens F30 and F30R, the cavity side board on the fire-exposed side remained in place during the test, which stresses the enhanced integrity behaviour of non-insulated double-layered assemblies. Further, it was verified that uninsulated double row stud walls have on average 20% (F30) to 22% (F30R) higher structural performance when compared to specimen F39 (single stud row, double-layered, uninsulated), which failed at 83 minutes with a load ratio that was half of that used for the double-stud specimens. The authors attributed this

effect to the enlarged cavity size of the double-stud wall assemblies, which slows the heat transfer mechanisms. Thermal bowing towards the furnace and away from the furnace was observed for non-insulated and insulated assemblies, respectively. No remarks were made concerning the air gap between the stud rows.

More recently, Magaraboosanam et al. (2019) [66] investigated the performance of full-scale load-bearing double-stud walls made of G550 lipped CFS studs lined with two layers of fire-resistant gypsum plasterboards exposed to the standard fire curve from AS 1530.4 [46]. As described in Figure 2.5, the stud rows were set apart by a 20 mm air gap. Specimens T1 and T2 were subjected to a load ratio of 0.4, whereas for specimen T3 the load ratio was 0.6.

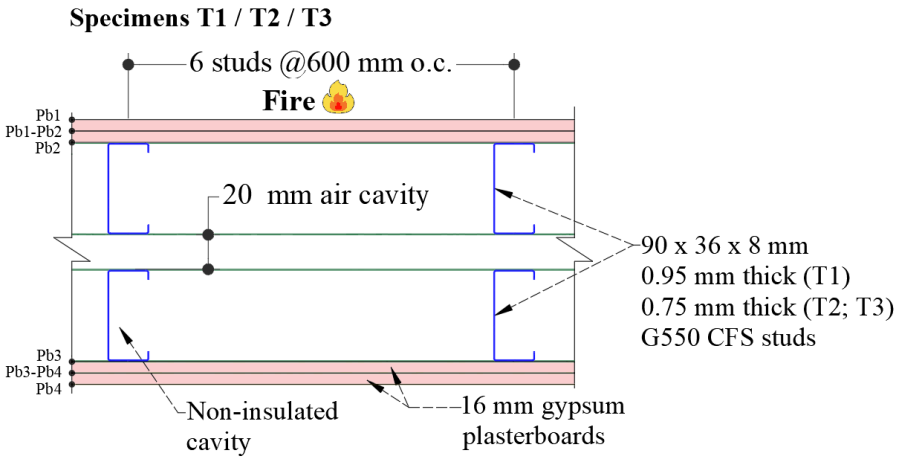

Figure 2.5- Double row stud walls specimens tested by Magarabooshanam et al. (2019).

At the end of the fire test, all specimens did not present insulation failure, analogous to the conclusions encountered by Kodur and Sultan (2006) [14]. The average thermal gradient between Pb2 and Pb3 was higher for specimen T2 when compared to T1, possibly due to plasterboard fall-off in specimen T2. Moreover, the presence of a wider cavity was essential to boost the insulation performance of specimens T1 and T2, since large temperature plateaus were noticed for the average temperature of Pb1-Pb2 between 80-120 minutes, which means that more heat is being transferred to the cavity. Consequently, the average temperature of Pb4 also presented a large temperature plateau within the same period. Such behaviour does not apply to specimen T3, as its structural failure occurred much earlier than that of tests T1 and T2. Regarding steel temperatures, the gap between the stud rows restrained the heat flux through conduction in the steel, thus more heat is transferred by radiation and convection to the cavity. The presence of a wider cavity and a gap between stud rows were held accountable for the

better insulation performance of the wall, irrespective of the steel thickness and load ratio, which contradicts Shoub and Son (1973)'s [64] conclusions on the role of the air gap between the stud rows in delaying the heat transfer mechanisms in the cavity. Also, the double-stud walls presented higher load-bearing capacity and enhanced thermal insulation when compared to single row stud walls under the same load ratio.

Since a single wall set-up was tested, the effects on the thermal performance of double-stud row LSF walls using different layers of gypsum plasterboards, low-strength CFS elements and diverse cavity configurations remains scarcely understood and further experimental tests and numerical investigations are needed.

Chapter 3

3 Experimental Standard Fire Tests

Double-stud LSF walls present a unique thermal performance at elevated temperatures when compared to single-stud assemblies, which is mainly due to the enlarged cavity size and the gap between the stud rows. However, the behaviour in standard fire conditions of different configurations of double-stud LSF walls, e.g. cavity insulation arrangements and the number of protective layers, is poorly understood. Thus, experimental tests are necessary to determine the fire resistance of these walls and provide comparative results to support further numerical analysis and fire design guidelines.

In this chapter, detailed information on the test assemblies and experimental standard tests conducted to assess the thermal performance at elevated temperatures and fire resistance of small-scale double-stud non-load-bearing LSF walls with and without ceramic fibre cavity insulation and lined with one or two protection layers are presented. The test observations and results are discussed and compared and the time-temperature profiles and insulation fire resistance time (I) is obtained for each assembly.

3.1 Test Specimens

The experimental program consisted of five asymmetrical small-scale specimens, each measuring 975 mm in width and 1000 mm in height. Table 3.1 presents the configurations of the specimens. The fire-exposed side of all specimens is the one shown for Specimen 1. The wall panels were either single or double-layered with gypsum plasterboards on both exposed and unexposed sides and the wall cavity was uninsulated, fully insulated, or partially insulated with ceramic fibre. The steel frame configuration was the same for all specimens. Extensive specifications concerning the materials, dimensions and fastening details of each specimen are available in Appendix A and Appendix B.

All experimental procedures were performed at the Laboratory of Structures and Mechanics of Materials of the Polytechnic Institute of Bragança. The standard fire tests were conducted by exposing one side of the specimen to ISO 834 [17] standard fire curve in a natural gas-fired furnace, running with four burners with 90 KW each, using a PID controller based on the temperature reading of one plate thermocouple. The assessment of the fire resistance and thermal performance of the walls, test set-up requirements, equipment and procedures were based on the stipulations of the European standards, namely EN 1363-1 [16] (Fire Resistance Tests – General Requirements) and EN 1364-1 [19] (Fire Resistance Tests for Non-load-bearing Elements- Walls).

Table 3.1- Configurations of the double-stud LSF wall specimens.

Test Nº	Insulation	Specimen Configuration	Objective
1	-	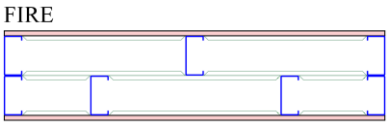	Investigate the thermal behaviour of a double-stud row in a wall specimen protected with one layer of gypsum plasterboard (1x1)
2	-	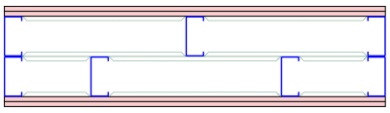	Investigate the thermal impact of additional protection layers in a specimen protected with two gypsum plasterboards (2x2)
3	Ceramic fibre	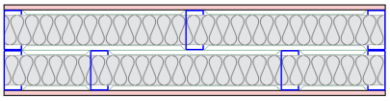	Investigate the thermal impact of full ceramic fibre cavity insulation in a wall specimen protected with one layer of gypsum plasterboard (1x1)
4	Ceramic fibre	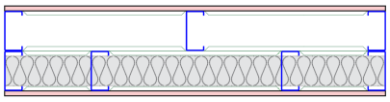	Investigate the thermal impact of partial ceramic fibre cavity insulation placed towards the unexposed side in a wall specimen protected with one layer of gypsum plasterboard (1x1)
5	Ceramic fibre	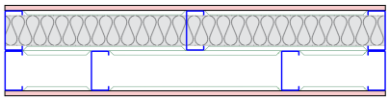	Investigate the thermal impact of partial ceramic fibre cavity insulation placed towards the fire-side in a wall specimen protected with one layer of gypsum plasterboard (1x1)

3.1.1 Steel Frame

Figure 3.1 shows the schematic details and specifications of the steel frame assembly and its elements. The steel frame configuration was composed of seven studs connected to tracks at the top, mid-height, and bottom portions of the framework. The studs and tracks are Class 4 C-shaped lipped sections made of S280GD galvanized steel with a nominal thickness

of 1.0 mm and minimum nominal yield strength of 280 MPa. The stud to track connections were executed using 4.2 x 19 mm wafer head self-drilling screws. The stud spacing and labelling are depicted in Figure 3.2, which illustrates a cross-section of Specimen 4, obtained from a cutting plane at 300 mm from the wall's bottom side.

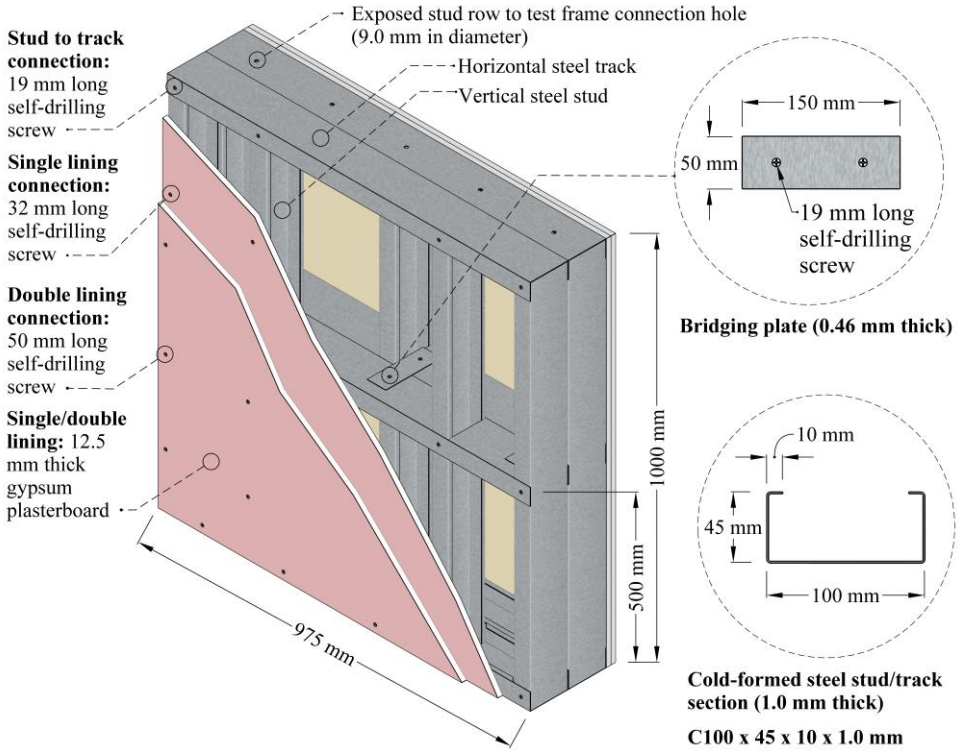

Figure 3.1- Schematic steel frame and lining details (specimen 2).

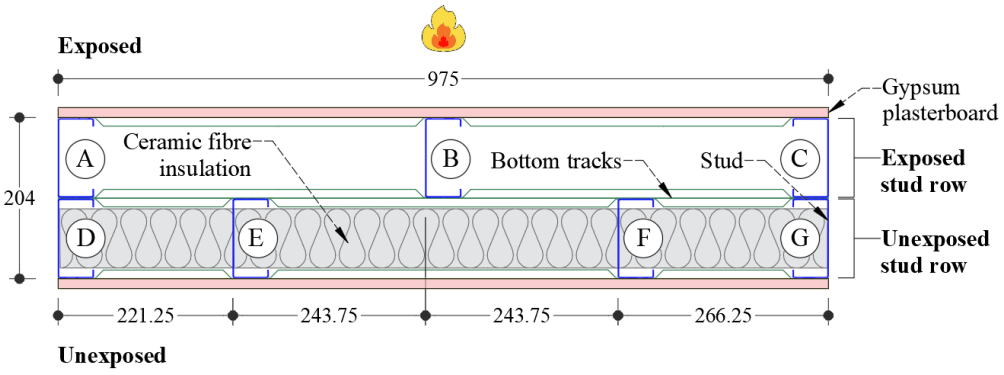

Figure 3.2- Stud locations in the steel frame and wall components (specimen 4).

As shown in the previous Figure 3.1 and the next Figure 3.3, the bridging between the stud rows was accomplished via three rectangular galvanized steel plates with a nominal thickness of 0.46 mm, attached alongside the mid-height set of noggin tracks by 4.2 x 19 mm

wafer head self-drilling screws. Furthermore, as the unexposed stud row remained projected from the test frame throughout the experimental procedure (Figure 3.3), the connections between the flanges of studs A, D and C, G, situated at the wall ends, were made via two 5 x 16 mm bolts with hexagonal heads for each pair of studs. Further details are thoroughly clarified in Appendix A.

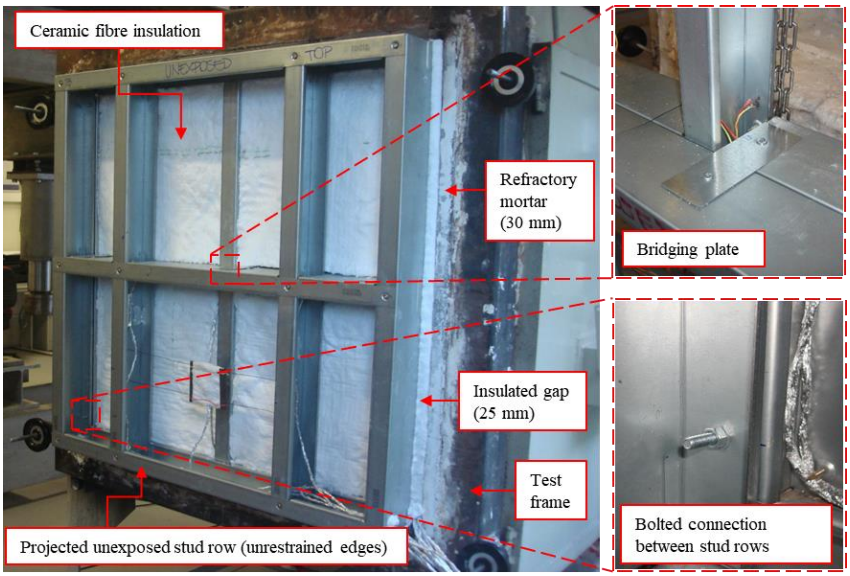

Figure 3.3 – Furnace apparatus, test frame and connection details of the steel frame (specimen 5).

3.1.2 Sheathing and Insulation

The walls were protected on both sides with one or two layers of 12.5 mm thick Type F fire-resistant gypsum plasterboards, with a density of 770 kg/m³ at 20 ºC. For single-layered assemblies, the gypsum plasterboard was fastened to the steel frame by 4.2 x 32 mm long flat head self-drilling screws, whilst double gypsum plasterboards were attached via both 4.2 x 32 mm and 4.2 x 50 mm flat head self-drilling screws (see Figure 3.1). As illustrated before in Table 3.1, Figure 3.2 and Figure 3.3, the wall cavity was either non-insulated, fully, or partially insulated with a 75 mm thick ceramic fibre blanket placed between the gaps of each respective stud row. The ceramic fibre has a density of 128 kg/m³ at 20 ºC.

3.1.3 Temperature Measurements

To measure the temperature distribution in the specimens, different configurations of thermocouples comprised by type K wires with 0.7 mm in diameter were employed, being each type appropriate to the range of temperatures expected and suitable to the characteristics of the materials in which the thermocouple was attached to.

Welded thermocouples (WT) were used to measure the temperature of the hot-flange, web, and cold-flange of the steel studs at mid-height. The temperature in the cavity and the ambient air temperature were evaluated using plate thermocouples (PT). The temperature at mid-thickness of the insulation and interface between gypsum plasterboards was assessed via twisted thermocouples (TT), and on the unexposed plasterboard, surface temperatures were collected by means of copper disk thermocouples (DT) protected with a silicate-fibre pad and located at the centre of each of the four quarters and at the geometric centre of the wall, according to the specifications of EN 1363-1 [16], whereas for the fire-exposed plasterboard, bed thermocouples (BT) were employed at mid-height of the wall. The evolution of the average and maximum temperatures throughout the test was obtained based on the single values of the thermocouples at each representative wall region, as described in Table 3.2. Additional information regarding the position of the thermocouples and their configurations is presented in Appendix B and subsequent section 3.3.

Table 3.2- Acronyms of the average and maximum temperatures for each representative region of the specimen.

Type of thermocouple	Average temperature acronym	Wall region
BT	EXP	Exposed gypsum plasterboard surface
WT	HF - EXP	Hot-flange of the studs along the exposed stud row
WT	WEB - EXP	Web of the studs along the exposed stud row
WT	CF - EXP	Cold-flange of the studs along the exposed stud row
PT	CAV - EXP	Wall cavity of the exposed stud row
PT	CAV - UNEXP	Wall cavity of the unexposed stud row
PT	AMB	Ambient air near the unexposed gypsum plasterboard
TT	PB - EXP	The interface between the plasterboards on the exposed side

Continues next page

Table 3.2- Acronyms of the average and maximum temperatures for each representative region of the specimen (continued).

Type of thermocouple	Average temperature acronym	Wall region
TT	PB - UNEXP	The interface between the plasterboards on the unexposed side
TT	INS - EXP	Mid- thickness of the insulation in the exposed stud row
TT	INS - UNEXP	Mid- thickness of the insulation in the unexposed stud row
DT	UNEXP	Unexposed gypsum plasterboard surface
Type of thermocouple	**Maximum temperature acronym**	**Wall region**
DT	UNEXP - MAX	Unexposed gypsum plasterboard surface

The average (IR-AVE), minimum (IR-MIN) and maximum values (IR-MAX) of the temperatures on the unexposed side was also analysed using a FLIR BT Series T365 Infrared Camera, which remained installed at 3.20 m distance from the unexposed surface of each specimen. The equipment has a data acquisition frequency of 1.25 Hz and the maximum temperature read is 350 ºC. To collect the experimental data, the temperature scale range was set between 15-250 ºC and the ambient temperature and gypsum plasterboard emissivity were 20 ºC and 0.8, respectively.

3.2 Test Set-up, Equipment and Procedure

Each stud row was assembled by first fastening the studs to tracks. The exposed stud row (studs A, B, C) was then attached to a 1000 x 1000 x 100 mm steel test frame (internal dimensions) on its top, bottom and left sides, using five 8 x 32 mm hexagonal head anchor bolts for each side, spaced at 200 mm centres, as seen in Figure 3.4. Only the right side of the exposed stud row was kept unrestrained by a 25 mm gap, properly insulated with ceramic fibre, as required by EN 1364-1 [67] (refer to Figure 3.3). The test frame was internally covered with a 30 mm thick refractory mortar (see Appendix A). The stud rows were connected using bridging steel plates and bolts as shown in the previous Figure 3.3. Subsequently, the thermocouples were positioned in the steel and wall cavity and thereafter, for insulated specimens, the ceramic fibre blanket was tightly inserted inside the cavity.

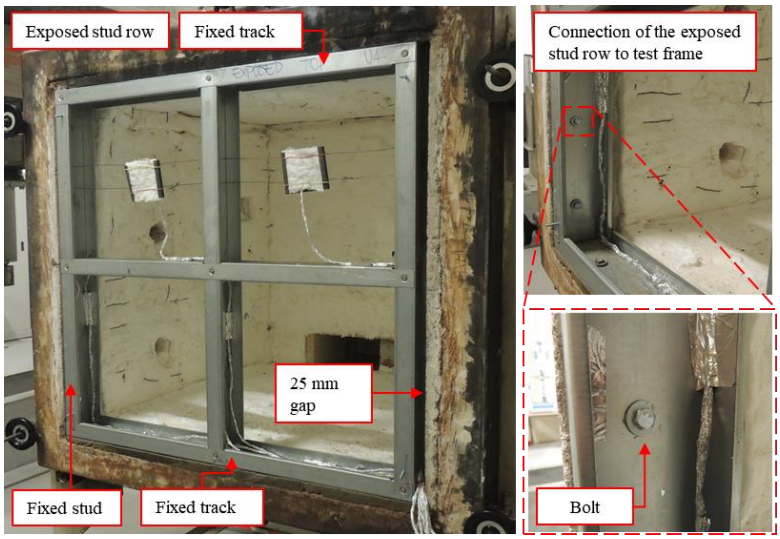

Figure 3.4 – Connection of the exposed stud row to test frame (specimen 4).

The unexposed stud row remained projected from the test frame to the unexposed side and completely unrestrained throughout the fire test and was clad with gypsum plasterboard along its edges, which were fixed through 4.2 x 32 mm flat head self-drilling screws, as represented in Figure 3.5. After the attachment of the gypsum sheathing on both exposed and unexposed sides, the gaps between the refractory mortar and the steel frame, as well as the dimpled surfaces of the plasterboard around the screw's edges were filled with gypsum plaster to avoid instabilities in the infrared measurements.

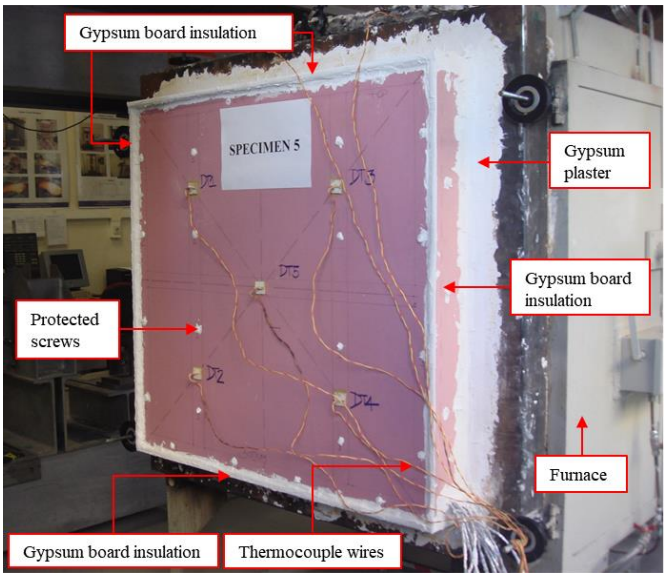

Figure 3.5 – Wall specimen placed in the furnace (specimen 5).

The furnace is built based on the requirements of EN 1363-1 [16] and has a compartment control volume of 1 m³ covered with ceramic fibre and ceramic bricks, and runs with four burners fuelled by natural gas, each with 90 kW maximum power. The internal temperature evolution was recorded using a plate thermocouple and calibrated according to ISO 834 [17] standard fire curve. The temperature data acquisition system is an MGC Plus by HBM with 21 channels available and 1 Hz of acquisition frequency.

The wall specimens were considered to have failed when the insulation criteria (I) was reached, whether regarding the requirements for the average (T_{ave}) or maximum (T_{max}) temperature on the unexposed protection layer, as expressed in the following Eqs. 3.1 and 3.2, in which $T_0 = 20\ °C$ [16]. The fire resistance in terms of structural and integrity adequacy of the specimens was not observed because of their small-scale dimensions.

$$T_{ave} = T_0 + 140 \quad \textbf{3.1}$$

$$T_{max} = T_0 + 180 \quad \textbf{3.2}$$

3.3 Observations, Results and Discussion

3.3.1 Specimen 1

Figure 3.6 illustrates the thermocouple attachments for Specimen 1. The test was carried out for approximately 77 minutes when the disk thermocouples on the unexposed side reached over 200 ºC. Additional information regarding the discrete temperatures of each thermocouple is offered in Appendix B.

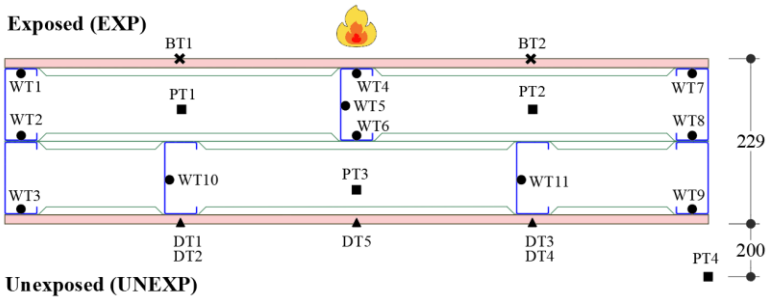

Figure 3.6 – Thermocouple attachments for Specimen 1.

The specimen's time-temperature profile is presented in Figure 3.7. The peak in the furnace temperature at the beginning of the test is owed to the furnace calibration system. It can be noticed that in the first 4-16 minutes, the typical temperature plateau is observed, which is due to the free water evaporation in the exposed gypsum plasterboard. Also, within the same time range, the studs present an almost uniform temperature distribution, given that the heating rate of the steel becomes sufficiently small. However, after 16 minutes, a steep temperature rise occurs, leading to dispersion in the average temperature values of steel and wall cavity, as the gypsum board on the fire exposed side lost its capacity to store heat and began to crack.

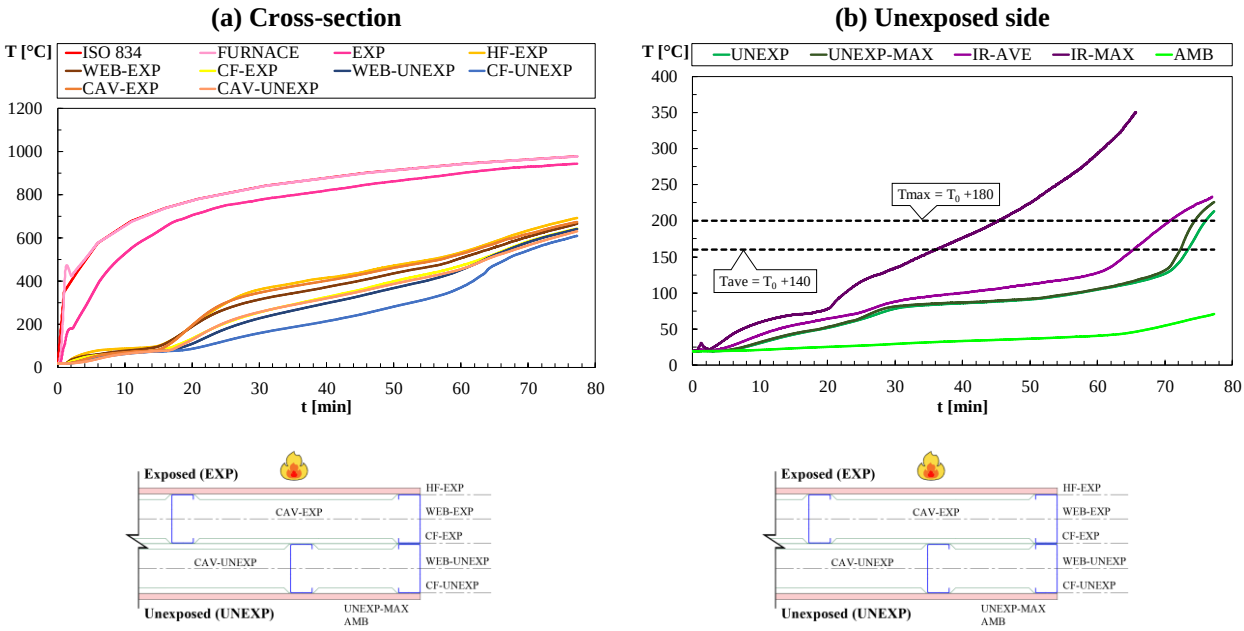

Figure 3.7 – Experimental time-temperature profile of Specimen 1.

Additionally, after 30 minutes of fire exposure, sizeable horizontal and vertical cracks opened between the positions of BT1, WT1 and WT4 (see Figure 3.8b), leading to an increase

in the temperature inside the cavity, particularly the values of PT1 and PT2, located along the exposed stud row (CAV-EXP). However, from 30 minutes and on, the temperature difference between PT1 and PT3 was around 100 ºC, as the enlarged cavity depth allows a more regular heat distribution because of natural convection within the enclosure.

Due to thermal expansion, the central stud on the exposed row (stud B) showed distortional buckling and web buckling at its mid-height, top and bottom parts, whereas stud C, located at the right end of the exposed row, suffered from distortional buckling at mid-height. Stud A had its web restrained, which avoided web buckling, and by the end of the test, the maximum temperature of its flanges WT1 and WT2 were 608 ºC and 568 ºC, respectively, while in stud B, WT4 was 693 ºC and WT6, 655 ºC. Stud C displayed the maximum values amongst flange temperatures, where WT7 and WT8 recorded at 77 minutes, 777 ºC and 707 ºC, respectively. During fire exposure, the heating rate of stud C was notably higher if compared to stud A, which may be related to their boundary conditions, since stud A was attached to the refractory mortar of the test frame, whereas stud C was covered with ceramic fibre along with its web. Nonetheless, web buckling did not occur in stud C.

Thermal bowing was not significantly experienced by the specimen and despite the instability modes detected, the steel frame remained in a good condition after the test, particularly the unexposed stud row, which exhibited lower steel temperatures and was unrestrained throughout the test, hence free to expand. Further details of the specimen's condition during and after the test are given in Appendix B.

As seen in Figure 3.8b, the plasterboard on the fire-side did not fall off in the course of the test, although large cracks were spotted on its surface, mostly on its left side, which considerably gave rise to the surface temperatures in the specimen after 16 minutes of fire exposure. The surface of the unexposed gypsum plasterboard revealed discolouration after 50 minutes, and as depicted in Figure 3.8a, at the end of the test, part of its right upper side had detached from the frame, indicating the existence of sizeable cracks on the surface of the unexposed plasterboard facing the wall cavity.

Figure 3.8 – Unexposed and exposed surfaces of Specimen 1 after the fire test.

The temperature on the unexposed surface (UNEXP) raised steadily until 70 minutes, 3 minutes prior to insulation failure (73 minutes). As for the IR-AVE values, at 62 minutes and forward, the measurements diverged from those of UNEXP and the records of IR-MAX were always greater than UNEXP-MAX. That was expected because the Infrared Camera was set to collect the temperature on an extensive area of the unexposed surface, which included hot spots such as screws, plasterboard detachments and crack formations (Figure 3.8a), whereas the disk thermocouples provided measurements at specific minor areas. Supplementary information regarding the Infrared outcomes is available in Appendix B.

About the thermal insulation behaviour of the specimen, the obtained insulation fire resistance time was met at 73 minutes regarding T_{ave} requirements, and at 74 minutes for T_{max}. It is important to note that the ambient air temperature near the unexposed side raised progressively during the experimental test, reaching a maximum of 70.8 ºC at 77 minutes.

3.3.2 Specimen 2

Specimen 2 had double gypsum plasterboards on both exposed and unexposed sides. Thus, the test was conducted up to 120 minutes. Figure 3.9 represents the arrangement of the thermocouple fixings in the test specimen. The assessment of the ambient temperature was not possible because of the number of channels available.

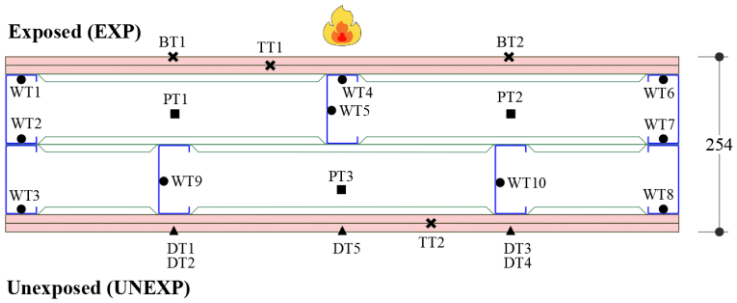

Figure 3.9 – Thermocouple attachments for Specimen 2.

Several integrity issues were identified throughout the test, which led to the malfunction of some thermocouples, and consequently to irregularities in the time-temperature profile of the wall, as indicated in Figure 3.10. The data from PB-UNEXP were recorded only during the first 8.7 minutes, thus it was decided not to show the temperatures at this region of the wall. It is possible that, in this case, the wires of TT2 had loosened during the procedure, or that the linking between the output and input terminals of the corresponding channel was faulty.

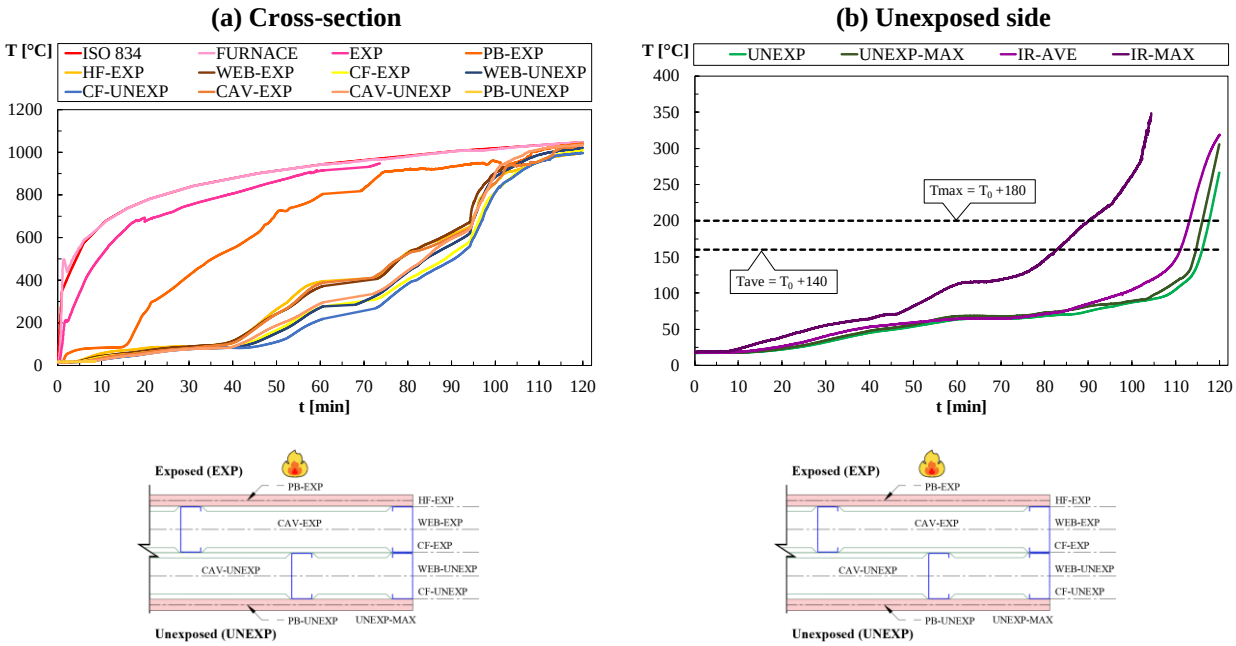

Figure 3.10 – Experimental time-temperature profile of Specimen 2.

From the analysis of Figure 3.10, the first segment of the characteristic temperature plateau occurs from 4 to 16 minutes. However, after this period, at around 90 °C, the exposed gypsum plasterboard experienced wide cracks along the mid-height set of tracks, where the BT1 measurements were being collected. In fact, it was noticed that at 20 minutes, BT1

exhibited an inconsistent temperature fluctuation, meaning that it had detached from the plasterboard, whereas the measurements of BT2 were lost later at 73 minutes.

After the appearance of large cracks on the fire-side board, the plasterboard in contact with the wall cavity was uncovered, and consequently, the temperature of PB-EXP increased abruptly, whilst the second segment of the temperature plateau ensued until 34 minutes. It can be seen in Figure 3.10 that, due to the additional protection layer and heat transfer to the cavity, the heating rate of PB-EXP seemed to have remained nearly flat between 60 to 69 minutes, while the steel and cavity temperatures increased slightly. This plateau is smaller than the first one given that the second protection layer on the exposed side will be subjected to higher fire compartment temperatures. Within the above-mentioned time window, the additional protection layer was still in place, although at 70 minutes, when EXP marked 931 ºC, significant portions of the exposed plasterboard began to fall off, as portrayed in Figure 3.11b. Subsequently, at 95 minutes, PB-EXP registered 946 ºC and sections of the gypsum board layer in contact with the steel frame started to crack and drop (Figure 3.11b), explaining the sudden increase of the temperatures towards the end of the fire test.

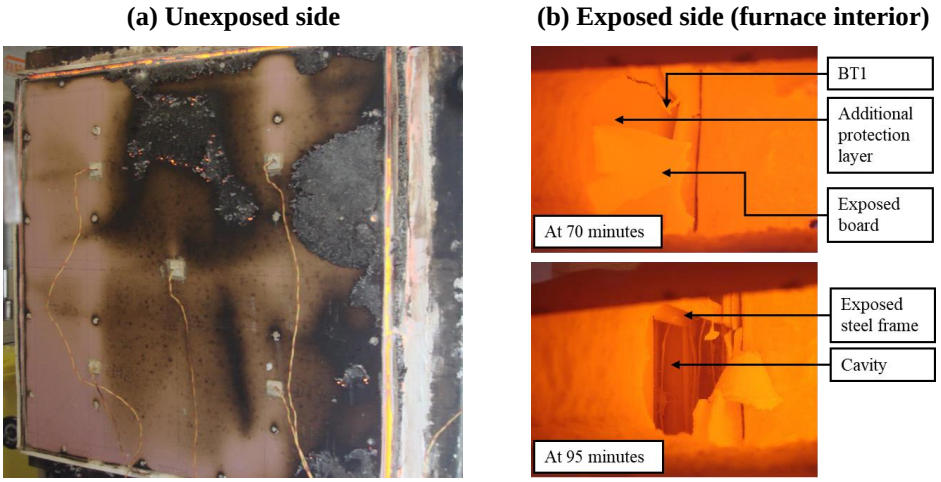

Figure 3.11 – Unexposed and exposed surfaces of Specimen 2 during the fire test.

The temperature of the hot-flange on the central stud of the exposed row (stud B) was critical to the instability behaviour of the steel frame, as it revealed local web buckling and distortional buckling. Comparable to Specimen 1, Stud C also presented distortional buckling, while local instabilities were not observed. Through the test, the flange temperatures were

higher in Stud C if compared to those of Stud A (see Appendix B), being this observation consistent with the previous specimen.

From Figure 3.11a, the unexposed surface of the specimen was severely damaged near the end of the experimental test, showing significant glowing along its edges and central region, that is, both of the unexposed protection layers were considerably affected by prolonged fire exposure. Regarding thermal insulation performance, the temperature on the unexposed side (UNEXP) raised steadily through the fire test until 98 minutes, 8 minutes prior to insulation failure. The insulation fire resistance time was met at 116 minutes regarding T_{ave} requirements, and at 116 min for T_{max}. Thereby, the provision of one additional protection layer on both sides of the specimen proved to enhance the insulation performance of the wall by approximately 40 minutes.

3.3.3 Specimen 3

Specimen 3 was designed with ceramic fibre insulation within both stud rows and was clad with one layer of gypsum plasterboard on the exposed and unexposed sides. Figure 3.12 illustrates the thermocouples employed to obtain the time-temperature profile of the specimen, shown in the following Figure 3.13, considering a test length of 200 minutes.

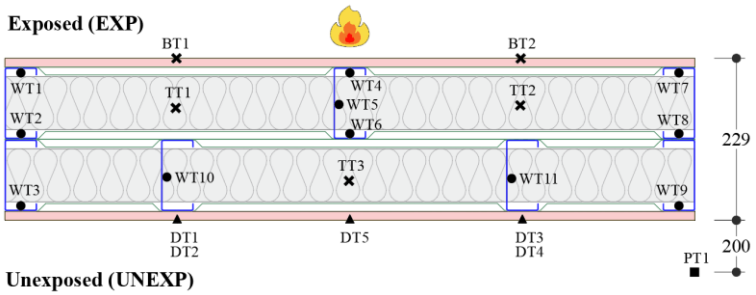

Figure 3.12 – Thermocouple attachments for Specimen 3.

After the temperature plateau period, at 16 minutes the temperatures rise sharply, indicating the occurrence of large cracks on the fire exposed plasterboard, as also observed in the previous experimental tests. However, concerning the temperatures on steel, when compared to Specimen 1's behaviour (Figure 3.7), at 30 minutes, the temperature of HF–EXP was on average 60 ºC higher in Specimen 3, demonstrating that the ceramic fibre insulation

increased the heating rate of the hot-flange on the exposed stud row. This pattern can be observed until 66 minutes when the HF–EXP of Specimen 3 increased abruptly as a consequence of the detachment from the steel frame of a significant area of the exposed plasterboard, which is visibly represented in the subsequent Figure 3.14c, d. At 66 minutes, the temperature of EXP was 938 ºC.

In contrast, at 30 minutes, the temperature of CF-EXP in Specimen 3 was on average 114 ºC lower than that of Specimen 1 at the same time instant, since the ceramic fibre insulation delays the heat transfer through the steel and wall cavity. Such behaviour confirms that, due to temperature build-up around the hot-flange, stud sections experience increased thermal gradients in cavity insulated walls. Still in that regard, as revealed in Appendix B, the exposed stud row was severely damaged, especially stud B (central stud), which suffered from distortional and web buckling as well as noticeable embrittlement. This fragile behaviour is associated with the melting of the zinc coat at high temperatures, which is a phenomenon known as Liquid Metal Embrittlement (LME). By the end of the test, the temperatures of the hot-flange on the exposed stud row, namely WT1, WT4 and WT7, were 942 ºC, 1172 ºC and 1045 ºC, respectively. As for the unexposed stud row, stud E also exhibited brittle fracturing behaviour.

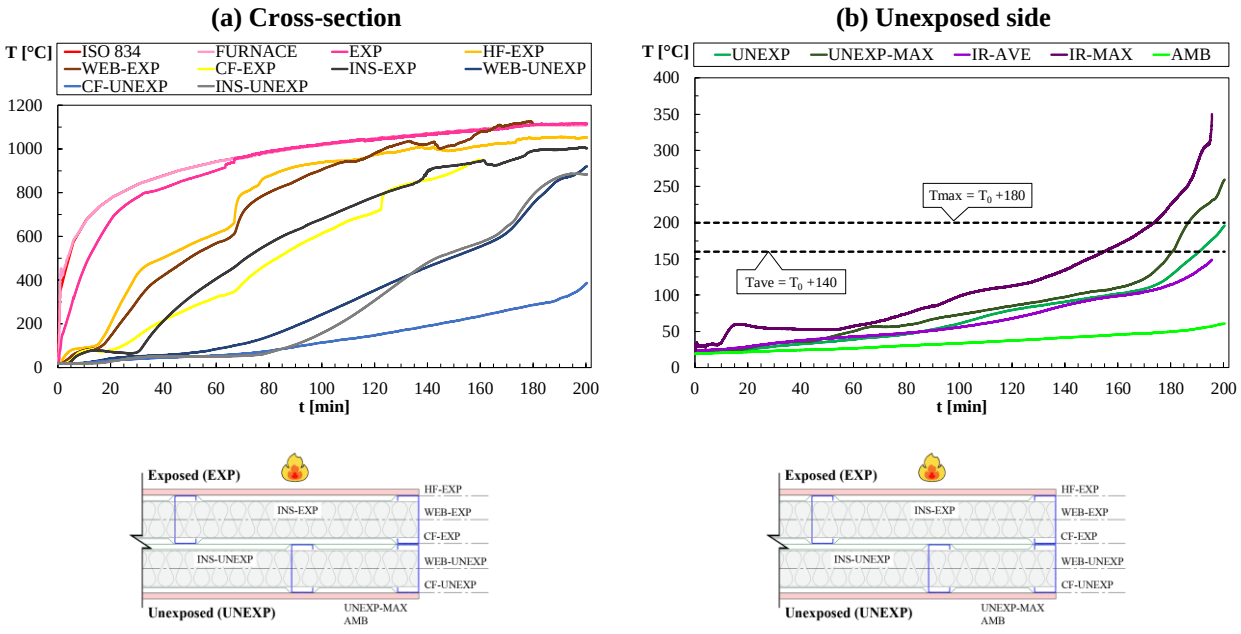

Figure 3.13 – Experimental time-temperature profile for Specimen 3.

Despite fall-off of the fire-exposed plasterboard, the temperature in the insulation (INS-EXP) continued to rise smoothly until the end of the fire test. Furthermore, it is clear in Figure

3.7 the large difference between INS-EXP and INS-UNEXP, as well as between HF-EXP and CF-UNEXP during the entire test, stressing out the role of the cavity insulation in delaying the heat transfer through the wall's cross-section. In this sense, it should be noted that the average temperature of CF-UNEXP in Specimen 3 reached 200 ºC at 144 minutes, while in Specimen 1 it occurred much earlier at 37 minutes.

From Figure 3.14a, the condition of the unexposed surface of the specimen at the end of the test was reasonably good, with evident discolouration and crack formations around its central portion. Moreover, as seen in Appendix B, the ceramic fibre insulation remained in place, since it was tightly inserted into the stud gap of each stud row. Additionally, despite reaching temperatures as high as 1070 ºC, no substantial loss of integrity of the ceramic fibre was detected. Nonetheless, the insulation positioned in exposed row displaced significantly sideways nearby the buckled segment of the central stud.

(a) Unexposed side **(b) Exposed side (furnace interior)**

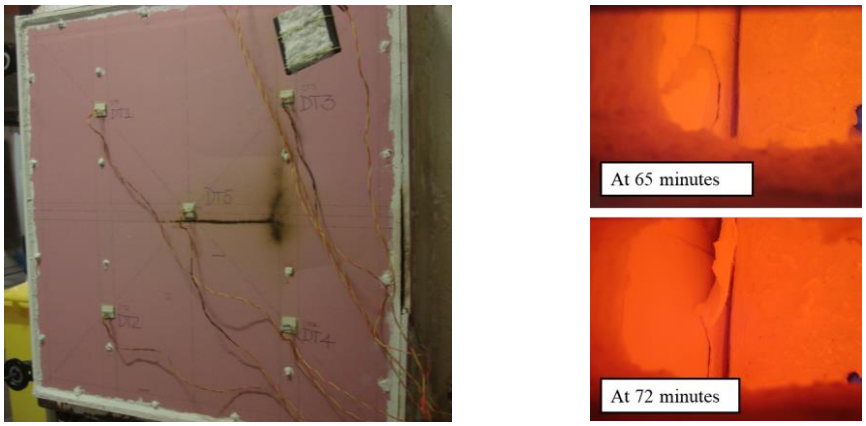

Figure 3.14 – Unexposed surface of Specimen 3 during the fire test and fall-off of the exposed gypsum plasterboard at different time instants.

Concerning thermal insulation performance, the temperature on the unexposed side (UNEXP) rose steadily during the fire test and the insulation fire resistance time was met at 190 minutes regarding T_{ave} requirements, and at 186 minutes for T_{max}.

3.3.4 Specimen 4

Specimen 4 was partially insulated with ceramic fibre, placed between the unexposed stud row and facing the cavity side of the unexposed plasterboard, as depicted in Figure 3.15, which also displays the thermocouple positions over the cross-section of the specimen.

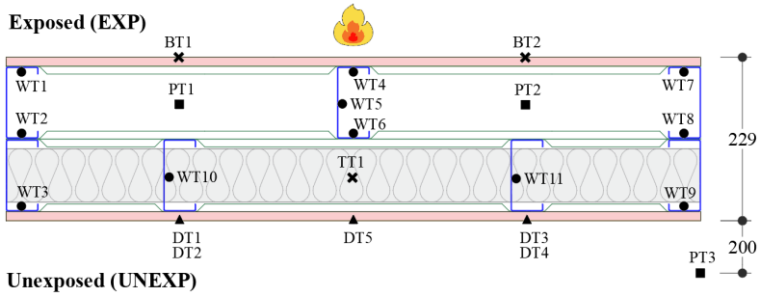

Figure 3.15 – Thermocouple attachments for Specimen 4.

The time-temperature profile obtained throughout 150 minutes of test is illustrated in Figure 3.13. The readings of WT9 are not accounted for in the average values of CF-UNEXP, since it had detached from the steel stud, probably caused by the handling of the specimen before the test. Also, WT3 and BT1 malfunctioned after 8.1 minutes and 67 minutes of fire exposure, respectively.

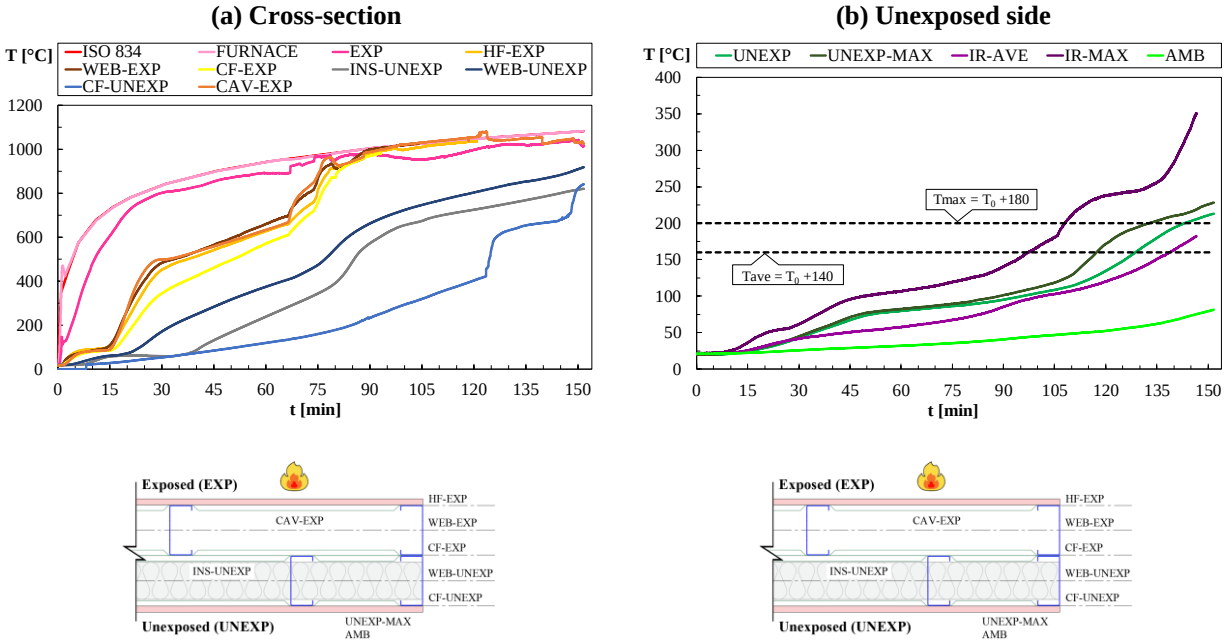

Figure 3.16 – Experimental time-temperature profile for Specimen 4.

The first large cracks in the gypsum plasterboard on the fire-side appeared after 18 minutes, causing the temperatures to rise steeply inside the cavity and on the exposed stud row. However, as cavity insulation was placed within the unexposed cavity, the average temperatures in the insulation and on the unexposed plasterboard and studs increased regularly, even after fall-off of the exposed sheathing layer at 67 minutes, when EXP recorded 892 ºC (see Figure 3.17b next). Still, it was noticed that the temperature of WEB-UNEXP remained higher than INS-UNEXP, since the studs E and F are in direct contact with the exposed cavity. Moreover, at 122 minutes, CF-UNEXP rises sharply, possibly because of voids between the insulation and the steel frame.

When compared to Specimen 1's performance, the temperatures of CAV-EXP, HF-EXP and CF-EXP in Specimen 4 reached significantly higher values, as cavity insulation slows the heat transfer rate to the unexposed surfaces of the wall, building up the heat on the exposed stud row. Consequently, stud B suffered from web and distortional buckling, whereas studs A and C experienced distortional instabilities. Furthermore, as previously observed for Specimen 3, HF-EXP and CF-UNEXP remained well distanced during most of the fire test.

As illustrated in Figure 3.17a, the unexposed surface of the wall presented an integral aspect after fire exposure, with some discolouration around the studs in contact with the exposed cavity (studs E and F) and no evidence of intense cracking on the side of the unexposed plasterboard facing cavity insulation. The temperature on the unexposed surface (UNEXP) rose steadily through the fire test and the insulation fire resistance time was met at 128 minutes regarding T_{ave} requirements, and at 132 minutes for T_{max}.

(a) Unexposed side **(b) Exposed side (furnace interior)**

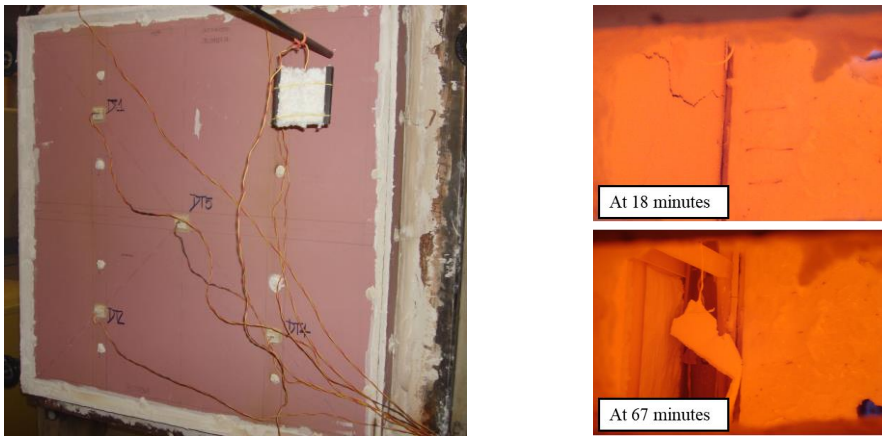

Figure 3.17 – Unexposed and exposed surfaces of Specimen 4 during the fire test.

3.3.5 Specimen 5

Figure 3.18 presents the thermocouple positions over the cross-section of Specimen 5, which was partially insulated with ceramic fibre placed between the exposed stud row and facing the fire-side. The time-temperature profile obtained throughout 200 minutes of fire test is illustrated in Figure 3.19 next. The records of BT2 were neglected after 134 minutes, as it started to present incompatible temperature fluctuations.

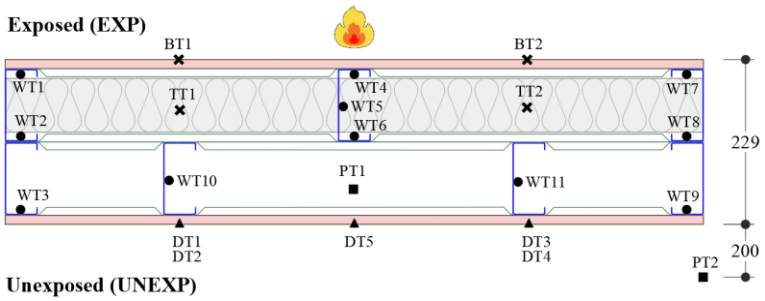

Figure 3.18 – Thermocouple attachments for Specimen 5.

The exposed gypsum plasterboard showed big cracks right after the initial dehydration plateau at 16 minutes, eventually falling off at 64 minutes when EXP was 948 ºC. Such events are reflected in the time-temperature profile of the specimen shown in Figure 3.19.

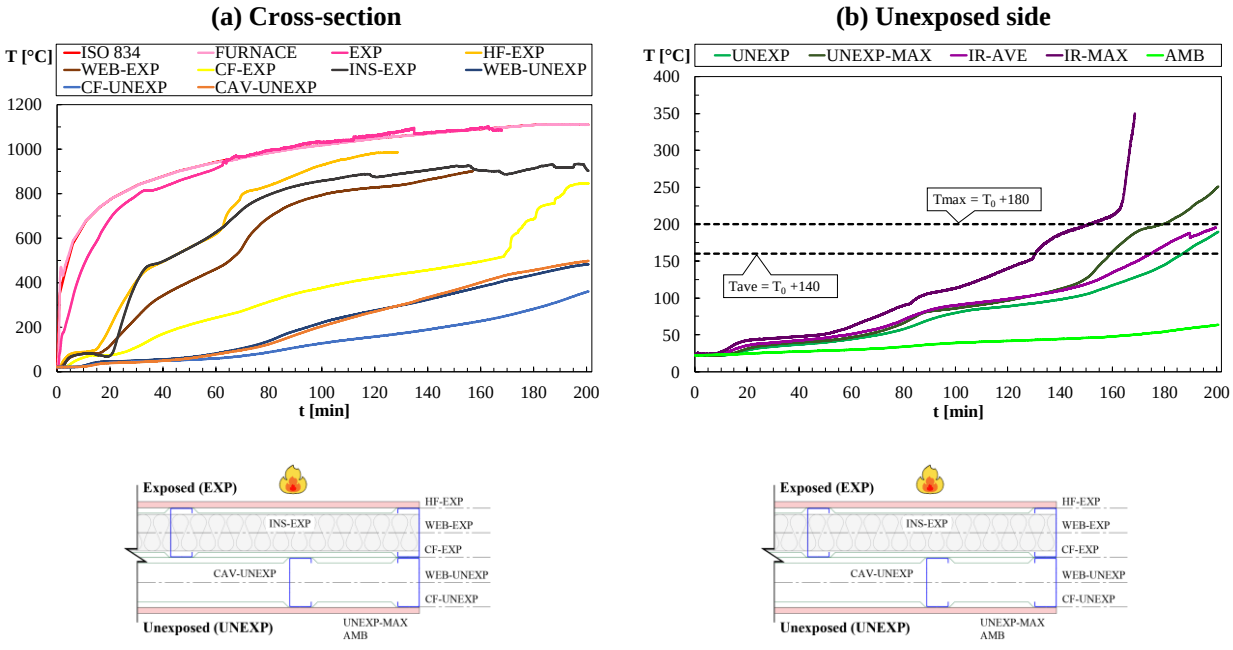

Figure 3.19 – Experimental time-temperature profile for Specimen 5.

Also, the heating rate of the studs on the insulated exposed row, namely HF-EXP and CF-EXP, was remarkedly high, although the flange temperatures of the exposed studs in Specimen 4 displayed greater values, which is linked to the fact that in Specimen 5, the heat that is built up over the exposed stud row is progressively transferred to the remaining cavity and unexposed surfaces of the wall. Such an effect is visible when the temperatures of CAV, WEB-UNEXP, CF-UNEXP and UNEXP become gradually larger after 64 minutes. Those same temperatures increased considerably more rapidly in Specimen 4, especially the average and maximum temperatures on the surface of the unexposed plasterboard.

Furthermore, the temperatures on stud B were critical, and it exhibited web and distortional buckling, while stud A suffered from distortional buckling only, whereas both experienced brittle fracturing. The unexposed stud row stayed almost intact, i.e., no instability modes and brittle fracturing behaviour were observed.

With respect to the insulation fire resistance of the specimen, the temperature on the unexposed surface (UNEXP) remained within a narrow temperature band until 40 minutes, evolving steadily afterwards. The insulation fire resistance time was met at 187 minutes regarding T_{ave} requirements, and at 179 minutes for T_{max}.

Figure 3.20a depicts the surface aspect of the unexposed gypsum plasterboard at the end of the fire test, showing that large cracks were opened on the surface of the unexposed board facing the cavity. The integrity issues observed in the exposed plasterboard are illustrated in Figure 3.20b.

(a) Unexposed side **(b) Exposed side**

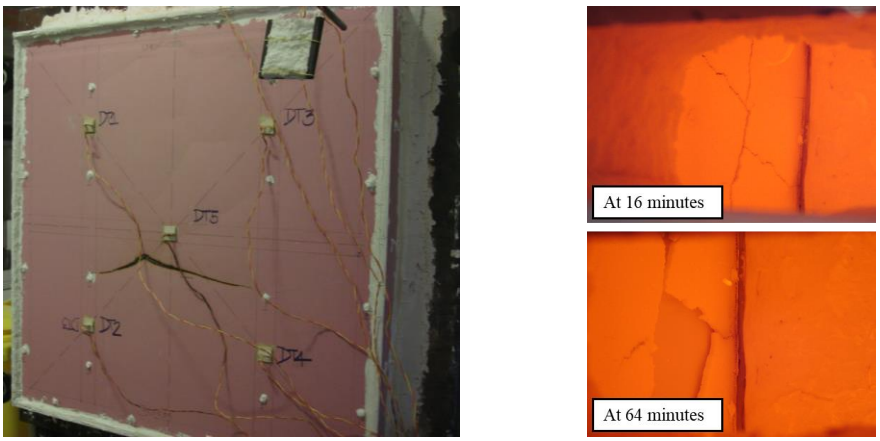

Figure 3.20 – Unexposed and exposed surfaces of Specimen 5 during the fire test.

3.4 Summary and Conclusions

Table 3.3 summarizes the fire resistance obtained for the double-stud LSF walls in terms of insulation requirements. The Fire Resistance Rating (FRR) was determined based on the minimum value between T_{ave} and T_{max}, obtained from the temperature measurements of the thermocouples. The fire classification of the specimens regarding insulation (I) performance was defined under EN 13501-2 [68].

Intended for comparison only, the thermal insulation behaviour of the specimens was similarly estimated based on the Infrared results for the average (T_{IR-ave}) and maximum (T_{IR-max}) temperatures on the unexposed side, which were consistently smaller when compared to the thermocouple measurements, since the Infrared camera collects higher temperatures associated with integrity loss of the unexposed gypsum plasterboard and other hot surfaces, such as metal components.

Table 3.3c

Specimen Nº	Test duration [minutes]	Fire resistance (T_{ave}) [minutes]	Fire resistance (T_{max}) [minutes]	Fire resistance (T_{IR-ave}) [minutes]	Fire resistance (T_{IR-max}) [minutes]	Fire resistance rating (FRR)
1	77	73	74	65	45	I60
2	120	116	116	111	90	I90
3	200	190	186	199	173	I180
4	150	128	132	138	108	I120
5	200	187	179	174	150	I120

The thermal performance of double-stud LSF wall is enhanced by the presence of a wider cavity, as it allows to reduce heat transfer through the cross-section. The experimental results showed that the provision of an additional protection layer increased the fire resistance of the wall without cavity insulation by approximately 40 minutes. Furthermore, the employment of ceramic fibre wall cavity insulation remarkedly improved the thermal performance of the specimens, although the steel frame remained severely damaged due to prolonged fire exposure and heat build-up around the hot-flange of the exposed stud row. Moreover, it was demonstrated that when the steel frame was partially insulated with ceramic fibre placed in the direction of the exposed gypsum plasterboard, an improved fire resistance

was attained, which was attributed to the fact that heat is being released to the remaining unexposed cavity, thus decelerating the temperature rise on the unexposed surfaces of the double-stud wall protected with one gypsum layer on both sides.

Chapter 4

4 Numerical Simulation – Advanced Calculation Method

Small and full-scale standard fire tests are costly and time-consuming. As an alternative, advanced calculation methods based on computer-aided numerical techniques are effective in assessing the thermal and structural performance of varied intricate engineering boundary-value problems associated with field variables, complex domains, irregular boundary conditions, material nonlinearities and geometric imperfections, where closed-form analytical solutions are not straightforwardly attainable, which is the case of load and non-load-bearing composite LSF structures subjected to fire.

In fire safety engineering, the Finite Element Method (FEM) has been progressively implemented to evaluate the thermal and structural behaviour of LSF walls at elevated temperatures, yielding safe and economic designs. The transient thermal response and fire resistance of such walls can be predicted by exposing the wall model to a standard time-temperature curve and applying suitable initial and boundary conditions. Also, effective material thermal properties for the relevant temperature range should be assigned. However, modelling integrity issues and mass transport phenomena is still limited, and the current practical approaches to tackle such issues rely mostly on user-input fire testing observations and effective material thermal properties. Additionally, since little information is provided concerning the fire behaviour of double-stud LSF walls, a numerical assessment is necessary to identify the simulation parameters, routines and model assumptions affecting their thermal patterns and fire resistance, which may significantly improve prescriptive and performance-based design specifications.

Thus, this chapter explores the main aspects of the development process of 3D models to simulate the thermal behaviour and predict the insulation fire resistance of double-stud LSF walls under a standard fire scenario. It also covers the resources and limitations of ANSYS® Multiphysics, which was employed to conduct a transient heat transfer analysis based on the FEM with a hybrid approach. The thermal models are validated according to the results previously acquired in the experimental tests and their accuracy is discussed.

4.1 FEM for Heat Transfer Phenomena

Steady and transient state heat transfer phenomena involving complex geometries, variable material properties and irregular boundary conditions are common in fire safety engineering. For such problems, which are governed by *continuous second-order differential equations*, it is often difficult to develop approximating functions to the field variables of interest. Thus, by discretizing the problem region and its governing equations, the FEM enables a local representation of the complex domain and its boundaries, for which is possible to devise piecewise approximate solutions using classical solution methods [69].

In the FEM for transient thermal analyses, the irregular or regular continuous domain is first divided into a mesh of nonoverlapping *finite elements* interconnected at common nodes, which are usually located along the boundaries of the element or in its interior (refer to Figure 4.1). Each node has specified nodal variables referred to as degrees of freedom (DOF) that are consistent with the element type and problem physics [70]. For each element, the governing equations of the problem are discretized into both spatial and temporal subdivisions. The spatial field variable is defined according to its unknown values at the nodes of the element and expressed in terms of *approximating functions* (also called interpolation or shape functions). Further, using a systematic approach, the elemental conservation equations are assembled into a set of either linear or nonlinear algebraic relations, which are obtained via *variational or weighted-residual methods*. Thus, by addressing the appropriate initial and boundary conditions of the problem, a *piecewise approximate solution* for the values of the field variables of interest over the *entire domain* is numerically obtained in a way that they satisfy the general governing equations and boundary conditions of the problem [69–71]. The primary objective in transient analyses is to find *nodal temperatures* at each time step of the solution, followed by other secondary quantities, namely *thermal gradients*, and *heat fluxes*. Therefore, the accuracy, continuity and convergence of the obtained field variables will depend on the mesh refinement and time step size, as well as on the element type (or shape functions).

4.1.1 Three-Dimensional Transient Heat Conduction

Figure 4.1 schematizes the cross-section of an LSF wall region characterized as a continuous dominium Ω with one of its the protection layers discretised into infinitesimal hexahedral elements represented as Ω^e, each with a volume dV. The in and out conduction heat

flow $\dot{h}_c$ at any given time interval is shown for x, y and z directions and $\dot{g}$ represents the rate of heat generation (or sink) inside the element.

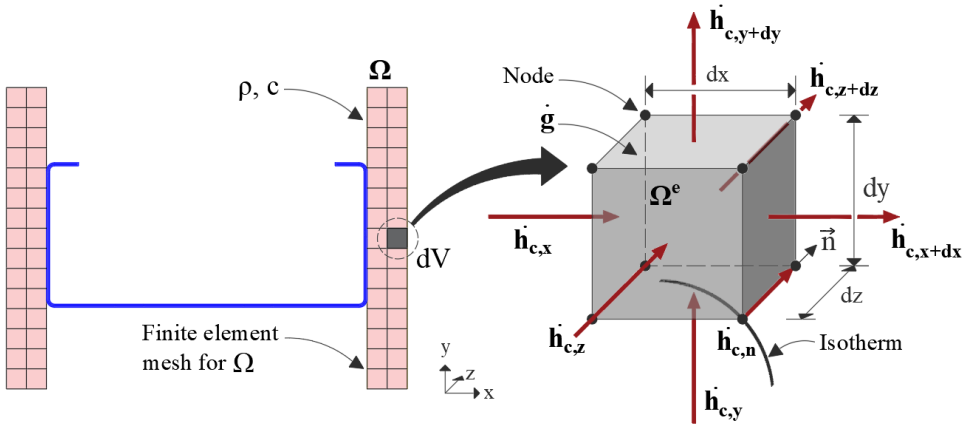

Figure 4.1 – Conduction heat flow on a hexahedral infinitesimal volume element

Referring to Eq.2.1, the total net conduction heat flow in the x direction is expressed according to the following Eq. 4.1, where $\dot{h}_{c,x+dx}$ results from a two-term Taylor series expansion.

$$\dot{h}_{c,x} - \dot{h}_{c,x+dx} = \frac{\partial}{\partial x}\left(\lambda \frac{\partial T}{\partial x}\right) dV \qquad \textbf{4.1}$$

Likewise, Eq. 4.1 can be written for y and z directions and the transient heat balance of the control volume is established along with the First Law of Thermodynamics, that is, the net rate of heat conduction through the element along all directions added to the amount of internal heat rate equals to the change in its energy content ΔU, as given by the following Eqs. 4.2a and 4.2b.

$$\sum_{x,y,z} \dot{h}_{c,in} - \sum_{x,y,z} \dot{h}_{c,out} + \dot{g}\, dV = \Delta U \qquad \textbf{4.2a}$$

$$\sum_{x,y,z} \dot{h}_{c,in} - \sum_{x,y,z} \dot{h}_{c,out} + \dot{g}\, dV = \rho c \frac{\partial T}{\partial t} dV \qquad \textbf{4.2b}$$

Writing Eq. 4.2b for three-dimensional conduction heat flow in Cartesian directions and dividing by dV yields

$$\forall\Omega, \qquad \frac{\partial}{\partial \mathrm{x}}\left(\lambda\frac{\partial \mathrm{T}}{\partial \mathrm{x}}\right)+\frac{\partial}{\partial \mathrm{y}}\left(\lambda\frac{\partial \mathrm{T}}{\partial \mathrm{y}}\right)+\frac{\partial}{\partial \mathrm{z}}\left(\lambda\frac{\partial \mathrm{T}}{\partial \mathrm{z}}\right)+\dot{\mathrm{g}}=\rho\mathrm{c}\frac{\partial \mathrm{T}}{\partial \mathrm{t}} \qquad \textbf{4.3}$$

The Eq. 4.3 represents the *transient state* governing equation of the conduction heat flow within the volume control of an isotropic stationary medium, with no directional variation of thermal conductivity, in which the temperature T varies with time t and position along the respective heat flow direction, and where ρ and c, both temperature dependant, are the density and specific heat of the medium, respectively, and $\dot{g}$ is the known rate of heat generation (or absorption) per unit volume. In the FEM, ρ is usually assumed to remain constant over the volume of the element, whereas c may vary.

In a simplified manner, for non-combustible materials, $\dot{g} = 0$ [72], thus Eq. 4.3 becomes

$$\forall\Omega, \qquad \nabla\left(\lambda\,\nabla \mathrm{T}\right)=\rho\mathrm{c}\frac{\partial \mathrm{T}}{\partial \mathrm{t}} \qquad \textbf{4.4}$$

The simplification $\dot{g} = 0$ is consistent with the objectives of this research. Carbon steels and ceramic fibre insulation are non-combustible materials and do not undergo phase-change processes for a wide temperature range. Although gypsum sheathing experiences endothermic and exothermic reactions under fire, such singularities are implicitly incorporated in its specific heat values.

4.1.2 Initial and Boundary Conditions

The energy balance inside a medium is well stated by Eq. 4.4, which is always valid within a continuous dominium regardless of its surface conditions. Consequently, for each direction of the coordinate system, specified conditions must be addressed to the bounding surfaces of the respective medium as heat transfer processes are controlled by the surrounding circumstances. For a composite structure bounded by a gas in which convection and radiation

occur, as seen in subsection 2.1.4, the convection and radiation heat flux boundary conditions (*Cauchy Condition*) in the positive $\vec{n}$ direction can be generally expressed as [22,73]

$$\dot{h}_{c,n}\big|_{boundary} = -\lambda \left.\frac{\partial T\,(n,t)}{\partial n} \cdot \vec{n}\right|_{boundary} = \dot{h}_{net,cv} + \dot{h}_{net,r} \qquad \textbf{4.5}$$

In the above equation, still referring to Figure 4.1, the left term denotes the heat flux vector at a given point belonging to an isothermal in the boundary surface of the medium, where $\vec{n}$ is the normal unit vector to that surface pointing towards the decreasing temperature. Also, ∂T is the temperature difference between the boundary surface and the inside of the body.

As for a perfectly insulated or adiabatic surface and in the case of assumed perfect contact between any two surfaces, the heat flux boundary condition is given by Eqs. 4.6a and, 4.6b, respectively. These boundary conditions are identified by *Newman*. Moreover, thermal conditions may be applied to a boundary surface by specifying known temperatures as expressed in Eq. 4.6c. This is called the *Dirichlet* type boundary condition.

$$-\lambda \left.\frac{\partial T\,(n,t)}{\partial n} \cdot \vec{n}\right|_{boundary} = 0 \qquad \textbf{4.6a}$$

$$-\lambda_A \left.\frac{\partial T\,(n,t)}{\partial n} \cdot \vec{n}\right|_{surface\ A} = -\lambda_B \left.\frac{\partial T\,(n,t)}{\partial n} \cdot \vec{n}\right|_{surface\ B} \qquad \textbf{4.6b}$$

$$T = T|_{boundary} \qquad \textbf{4.6c}$$

Additionally, in transient heat transfer analyses, an initial condition is required to satisfy the second-order general heat conduction equation. Hence, assuming an initial uniform temperature distribution over the entire model, the initial condition at time $t = 0$ is prescribed as $T\,(n, 0) = T_0$.

4.1.3 Galerkin Finite Element Method

The method of the Weighted Residual along with the weak-form or weighed-integral statement is often employed to provide an approximate solution to the heat conduction

governing equation, making possible to obtain the nodal temperatures and the energy balance in the domain as functions of time, considering all relevant heat transfer modes, initial and boundary conditions. In transient analyses, in addition to a region subdivision, Eq. 4.4 is required to be discretized into spatial and temporal variables.

Using the Galerkin Finite Element Method, for a finite element mesh denoted as Ω_m comprised of m nodes, its global temperature field T is approximated over space as $\bar{T}$, according to the following Eq. 4.7, where N_k are the appropriately selected shape functions and T_k are the time-dependent unknown nodal temperatures. The key objective of using unknown nodal temperatures is to impose continuity to $\bar{T}$ along the boundaries between the elements [69].

$$\forall \Omega_m, \qquad T \approx \bar{T} = \sum_{k=1}^{m} N_k T_k \tag{4.7}$$

The shape functions shall be consistent with the element type and its boundary conditions, as well as with the problem physics (field variables of interest) and they usually assume the form of polynomials of n^{th} degree, which are readily differentiated and integrated. Additionally, regarding heat conduction problems, the shape functions ought to be twice-differentiable with respect to all relevant directions to assure solution convergence. However, such differentiability requirements can be reduced by employing the weak-form statement along with the Galerkin method.

If $\bar{T}$ is substituted in Eq. 4.4, a scalar residue at any point in Ω_m arises and the Galerkin method demands that its integral in the dominium must be cancelled. Consequently, for any function ψ_k, the parameters T_k of the previous equation can be determined by satisfying the *weighed-residual statement* of Eq. 4.4, that is.

$$\forall \Omega_m, \qquad \int_{\Omega_m} \psi_k \left[\nabla (\lambda \nabla \bar{T}) - \rho c \frac{\partial \bar{T}}{\partial t} \right] d\Omega_m = 0 \tag{4.8}$$

where ψ_k are the k *weighting functions*. The purpose of assigning weighting functions is to distribute equally the differentiation of ψ and T, which is essential to solving Eq. 4.8 using numerical integration and at the same time guarantee the continuity and convergence of the

solution. In a Galerkine approximation, $\psi_k = N_k$, where now N_k is required to be at least once-differentiable in every appropriate direction (linear shape functions), that is, temperature continuity along the element's interfaces for compatibility requirements (C^0) and temperature and heat flux continuity within the elements for completeness (C^1) are provided.

Integrating by parts the previous expression and further substituting the temperature field approximation $\bar{T}$, Eq. 4.8 can be assembled into a linear or nonlinear finite element assemblage comprised by a number of k independent equations, termed the *weighed-residual finite element model*, as follows

$$[\mathrm{C}]\{\dot{\mathrm{T}}\} + [\mathrm{L}]\{\mathrm{T}\} = \{\mathrm{q}\} \qquad \textbf{4.9}$$

where $[C]$ is the assemblage of the elemental capacitance matrices, $\{\dot{T}\}$ is the vector of the time derivatives of the nodal temperatures, $[L]$ represents the conductivity matrix, $\{T\}$ is the vector of the unknown time-dependent nodal temperatures over the domain and $\{q\}$ is the assemblage of the thermal forces over each element. Introducing the boundary conditions along their respective portions of the domain into $\{q\}$, the temperature field $\{T\}$ may be determined as a function of time.

Since in this research the thermal properties of the medium are temperature-dependant and radiation is applied, the solution of Eq.4.9 is highly nonlinear and requires an iterative process coupled with numerical integration. Moreover, it should be noted that the matrix $[L]$ would include the effects of the specified boundary conditions and the terms of the thermal conductivity matrix of the medium.

Additionally, Eq.4.9 demands the discretization of its transient terms $\dot{T}$, for which a finite difference approximation is suitable. The first order temporal discretization is then formulated as per [22,74]

$$\dot{\mathrm{T}} \approx \frac{\mathrm{T_{i+1}} - \mathrm{T_i}}{\Delta \mathrm{t}} \qquad \textbf{4.10}$$

being i the subscript denoting the time step number. Thus, for a given time step size Δt (which may change during the solution process), the nodal temperatures T_{i+1} at the next time level $t_{i+1} = (i+1)\Delta t$ may be determined from the nodal temperatures T_i at $t_i = i\Delta t$ and

known q_i, q_{i+1} load increments. Using a *fully implicit transient scheme*, Eq.4.9 can be rewritten as

$$\left[\mathrm{L} + \frac{\mathrm{C}}{\Delta \mathrm{t}}\right] \{\mathrm{T_{i+1}}\} = \left\{\mathrm{C}\frac{\mathrm{T_i}}{\Delta \mathrm{t}} + \mathrm{q_{i+1}}\right\} \qquad \textbf{4.11}$$

The initial condition establishes that for $i = 0$, $t_0 = 0$, then $\mathrm{T_i} = \mathrm{T_0}$. From this point, if the convergence criterion is met, the iterative process is carried out until the solution at the desired time is reached. The main advantage of the implicit method is that the time step size is not restricted and although it requires extra computational effort, the solution will always converge. Further details are exhaustedly discussed in the dedicated publications of Nithiarasu et al. (2016) [22], Baskharone and Erian (2013) [70], and Reddy and Gartling (2018) [69].

4.2 3D Thermal Models of Double-stud LSF Walls

4.2.1 ANSYS® Multiphysics

The ANSYS® Multiphysics is a FEM-based software package that allows the geometry conception and thermal analysis of both linear and nonlinear steady or transient heat transfer problems comprised by 1D, 2D or 3D domains. The program provides a wide set of line, area, or volume finite elements with a varying number of nodes with different degrees of freedom and interpolation functions, selected in accordance with the analysis subject. The complex boundary conditions and the related material thermal properties can be applied as tabular or functional temperature-dependent quantities [71].

In transient analyses, the ANSYS® solver handles the three primary modes of heat transfer. Convection is specified as an external surface load on conducting solid or shell elements. The film coefficient may be defined as a temperature-dependent parameter if desired. As for the radiation effects, using the radiosity solver method, generalized radiation interactions between two or more surfaces within an enclosure can be addressed to 2D or 3D elements having a temperature DOF, in which the temperature variation in each enclosure is defined according to a space node. An enclosure can be comprised of multiple grey diffuse radiating

surfaces with known emissivities, where the emissivity of each material model may change with temperature. The view factor between the surfaces within a 3D enclosure is calculated using the hemicube method.

The computed heat fluxes will act as boundary conditions for the conduction analysis throughout the finite element model. For new nodal temperatures at each time step, new surface heat flux conditions are determined and the nodal temperatures at the next time step are found for the entire model.

4.2.2 Finite Element Model

ANSYS® provides a graphic interface that allows the user to define geometric entities such as *keypoints*, *lines*, *areas*, and *volumes* according to the geometric features of the problem. In the present study, the 3D LSF walls are comprised of three or four *isotropic* material models: gypsum plasterboard, steel, air, and cavity insulation, each with its own set of thermal properties and assigned element type. For each material model, the lines are subdivided into appropriate segments that will define the mesh size and density. Areas are obtained from lines, and volumes through the extrusion of areas. Figure 4.2 shows the 3D finite element model of a composite LSF double-stud wall and the type of finite element assigned to each material model. In this investigation, the mesh size and density were defined based on a sensitivity analysis and previous numerical research [60].

(a) Steel mesh (SHELL131 finite elements)

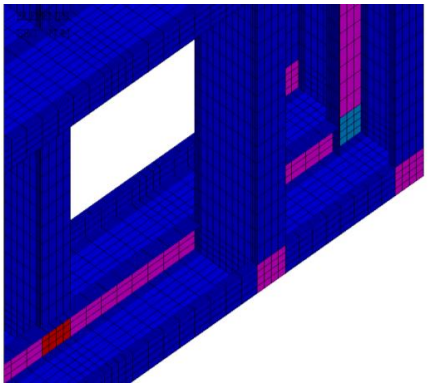

(b) Gypsum plasterboard, cavity insulation, and air layer mesh (SOLID70 finite elements)

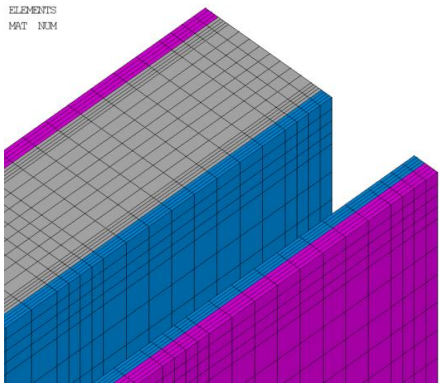

Figure 4.2- Finite element mesh of a double-stud LSF wall model (model specimen 5).

4.2.3 Finite Elements and Solution Method

For thermal analyses, mass, link, solid or shell elements are available, where the degrees of freedom at the nodes are temperatures [71]. For the 3D LSF wall models, shell elements were addressed to the steel profiles and solid elements to the gypsum plasterboard, air, and cavity insulation.

As illustrated in the following Figure 4.3a, SHELL131 is a layered quadrilateral thermal shell with four nodes, with up to 32 DOF per node. For each layer, a thickness must be attributed. In the proposed models, a single-layer plane thickness was set according to steel nominal thickness. The joints between studs and tracks were assumed to remain perfectly rigid, which is accomplished by allowing multiple thicknesses to the shell elements in the domain of the overlapping regions (refer to Figure 4.2). Linear shape functions are selected to represent the field variable in the planes of the element and, as the steel thickness is sufficiently small, a linear variation of the temperature through the layer thickness was also assumed. The integrals appearing in the finite element formulation are numerically evaluated using the full Gaussian integration method with 2 x 2 points in-plane and 3 points through-thickness. Furthermore, when the shell element is directly attached to an underlying solid element, the temperature TEMP in the solid was set to replace TBOT in the shell (see Figure 4.3a). For this purpose, one should select the option “paint” for the shell finite element.

(a) SHELL131 Finite Element **(b) SOLID70 Finite Element**

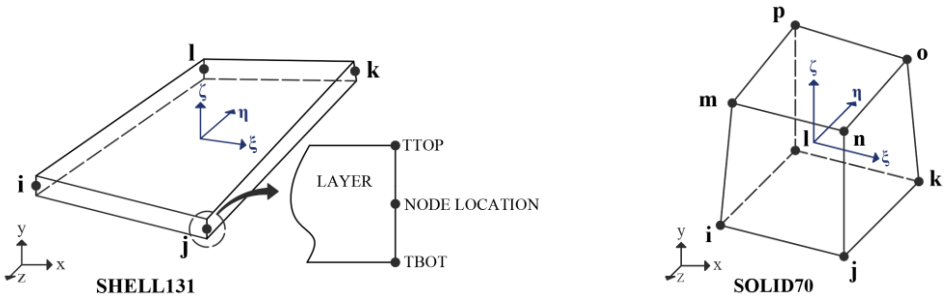

Figure 4.3- Finite elements for heat transfer analyses.
Adapted from ANSYS® (2007).

Figure 4.3b shows SOLID70, an 8-node brick thermal solid with one temperature DOF per node in which the nodal field variable is approximated by linear shape functions. This element also employs the full Gaussian integration with 2 x 2 x 2 points.

For both SHELL131 and SOLID70 elements, the values of the field variable are calculated at the integration points and extrapolated to the nodes of the element. Also, when applicable, the film coefficient was set to be evaluated at the average film temperature.

The global system of equations is solved through an iterative process using the full Newton-Raphson scheme. In this method, the vector of the thermal loads and the conductivity matrix is updated at each iteration cycle. The converge criterion is achieved when the relative residual of the solution obtained between consecutive time steps is smaller than a tolerance times a reference value. For the present thermal analyses, the heat flow convergence criterion was selected, with a tolerance of 1.0×10^{-3} and a minimum reference value of 1.0×10^{-6}.

ANSYS allows the employment of automatic time-stepping, where the time increment is optimized according to the solution progress. In the present study, the time step size was 60 seconds, restricted to a minimum and maximum time step of 1 and 60 seconds, respectively.

4.2.4 Initial and Boundary Conditions

In the present investigation, a transient state nonlinear behaviour is chosen for the discretized models, in which the boundary conditions for the fire-exposed side of the wall models are defined as per Eqs. 2.6a, 2.6a [74].

Regarding standard fire exposure, the EN 1991-1-2 [24] establishes that for the exposed side of a construction element, $\alpha_{cv} = 25$ [W/m²K] can be admitted when using standard fire ISO 834 [17], whilst for the unexposed side, α_{cv} equals 9.0 [W/m²K] when assuming the effects of combined radiation and convection. Additionally, the fire is considered as a black body, that is, $\varepsilon_f = 1.0$ and ε_m depends on the material type (refer to section 4.2.5 next). For composite wall panels under standard fire conditions, the initial temperature is specified according to ISO 834 [17], that is, $T_0 = 20$ °C applied to all nodes of the respective model.

EN 1991-1-2 [24] does not state the parameters for heat transfer between surface areas and the cavity region. Accordingly, as convection and radiation occur in LSF wall cavities, convection and radiation boundary conditions must be addressed to these regions, as shown in the following Figure 4.4. Thus, based on previous numerical research [60], for the exposed stud row, the film coefficient in the plasterboard-cavity interface as well as in the steel areas oriented towards the cavity, was set to $\alpha_{cv} = 17$ [W/m²K]. As for the surface areas on the unexposed stud row, the convection coefficient is $\alpha_{cv} = 13$ [W/m²K]. The temperature evolution for both

radiation and convection effects in the cavity derives from the experimental results and is termed $T_{CAV-EXP}$ or $T_{CAV-UNEXP}$ (hybrid approach).

Also, except for the areas on the exposed side, at the cavity-gypsum plasterboard or cavity-insulation interfaces, a 10 mm thick air thermal boundary layer was included assuming that the heat transfer through this layer occurs by conduction.

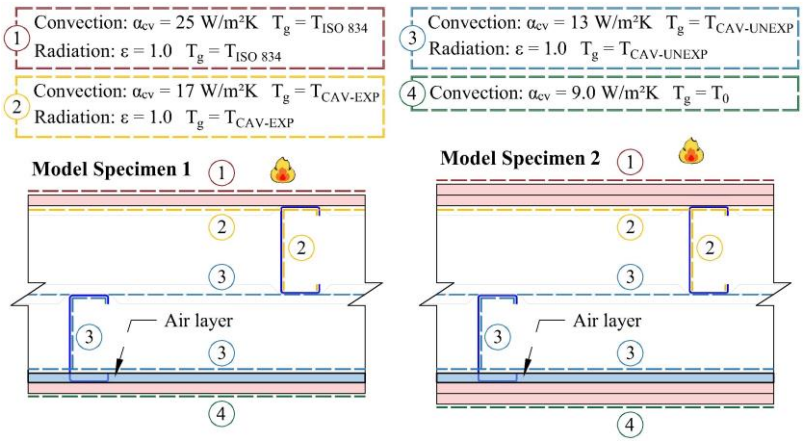

Figure 4.4- Boundary conditions of the model specimens without cavity insulation.

For cavity insulated models, the nodes along the mid-thickness of the ceramic fibre blanket followed the respective average temperatures collected in the experimental tests ($T_{INS-EXP}$ and $T_{INS-UNEXP}$), according to Figure 4.5.

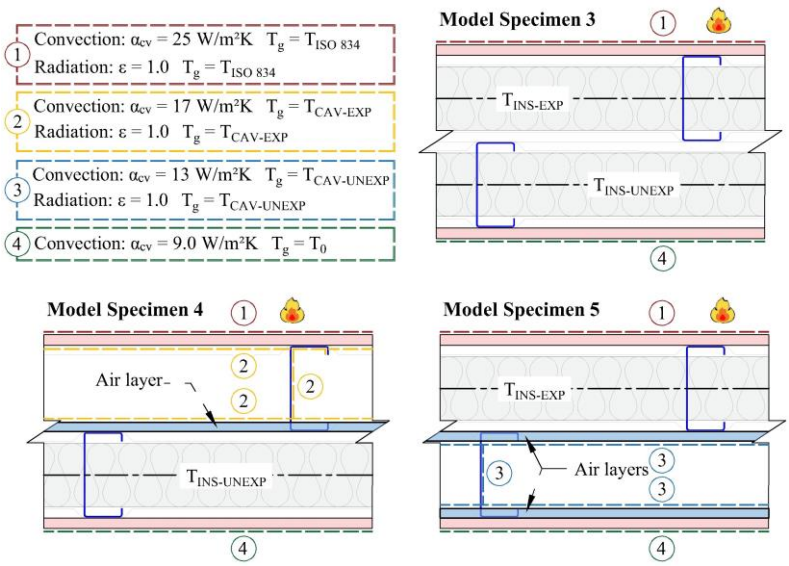

Figure 4.5- Boundary conditions of the model specimens with cavity insulation.

Radiation and convection were assigned to the gypsum plasterboard insulation areas around the unexposed stud row, with $\alpha_{cv} = 9.0$ [W/m²K]. The remaining sides of the models in contact with the test frame are considered as adiabatic surfaces according to Eq. 4.6a and, although there are thermal losses due to surface irregularities, gaps and thermal expansion of the materials, perfect contact along the interfaces of the elements was presumed.

4.2.5 Material Thermal Properties

The specific heat and thermal conductivity of the gypsum plasterboard used in this research follow the recommendations of Sultan (1996) [40] and are illustrated in Figure 4.6. In their study, the authors analysed the fire resistance of load-bearing wall assemblies manufactured with Type X fire-resistant gypsum plasterboards with a bulk density of 750 kg/m³ at 20 ºC, comparable to the Type F fire-resistant gypsum plasterboards that are employed in the present study, with a bulk density of 770 kg/m³ at 20 ºC.

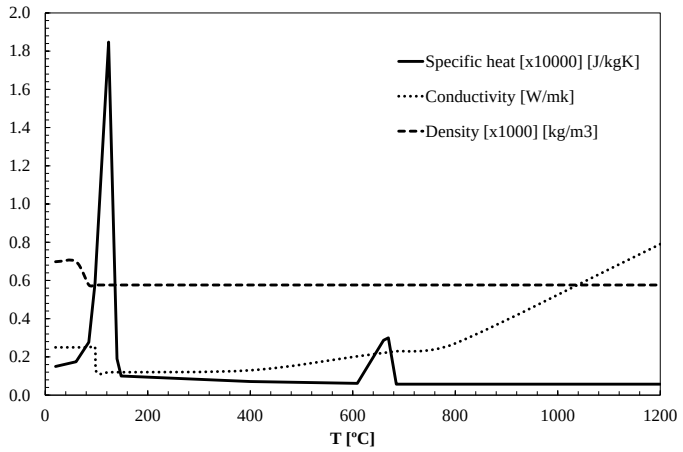

Figure 4.6- Effective thermal properties of gypsum plasterboard. Adapted from Sultan [40].

The energy consumed by the endothermic phases in the calcination reactions is incorporated in the specific heat values presented and the effects of ablation and porous radiation and convection are apparently accounted for in the values of thermal conductivity. The thermal conductivity at 20 ºC given by the manufacturer is similar to that of Sultan (1996) [40]. The density of the Type-F gypsum plasterboard was adapted using the values of Sultan

(1996) [40] and the drop in its value at 80 º C is due to the free water evaporation (see Appendix C). Moreover, the emissivity is considered equal to 0.8, constant.

As for the ceramic fibre, the properties are given following the manufacturer's specifications [75] and are shown in Figure 4.7. Because of the ceramic fibre's integrity at high temperatures and anhydrous character, the density is considered 128 kg/m³ at all temperatures, while specific heat remains approximately constant. The thermal conductivity increases expressively after 200 ºC as to include the effects of ablation and account for porous radiation and convection. The emissivity is 0.9 constant.

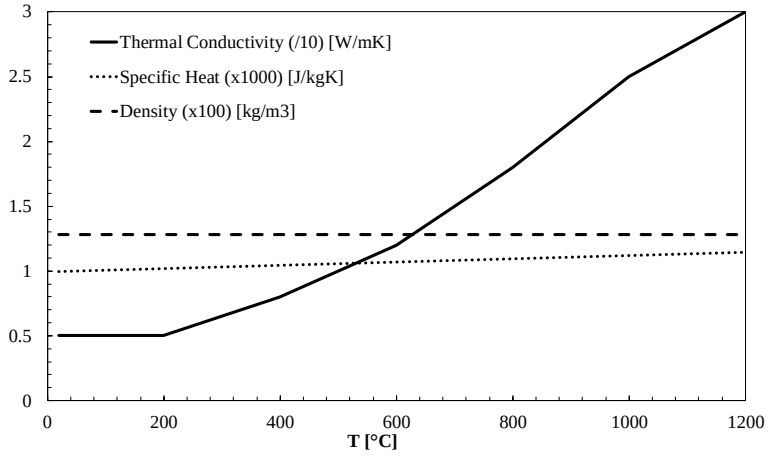

Figure 4.7- Thermal properties of ceramic fibre insulation.
Adapted from Morgan Advanced Materials [75]**.**

For carbon CFS elements, their thermophysical properties are given by EN 1993-1-2 [38] and are represented in Figure 4.8. The emissivity of carbon steels is 0.7 at all temperatures, as stated by EN 1991-1-2 [24].

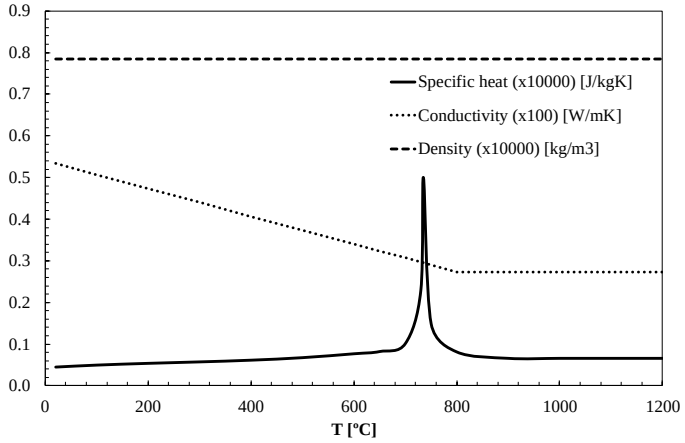

Figure 4.8- Thermal properties of carbon steel.
EN 1991-1-2 [24].

Figure 4.9 represents the variation of the thermal properties of the air with temperature, adapted from Çengel and Ghajar [76]. The properties are evaluated at 1 atm pressure. For the modelling purposes of this research, the air emissivity is taken as 1.0, constant at all temperatures.

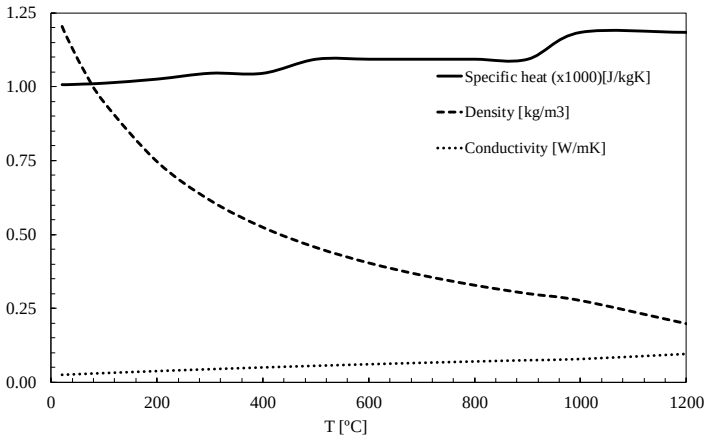

Figure 4.9- Thermal properties of air.
Adapted from Çengel and Ghajar [76]**.**

4.3 Numerical Validation and Discussion

Figure 4.10 and Figure 4.11 illustrate the comparison between the experimental and numerical results for the temperature development in Model Specimens 1 and 2, respectively,

expressed in terms of average and maximum temperatures. The data were collected at selected nodes throughout the finite element mesh (see Appendix D for detailed information).

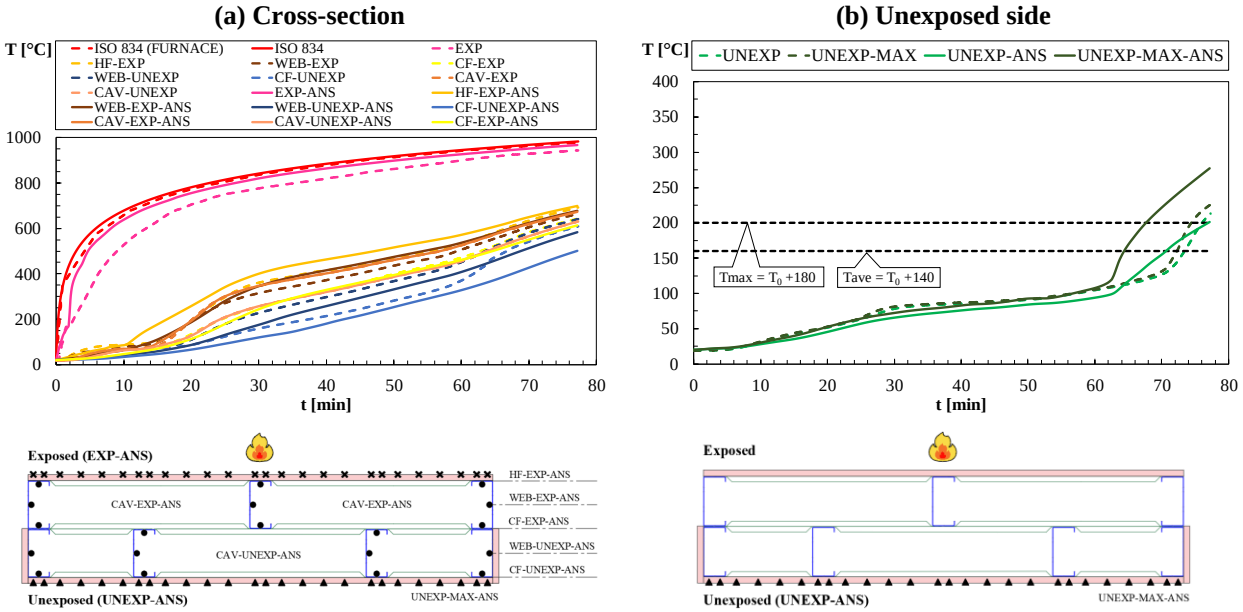

Figure 4.10- Numerical and experimental results for Model Specimen 1.

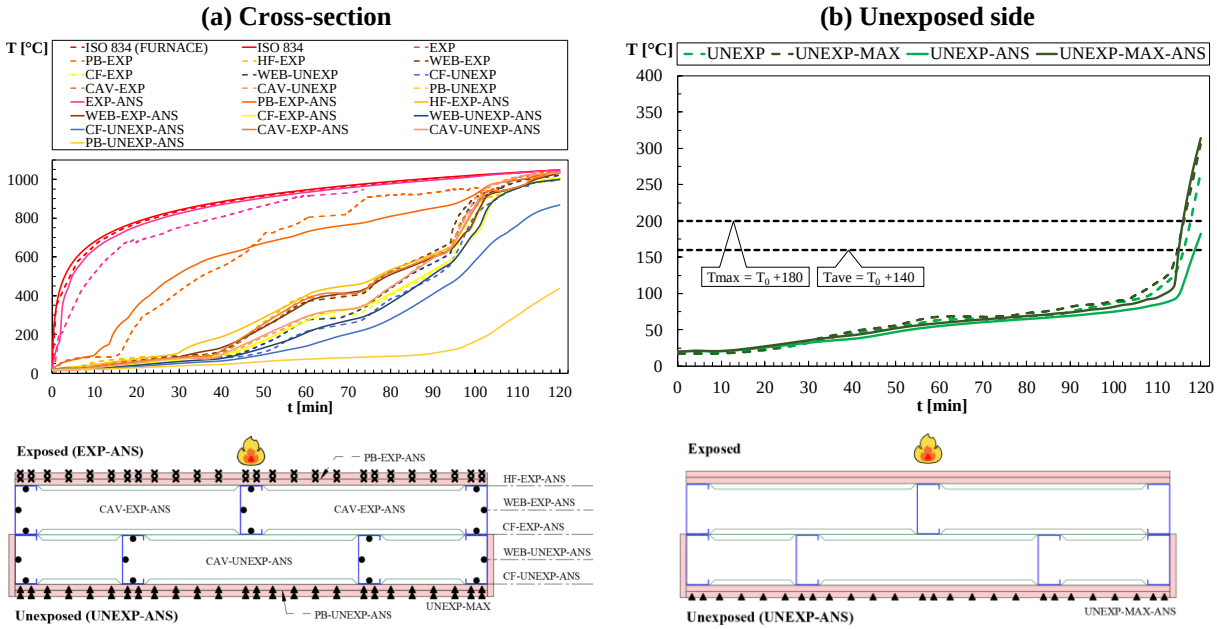

Figure 4.11- Numerical and experimental results for Model Specimen 2.

Regarding the temperature development on the exposed surface of the models, it is noteworthy that the furnace temperature used to represent ISO 834 standard fire curve is lower than the curve employed in the simulations. Accordingly, the numerical results are higher than the experimental ones. This pattern is also observed for the temperatures of the hot-flange and

web of the exposed stud row, especially in Model Specimen 1, with the numerical temperature profile of the exposed cold-flange approaching the experimental values. Conversely, the computed temperatures of the web and cold-flange of the unexposed stud row were lower when compared to the measured data, which is related with the lower temperatures in the unexposed cavity as well as with the air layer employed in the simulations. Moreover, a great difference between PB-EXP and PB-EXP-ANS in Model Specimen 2 was noticed. This is explained by the fact that the exposed gypsum plasterboard is assumed to remain in place throughout the analysis procedure.

Concerning the average and maximum temperatures on the unexposed side of both uninsulated models, good agreement was obtained during most of the simulation period, with the temperatures diverging in the last minutes of fire exposure. Such behaviour can be justified by the steep increase in the thermal conductivity of the gypsum plasterboard after 800 ºC, increased radiation effects in the cavity over temperature rise and perfect contact between the elements. For Model Specimen 2, the numerical insulation failure in terms of T_{ave} was higher than the experimental record, which is linked with the additional protection layer on the unexposed side.

As for the models with wall cavity insulation, Figure 4.12, Figure 4.13 and Figure 4.14 show the comparison between the experimental and numerical results for the temperature development in Model Specimens 3, 4 and 5, respectively, expressed in terms of average and maximum temperatures.

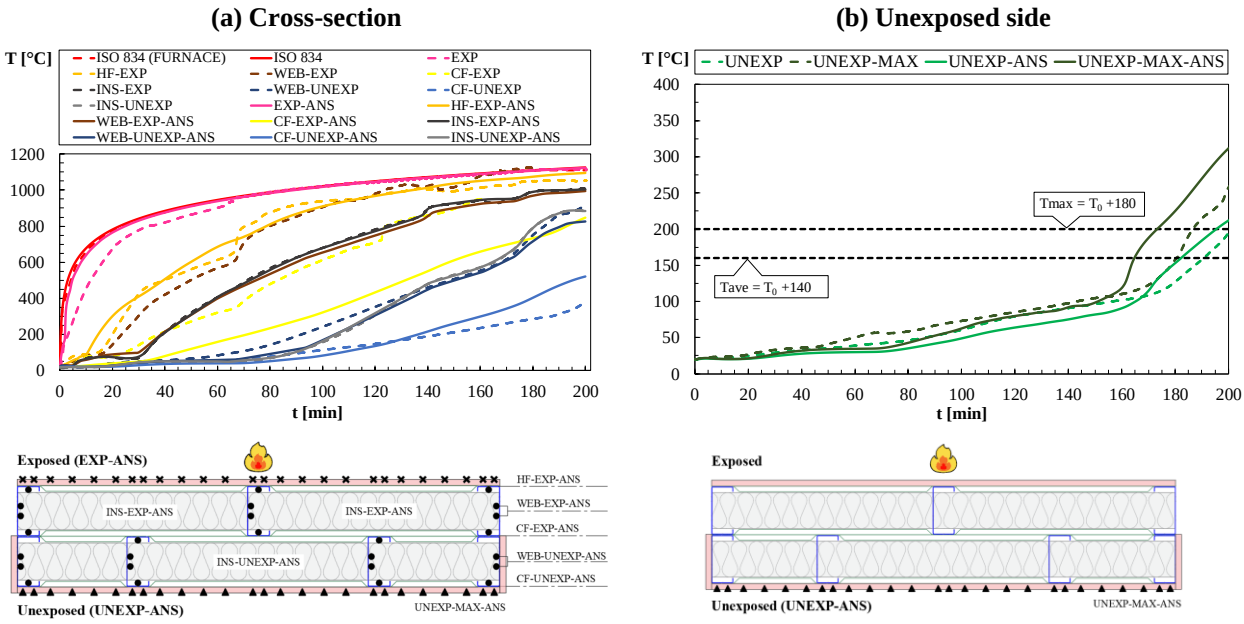

Figure 4.12- Numerical and experimental results for Model Specimen 3.

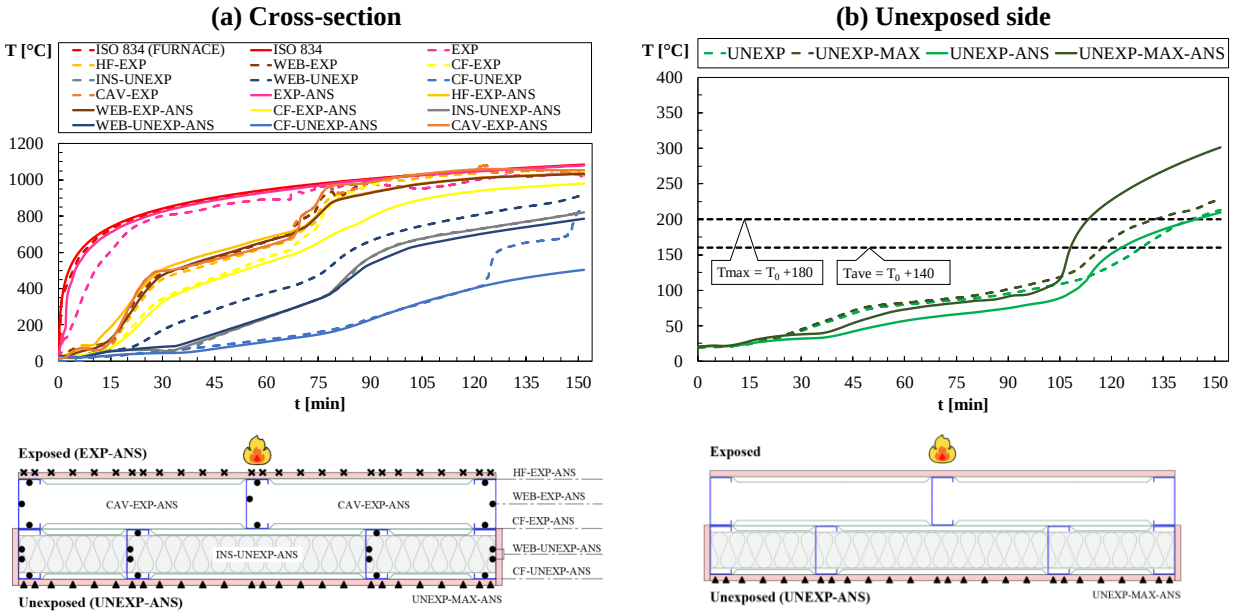

Figure 4.13- Numerical and experimental results for Model Specimen 4.

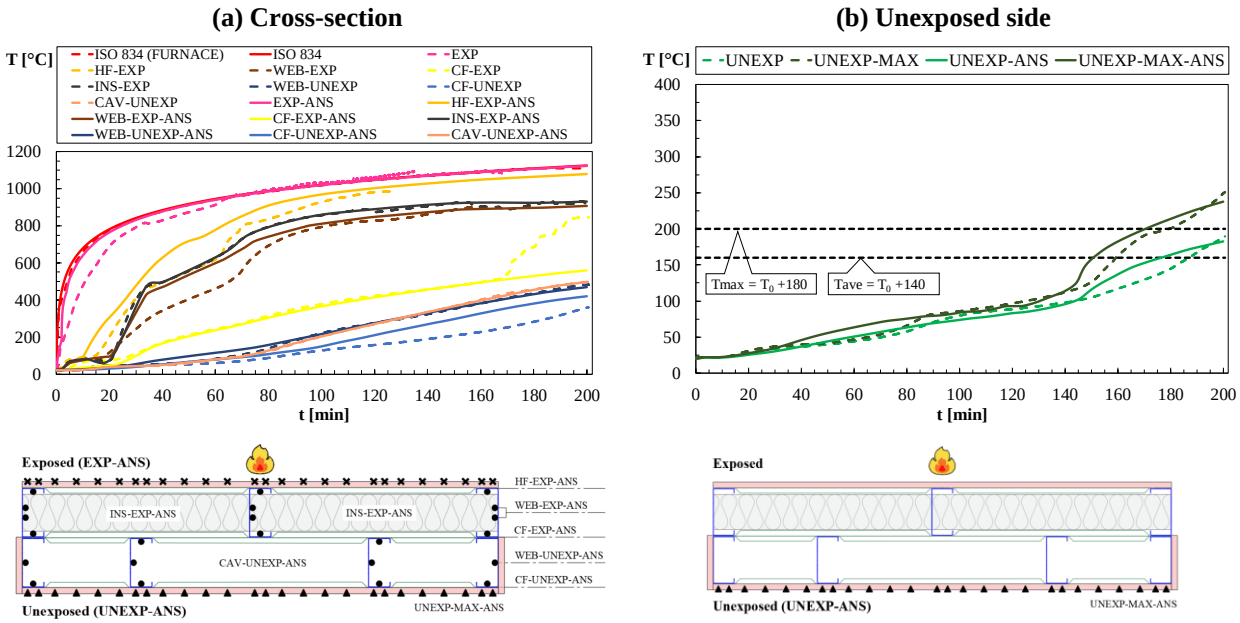

Figure 4.14- Numerical and experimental results for Model Specimen 5.

Referring to Model Specimen 3, as both cavities are filled with ceramic fibre insulation and perfect contact between the different material models is assumed, a difference is noticed in the heat development of CF-EXP-ANS. In contrast, as the temperatures of INS-UNEXP-ANS rise, the heating rate of CF-UNEXP-ANS tends to increase at a higher rate than CF-UNEXP after 135 minutes.

The computed temperatures over the cross-section of the models with partial insulation match reasonably well with the experimental results. In Model Specimen 4, when WEB-EXP-ANS is compared to WEB-EXP and CF-EXP-ANS to CF-EXP, a notable agreement is observed up to 60 minutes. Similarly, a good correlation exists between CF-UNEXP-ANS and CF-UNEXP until 125 minutes. In Specimen 5, the agreement is particularly strong between WEB-UNEXP-ANS and WEB-UNEXP during the entire simulation, as well as between CF-EXP-ANS and CF-EXP until 170 minutes. This may be linked with the protection offered by the air layers. Nevertheless, when elevated temperatures are achieved, especially in the last stages of fire, the existence of the air layer protection in both partially insulated models and the perfect contact between the materials seem to have hindered the numerical results.

In all cavity insulated models, the temperatures of the web of both exposed and unexposed insulated rows tend to follow the temperature evolution of the nodes located along the mid-thickness of the insulation in which the temperature boundary conditions were applied. Thus, for those regions the deviation between the measured and modelled data is substantial.

As also observed for Model Specimens 1 and 2, the computed average and maximum temperatures on the unexposed side of the cavity insulated specimens were generally higher than the experimental results during the last stages of the fire development. In terms of maximum temperatures, higher discrepancies between experimental and numerical results were noticed for Model Specimens 3 and 4, with insulation placed in the unexposed cavity. This is due to the perfect contact of the insulation with the unexposed gypsum plasterboard.

4.4 Summary and Conclusions

Table 4.1 presents the comparison between the experimental and analytical fire resistance obtained for the double-stud LSF walls concerning T_{ave} and T_{max} insulation requirements. The highest absolute relative errors are related to the maximum temperatures on the unexposed side (T_{max}) of Model Specimens 1, 3 and 4. As aforementioned in the previous section, this variance was mainly attributed to the perfect contact between the materials, which prevents heat loss due to gaps and surface irregularities. For T_{ave} requirements, good agreement was obtained for all model specimens.

Table 4.1- Comparison between the experimental and numerical fire resistance of the specimens

Model Specimen Nº	Experimental		Numerical		Absolute relative error	
	Fire resistance (T_{ave}) [min]	Fire resistance (T_{max}) [min]	Fire resistance (T_{ave}) [min]	Fire resistance (T_{max}) [min]	(T_{ave}) [%]	(T_{max}) [%]
1	73	74	70	67	4.1	9.5
2	116	116	118	115	1.7	0.86
3	190	186	181	172	4.7	7.5
4	128	132	122	112	4.7	15.1
5	187	179	176	170	4.2	5.0

For Model Specimen 2, the fire resistance regarding T_{ave} was slightly overestimated, with an absolute relative error of 1.7 %. However, except for Model Specimen 2, the results of the FE thermal analysis were conservative if compared to the experimental tests. Potential sources of errors are associated with the numerical error of the solution method and to the selected finite element mesh, as well as with the material properties used and non-temperature-dependent parameters.

It was observed that when intending to consider the effects of a wider cavity in the heat transfer mechanisms, it is important to assign different curves to represent the temperature evolution within each cavity. Also, employing the concept of an air thermal boundary layer located at appropriate regions of the models was significant to attain enhanced results. Yet, further investigations are necessary to conduct an in-depth evaluation of the influence of thermal boundary layers in LSF wall cavities.

Chapter 5

5 Simplified Calculation Method

The provision of a simplified method to predict the thermal response of LSF walls under fire conditions is essential to develop hands-on design models in construction practice. A great variety of simple formulas are available in the literature comprising distinct types of single-stud LSF walls, but there is still a lack of an appropriate simple method that applies to a more diverse range of wall assemblies. Also, the applicable existing regulations do not provide a simple design method to assess the fire behaviour of LSF walls.

In the context of wall assemblies subjected to fire, the timber standard EN 1995-1-2 [77] in its Annex E offers a simplified method to verify the separation function of timber walls clad with different types of boards, with or without cavity insulation. Nevertheless, as only a limited number of timber wall configurations was considered, the results obtained are usually over-conservative. In this sense, Frangi [78] adapted the methodology of EN 1995-1-2 [77] to include a wide variety of timber wall structures by using an improved design approach. In the new proposal, it is possible to consider the contribution to the fire resistance of an unlimited number of layers and the cavity of the construction element may be filled or not with insulation. Deduced from a series of experimental tests and extensive parametric numerical analysis, the design parameters influencing the insulation behaviour of the assemblies were determined and enhanced results were attained when compared to EN 1995-1-2 [77]. Although the method was originally developed to assess the insulation behaviour of timber structures, it can be adapted to model heat transfer paths through the layers of single and double-stud LSF wall assemblies, without considering the influence of heat flow through steel elements.

Therefore, this chapter addresses the employment of the improved design model to predict the insulation fire resistance of the double-stud LSF wall assemblies related to this research. For that purpose, the coefficients of the original improved design model were adapted to include the special features of double-stud LSF walls. The results obtained using the modified simplified approach are compared with those acquired in the experimental and numerical evaluations.

5.1 Outline of the Improved Design Model

In the improved design model proposed by Frangi [78], the fire resistance in terms of insulation requirements t_{ins} [min] of the entire assembly is obtained from the contribution of each component layer (claddings, voids or insulated cavities) according to their function and interaction in the configuration considered, which is given by

$$t_{ins} = \sum_{i=1}^{i=n-1} t_{prot,i} + t_{ins,n} \qquad \textbf{5.1}$$

In which $\sum_{i=1}^{i=n-1} t_{prot,i}$ [min] is the sum of the protection values of the component layers preceding the last layer of the assembly on the unexposed side and $t_{ins,n}$ [min] represents the insulation value of the last layer of the assembly on the unexposed side, as represented in Figure 5.1.

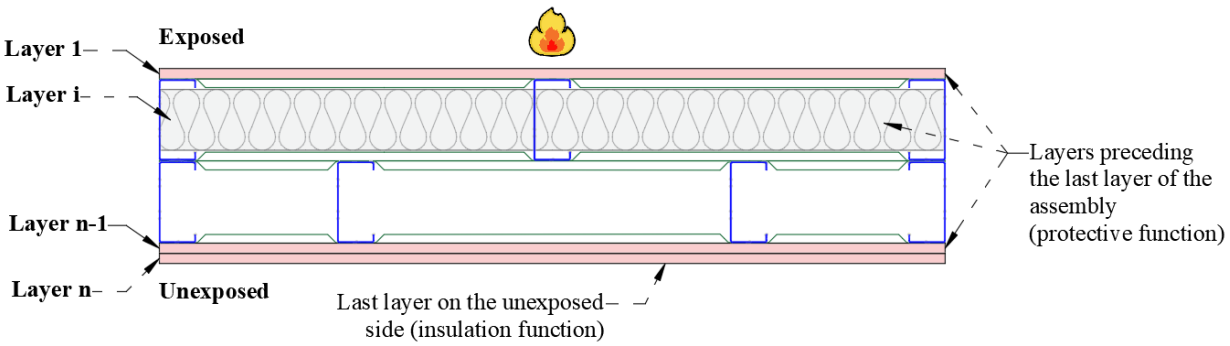

Figure 5.1- Arrangement of the layers with protective and insulation function in an LSF wall.

The protection $t_{prot,i}$ and insulation $t_{ins,n}$ values of the layer are calculated considering its respective position in the wall configuration, as follows

$$t_{prot,i} = \left(t_{prot,0,i}\, k_{pos,exp,i}\, k_{pos,unexp,i} + \Delta t_i\right) \qquad \textbf{5.2a}$$

$$t_{ins,n} = \left(t_{ins,0,i}\, k_{pos,exp,n} + \Delta t_n\right) \qquad \textbf{5.2b}$$

In the previous expressions, $t_{prot,0,i}$ [min] and $t_{ins,0,n}$ [min] are the basic protection and insulation values of the layer being considered, respectively, which are dependable mainly on the type of material and thickness of the layer. These values are calculated according to Table E.1 available in Appendix E. Moreover, $k_{pos,exp,i}$ and $k_{pos,exp,n}$ are the position coefficients that relate to the influence of the layers preceding the layer considered (see Table E.2, Appendix E) and $k_{pos,unexp,i}$ is the position coefficient that considers the influence of the layer backing the layer considered, as seen in Table E.3. Additionally, Δt_i [min] and Δt_n [min] are the correction times for layers protected by Type F gypsum plasterboards obtained as per Table E.4.

The protective effect of void cavities is considered by modifying the position coefficients of the layers on the exposed and unexposed side of the cavity, as shown in Table E.5. However, regarding the model specimens of this research with single or double cavities, as well as with partial ceramic fibre cavity insulation, the correction coefficients of the original improved design model were modified due to the enlarged cavity size of double-stud LSF assemblies and enhanced thermal performance of the ceramic fibre. Thus, in the case of double-sized cavities (Specimens 1 and 2), regarding the layer placed on the unexposed side of the cavity, the correction coefficient was modified from 1.6 to 3.2. Also, it was verified in the experimental tests that the remaining cavity and the integrity of the ceramic fibre insulation impact significantly the insulation behaviour of partially insulated assemblies. Therefore, when the ceramic fibre blanket is placed on the exposed side of the cavity (Specimen 5), the value of $k_{pos,unexp,i} = 1$ for the layer on the unexposed side of the cavity was found to be over-conservative and was further calibrated to $k_{pos,unexp,i} = 2.6$. It is noteworthy that the expressions used to derive the basic values and position coefficients, as well as the correction times of the ceramic fibre, are equal to those employed for rock fibre in the original method, being the proposed modifications made restricted to the corrections related with the cavity protection.

5.2 Results and Discussion

To comprehend how the method was applied to estimate the insulation fire resistance of the double-stud LSF wall specimens, a step by step procedure is presented in Appendix F. To predict the insulation fire resistance of the assembly, a single heat transfer path was assessed,

without considering the influence of the steel studs. Table 5.1 presents the results obtained with the modified improved design model and a comparison with the experimental and numerical figures.

The comparison with the experimental and numerical results was only possible in terms of the average temperature on the unexposed side of the specimen, given that the improved design method was originally conceived by considering this criterion. From Table 5.1, the insulation fire resistance of the assemblies was estimated with a reasonable agreement with the experimental and numerical findings and the highest difference is observed for Specimen 2. Generally, the modified improved design model leads to slightly more conservative results when compared with the numerical data, which is related to the assumptions employed to derive the simplified approach.

Table 5.1- Insulation fire resistance of the specimens using the modified improved design model and comparison with the experimental and numerical results.

Simplified Model Specimen Nº	Experimental	Numerical	Simplified	Relative error	
	Fire resistance (T_{ave}) [min]	Fire resistance (T_{ave}) [min]	Fire resistance (T_{ave}) [min]	Experimental vs. simplified [%]	Numerical vs. simplified [%]
1	73	70	67	8.2	4.3
2	116	118	104	10.3	11.9
3	190	181	174	8.4	3.9
4	128	122	118	7.8	3.3
5	187	176	175	6.4	4.0

It was confirmed that a wider cavity and the use of ceramic fibre cavity insulation enhances the insulation performance of the assemblies and that such factors should be considered in the simplified approach by modifying the correction coefficients related with the cavity effect. Thus, the improved design model can be adapted to estimate the insulation fire resistance of double-stud LSF walls, although further studies are necessary to develop exclusive expressions for the ceramic fibre and to investigate the effects of the ceramic fibre insulation thickness and cavity size.

Chapter 6

6 Conclusion and Recommendations

The underlying investigation addresses the experimental, numerical, and simplified evaluation of the thermal insulation performance of double-stud LSF walls subjected to ISO 834 standard fire curve. A series of experimental tests were developed to provide useful data regarding thermal transmission effects of diverse configurations of double-stud LSF walls and the fire resistance of the specimens was determined based on the applicable standard requirements. In this matter, a comprehensive numerical study using ANSYS® Multiphysics was carried out to predict the fire resistance of double-stud LSF walls and identify the relevant parameters of the hybrid simulation approach. Also, a simplified approach was developed by modifying the improved design method, which led to a practical solution to estimate the insulation response of the specimens. The fire resistance regarding the thermal insulation criterion (I) of the model specimens using the numerical and simplified evaluation was estimated in good agreement with the experimental results.

The experimental tests showed that a wider cavity is beneficial to the thermal insulation behaviour of LSF walls as it allows a more uniform heat distribution within the cavity and reduces the heating rate of the unexposed surfaces. The use of ceramic fibre cavity insulation greatly enhances the fire resistance of the walls. However, when the insulation is in contact with the steel, heat build-up occurs around the hot-flange of the steel studs, increasing the heating rate of the steel sections, especially if the insulation is tightly inserted within the cavity. Also, regarding the thermal performance of partially insulated specimens, placing the insulation towards the unexposed gypsum plasterboard is detrimental to the fire behaviour of the wall due to increased temperatures and therefore radiation and convection effects in the exposed stud row. When the insulation blanket is placed towards the exposed side, higher fire resistance is achieved, which was attributed to the slow heat release from the insulation to the remaining unexposed cavity.

As double-stud LSF walls behave differently than single-stud assemblies, a new hybrid modelling approach was proposed in this work, in which different temperature curves deriving from the experimental tests are addressed to the unexposed and exposed cavities and insulation layers. This greatly improves the fire resistance of the models, avoiding over-conservative results. Likewise, the employment of an air thermal boundary layer in uninsulated and partially insulated model specimens proved to be relevant to acquire consistent results. However, the models can still be adapted to provide more accurate results and further investigations are necessary to assess the effects and applicability of thermal boundary layers in LSF walls, as well as to propose alternative methodologies. Moreover, the assumed perfect contact between the material models proved to be a potential source of error, especially regarding insulated model specimens, and the use of non-temperature-dependant parameters, finite element mesh and material thermal properties may be related with the errors observed.

The simplified approach employed in this research was able to estimate reasonably the insulation fire resistance of the specimens. However, as it was founded on the improved design model, originally developed for timber walls with a smaller cavity and insulated or non-insulated with rock or glass fibre insulation, it is needed to obtain specific expressions to consider the effects of the cavity size, type and thickness of the insulation.

6.1 Recommendations for Further Studies

The provision of experimental data and modelling techniques expressively contributes to the development of design models in construction practice, and the use of practical engineering tools are of great importance to accurately represent diverse physics phenomena. In this context, additional research must be conducted to better comprehend the fire behaviour of double-stud LSF walls and expand the knowledge regarding the thermal and structural behaviour of these assemblies:

- Conduct experimental and numerical investigation regarding the structural behaviour of double-stud LSF walls under fire;
- Include a wide variety of construction materials and their thermal and structural response, contribution, or detriment to the fire resistance of double-stud LSF walls, including different cold-formed steel sections;

- Investigate the effects of assorted framework configurations on the thermal and structural behaviour of double-stud LSF walls under fire;
- Conduct an experimental analysis of the thermal properties of the materials employed to identify possible discrepancies between measured and modelled data;
- Perform numerical and experimental investigations considering different fire curves, including natural fire models;
- Carry out a set of parametric analysis to identify a wide range of parameters affecting the fire resistance of the double-stud LSF walls, e.g. insulation thickness, geometry and properties of the studs and tracks, the thickness of the gypsum plasterboard and other protective materials, different types of cavity insulation and their respective positions in the assembly;
- Develop a simplified design approach to predict the fire resistance of double-stud LSF walls supported by parametric analyses, experimental tests, and previous research.

References

[1] CSSBI, The Lightweight Steel Frame House Construction Handbook, Can. Sheet Steel Build. Inst. (2005) 151.

[2] A.D. Ariyanayagam, Fire Performance and Design of Light Gauge Steel Frame Wall Systems Exposed to Realistic Design Fires, Queensland University of Technology, 2013.

[3] B. Baleshan, Numerical and Experimental Studies of Cold-formed Steel Floor Systems under Standard Fire Conditions, Queensland University of Technology, 2012.

[4] S. Gunalan, Structural Behaviour and Design of Cold-formed Steel Wall Systems Under Fire Conditions, Queensland University of Technology, 2011.

[5] J. Vallée, Reliability of Fire Barriers, Lund University, 2016.

[6] P.J. Grubb, M.T. Gorgolewski, R.M. Lawson, Building Design Using Cold Formed Steel Sections: Light Steel Framing in Residential Construction, SCI Publ. P301. (2001) 97.

[7] LSK, European Lightweight Steel-framed Construction, (2005) 92.

[8] E. Yandzio, R.M. Lawson, A.G.J. Way, Light Steel Framing in Residential Construction, SCI Publ. P402. (2015) 125.

[9] P. Keerthan, M. Mahendran, Numerical Studies of Gypsum Plasterboard Panels Under Standard Fire Conditions, Fire Saf. J. 53 (2012) 105–119. doi:10.1016/j.firesaf.2012.06.007.

[10] NAHB Reasearch Center, Residential Steel Framing: Fire and Acoustic Details, (2002) 72.

[11] S. Kesawan, M. Mahendran, A Review of Parameters Influencing the Fire Performance of Light Gauge Steel Frame Walls, Fire Technol. 54 (2018) 3–35. doi:10.1007/s10694-017-0669-8.

[12] W. Y.C., Steel and Composite Structures: Behaviour and Design for Fire Safety, Spon Press and Taylor & Francis, London, United Kingdom, 2005.

[13] A.D. Ariyanayagam, M. Mahendran, Influence of cavity insulation on the fire resistance of light gauge steel framed walls, Constr. Build. Mater. 203 (2019) 687–710. doi:10.1016/j.conbuildmat.2019.01.076.

[14] V.K.R. Kodur, M.A. Sultan, Factors Influencing Fire Resistance of Load-Bearing Steel Stud Walls, Fire Technol. 42 (2006) 5–26. doi:10.1007/s10694-005-3730-y.

[15] J. T. Gerlich, P. C. R. Collier, A. H. Buchanan, Design of Light Steel-framed Walls for Fire Resistance, Fire Mater. 20 (1996) 79–96. doi:10.1002/(SICI)1099-1018(199603)20:2<79::AID-FAM566>3.0.CO;2-N.

[16] European Commitee for Standardization, EN 1363-1 Fire Resistance Tests - Part 1: General Requirements, (2012) 52.

[17] International Organization for Stardardization, ISO 834-1 Fire-Resistance Tests - Elements of Building Construction Part 1: General Requirements, (1999).

[18] CSSBI, Lighweight Steel Framing Architectural Design Guide, (2002) 68.

[19] E.C. for Standardization, EN 1364-1 Fire Resistance Tests for Non-Loadbearing Elements - Part 1: Walls, (1999) 32.

[20] T.L. Bergman, A.S. Lavine, Fundamentals of Heat and Mass Transfer, 8th ed., John Wiley & Sons, Inc., Hoboken, New Jersey, 2017.

[21] R. Karwa, Heat and Mass Transfer, Springer, Singapore, 2017.

[22] P. Nithiarasu, R.W. Lewis, K.N. Seetharamu, Fundamentals of the finite element method for heat and mass transfer, 2nd ed., Wiley & Sons, Ltd., Chichester, United Kingdom, 2016. doi:10.1002/0470014164.

[23] A.H. Buchanan, A.K. Abu, Structural Design for Fire Safety, 2nd ed., John Wiley & Sons, Ltd., Chichester, United Kingdom, 2017.

[24] European Commitee for Standardization, EN 1991-1-2 Eurocode 1 : Actions on Structures - Part 1-2 : General Actions - Actions on Structures Exposed to Fire, (2002) 59.

[25] J.T.H. Gerlich, Design of Loadbearing Light Steel Frame Walls for Fire Resistance, University of Canterbury, 1995.

[26] D.A. Kontogeorgos, M.A. Founti, Gypsum Board Reaction Kinetics at Elevated Temperatures, Thermochim. Acta. 529 (2012) 6–13. doi:10.1016/j.tca.2011.11.014.

[27] D.I. Kolaitis, M.A. Founti, Development of a solid reaction kinetics gypsum dehydration model appropriate for CFD simulation of gypsum plasterboard wall assemblies exposed to fire, Fire Saf. J. 58 (2013) 151–159. doi:10.1016/j.firesaf.2013.01.029.

[28] I. Rahmanian, Thermal and Mechanical Properties of Gypsym Boards and Their Influences on Fire Resistance of Gypsum Board Based Systems, University of Manchester, 2011.

[29] L. Gunawan, Numerical Models to Simulate the Thermal Performance of LSF Wall Panels, Queensland University of Technology, 2011.

[30] S. Kesawan, M. Mahendran, Fire tests of load-bearing LSF walls made of hollow flange channel sections, J. Constr. Steel Res. 115 (2015) 191–205. doi:10.1016/j.jcsr.2015.07.020.

[31] P. Kolarkar, M. Mahendran, Experimental Studies of Non-Load Bearing Steel Wall Systems Under Fire Conditions, Fire Saf. J. 53 (2012) 85–104. doi:10.1016/j.firesaf.2012.06.009.

[32] W. Chen, J. Ye, Y. Bai, X.L. Zhao, Improved Fire Resistant Performance of Load Bearing Cold-Formed Steel Interior and Exterior Wall Systems, Thin-Walled Struct. 73 (2013) 145–157. doi:10.1016/j.tws.2013.07.017.

[33] A.D. Ariyanayagam, S. Kesawan, M. Mahendran, Detrimental Effects of Plasterboard Joints on the Fire Resistance of Light Gauge Steel Frame Walls, Thin-Walled Struct. 107 (2016) 597–611. doi:10.1016/j.tws.2016.07.003.

[34] S. Gunalan, M. Mahendran, Finite Element Modelling of Load Bearing Cold-Formed Steel Wall Systems Under Fire Conditions, Eng. Struct. 56 (2013) 1007–1027. doi:10.1016/j.engstruct.2013.06.022.

[35] M. Feng, Y.. Wang, J.. Davies, Thermal Performance of Cold-Formed Thin-Walled Steel Panel Systems in Fire, Fire Saf. J. 38 (2003) 365–394. doi:10.1016/s0379-7112(02)00090-5.

[36] A.D. Ariyanayagam, M. Mahendran, Numerical Modelling of Load Bearing Light Gauge Steel Frame Wall Systems Exposed to Realistic Design Fires, Thin-Walled Struct. 78 (2014) 148–170. doi:10.1016/j.tws.2014.01.003.

[37] H.D. Craveiro, J. Paulo, C. Rodrigues, A. Santiago, L. Laím, Review of the High Temperature Mechanical and Thermal Properties of the Steels Used in Cold Formed Steel Structures - The Case of the S280 Gd+Z Steel, Thin Walled Struct. 98 (2016) 154–168. doi:10.1016/j.tws.2015.06.002.

[38] European Commitee for Standardization, EN 1993-1-2 Eurocode 3: Design of Steel Structures - Part 1-2: General Rules - Structural Fire Design, (2005) 78.

[39] A.D. Ariyanayagam, M. Mahendran, Influence of Cavity Insulation on the Fire Resistance of Light Gauge Steel Framed Walls, Constr. Build. Mater. 203 (2019) 687–710. doi:10.1016/j.conbuildmat.2019.01.076.

[40] M.A. Sultan, A Model for Predicting Heat Transfer Through Noninsulated Unloaded Steel-Stud Gypsum Board Wall Assemblies Exposed to Fire, Fire Technol. 32 (1996) 239–259. doi:10.1007/bf01040217.

[41] M.A. Sultan, V.R. Kodur, Light-Weight Frame Wall Assemblies: Parameters for Consideration in Fire Resistance Performance-Based Design, Fire Technol. 36 (2000) 75–88. doi:10.1023/A:1015446207222.

[42] P. Keerthan, M. Mahendran, Thermal Performance of Composite Panels Under Fire Conditions Using Numerical Studies: Plasterboards, Rockwool, Glass Fibre and Cellulose Insulations, Fire Technol. 49 (2013) 329–356. doi:10.1007/s10694-012-0269-6.

[43] F. Alfawakhiri, M.A. Sultan, Fire Resistance of Loadbearing LSF Assemblies, 15th Int. Spec. Conf. Cold- Form. Steel Struct. (2000) 545–561.

[44] Y. Dias, P. Keerthan, M. Mahendran, Predicting the Fire Performance of LSF Walls Made of Web Stiffened Channel Sections, Eng. Struct. 168 (2018) 320–332. doi:10.1016/j.engstruct.2018.04.072.

[45] K. Poologanathan, M. Mahendran, Numerical Modelling of Load Bearing LSF Walls Under Fire Conditions, in: Struct. Fire-SIF'2012 Proc. 7th Int. Conf. Struct. Fire, Zurich, Switzerland, 2012: pp. 205–214.

[46] Standards Australia, AS 1530.4 - Methods for Fire Tests on Building Materials, Components and Structures, (2005) 151.

[47] A.Y. Nassif, I. Yoshitake, A. Allam, Full-Scale Fire Testing and Numerical Modelling of the Transient Thermo-Mechanical Behaviour of Steel-Stud Gypsum Board Partition Walls, Constr. Build. Mater. 59 (2014) 51–61. doi:10.1016/j.conbuildmat.2014.02.027.

[48] I.D. Thanasoulas, I.K. Vardakoulias, D.I. Kolaitis, C.J. Gantes, M.A. Founti, Thermal and Mechanical Computational Study of Load-Bearing Cold-Formed Steel Drywall Systems Exposed to Fire, Fire Technol. 52 (2016) 2071–2092. doi:10.1007/s10694-016-0604-4.

[49] A.D. Ariyanayagam, P. Keerthan, M. Mahendran, Thermal Modelling of Load Bearing Cold-Formed Steel Frame Walls Under Realistic Design Fire Conditions, Adv. Steel Constr. 13 (2017) 160–189. doi:10.18057/IJASC.2017.13.2.5.

[50] M. Rusthi, P. Keerthan, M. Mahendran, A. Ariyanayagam, Investigating the Fire Performance of LSF Wall Systems Using Finite Element Analyses, J. Struct. Fire Eng. 8 (2017) 354–376. doi:10.1108/JSFE-04-2016-0002.

[51] W. Chen, J. Ye, X. Li, Thermal Behavior of Gypsum-Sheathed Cold-Formed Steel Composite Assemblies Under fire Conditions, J. Constr. Steel Res. 149 (2018) 165–179. doi:10.1016/j.jcsr.2018.07.023.

[52] W. Chen, J. Ye, X. Li, Fire Experiments of Cold-Formed Steel Non-Load-Bearing Composite Assemblies Lined With Different Boards, J. Constr. Steel Res. 158 (2019) 290–305. doi:10.1016/j.jcsr.2019.04.003.

[53] A.D. Ariyanayagam, M. Mahendran, Experimental Study of Non-Load Bearing Light Gauge Steel Framed Walls in Fire, J. Constr. Steel Res. 145 (2018) 529–551. doi:10.1016/j.jcsr.2018.02.023.

[54] A.D. Ariyanayagam, M. Mahendran, Fire Performance of Load Bearing LSF Wall Systems Made of Low Strength Steel Studs, Thin-Walled Struct. 130 (2018) 487–504. doi:10.1016/j.tws.2018.05.018.

[55] I.D. Thanasoulas, I.K. Vardakoulias, D.I. Kolaitis, C.J. Gantes, M.A. Founti, Coupled Thermo-Mechanical Simulation for the Performance-Based Fire Design of CFS Drywall Systems, J. Constr. Steel Res. 145 (2018) 196–209. doi:10.1016/j.jcsr.2018.02.022.

[56] P.A.G. Piloto, M.S. Khetata, A.B.R. Gavilán., Fire performance of non-loadbearing light steel framing walls - numerical simulation, 7Th Int. Conf. Mech. Mater. Des. 2 (2017) 1603–1610.

[57] M. Khetata, L. Fernandes, C. Marinho, P. Piloto, A. Gavilán, H. Razuk., Fire resistance of non-loadbearing light steelframing walls: numerical validation, in: XI Port. Congr. Steel Compos. Constr. – C. 2017, Portuguese Association for Steel and Composite Construction, Coimbra, Potugal, 2017: pp. 853–862.

[58] P.A.G. Piloto, M.S. Khetata, A.B.R. Gavilán, Fire Performance of Non-Loadbearing Light Steel Framing Walls-Numerical and simple calculation methods, MATTER Int. J. Sci. Technol. 3 (2017) 13–23. doi:https://dx.doi.org/10.20319/mijst.2017.33.1323 FIRE.

[59] P.A.G. Piloto, Fire resistance of cold-formed steel walls with composite panels : Results from insulation rating (I) and loadbearing prediction rating (R), Metálica Int. (2018) 12–17.

[60] S.M. Khetata, P.A. Piloto, A.B. Gavilán, Fire resistance of composite non-load bearing light steel framing walls, J. Fire Sci. 38 (2020) 136–155. doi:10.1177/0734904119900931.

[61] A. Shahbazian, Y.C. Wang, A fire resistance design method for thin-walled steel studs in wall panel constructions exposed to parametric fires, Thin-Walled Struct. 77 (2014) 67–76. doi:10.1016/j.tws.2013.12.001.

[62] A. Shahbazian, Y.C. Wang, A simplified approach for calculating temperatures in axially loaded cold-formed thin-walled steel studs in wall panel assemblies exposed to fire from one side, Thin-Walled Struct. 64 (2013) 60–72. doi:10.1016/j.tws.2012.12.005.

[63] S. Gunalan, M. Mahendran, Fire performance of cold-formed steel wall panels and prediction of their fire resistance rating, Fire Saf. J. 64 (2014) 61–80. doi:10.1016/j.firesaf.2013.12.003.

[64] B.C. Son, H. Shoub, Fire Endurance Tests of Double Module Walls of Gypsum Board and Steel Studs, Washington, D.C., 1973.

[65] American Society for Testing and Materials, ASTM E119 - Standard Test Methods for Fire Tests of Building Construction and Materials, (2019).

[66] H. Magarabooshanam, A. Ariyanayagam, M. Mahendran, Behaviour of Load Bearing Double Stud LSF Walls in Fire, Fire Saf. J. 107 (2019) 15–28. doi:10.1016/j.firesaf.2019.05.003.

[67] European Commitee for Standardization, EN 1364-1 Fire Resistance Tests for Non-Loadbearing Elements - Part 1: Walls, (1999) 32.

[68] European Commitee for Standardization, EN 13501-2 Fire Classification of Construction Products and Building Elements Part 2: Classification Using Data from Fire Resistance Tests, Excluding Ventilation Services, (2009) 79.

[69] D.K. Reddy, J.N, Gatling, The Finite Element Method in Heat Transfer and Fluid Dynamics, 3rd ed., CRC Press, Broken Sound Parkway, NW, 2018. doi:10.1201/9781439882573.

[70] E.A. Baskharone, The Finite Element Method With Heat Transfer and Fluid Mechanics Applications, 1st ed., Cambridge University Press, New York, NY, 2014. doi:10.1017/CBO9781139626668.

[71] I. Guve, E. Madenci, The Finite Element Method and Applications in Engineering Using Ansys, 2nd ed., Springer, New York, NY, 2015.

[72] J.M. Franssen, P.V. Real, Fire Design of Steel Structures, 2nd ed., ECCS – European Convention for Constructional Steelwork, 2015.

[73] Y.C. Wang, Steel and Composite Structures: Behaviour and Design for Fire Safety, Spon Press and Taylor & Francis, London, United Kingdom, 2005.

[74] F.F. Ribeiro, Numerical Simulation of Composite Slabs With Steel Deck Under Fire Conditions, Polytechnic Institute of Bragança, 2019.

[75] Morgan Advanced Materials, Data Sheet: Superwool Blanket, (2016) 3.

[76] Y.A. Çengel, A.J. Ghajar, Heat and Mass Transfer: Fundamentals & Applications, 5th ed., McGraw-Hill Education, New York, NY, 2015.

[77] European Commitee for Standardization, EN 1995-1-2 Design of Timber Structures - Part 1-2: General - Structural Fire Design, (2004) 69.

[78] A. Frangi, V. Schleifer, M. Fontana, Design Model for the Verification of the Separating Function of Light Timber Frame Assemblies, Eng. Struct. 32 (2010) 1184–1195. doi:10.1016/j.engstruct.2009.12.044.

Appendixes

A Steel Frame and Test Equipment Details

A.1 Steel Frame

Steel Frame Configuration	**Cold-formed Steel Specifications**	
Number of studs: 7	Stud/track section:	C100 x 45 x 10 mm
Number of tracks: 6	Thickness/grade:	1.0 mm/S280GD

Schematic Representation *measurements in millimetres

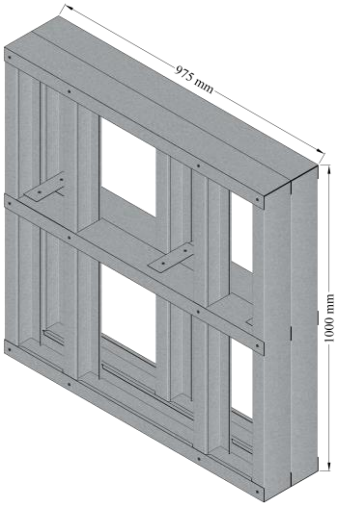

Labels:

Steel frame

Stud/track lipped section details:

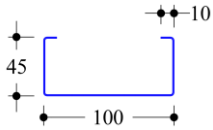

Cross-section/stud labels: **cross-section at 300 mm from steel frame base*

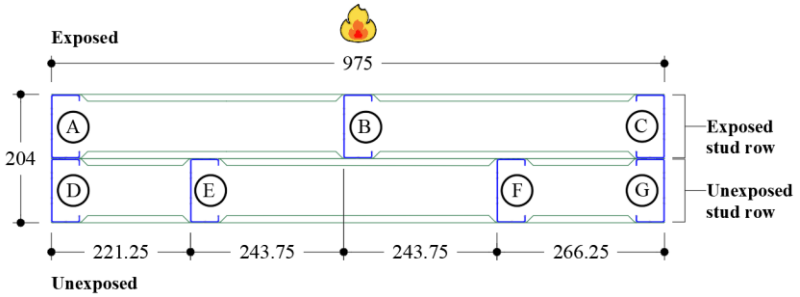

Construction Details

Connections between stud rows *measurements in millimetres

Detail:

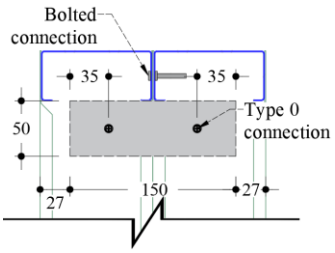

Position of the bridging plates and bolted connections:

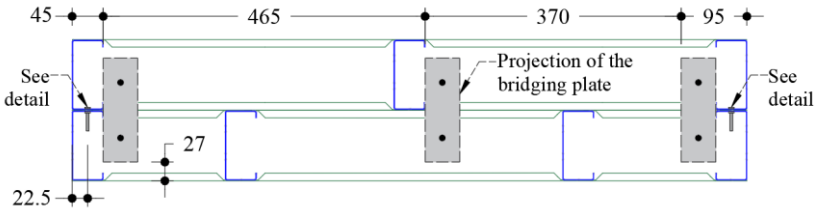

Bridging plate to steel frame connection: 0 – 4.2 x 19 mm wafer head self-drilling screw

Construction Details

Connections between stud rows

Bridging plates:

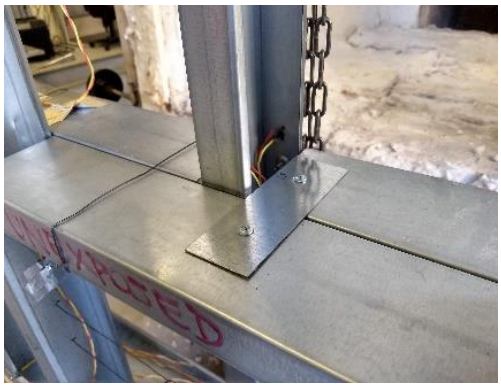

Bolted connection:

Construction Details

Stud to track connections *measurements in millimetres

Unexposed stud row:

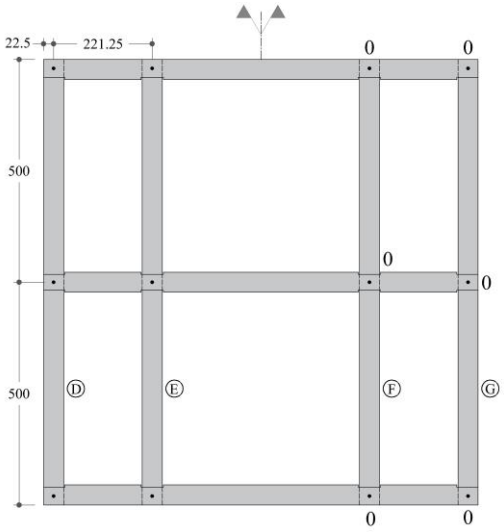

View from the unexposed side

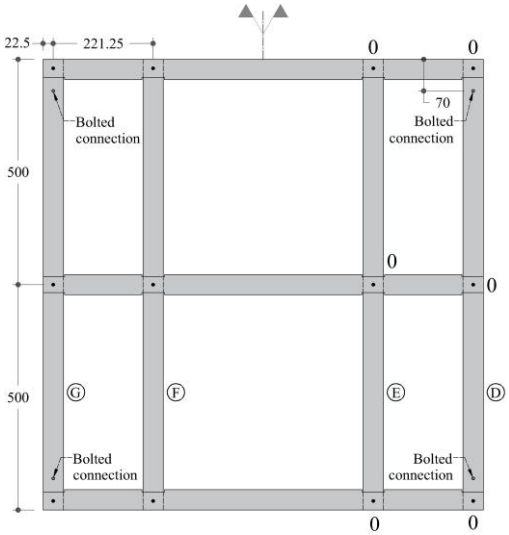

View from the exposed side

Exposed stud row:

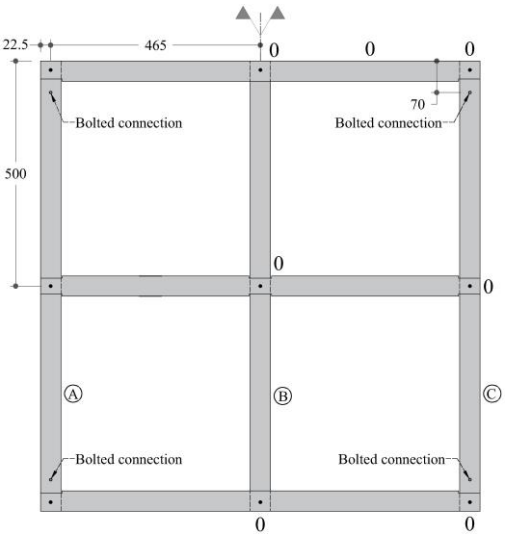

View from the unexposed side

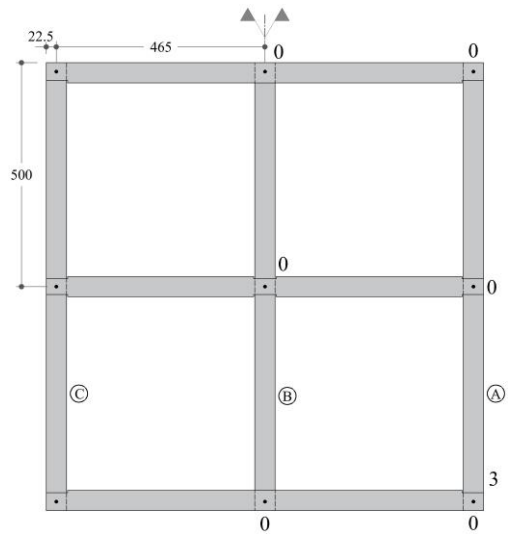

View from the exposed side

Stud to track connections: 0 – 4.2 x 19 mm wafer head self-drilling screw

Connection between stud rows (bolted connection): 5 x 32 mm hexagonal head bolts

A.1 Test Frame

Test Frame Description

Schematic Representation (Steel frame Set-up) *measurements in millimetres

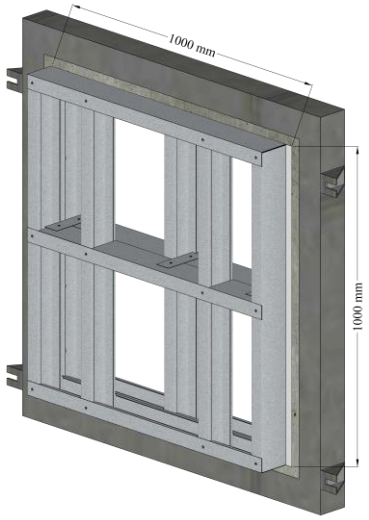

Labels:

- Steel frame
- Test frame (steel)
- Refractory mortar
- Ceramic fibre insulation

Cross-section: **cross-section at 420 mm from test frame base*

**measurements in millimetres*

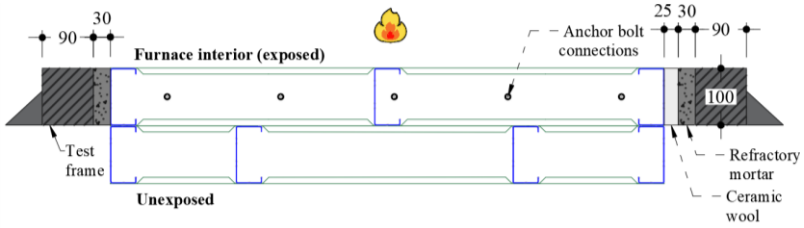

Construction Details

Exposed stud row to test frame connections *measurements in millimetres

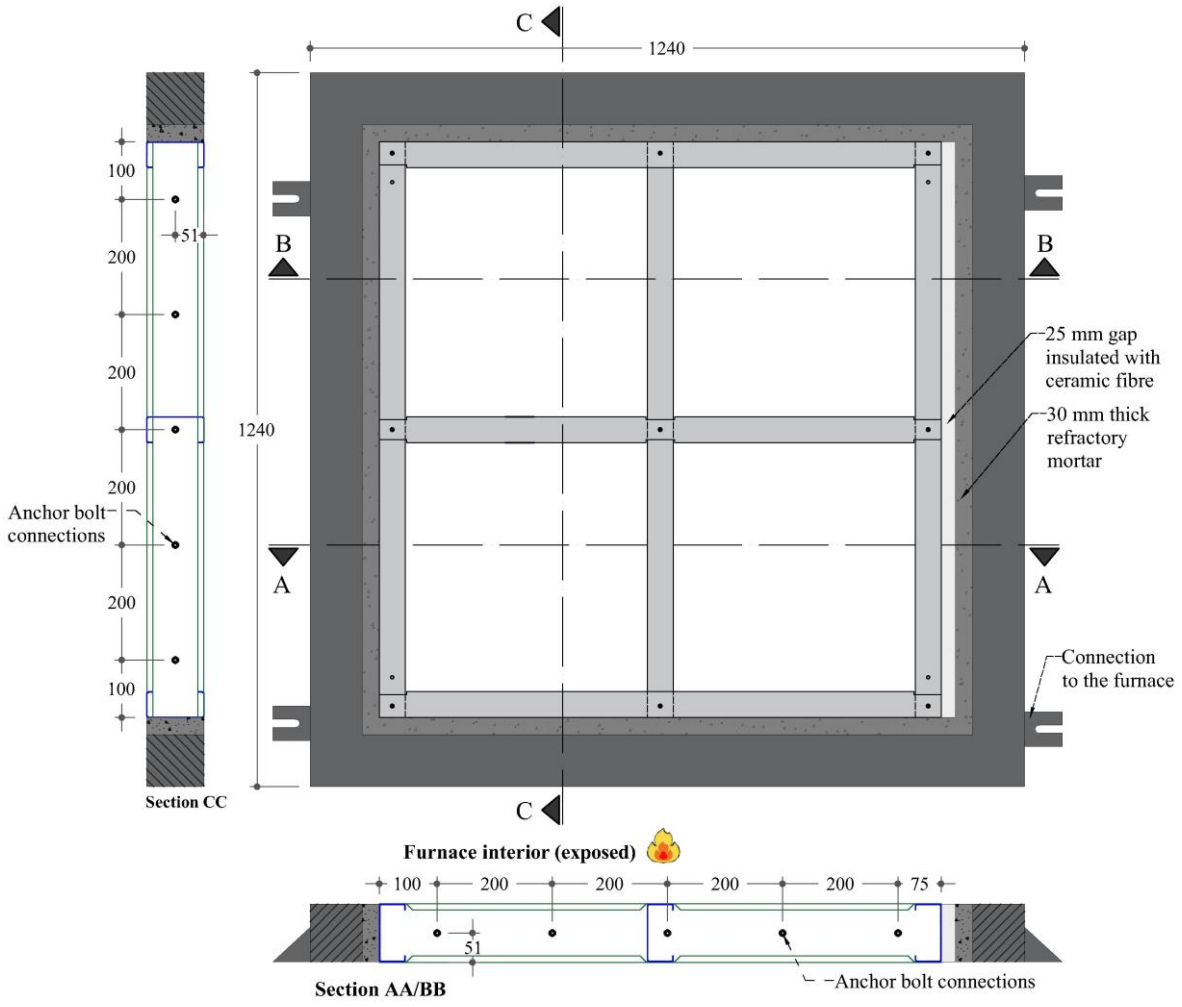

Construction Details
Exposed stud row to test frame connections

Anchor bolts: 8 x 50 mm (hexagonal head)

Connection settled:

A.2 Thermocouples

Thermocouples	
Type of wire: Type K	
Wire diameter: 0.7 mm	
Welded Thermocouple (WT)	**Bed thermocouple (BT)**
	
Welded thermocouple on steel stud	*Bed thermocouple on gypsum board (twisted tip)*
Twisted Thermocouples (TT)	
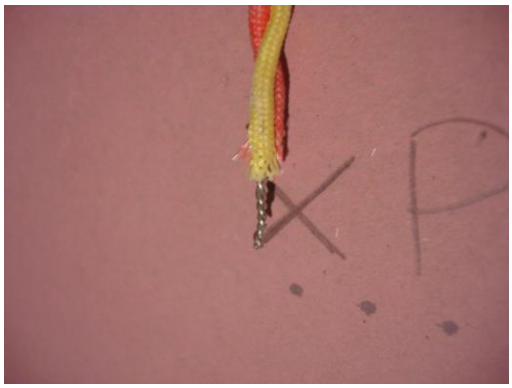	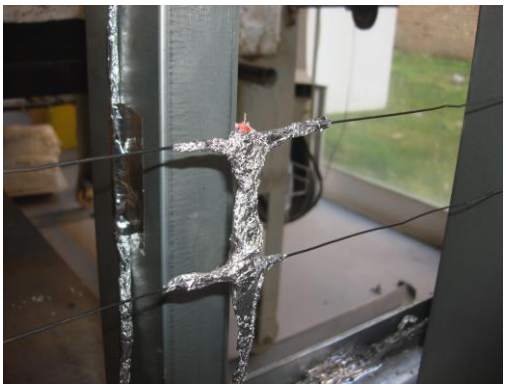
Twisted thermocouple on gypsum board	*Twisted thermocouple in ceramic fibre*
Plate thermocouple (PT)	**Disk thermocouple (DT)**
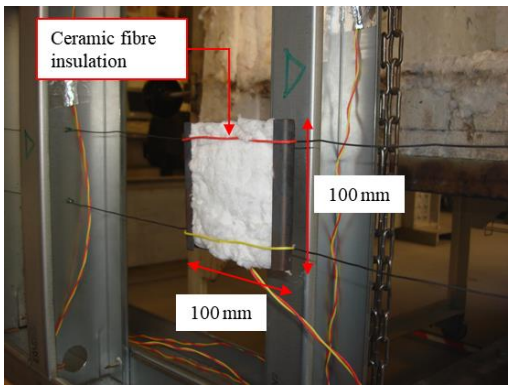	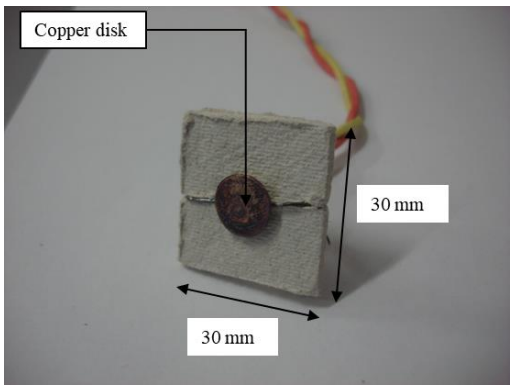
Plate thermocouple in the wall cavity	*Disk thermocouple on gypsum plasterboard*

B Technical Files – Experimental Tests

B.1 Specimen 1

Specimen 1 – Non-load-bearing Double-stud LSF Wall	**Thermal Insulation Performance**	
Gypsum plasterboard: 12.5 mm thick Type F fire-resistant	Fire resistance (T_{ave}) [minutes]:	73
Gypsum plasterboards on the exposed side: 1	Fire resistance (T_{max}) [minutes]:	76
Gypsum plasterboards on the unexposed side: 1	Fire-resistance rating (FRR):	I60
Cavity insulation: -		

Schematic Representation

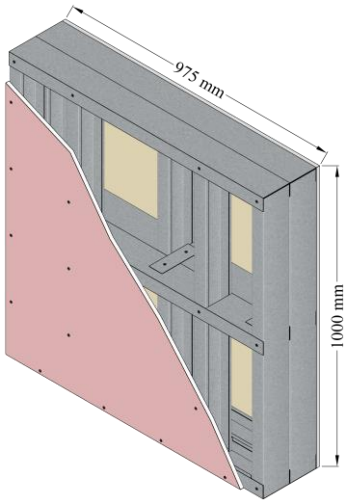

Labels:

- Gypsum plasterboard
- Steel frame

Steel Frame Description

Stud/track section: C100 x 45 x 10 mm
Steel thickness/grade: 1.0 mm / S280GD
Stud to track connections: 4.2 x 19 mm wafer head self-drilling screw

Cross-section:

*measurements in millimetres

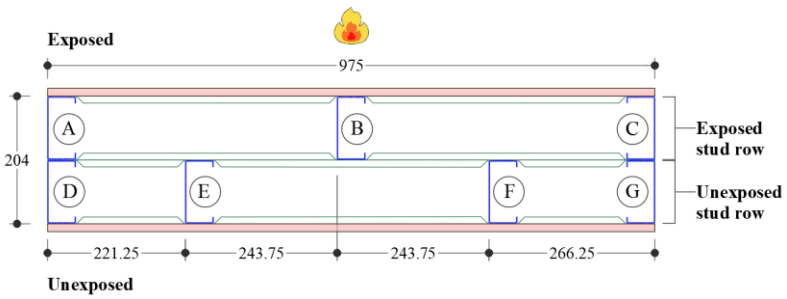

Construction Details

Gypsum plasterboard fastening

*measurements in millimetres

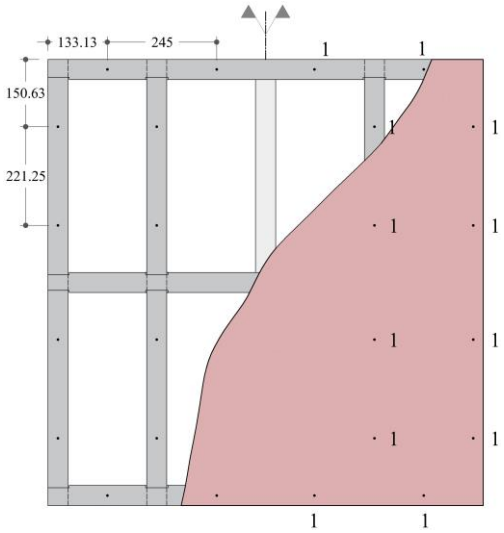

View from the unexposed side

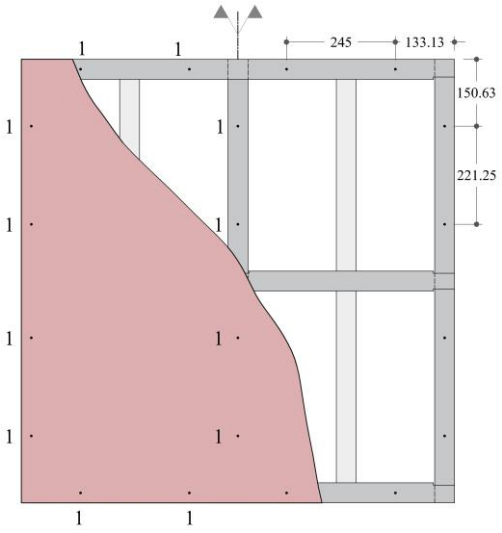

View from the exposed side

Gypsum plasterboard to steel frame connections: 1 – 4.2 x 32 mm flat head self-drilling screw

Test No.1 - Information

Date: 11th October 2019

Test length: 77 minutes

Test Set-Up

Steel frame

Unexposed surface

Test Set-up Details *measurements in millimetres

Cross-section:

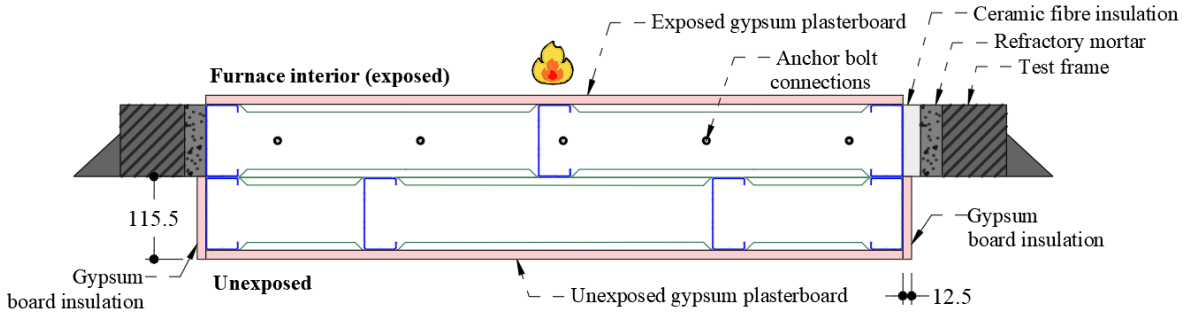

Detail of gypsum board insulation on the unexposed stud row:

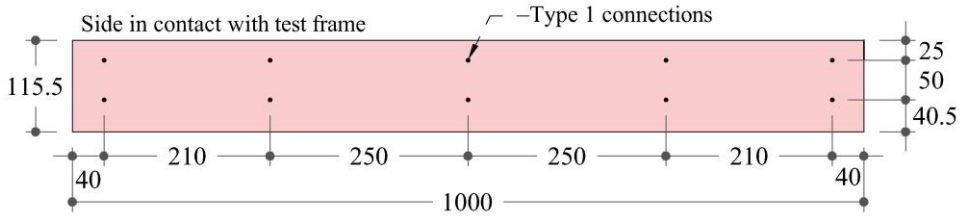

Gypsum board insulation - On all sides of the unexposed stud row

Gypsum board insulation to steel frame connections: 1 – 4.2 x 32 mm flat head self-drilling screw

Thermocouple Attachments *measurements in millimetres

Thermocouples:

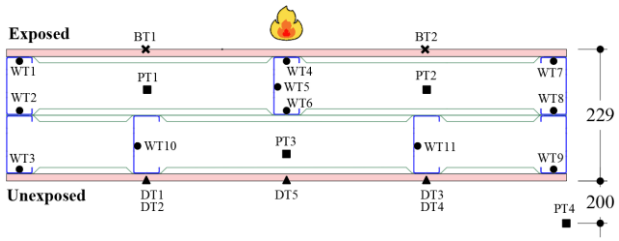

Average and maximum temperatures:

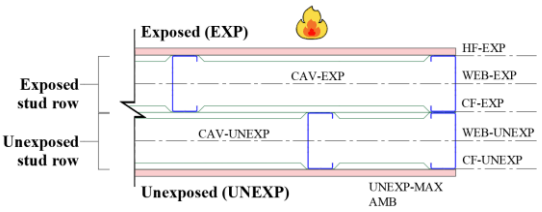

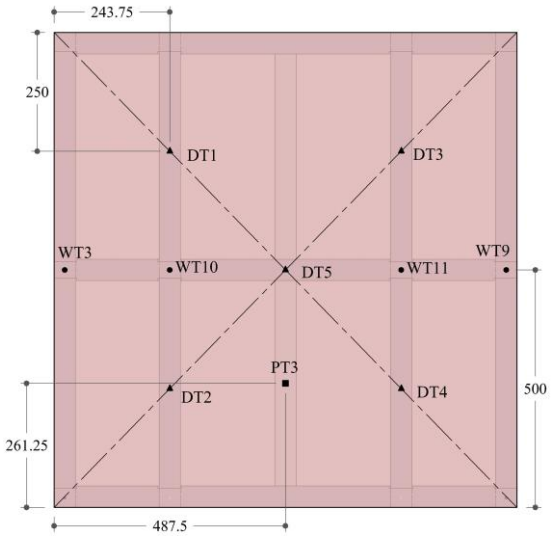

View from the unexposed surface

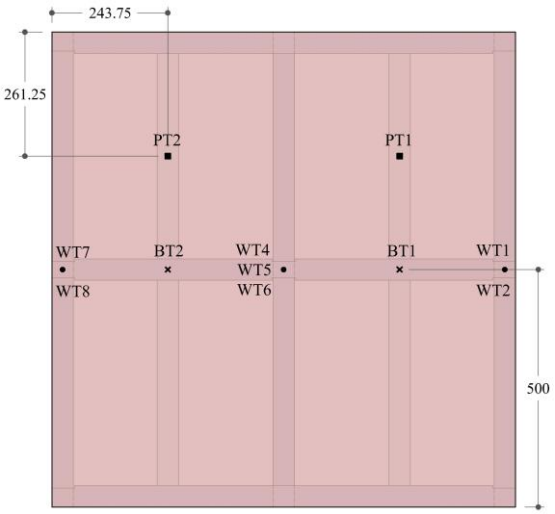

View from the exposed surface

Thermocouple type and location:	WT – Welded thermocouple on steel stud	
	DT – Disk thermocouple on gypsum plasterboard	
	BT – Bed thermocouple on gypsum plasterboard	
	PT – Plate thermocouple in the wall cavity or ambient	
Average and maximum temperatures:	EXP: BT1; BT2	(Average)
	HF-EXP: WT1; WT4; WT7	(Average)
	WEB-EXP: WT5	(Average)
	CF-EXP: WT2; WT6; WT8	(Average)
	WEB-UNEXP: WT10; WT11	(Average)
	CF-UNEXP: WT3; WT9	(Average)
	CAV-EXP: PT1; PT2	(Average)
	CAV-UNEXP: PT3	(Average)
	UNEXP: DT1; DT2; DT3; DT4; DT5	(Average)
	UNEXP-MAX: DT1; DT2; DT3; DT4; DT5	(Maximum)
	AMB: PT4	(Average)

Visual Observations

Gypsum plasterboard

Unexposed surface after fire exposure

Cracks on the exposed surface

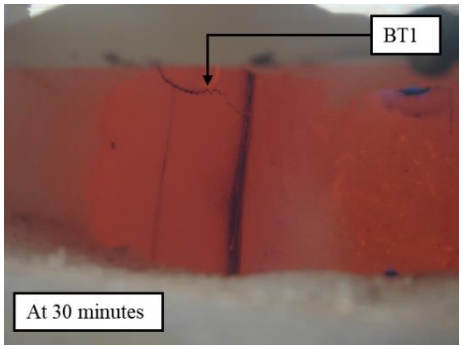

Cracks on the exposed plasterboard (furnace interior)

Fall-off of the fire exposed plasterboard due to handling after the test

Steel frame

Steel frame condition after the test

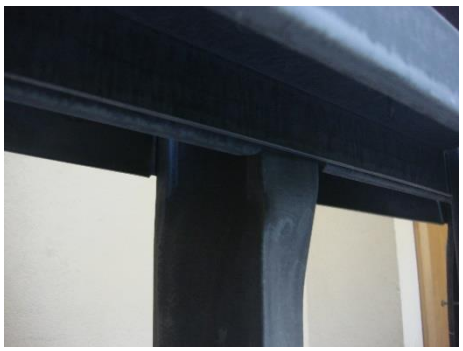

Web and distortional buckling in stud B (top)

Web and distortional buckling in stud B (mid-height)

Distortional buckling in stud C (mid-height)

Time-Temperature Profiles (Thermocouples Measurements) **Test duration:** 77 minutes

EXP

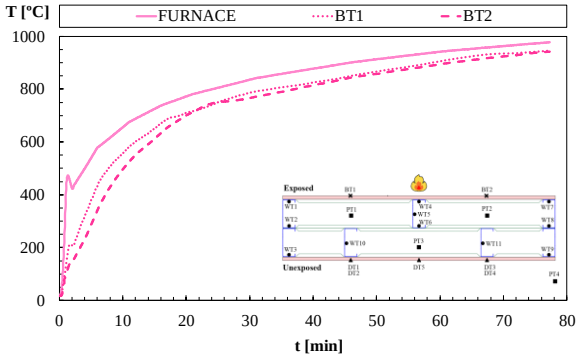

HF-EXP

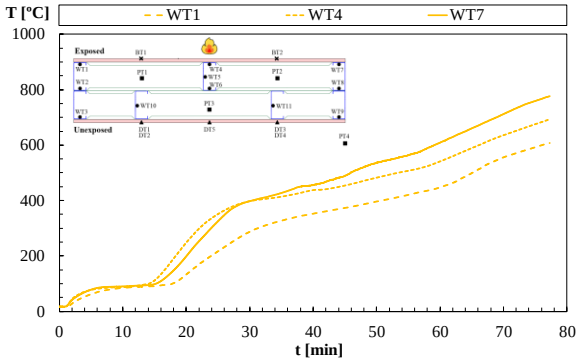

WEB-EXP

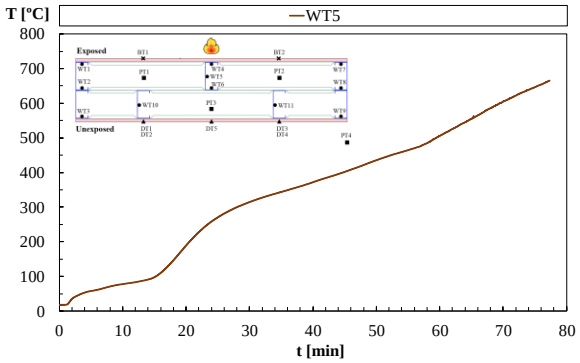

CF-EXP

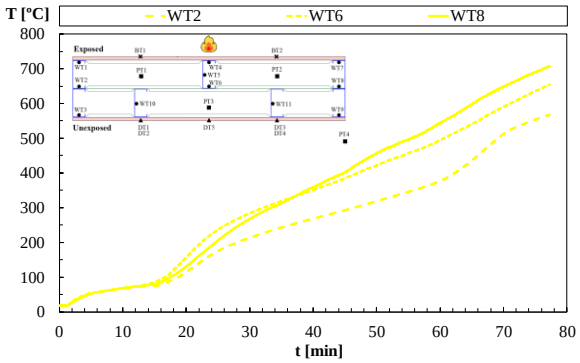

WEB-UNEXP

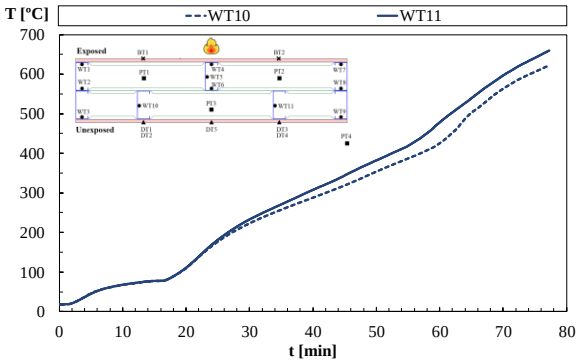

CF-UNEXP

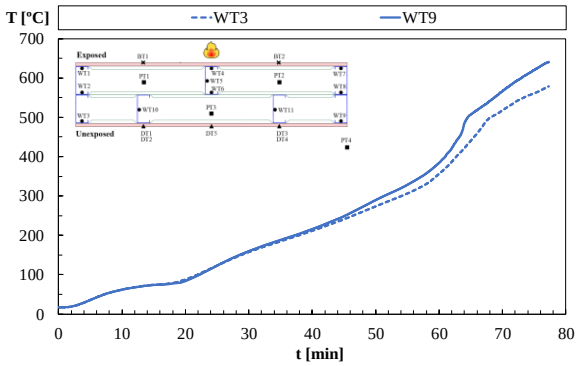

CAV-EXP

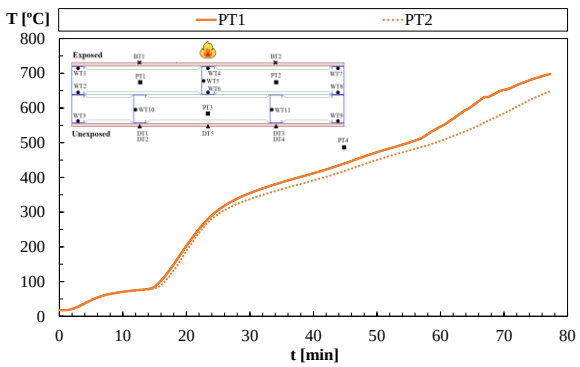

CAV-UNEXP

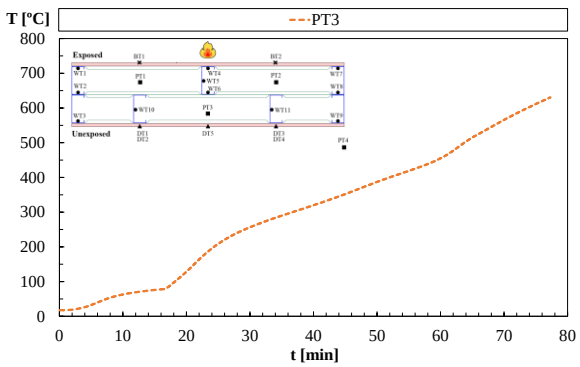

UNEXP / UNEXP-MAX / AMB

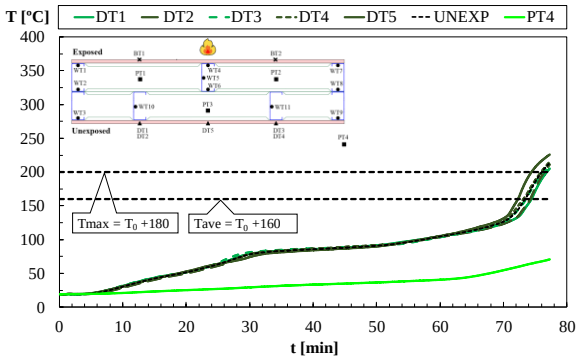

Time-Temperature Profiles (Infrared Measurements) **Test duration:** 77 minutes

IR-MAX, IR-AVE, IR-MIN

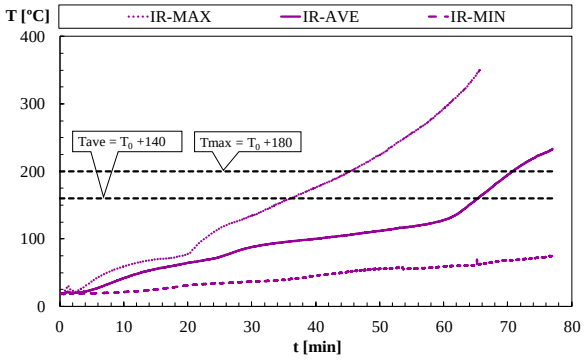

Infrared parameters

Gypsum plasterboard emissivity:	0.8
Distance of the camera from the unexposed surface [m]:	3.2
Measurement rectangle:	
Width [m]:	0.821
Height [m]:	0.896
Area [m²]:	0.736

Measurement Rectangle

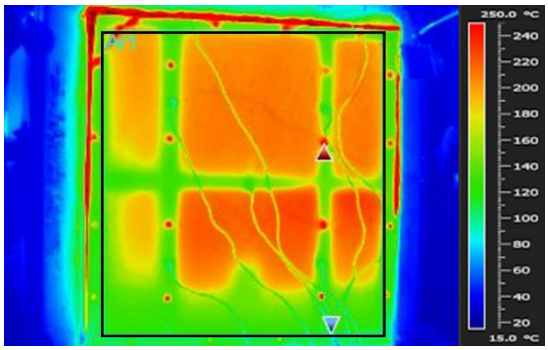

t = 0 minutes

t = 10 minutes

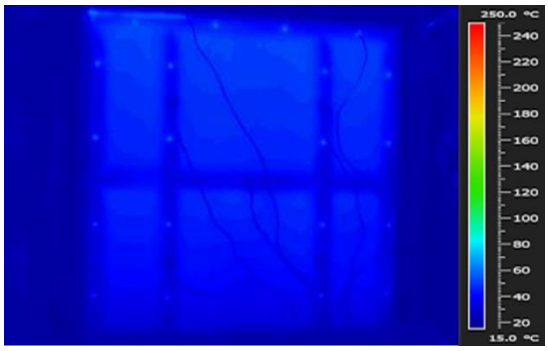

t = 20 minutes

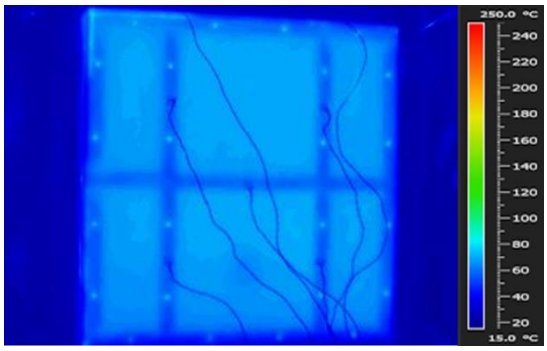

t = 30 minutes

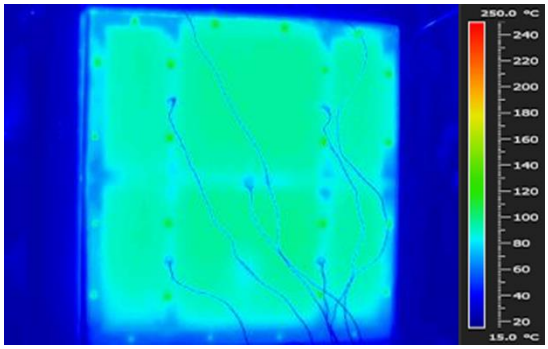

t = 40 minutes

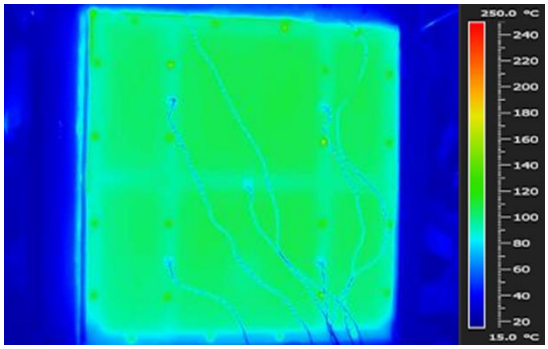

t = 50 minutes

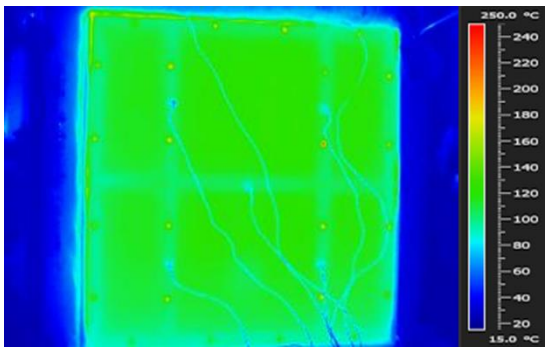

t = 60 minutes

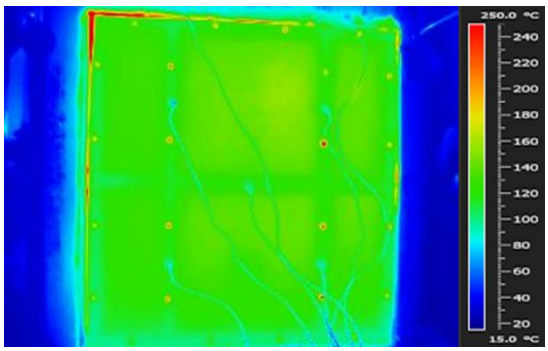

t = 70 minutes

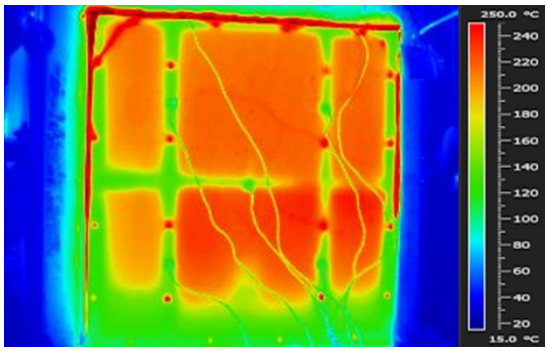

t = 77 minutes

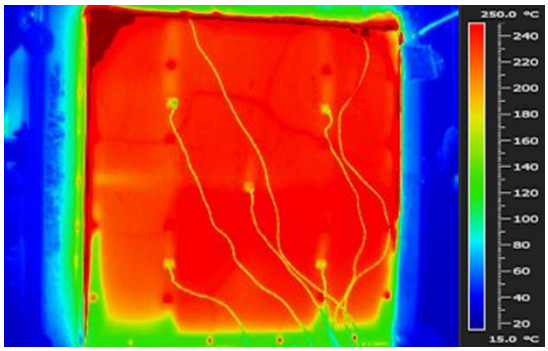

B.2 Specimen 2

Specimen 2 – Non-load-bearing Double-stud LSF Wall	**Thermal Insulation Performance**	
Gypsum plasterboard: 12.5 mm thick Type F fire-resistant	Fire resistance (T_{ave}) [minutes]:	116
Gypsum plasterboards on the exposed side: 2	Fire resistance (T_{max}) [minutes]:	116
Gypsum plasterboards on the unexposed side: 2	Fire-resistance rating (FRR):	I90
Cavity insulation: -		

Schematic Representation

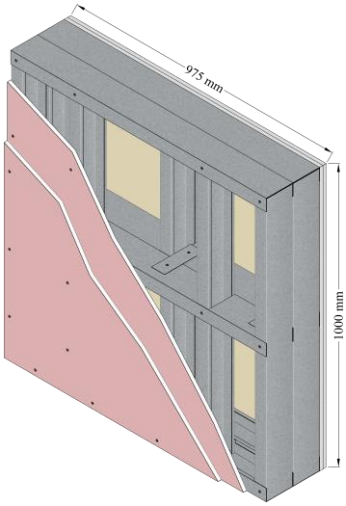

Labels:

- Gypsum plasterboard
- Steel frame

Steel Frame Description

Stud/track section: C100 x 45 x 10 mm

Steel thickness/grade: 1.0 mm / S280GD

Stud to track connections: 4.2 x 19 mm wafer head self-drilling screw

Cross-section:

*measurements in millimetres

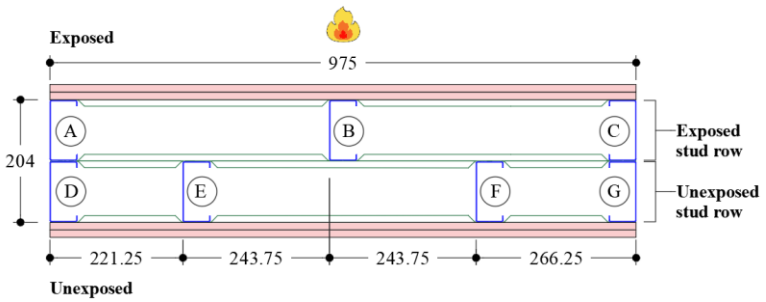

Construction Details

Gypsum plasterboard fastening

*measurements in millimetres

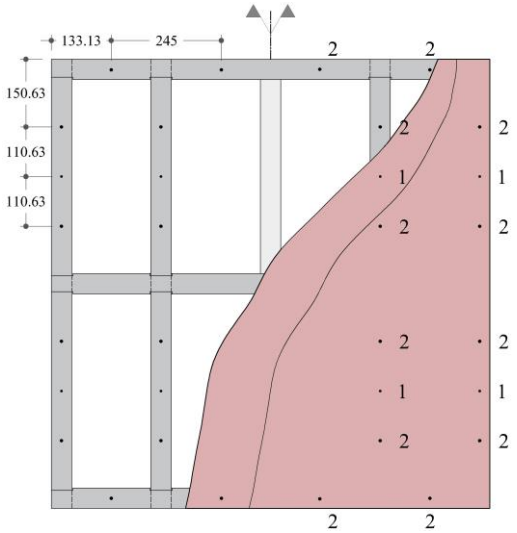

View from the unexposed side

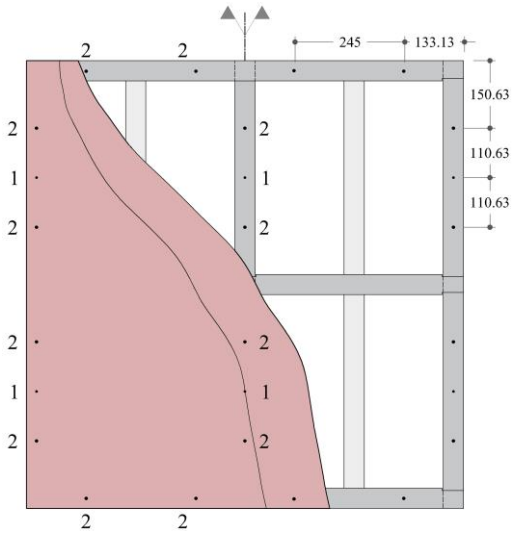

View from the exposed side

Gypsum plasterboard to steel frame connections:

1 – 4.2 x 32 mm flat head self-drilling screw

2 – 4.2 x 50 mm flat head self-drilling screw

Test No.2 - Information

Date: 21st October 2019

Test length: 120 minutes

Test Set-Up

Steel frame

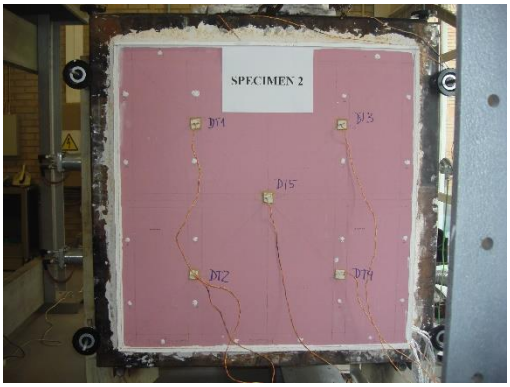

Unexposed surface

Test Set-up Details *measurements in millimetres

Cross-section:

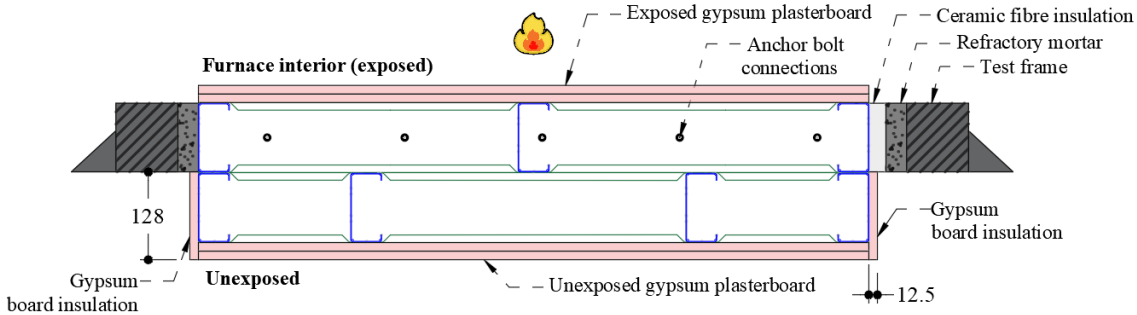

Detail of gypsum board insulation on the unexposed stud row:

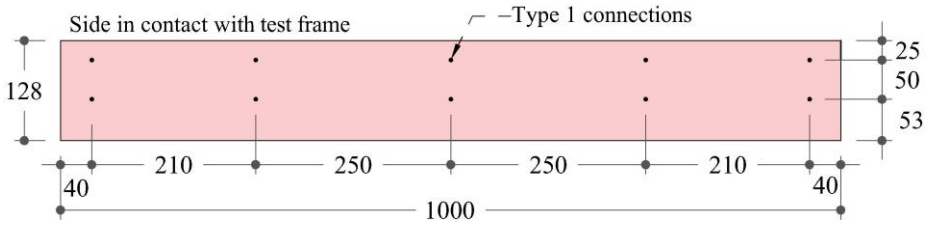

Gypsum board insulation - On all sides of the unexposed stud row

Gypsum board insulation to steel frame connections: 1 – 4.2 x 32 mm flat head self-drilling screw

Thermocouple Attachments *measurements in millimetres

Thermocouples:

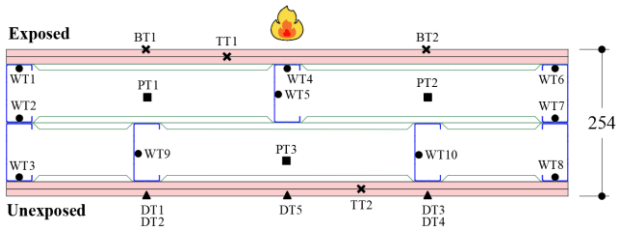

Average and maximum temperatures:

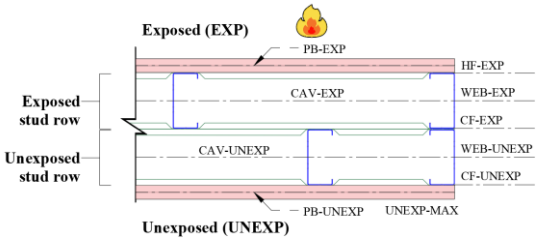

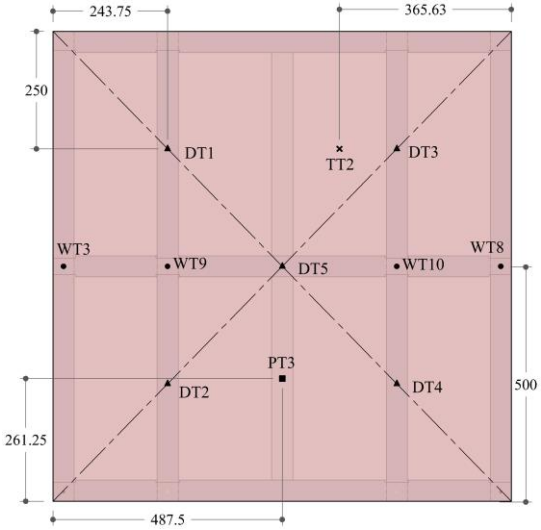

View from the unexposed surface

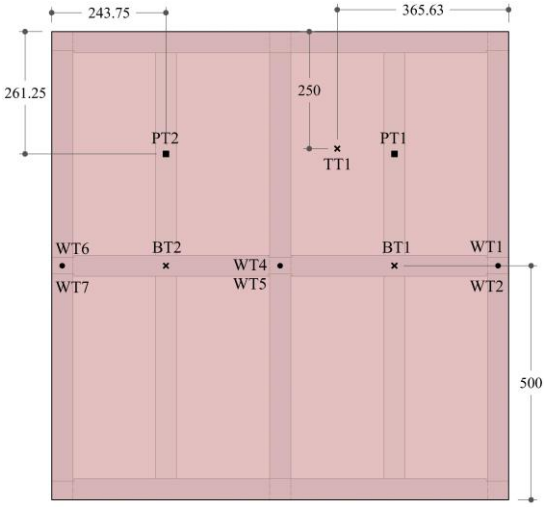

View from the exposed surface

Thermocouple type and locations:	WT – Welded thermocouple on steel stud	
	DT – Disk thermocouple on gypsum plasterboard	
	BT – Bed thermocouple on gypsum plasterboard	
	TT – Twisted thermocouple between gypsum plasterboards	
	PT – Plate thermocouple in the wall cavity	
Average and maximum temperatures:	EXP: BT1; BT2	(Average)
	PB-EXP: TT1	(Average)
	PB-UNEXP: TT2	(Average)
	HF-EXP: WT1; WT4; WT6	(Average)
	WEB-EXP: WT5	(Average)
	CF-EXP: WT2; WT7	(Average)
	WEB-UNEXP: WT9; WT10	(Average)
	CF-UNEXP: WT3; WT8	(Average)
	CAV-EXP: PT1; PT2	(Average)
	CAV-UNEXP: PT3	(Average)
	UNEXP: DT1; DT2; DT3; DT4; DT5	(Average)
	UNEXP-MAX: DT1; DT2; DT3; DT4; DT5	(Maximum)

Visual Observations

Gypsum plasterboard

Unexposed surface after fire exposure

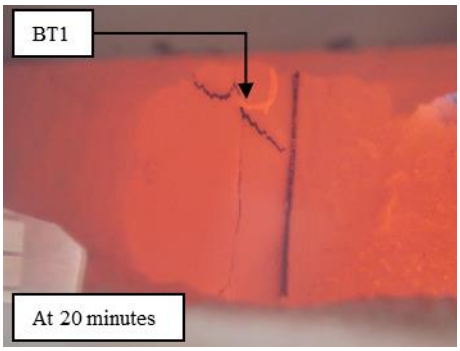

Cracks on the exposed plasterboard (furnace interior)

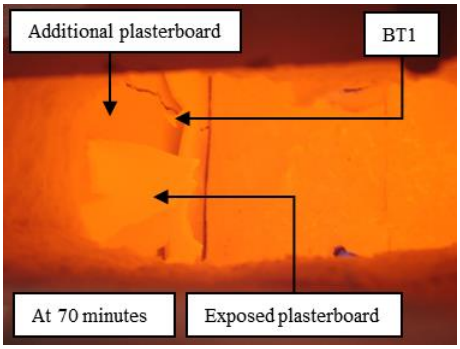

Fall-off of the fire exposed plasterboard and cracks on the second protection layer

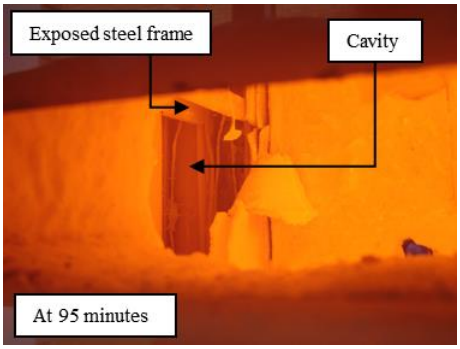

Fall-off of the additional protection layer in contact with the steel frame

Steel frame

Steel frame condition after the test

Distortional buckling in stud B (upper portion)

Web buckling in stud B (upper portion)

Distortional buckling in stud C (mid-height)

Time-Temperature Profiles (Thermocouples Measurements) **Test duration:** 120 minutes

EXP

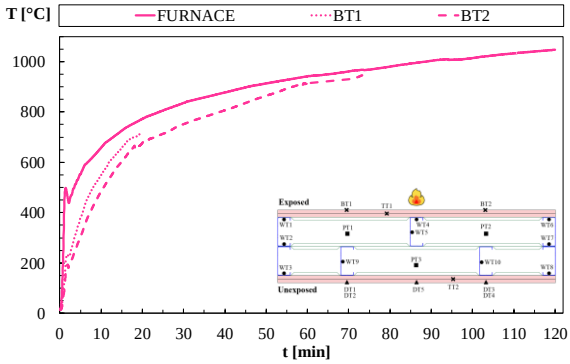

PB-EXP

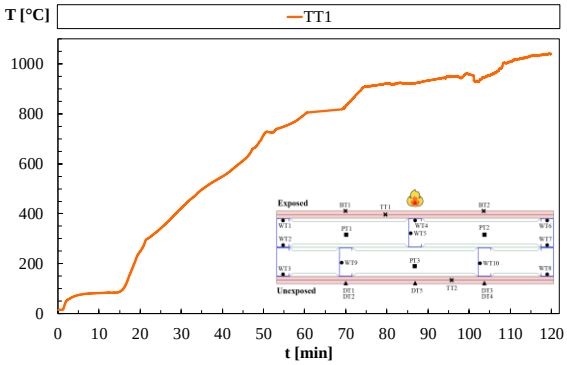

HF-EXP

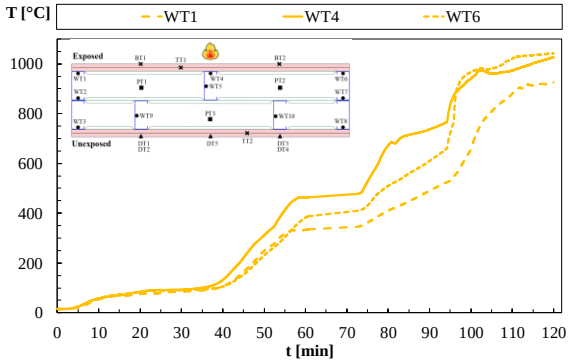

WEB-EXP

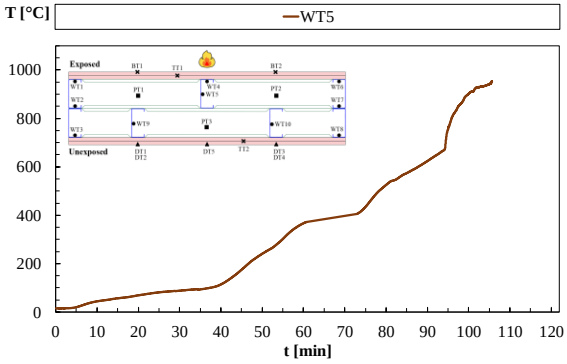

CF-EXP

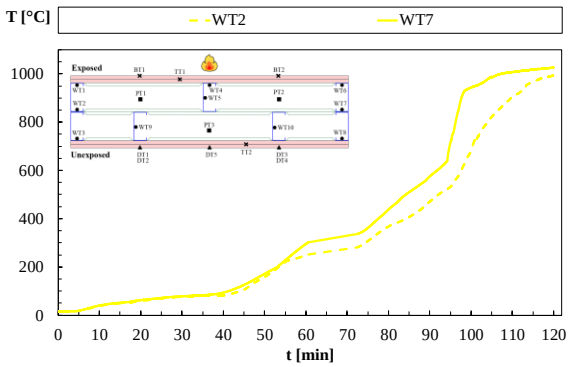

WEB-UNEXP

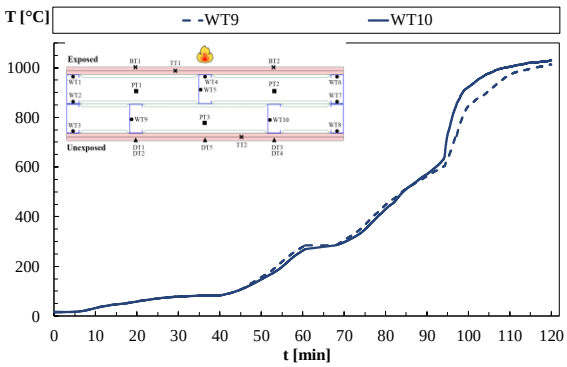

CF-UNEXP

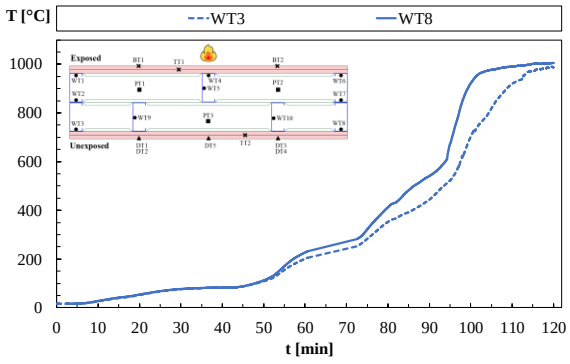

CAV-EXP

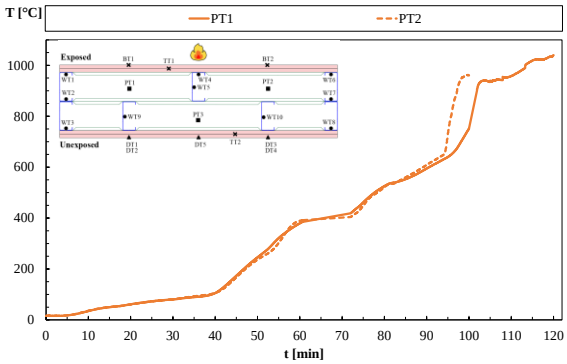

CAV-UNEXP

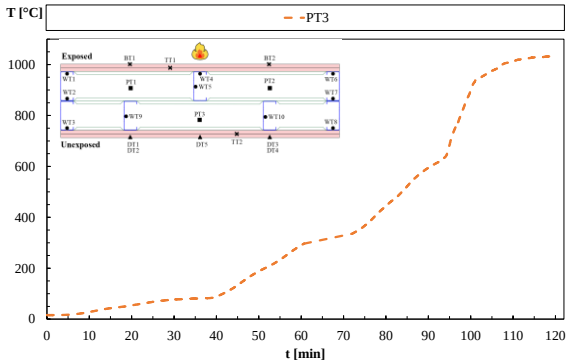

PB-UNEXP

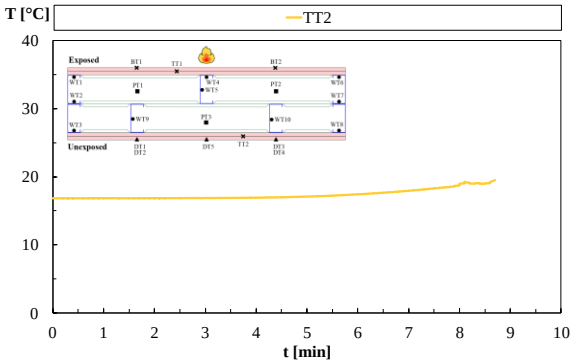

UNEXP / UNEXP-MAX

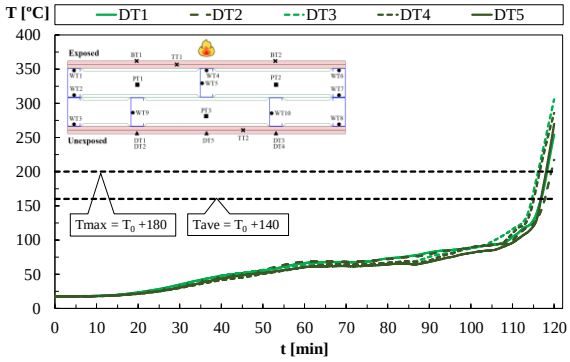

Time-Temperature Profiles (Infrared Measurements) **Test duration:** 120 minutes

IR-MAX, IR-AVE, IR-MIN

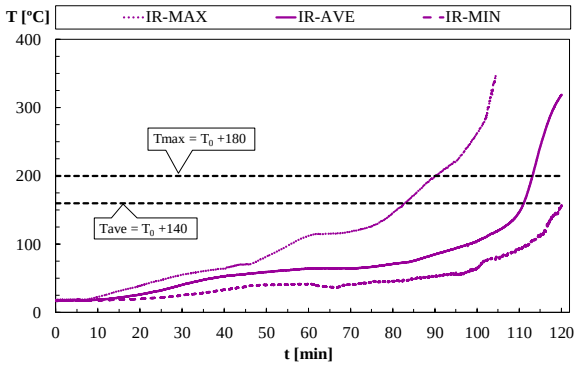

Infrared parameters

Gypsum plasterboard emissivity:	0.8
Distance of the camera from the unexposed surface [m]:	3.2
Measurement rectangle:	
Width [m]:	0.783
Height [m]:	0.841
Area [m²]:	0.658

Measurement Rectangle

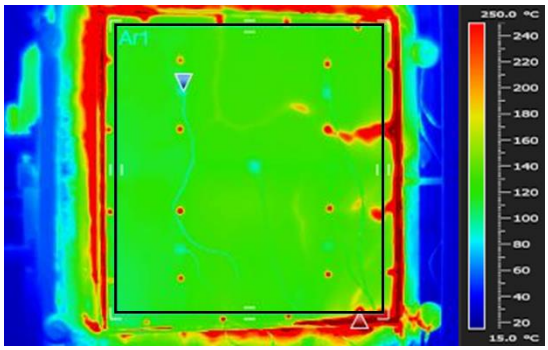

t = 0 minutes

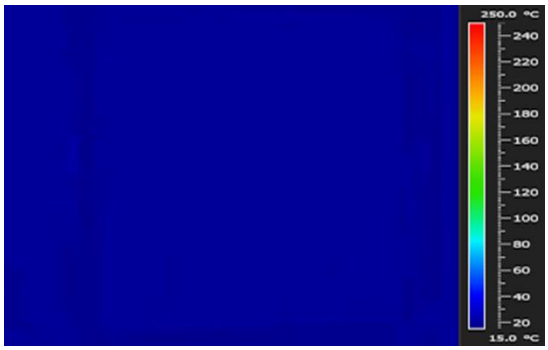

t = 10 minutes

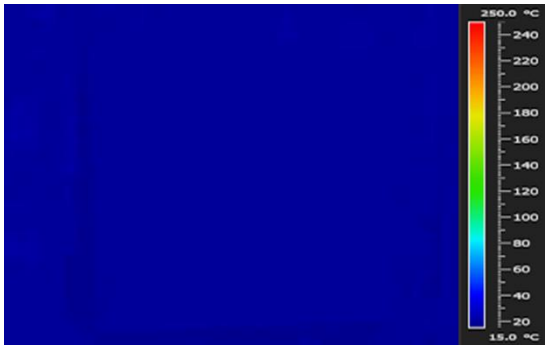

t = 20 minutes

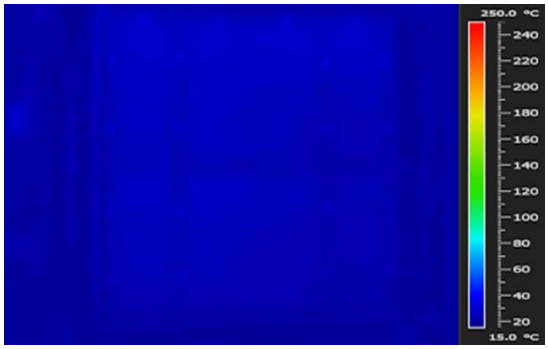

t = 30 minutes

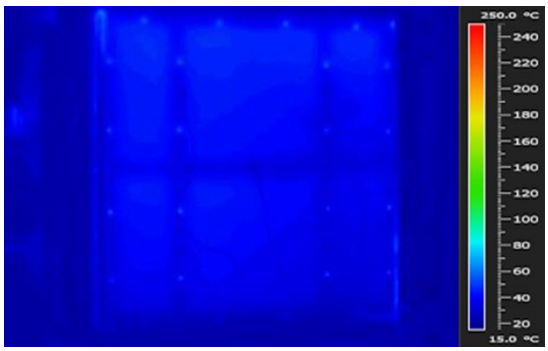

t = 40 minutes

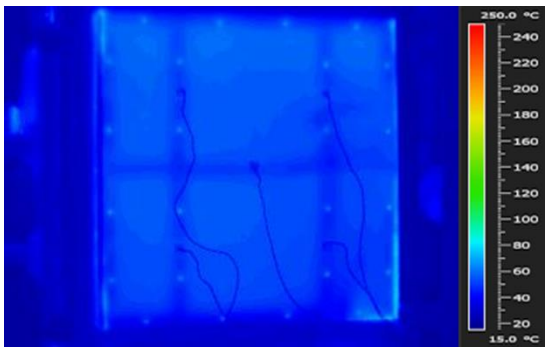

t = 50 minutes

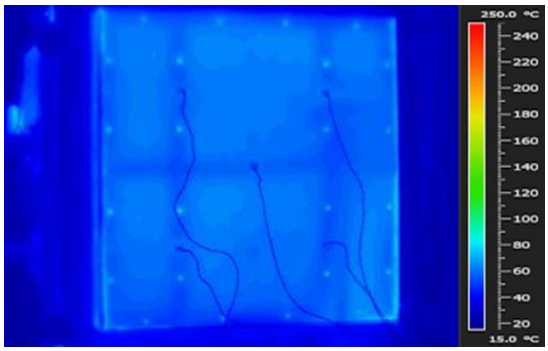

t = 60 minutes

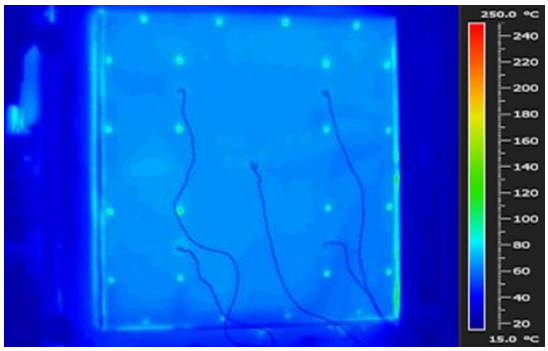

t = 70 minutes

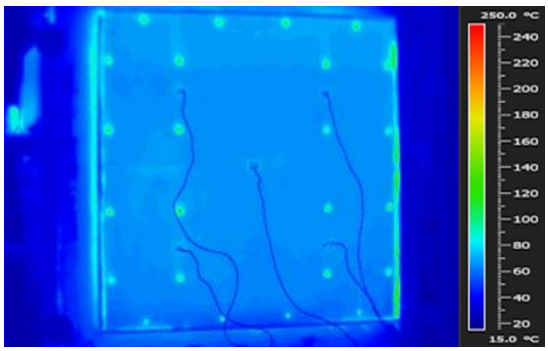

t = 80 minutes

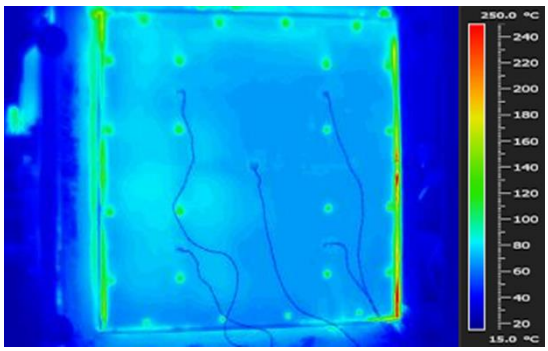

t = 90 minutes	**t = 100 minutes**
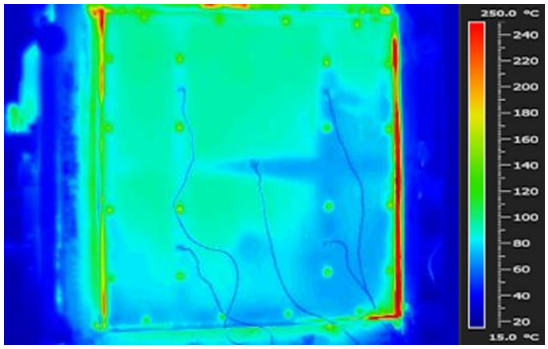	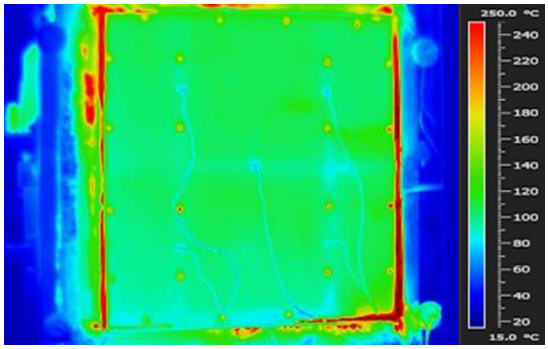
t = 110 minutes	**t = 120 minutes**
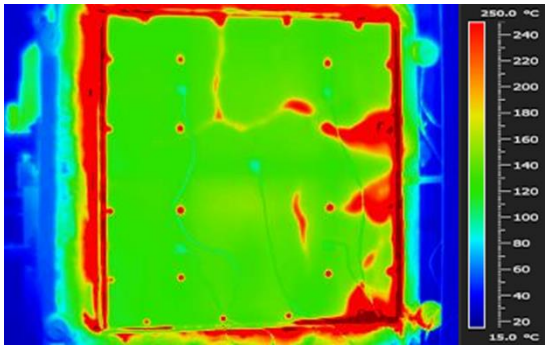	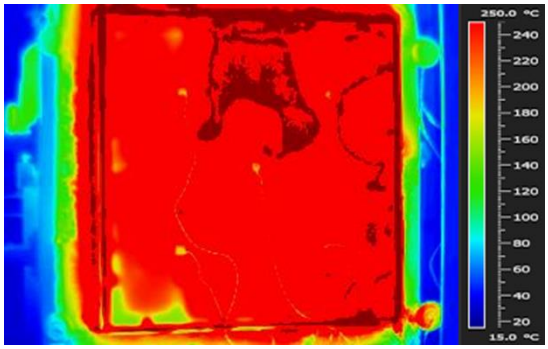

B.3 Specimen 3

Specimen 3 – Non-load-bearing Double-stud LSF Wall	**Thermal Insulation Performance**	
Gypsum plasterboard: 12.5 mm thick Type F fire-resistant	Fire resistance (T_{ave}) [minutes]:	190
Gypsum plasterboards on the exposed side: 1	Fire resistance (T_{max}) [minutes]:	186
Gypsum plasterboards on the unexposed side: 1	Fire-resistance rating (FRR):	I180
Cavity insulation: 75 mm thick ceramic fibre		

Schematic Representation

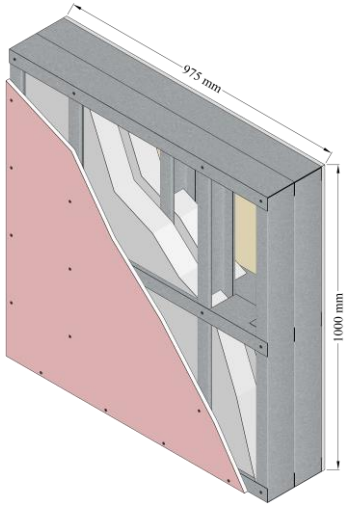

Labels:

- Gypsum plasterboard
- Steel frame
- Ceramic fibre

Steel Frame Description

Stud/track section: C100 x 45 x 10 mm

Steel thickness/grade: 1.0 mm / S280GD

Stud to track connections: 4.2 x 19 mm wafer head self-drilling screw

Cross-section:

*measurements in millimetres

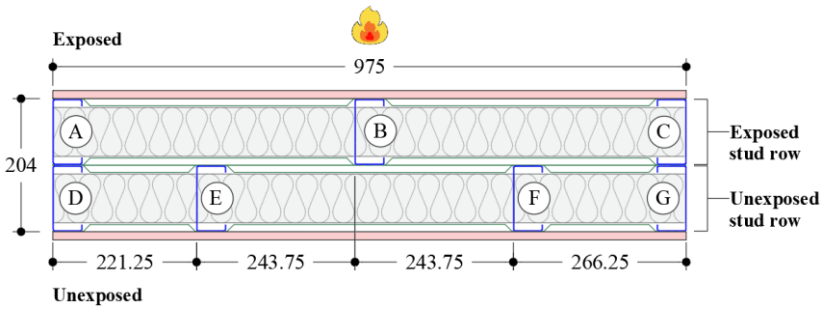

Construction Details

Gypsum plasterboard fastening

*measurements in millimetres

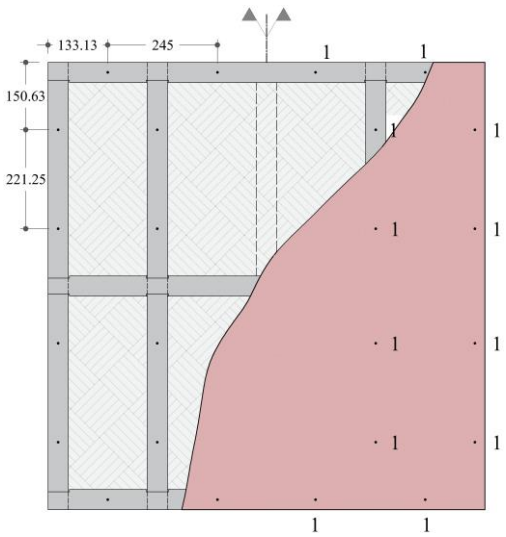

View from the unexposed side

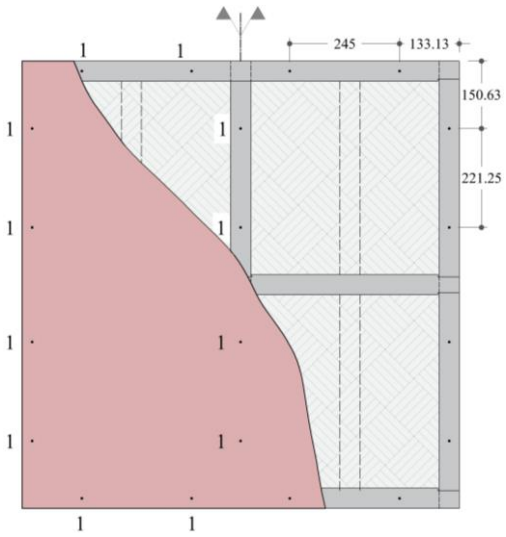

View from the exposed side

Gypsum plasterboard to steel frame connections: 1 – 4.2 x 32 mm flat head self-drilling screw

Test No.3 - Information

Date: 28th October 2019

Test length: 200 minutes

Test Set-Up

Framework insulated with ceramic fibre

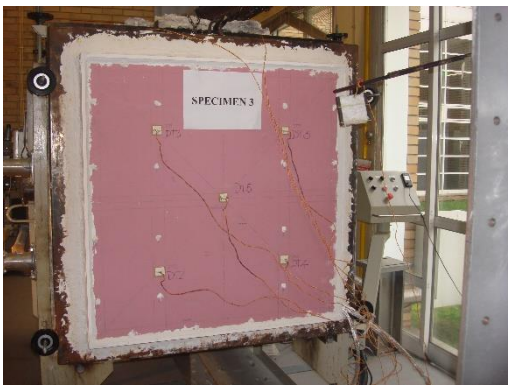

Unexposed surface

Test Set-up Details *measurements in millimetres

Cross-section:

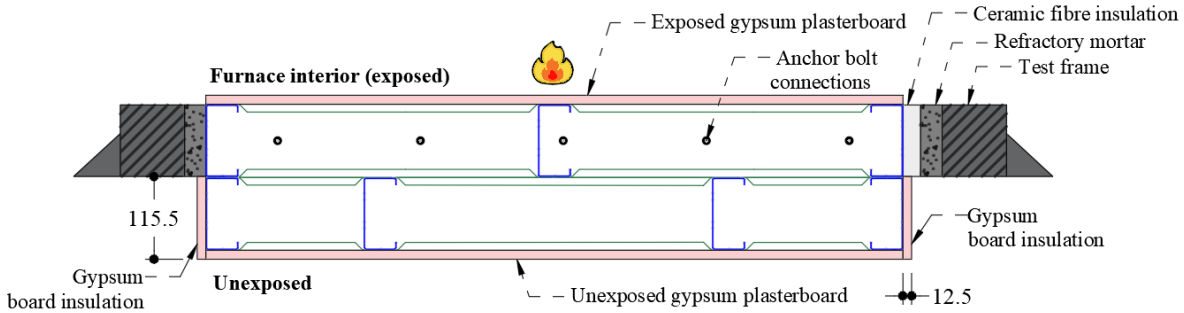

*The representation of the ceramic fibre insulation is intentionally omitted for comprehension purposes

Detail of gypsum board insulation on the unexposed stud row:

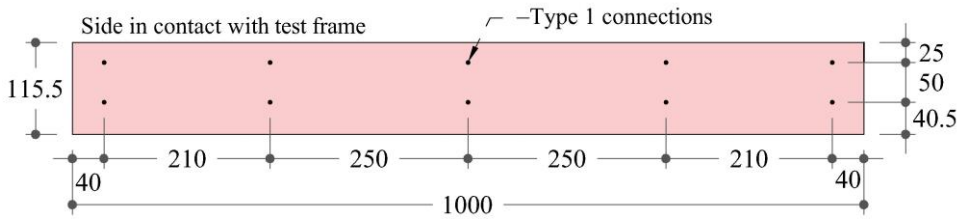

Gypsum board insulation - On all sides of the unexposed stud row

Gypsum board insulation to steel frame connections: 1 – 4.2 x 32 mm flat head self-drilling screw

Thermocouple Attachments *measurements in millimetres

Thermocouples:

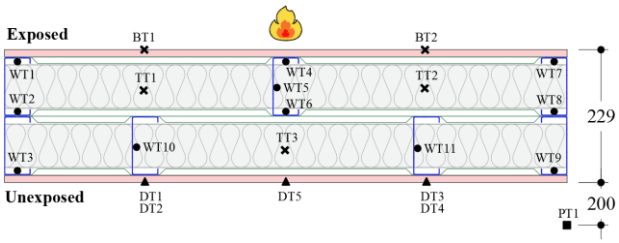

Average and maximum temperatures:

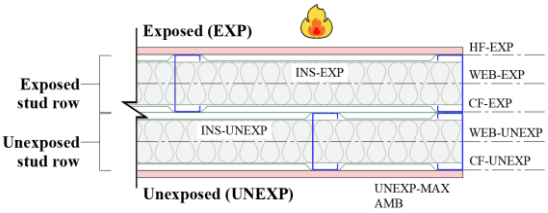

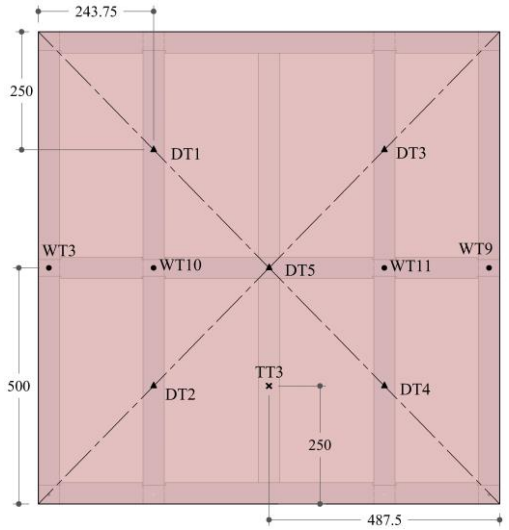

View from the unexposed surface

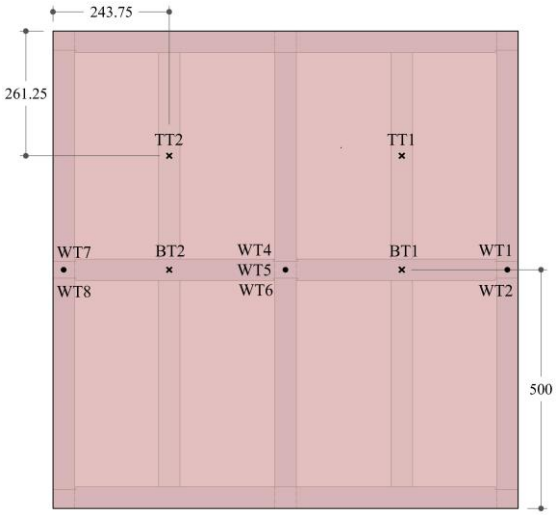

View from the exposed surface

Thermocouple locations:	WT – Welded thermocouple on steel stud	
	DT – Disk thermocouple on gypsum plasterboard	
	BT – Bed thermocouple on gypsum plasterboard	
	TT – Twisted thermocouple within cavity insulation	
	PT – Plate thermocouple in the ambient	
Average and maximum temperatures:	EXP: BT1; BT2	(Average)
	INS-EXP: TT1; TT2	(Average)
	INS-UNEXP: TT3	(Average)
	HF-EXP: WT1; WT4; WT7	(Average)
	WEB-EXP: WT5	(Average)
	CF-EXP: WT2; WT6; WT8	(Average)
	WEB-UNEXP: WT10; WT11	(Average)
	CF-UNEXP: WT3; WT9	(Average)
	UNEXP: DT1; DT2; DT3; DT4; DT5	(Average)
	UNEXP-MAX: DT1; DT2; DT3; DT4; DT5	(Maximum)
	AMB: PT1	(Average)

Visual Observations

Gypsum plasterboard

Unexposed surface after fire exposure

Exposed side after fire exposure

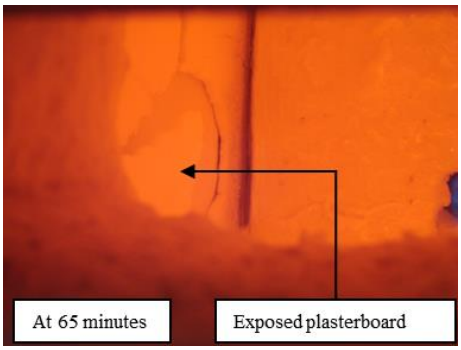

Exposed plasterboard beginning to fall-off (furnace interior)

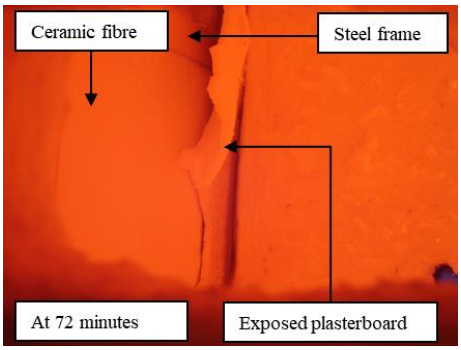

Substantial fall-off of the exposed plasterboard

Steel frame

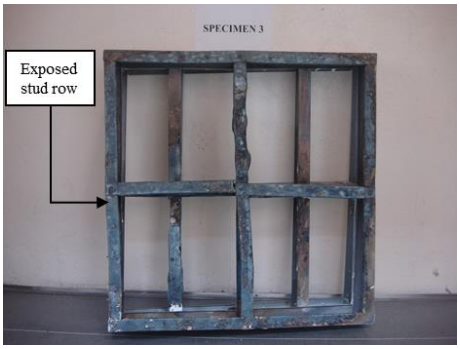

Steel frame condition after the test

Web and distortional buckling in stud B (upper part)

Brittle fracturing behaviour of the steel

Distortional buckling in stud C (mid-height)

Time-Temperature Profiles (Thermocouples Measurements) **Test duration:** 200 minutes

EXP

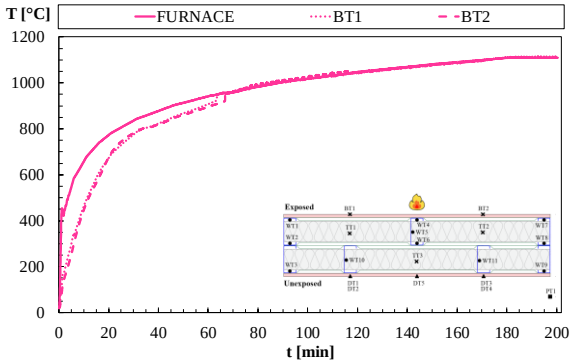

HF-EXP

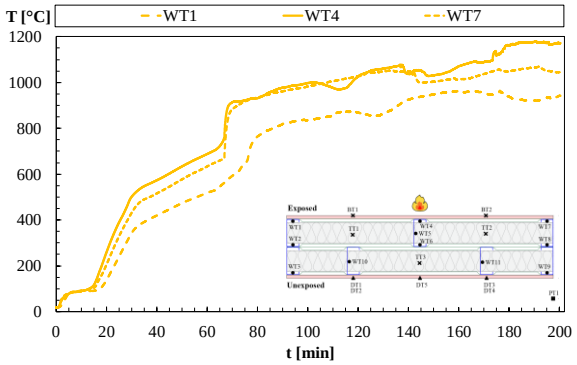

WEB-EXP

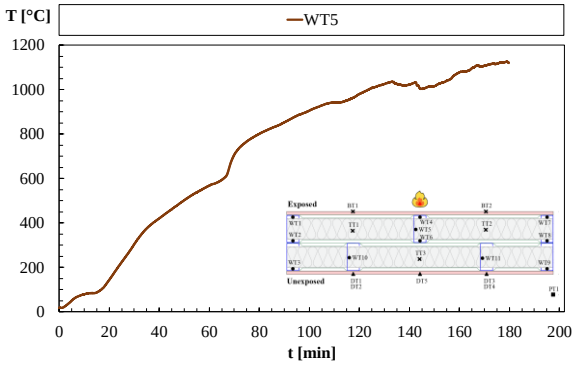

CF-EXP

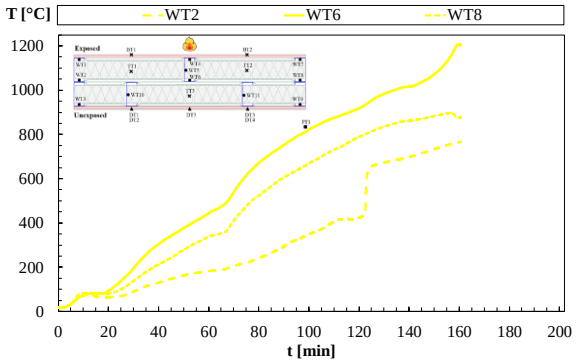

INS-EXP

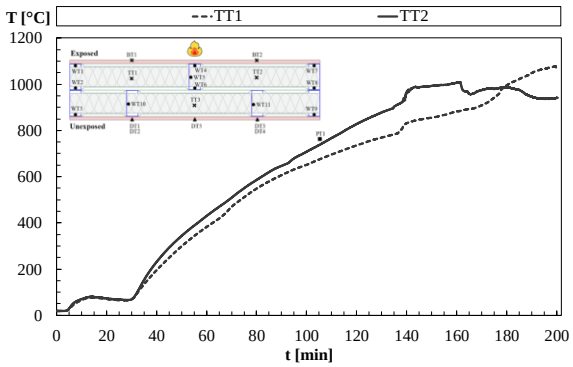

WEB-UNEXP

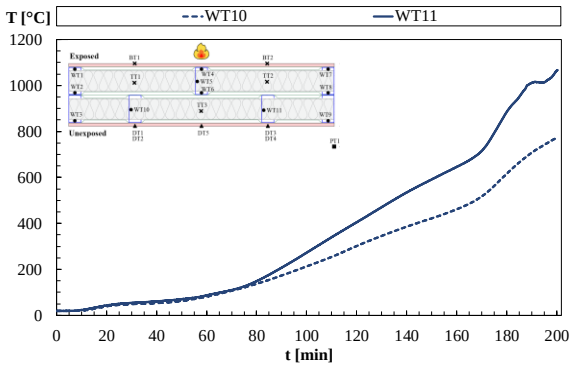

CF-UNEXP

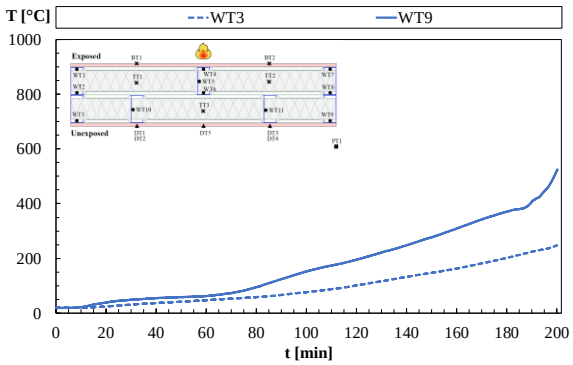

INS-UNEXP

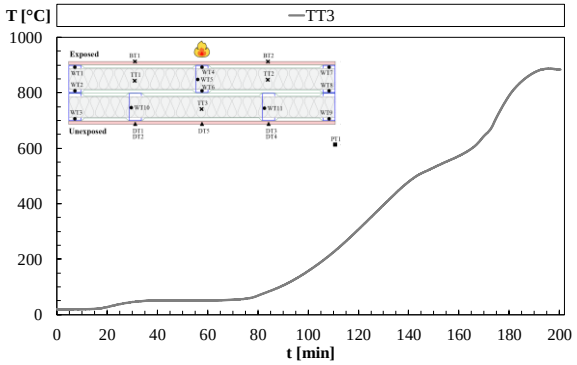

UNEXP / UNEXP-MAX / AMB

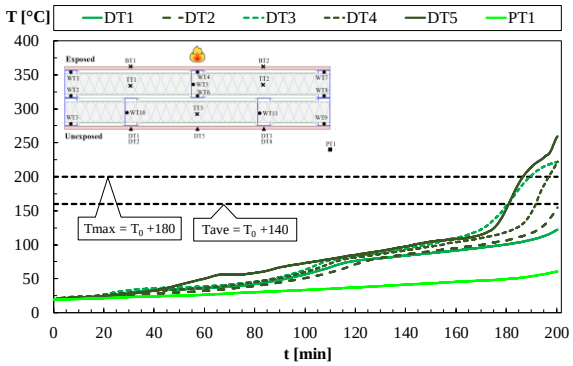

Time-Temperature Profiles (Infrared Measurements) **Test duration:** 200 minutes

IR-MAX, IR-AVE, IR-MIN

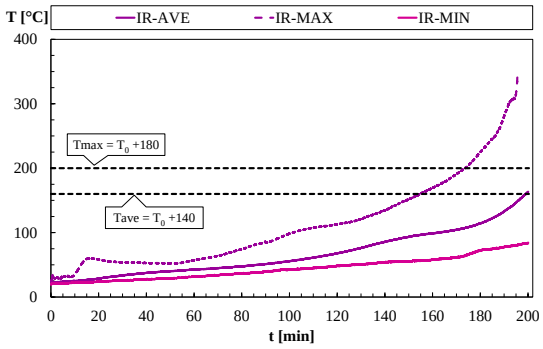

Infrared parameters

Gypsum plasterboard emissivity:	0.8
Distance of the camera from the unexposed surface [m]:	3.2
Measurement rectangle:	
Width [m]:	0.833
Height [m]:	0.854
Area [m²]:	0.711

Measurement Rectangle

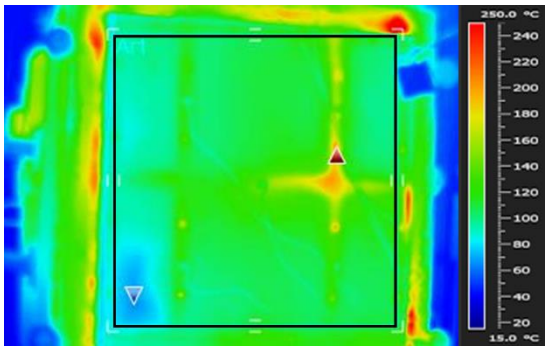

t = 0 minutes

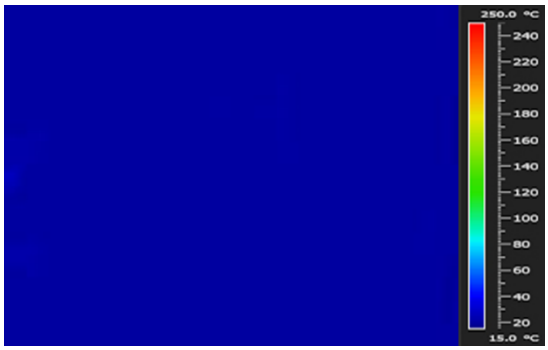

t = 10 minutes

t = 20 minutes

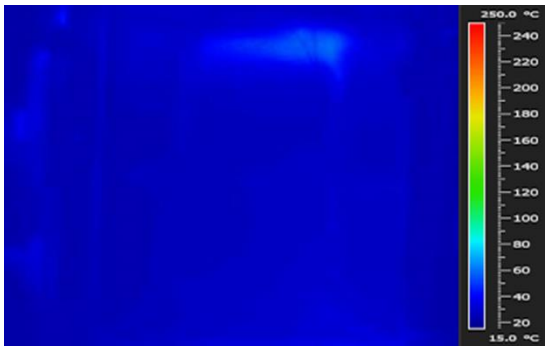

t = 30 minutes

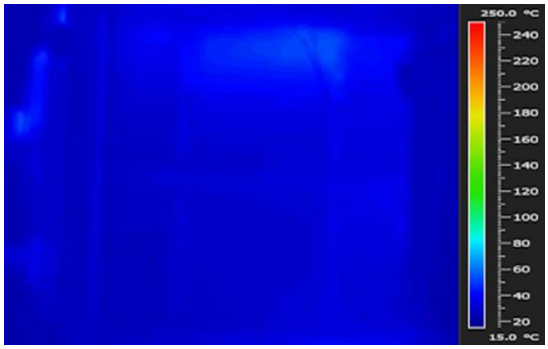

t = 40 minutes

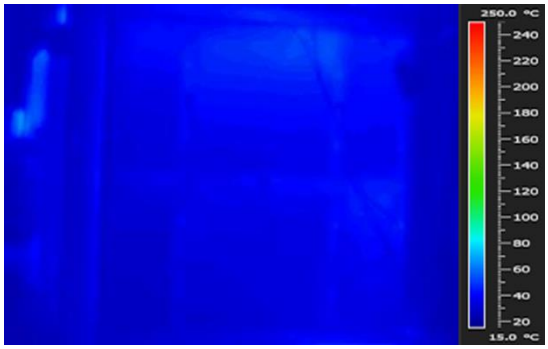

t = 50 minutes

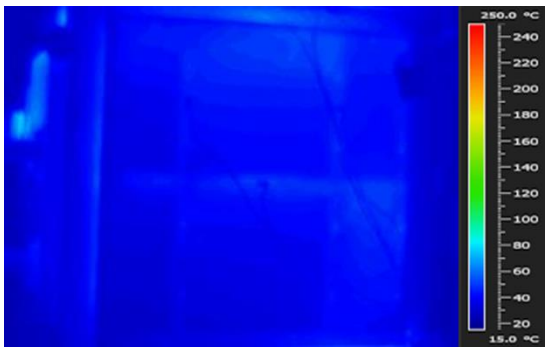

t = 60 minutes

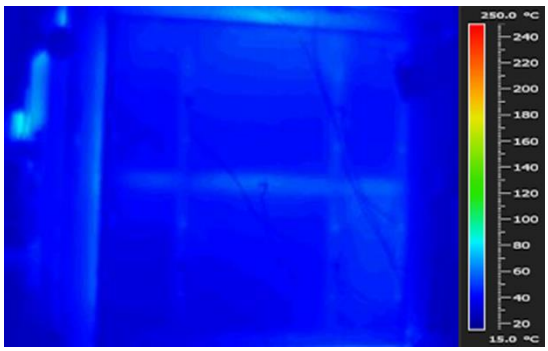

t = 70 minutes

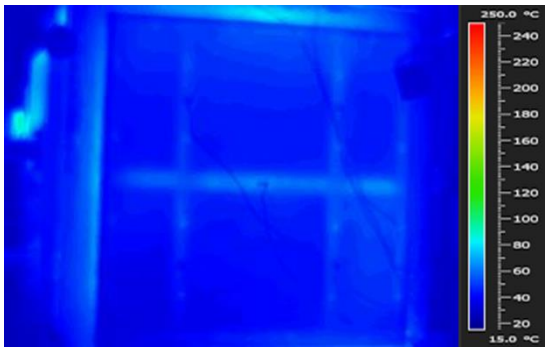

t = 80 minutes

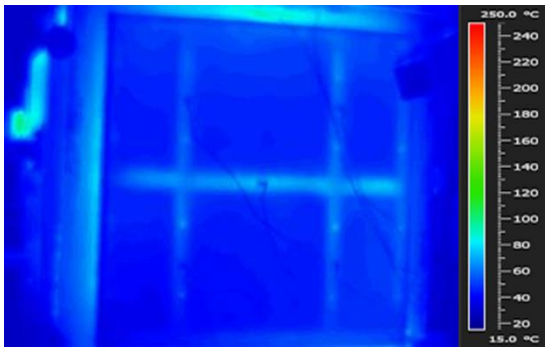

t = 90 minutes

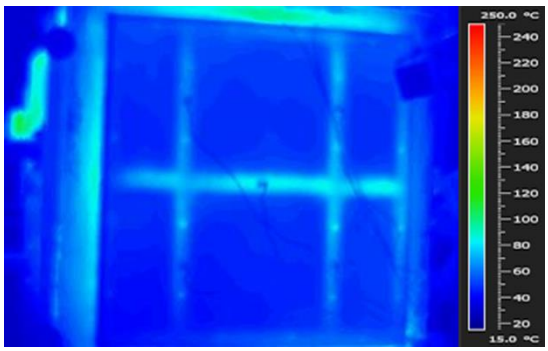

t = 100 minutes

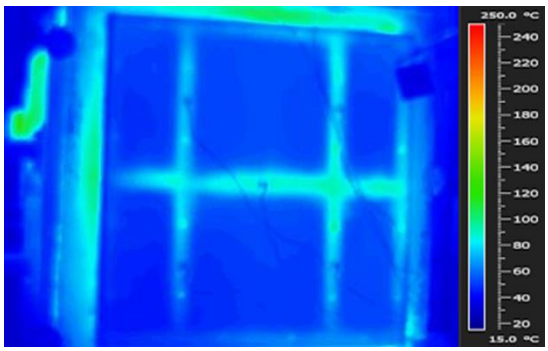

t = 110 minutes

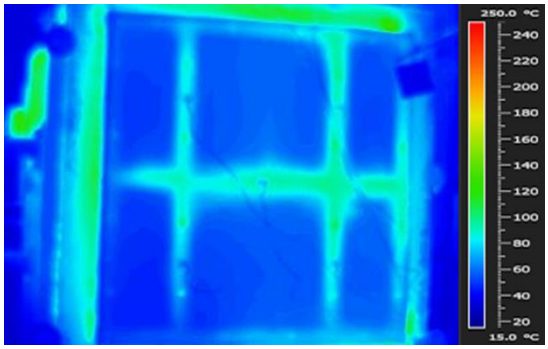

t = 120 minutes

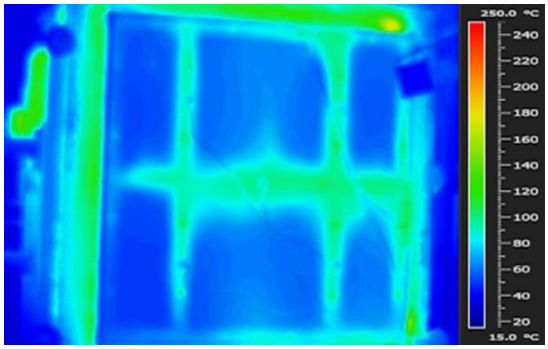

t = 130 minutes

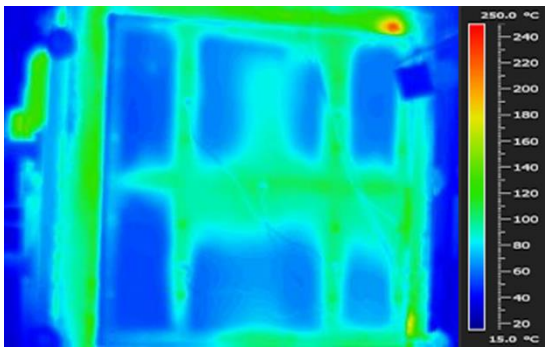

t = 140 minutes

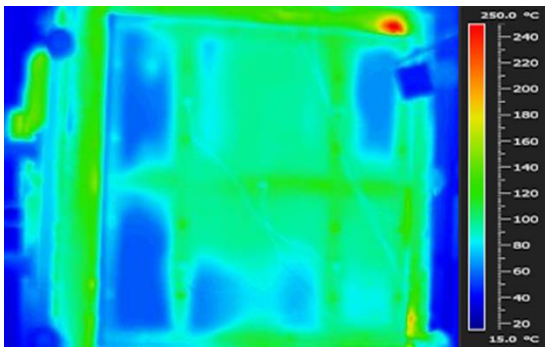

t = 150 minutes

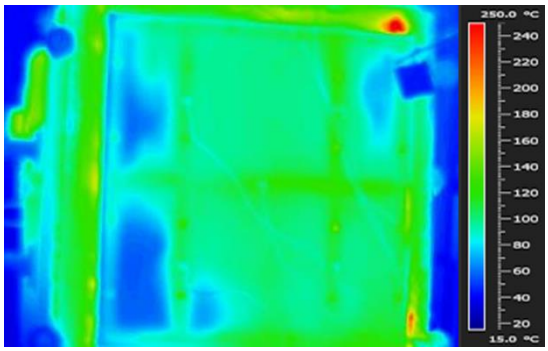

t = 160 minutes

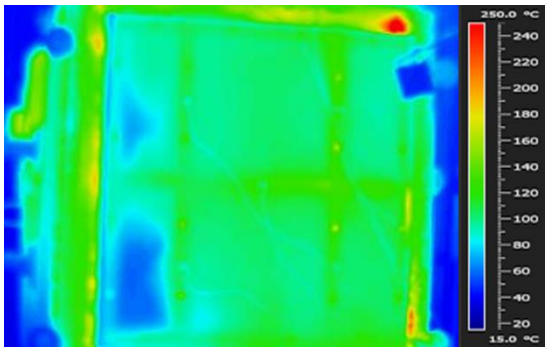

t = 170 minutes

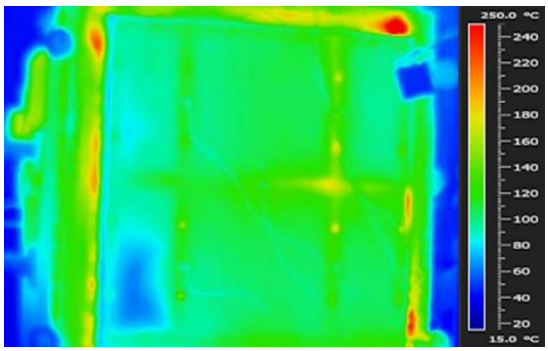

t = 180 minutes

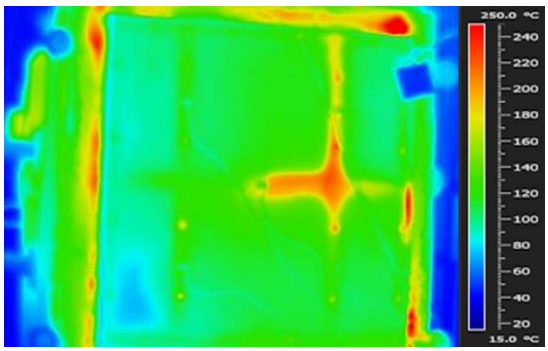

t = 190 minutes	t = 200 minutes
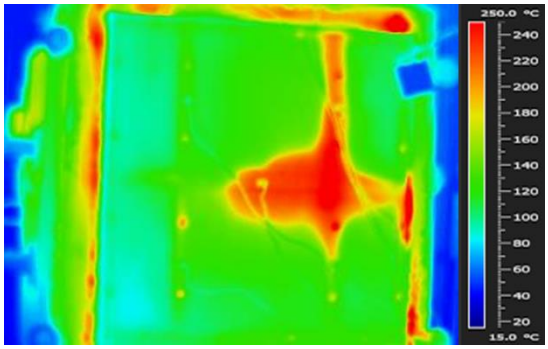	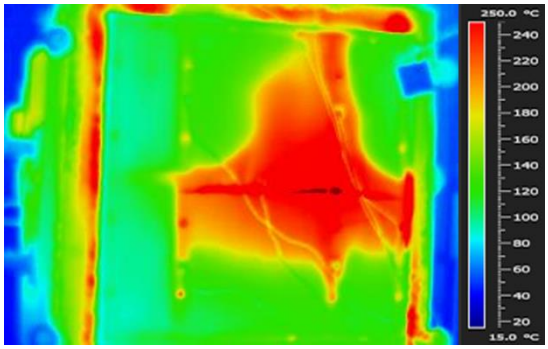

B.4 Specimen 4

Specimen 4 – Non-load-bearing Double-stud LSF Wall	**Thermal Insulation Performance**	
Gypsum plasterboard: 12.5 mm thick Type F fire-resistant	Fire resistance (T_{ave}) [minutes]:	128
Gypsum plasterboards on the exposed side: 1	Fire resistance (T_{max}) [minutes]:	132
Gypsum plasterboards on the unexposed side: 1	Fire-resistance rating (FRR):	I120
Cavity insulation: 75 mm thick ceramic fibre		

Schematic Representation

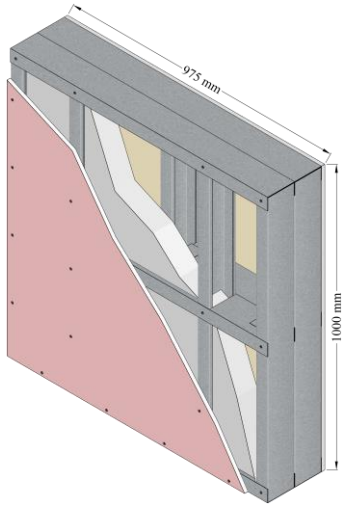

Labels:

- Gypsum plasterboard
- Steel frame
- Ceramic fibre

Steel Frame Description

Stud/track section: C100 x 45 x 10 mm
Steel thickness/grade: 1.0 mm / S280GD
Stud to track connections: 4.2 x 19 mm wafer head self-drilling screw

Cross-section:

*measurements in millimetres

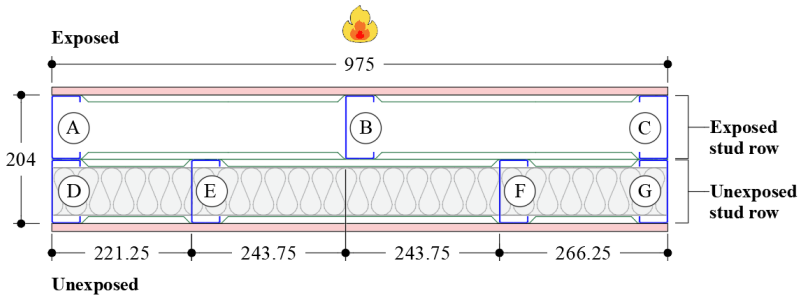

Construction Details

Gypsum plasterboard fastening

*measurements in millimetres

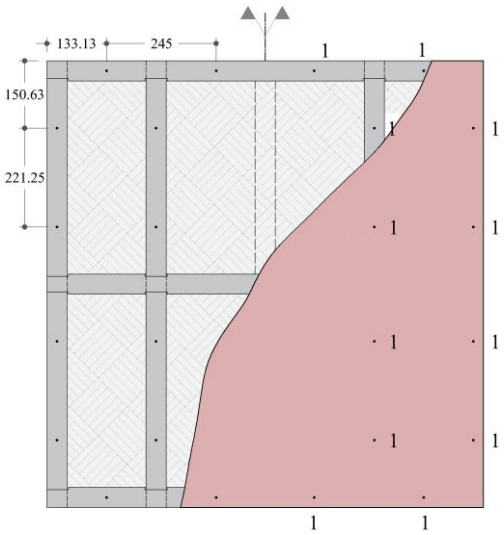

View from the unexposed side

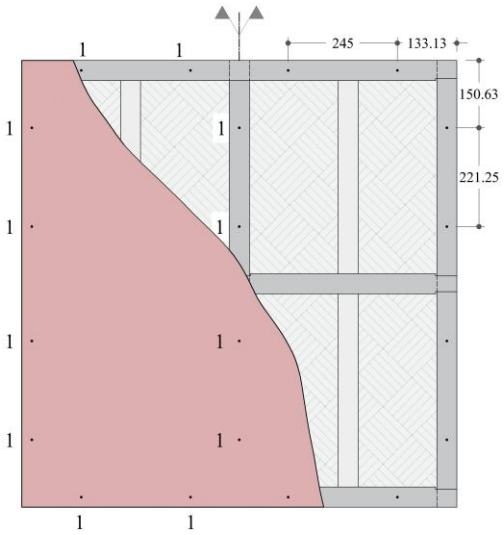

View from the exposed side

Gypsum plasterboard to steel frame connections: 1 – 4.2 x 32 mm flat head self-drilling screw

Test No.4 - Information

Date: 11th December 2019

Test length: 150 minutes

Test Set-Up

Steel frame

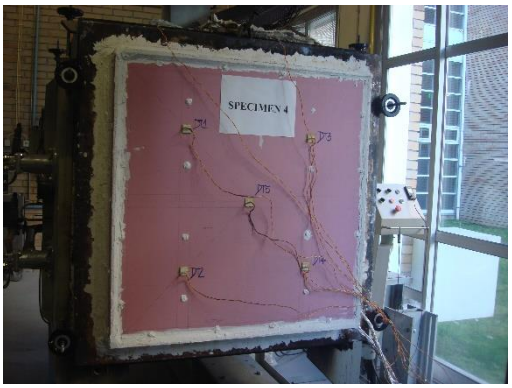

Unexposed surface

Test Set-up Details *measurements in millimetres

Cross-section:

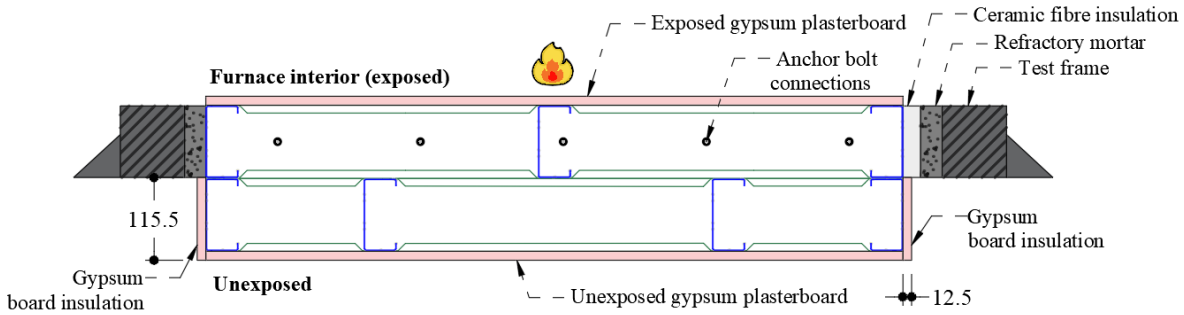

*The representation of the ceramic fibre insulation is intentionally omitted for comprehension purposes

Detail of gypsum board insulation on the unexposed stud row:

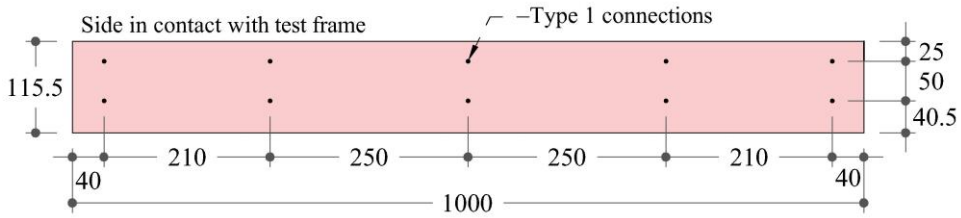

Gypsum board insulation - On all sides of the unexposed stud row

Gypsum board insulation to steel frame connections: 1 – 4.2 x 32 mm flat head self-drilling screw

Thermocouple Attachments *measurements in millimetres

Thermocouples:

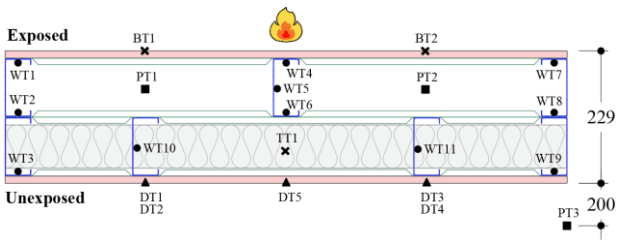

Average and maximum temperatures:

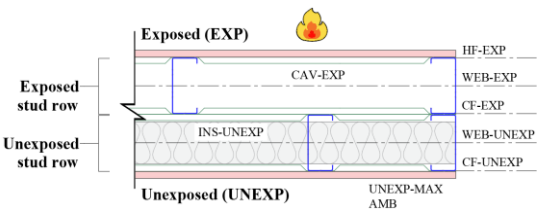

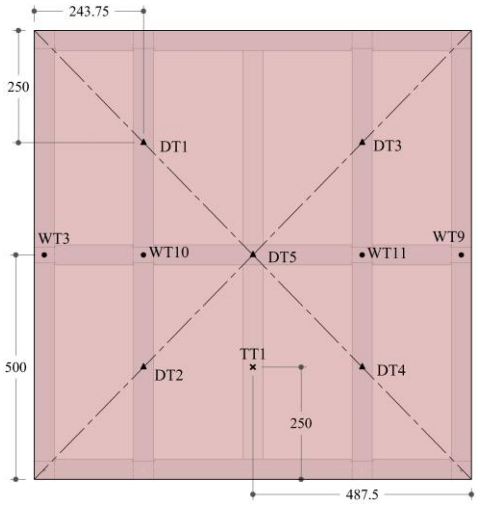

View from the unexposed surface

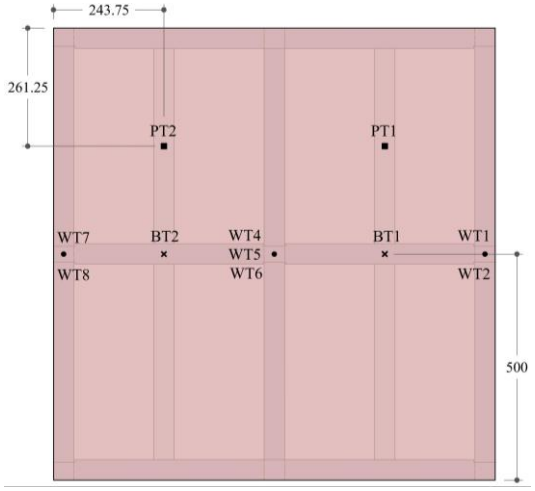

View from the exposed surface

Thermocouple locations:	WT – Welded thermocouple on steel stud	
	DT – Disk thermocouple on gypsum plasterboard	
	BT – Bed thermocouple on gypsum plasterboard	
	TT – Twisted thermocouple within cavity insulation	
	PT – Plate thermocouple in the wall cavity or ambient	
Average and maximum temperatures:	EXP: BT1; BT2	(Average)
	INS-UNEXP: TT1	(Average)
	HF-EXP: WT1; WT4; WT7	(Average)
	WEB-EXP: WT5	(Average)
	CF-EXP: WT2; WT6; WT8	(Average)
	WEB-UNEXP: WT10; WT11	(Average)
	CF-UNEXP: WT3; WT9	(Average)
	CAV-EXP: PT1; PT2	(Average)
	UNEXP: DT1; DT2; DT3; DT4; DT5	(Average)
	UNEXP-MAX: DT1; DT2; DT3; DT4; DT5	(Maximum)
	AMB: PT1	(Average)

Visual Observations

Gypsum plasterboard

Unexposed surface after fire exposure

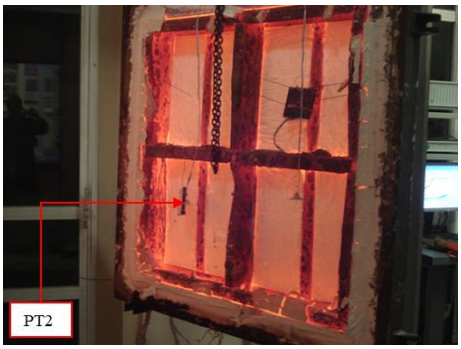

Exposed side after fire exposure

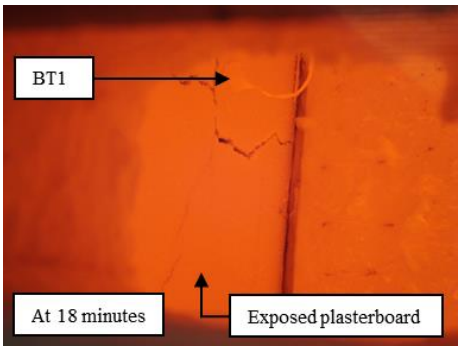

Cracks on the exposed plasterboard

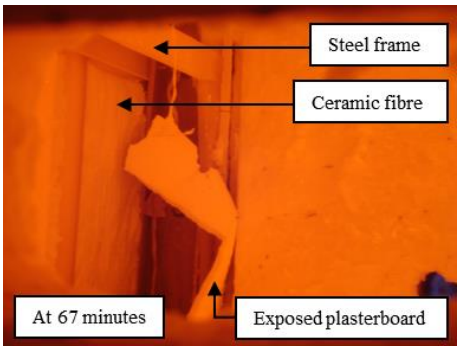

Fall-off of the exposed plasterboard

Steel frame

Steel frame condition after the test

Distortional buckling in stud B (lower part)

Web buckling in stud B (upper part)

Web buckling in stud B (mid-height)

Distortional buckling in stud A (mid-height) and stud B (upper part)

Distortional buckling in stud C (mid-height)

Time-Temperature Profiles (Thermocouples Measurements) **Test duration:** 150 minutes

EXP

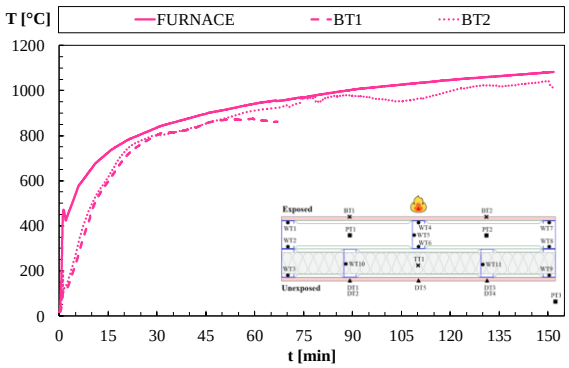

HF-EXP

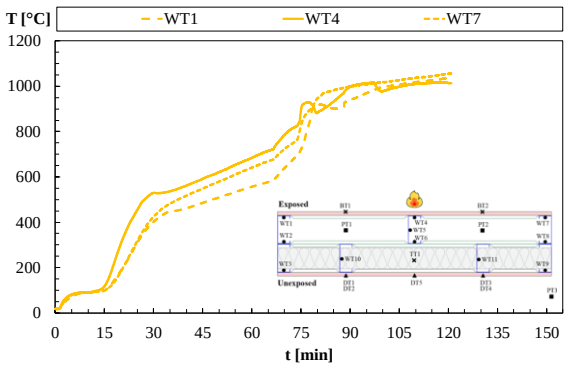

WEB-EXP

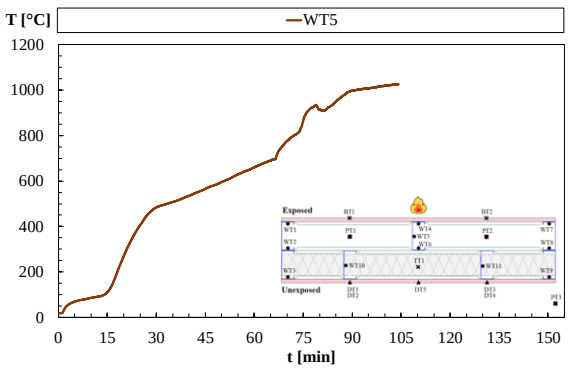

CF-EXP

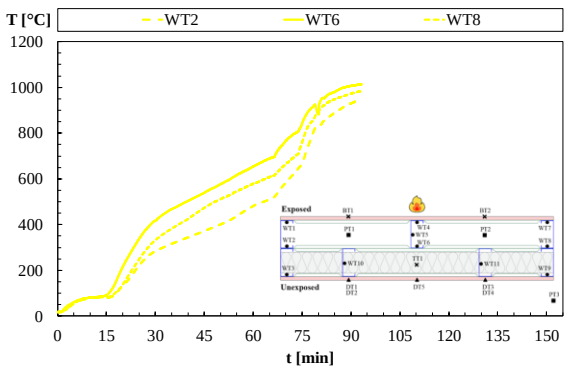

INS-UNEXP

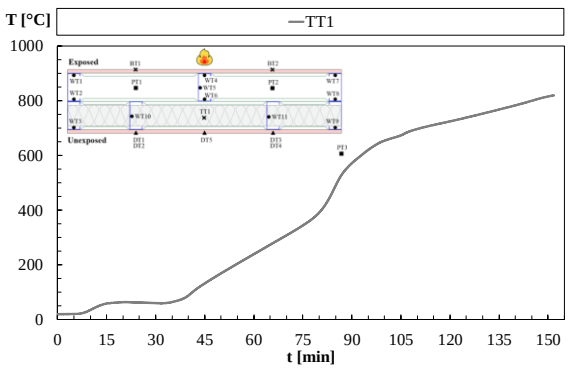

WEB-UNEXP

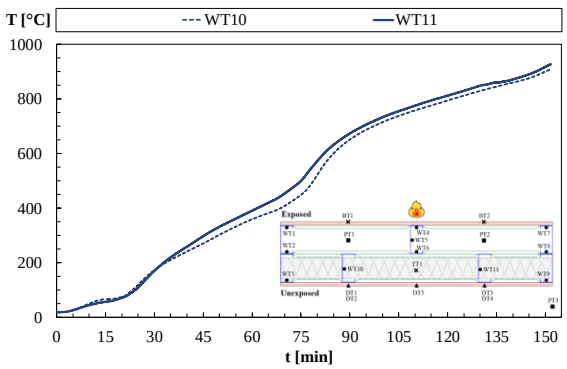

CF-UNEXP

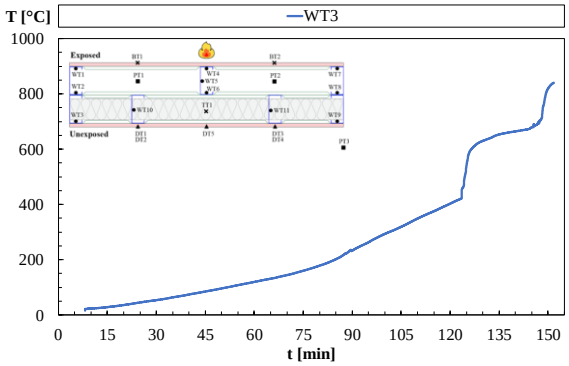

CAV-EXP

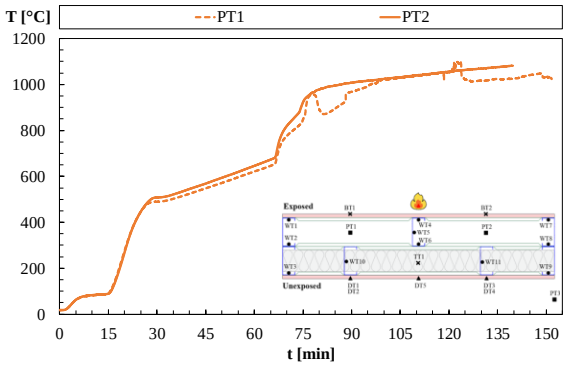

UNEXP / UNEXP-MAX / AMB

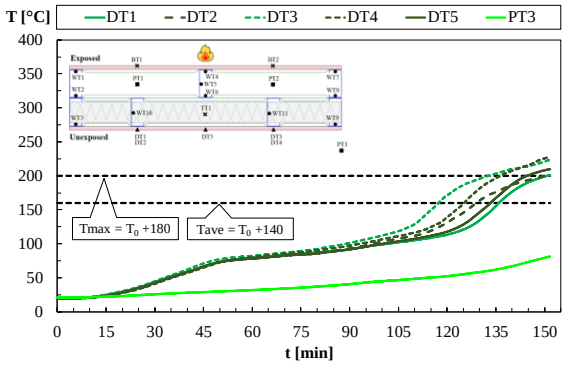

Time-Temperature Profiles (Infrared Measurements) **Test duration:** 150 minutes

IR-MAX, IR-AVE, IR-MIN

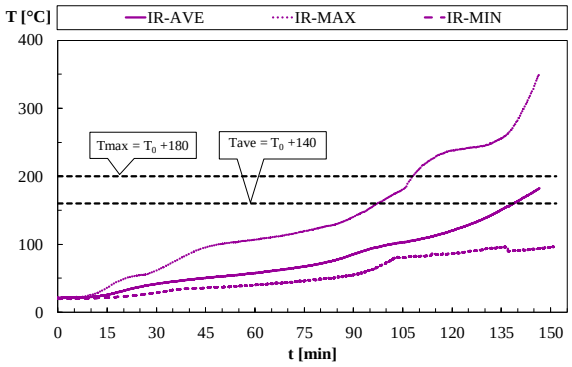

Infrared parameters

Gypsum plasterboard emissivity:	0.8
Distance of the camera from the unexposed surface [m]:	3.2
Measurement rectangle:	
Width [m]:	0.746
Height [m]:	0.879
Area [m²]:	0.656

Measurement Rectangle

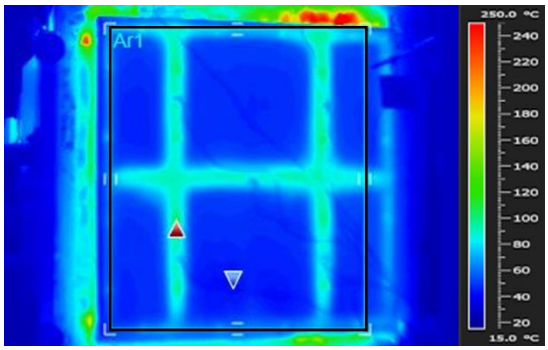

t = 0 minutes

t = 10 minutes

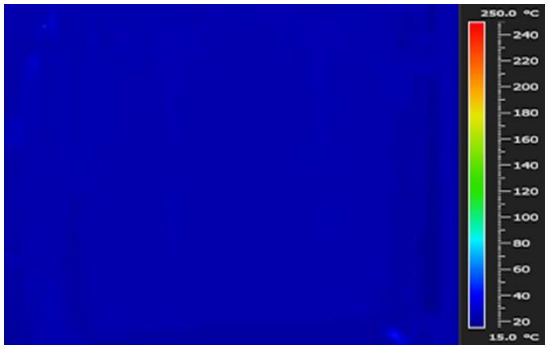

t = 20 minutes

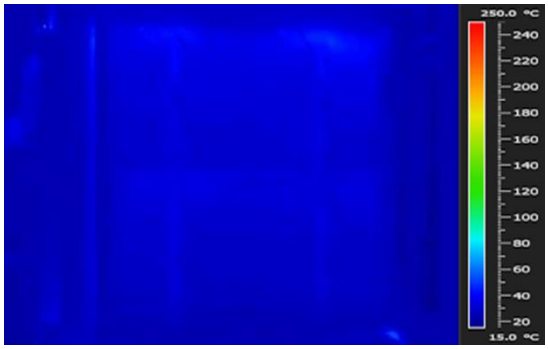

t = 30 minutes

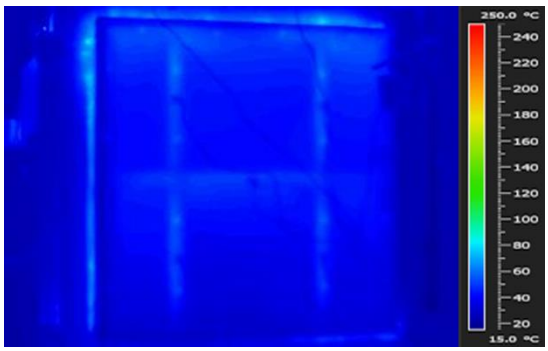

t = 40 minutes

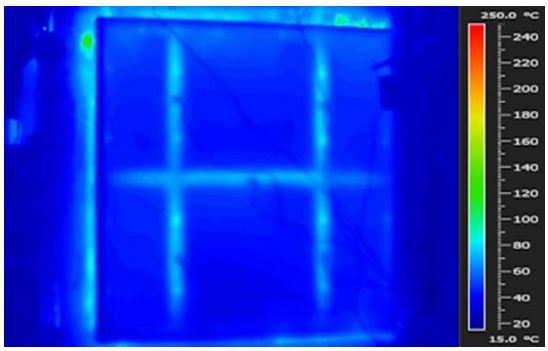

t = 50 minutes

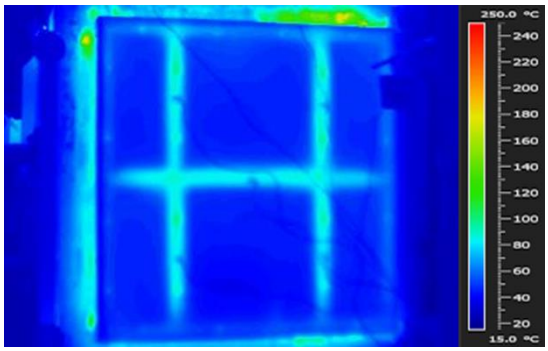

t = 60 minutes

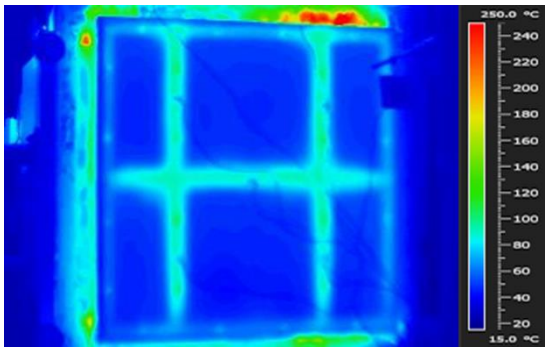

t = 70 minutes

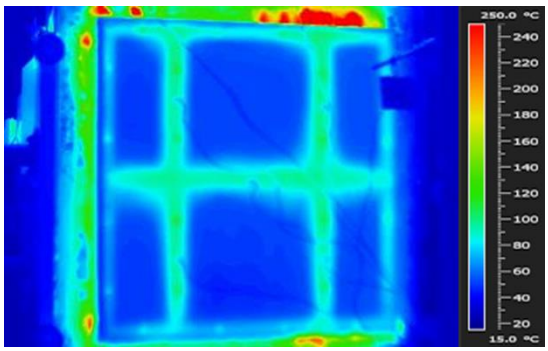

t = 80 minutes

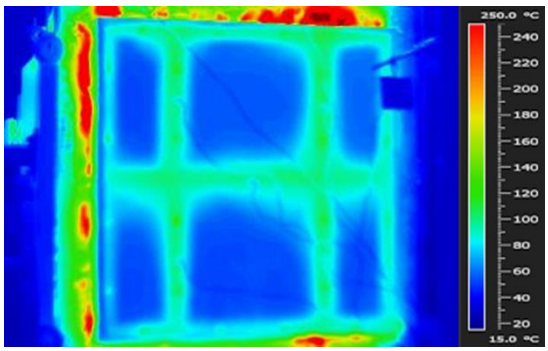

t = 90 minutes

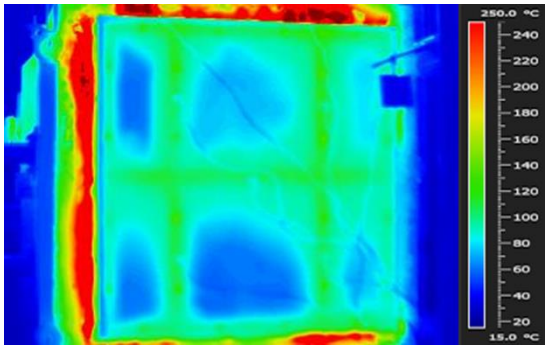

t = 100 minutes

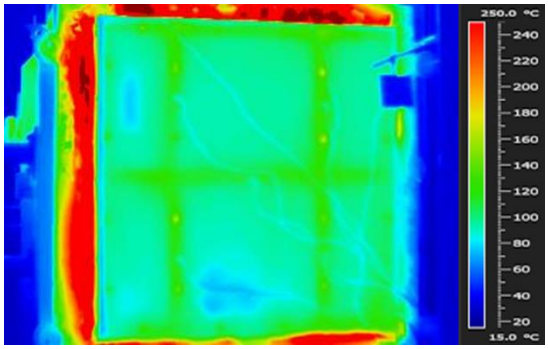

t = 110 minutes

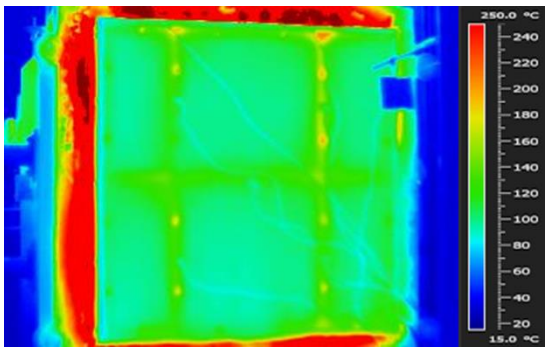

t = 120 minutes

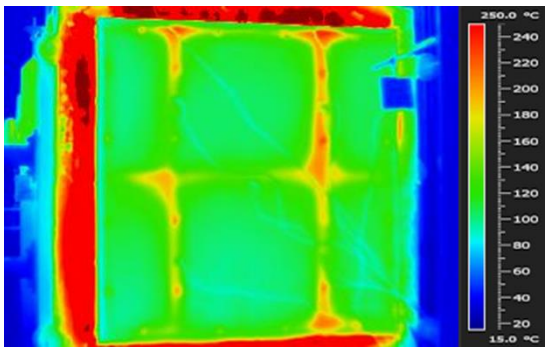

t = 130 minutes

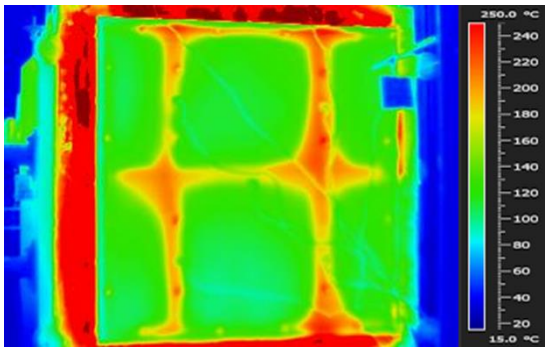

t = 140 minutes

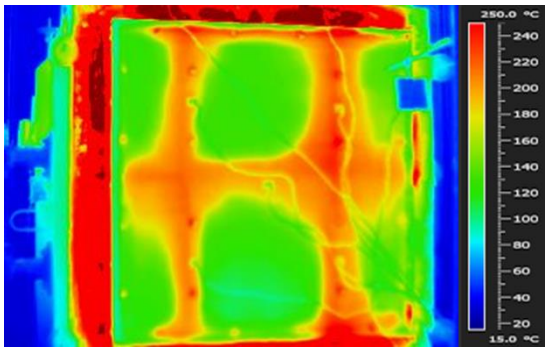

t = 150 minutes

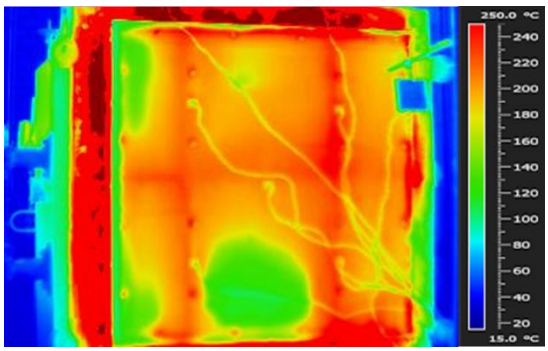

B.5 Specimen 5

Specimen 5 – Non-load-bearing Double-stud LSF Wall	**Thermal Insulation Performance**	
Gypsum plasterboard: 12.5 mm thick Type F fire-resistant	Fire resistance (T_{ave}) [minutes]:	187
Gypsum plasterboards on the exposed side: 1	Fire resistance (T_{max}) [minutes]:	179
Gypsum plasterboards on the unexposed side: 1	Fire-resistance rating (FRR):	I120
Cavity insulation: 75 mm thick ceramic fibre		

Schematic Representation

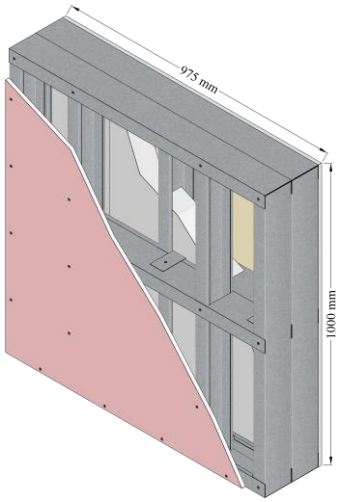

Labels:

- Gypsum plasterboard
- Steel frame
- Ceramic fibre

Steel Frame Description

Stud/track section: C100 x 45 x 10 mm

Steel thickness/grade: 1.0 mm / S280GD

Stud to track connections: 4.2 x 19 mm wafer head self-drilling screw

Cross-section:

*measurements in millimetres

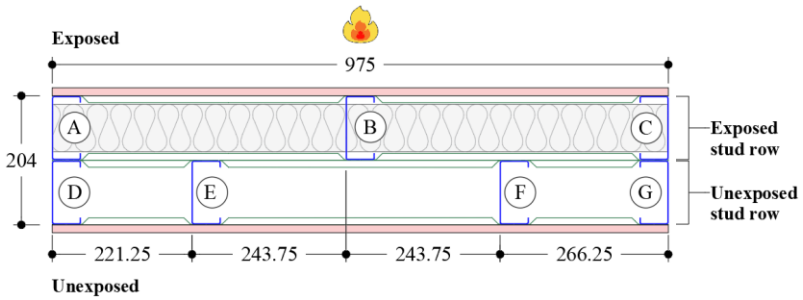

Construction Details

Gypsum plasterboard fastening

*measurements in millimetres

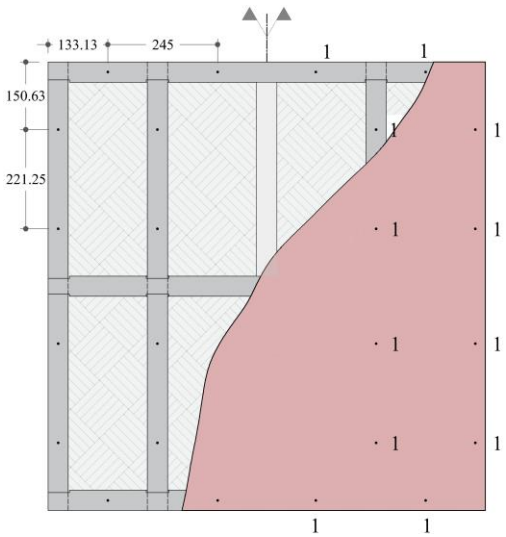

View from the unexposed side

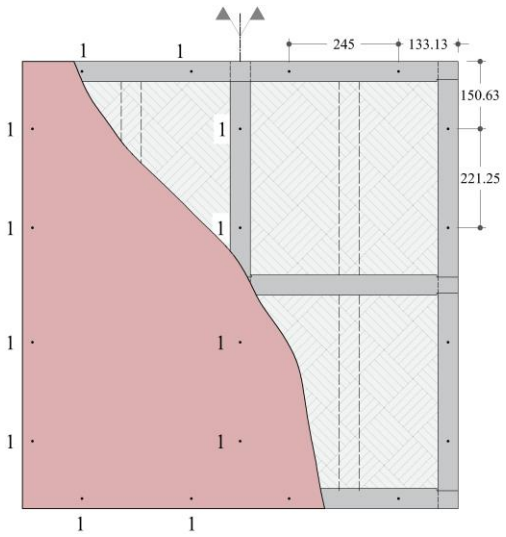

View from the exposed side

Gypsum plasterboard to steel frame connections: 1 – 4.2 x 32 mm flat head self-drilling screw

Test No.5 - Information

Date: 13th November 2019

Test length: 200 minutes

Test Set-Up

Steel frame

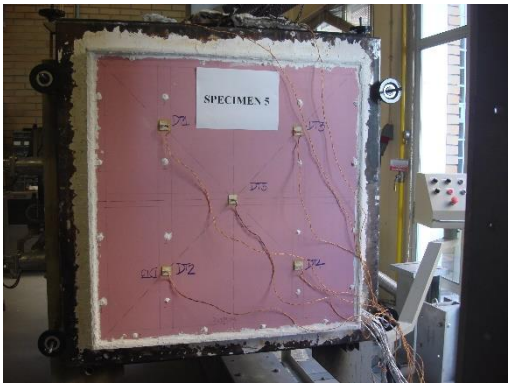

Unexposed surface

Test Set-up Details *measurements in millimetres

Cross-section:

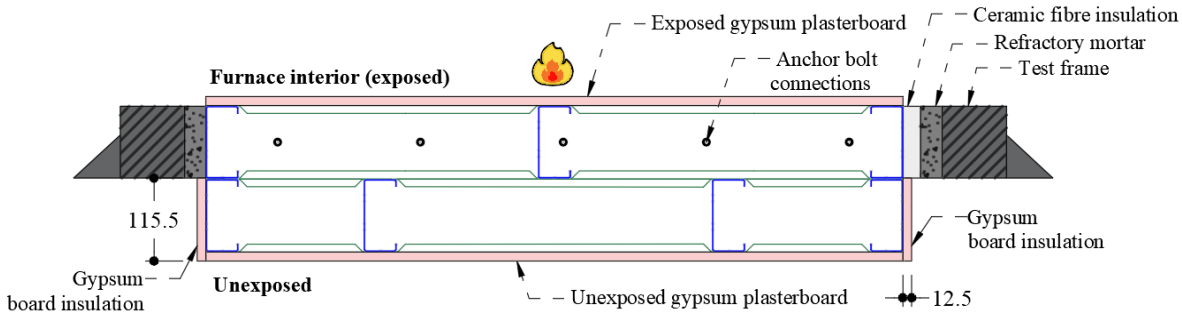

*The representation of the ceramic fibre insulation is intentionally omitted for comprehension purposes

Detail of gypsum board insulation on the unexposed stud row:

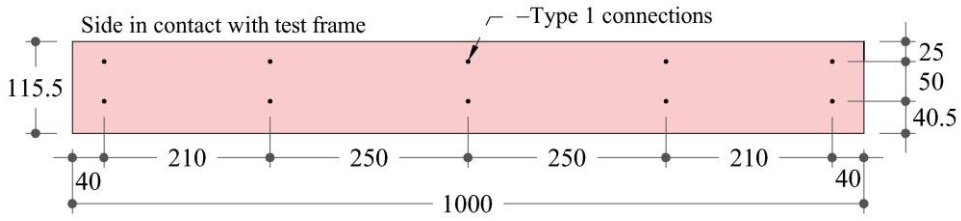

Gypsum board insulation - On all sides of the unexposed stud row

Gypsum board insulation to steel frame connections: 1 – 4.2 x 32 mm flat head self-drilling screw

Thermocouple Attachments *measurements in millimetres

Thermocouples:

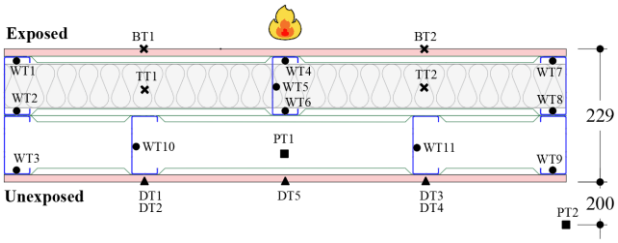

Average and maximum temperatures:

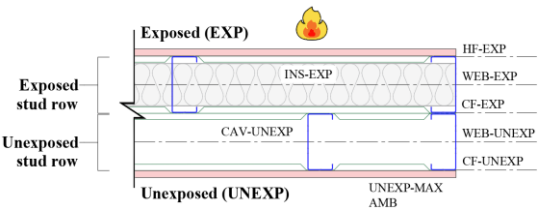

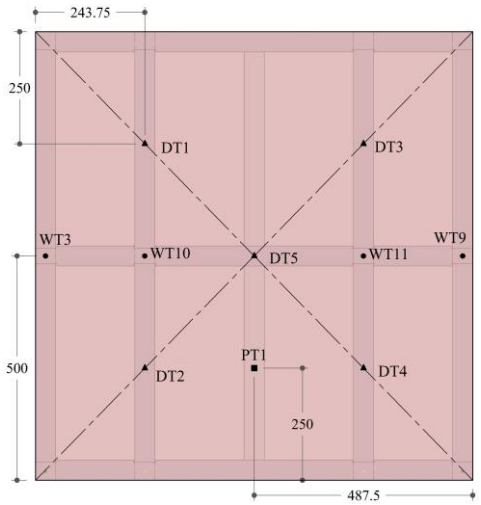

View from the unexposed surface

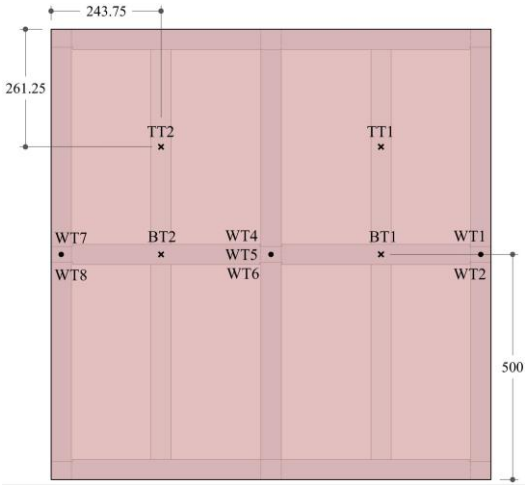

View from the exposed surface

Observations:	WT – Welded thermocouple on steel stud	
	DT – Disk thermocouple on gypsum plasterboard	
	BT – Bed thermocouple on gypsum plasterboard	
	TT – Twisted thermocouple within cavity insulation	
	PT – Plate thermocouple in the wall cavity or ambient	
Average and maximum temperatures:	EXP: BT1; BT2	(Average)
	INS-EXP: TT1; TT2	(Average)
	HF-EXP: WT1; WT4; WT7	(Average)
	WEB-EXP: WT5	(Average)
	CF-EXP: WT2; WT6; WT8	(Average)
	WEB-UNEXP: WT10; WT11	(Average)
	CF-UNEXP: WT3; WT9	(Average)
	CAV-UNEXP: PT1	(Average)
	UNEXP: DT1; DT2; DT3; DT4; DT5	(Average)
	UNEXP-MAX: DT1; DT2; DT3; DT4; DT5	(Maximum)
	AMB: PT2	(Average)

Visual Observations

Gypsum plasterboard

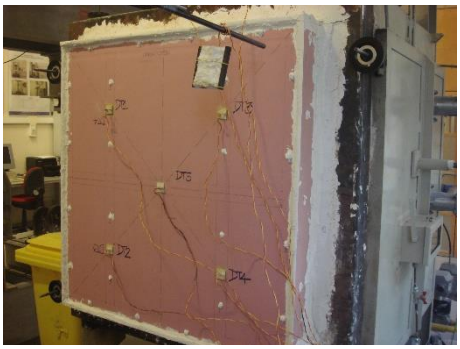

Unexposed surface after fire exposure

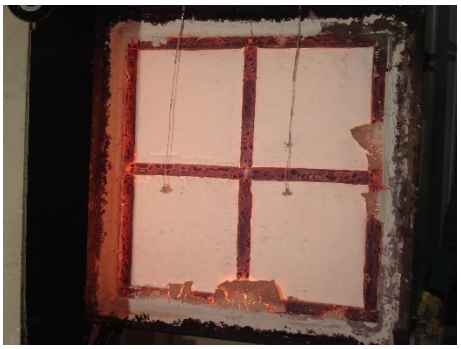

Exposed side after fire exposure

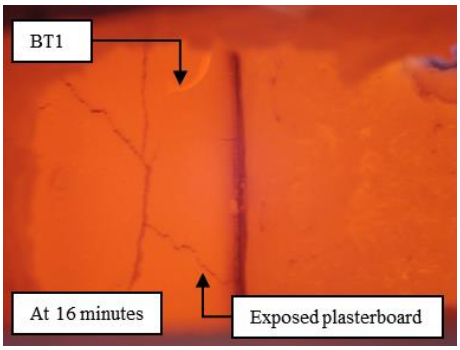

Large cracks on the fire exposed plasterboard (furnace interior)

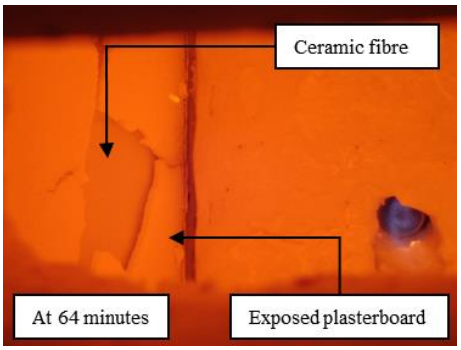

Fall-off of the exposed plasterboard

Steel frame

Steel frame condition after the test

Web and distortional buckling in stud B (upper part)

Distortional buckling in stud A (lower part)

Distortional buckling in stud C (mid-height)

Brittle fracturing behaviour of the steel

Brittle fracturing behaviour of the steel

Time-Temperature Profiles (Thermocouples Measurements) **Test duration:** 200 minutes

EXP

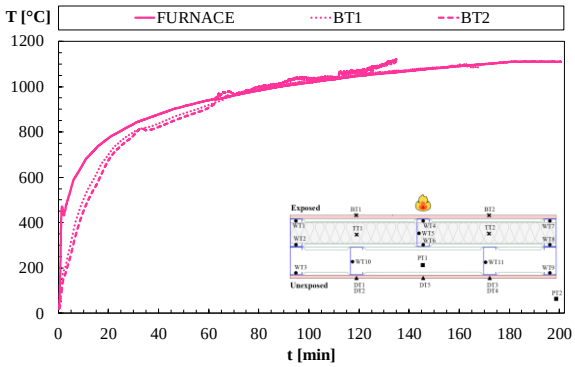

HF-EXP

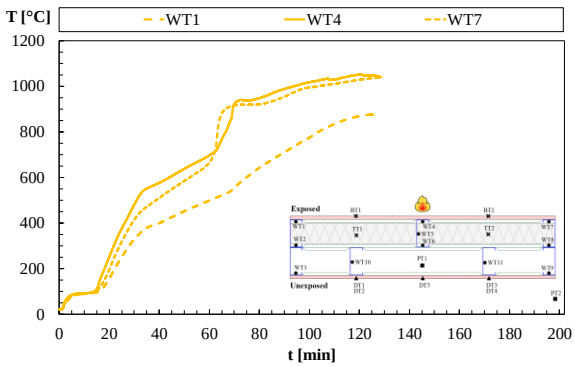

WEB-EXP

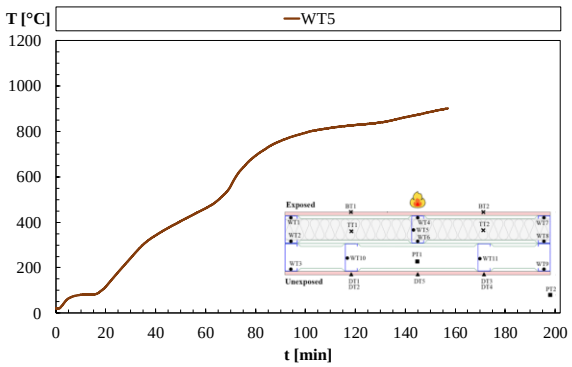

CF-EXP

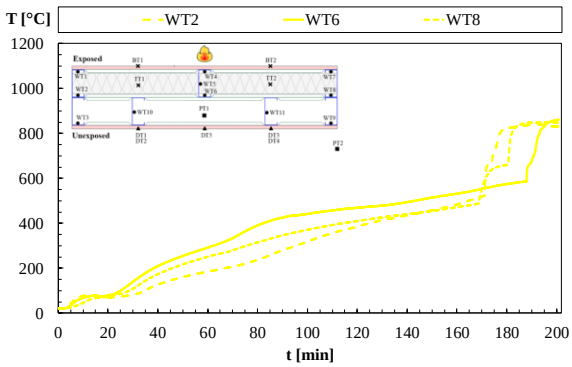

INS-EXP

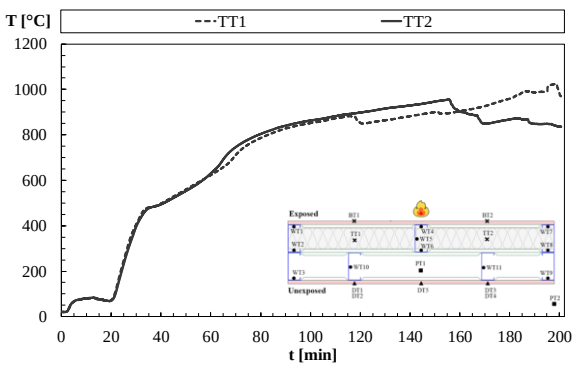

WEB-UNEXP

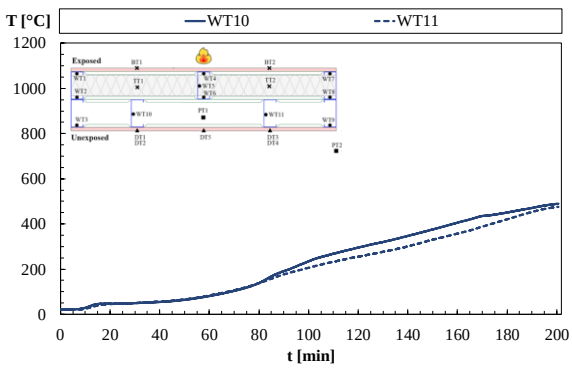

CF-UNEXP

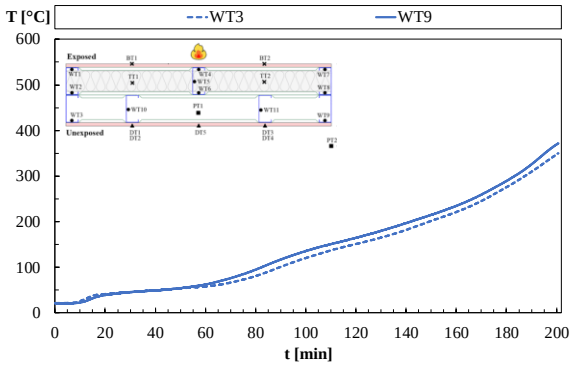

CAV-UNEXP

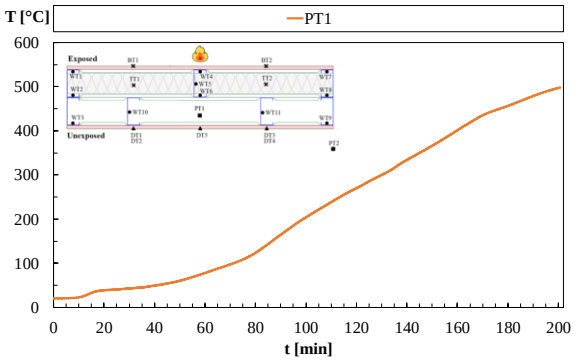

UNEXP / UNEXP-MAX / AMB

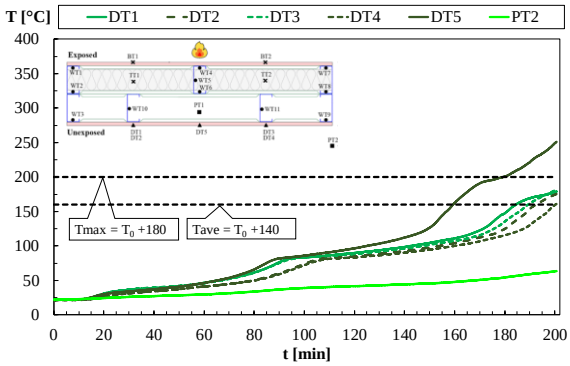

Time-Temperature Profiles (Infrared) **Test duration:** 200 minutes

IR-MAX, IR-AVE, IR-MIN

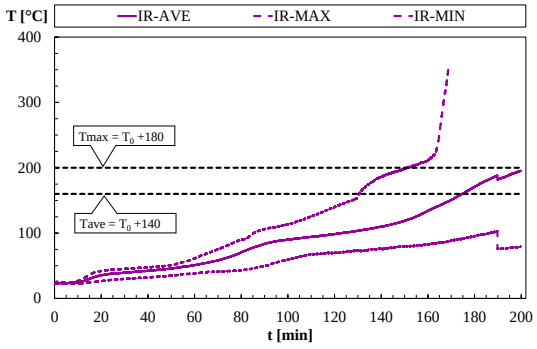

Infrared parameters

Gypsum plasterboard emissivity:	0.8
Distance of the camera from the unexposed surface [m]:	3.2
Measurement rectangle:	
Width [m]:	0.758
Height [m]:	0.845
Area [m²]:	0.640

Measurement Rectangle

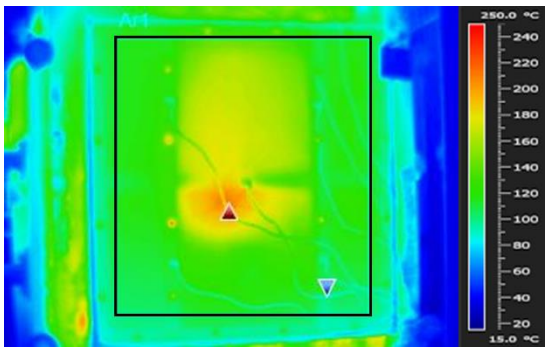

t = 0 minutes

t = 10 minutes

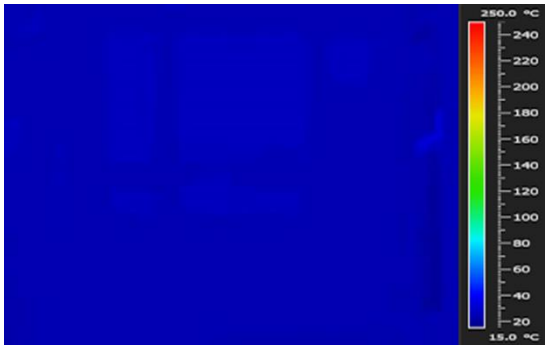

t = 20 minutes

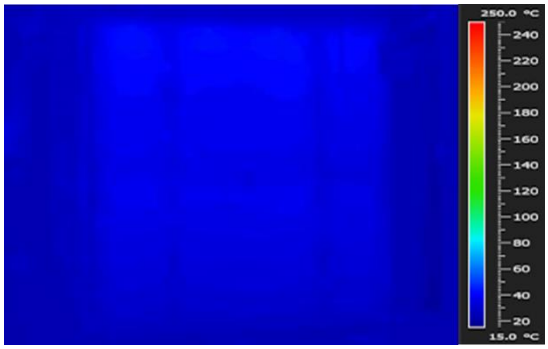

t = 30 minutes

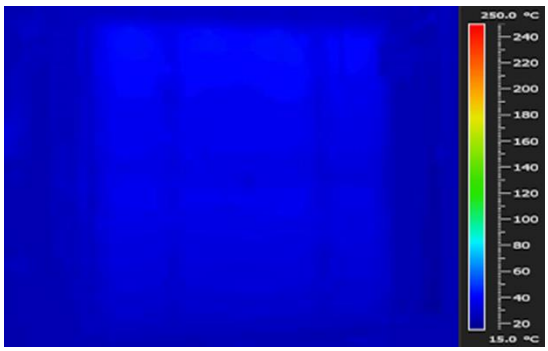

t = 40 minutes

t = 50 minutes

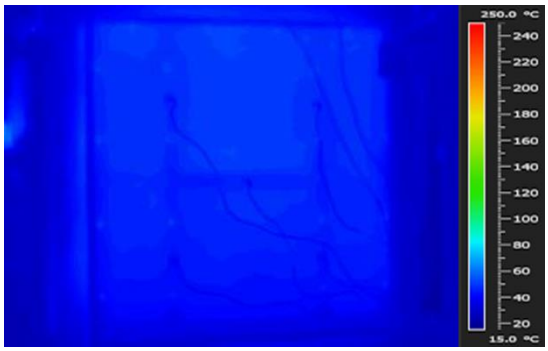

t = 60 minutes

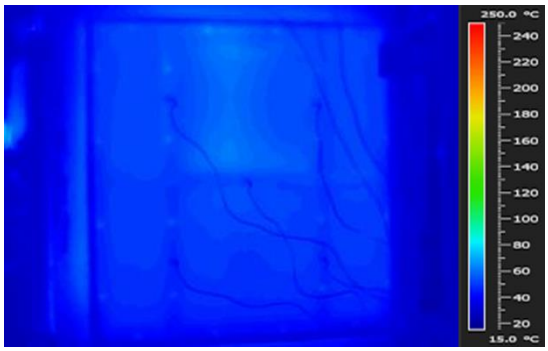

t = 70 minutes

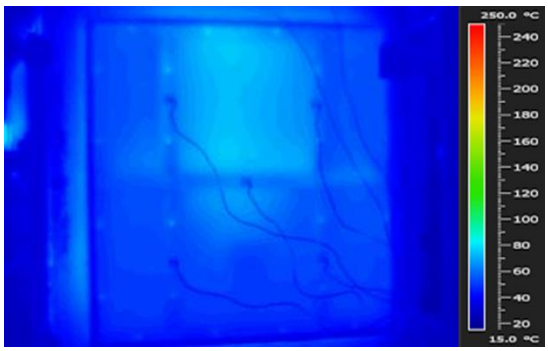

t = 80 minutes

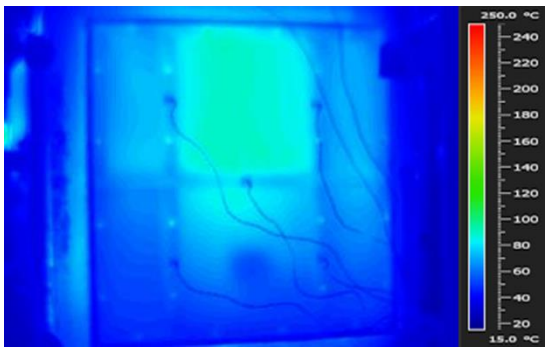

t = 90 minutes

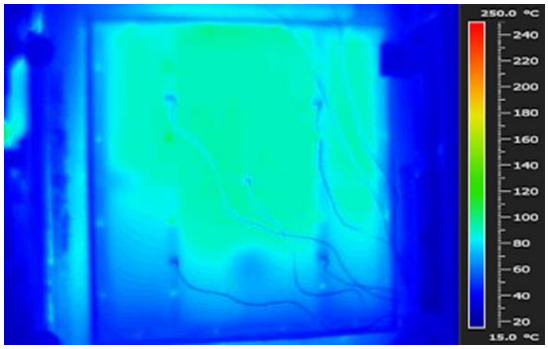

t = 100 minutes

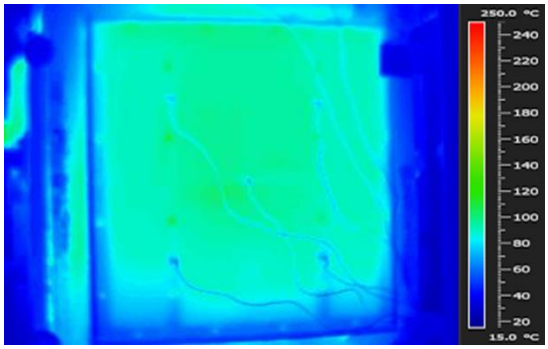

t = 110 minutes

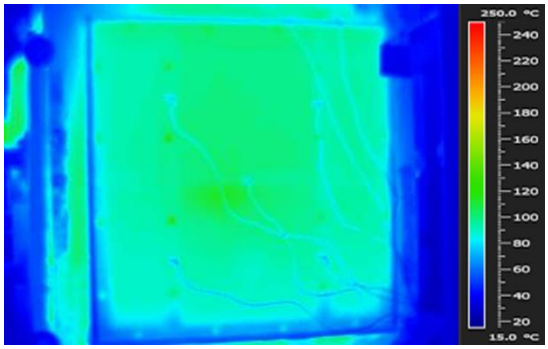

t = 120 minutes

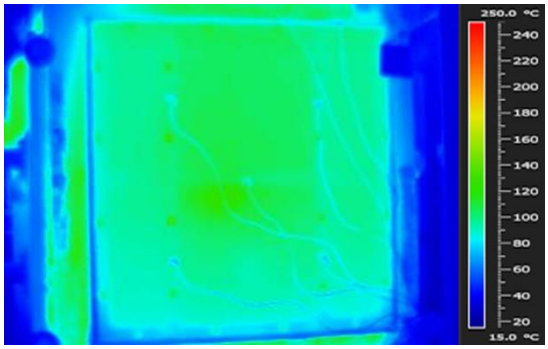

t = 130 minutes

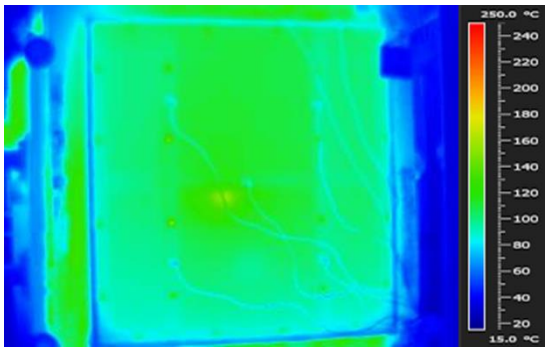

t = 140 minutes

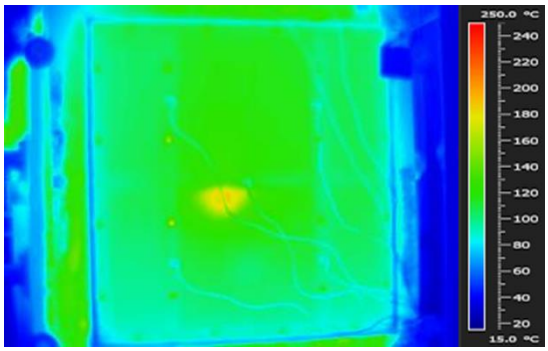

t = 150 minutes

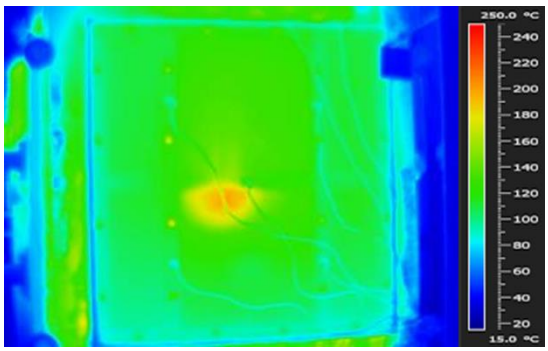

t = 160 minutes

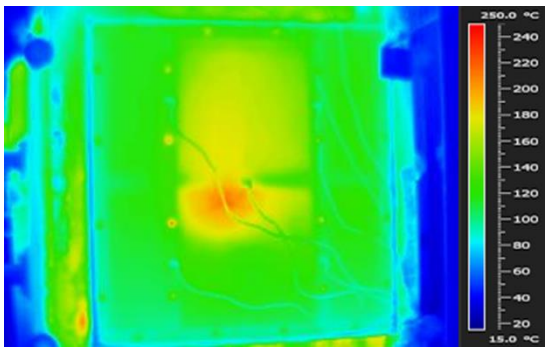

t = 170 minutes	t = 180 minutes
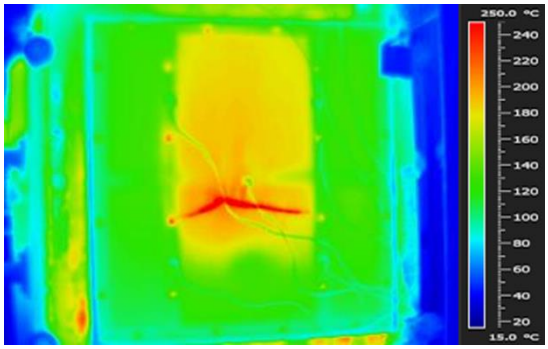	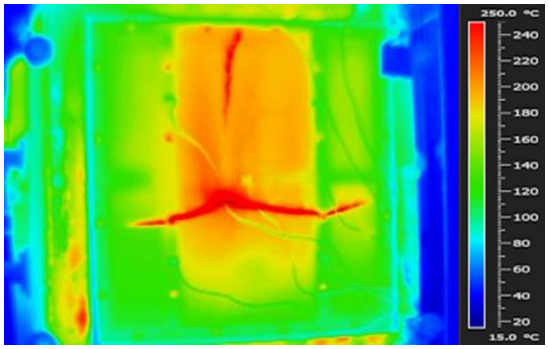
t = 190 minutes	**t = 200 minutes**
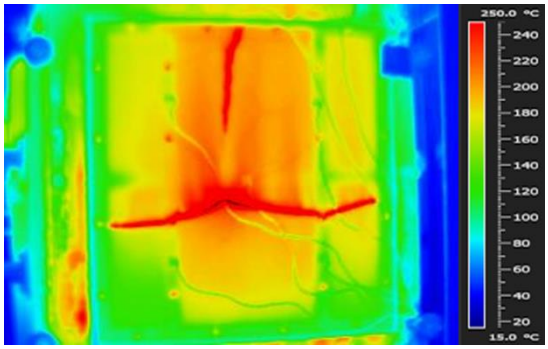	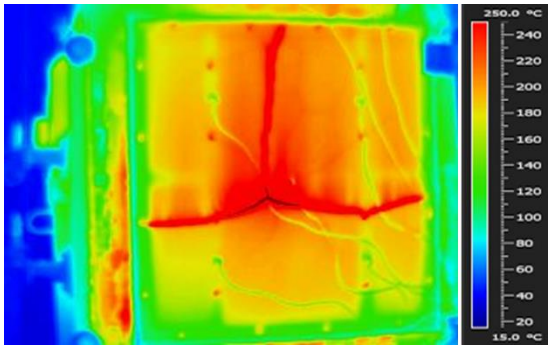

C Material Thermal Properties

C.1 Cold-formed Steel

Table C.1 – Steel thermal properties for the relevant temperature range.

Thermal property	Temperature range (T) [ºC]	Property value	Reference
Specific heat [J/kg·K]	$20 \leq T < 600$	$425 + 0.773T - 0.00169 \cdot T^2 + 0.00000222 \cdot T^3$	EN 1993-1-2 [38]
	$600 \leq T < 735$	$666 + 13002 / (738 - T)$	
	$735 \leq T < 900$	$545 + 17820 / (T - 731)$	
	$900 \leq T \leq 1200$	650	
Density [kg/m³]	$T \geq 20$	7850	EN 1993-1-2 [38]
Thermal conductivity [W/m·K]	$20 \leq T < 800$	$54 - 0.00333 \cdot T$	EN 1993-1-2 [38]
	$800 \leq T \leq 1200$	27.3	

C.2 Ceramic Fibre

Table C.2 – Ceramic fibre thermal properties for the relevant temperature range.

Thermal property	Temperature range (T) [ºC]	Property value	Reference
Specific heat [J/kg·K]	T = 20	995	Morgan Advanced Materials [75]
	T = 200	1017	
	T = 300	1030	
	T = 600	1068	
	T = 800	1093	
	T = 1090	1130	
	T = 1200	1144	

Continues next page

Table C.2 – Ceramic fibre thermal properties for the relevant temperature range (continued).

Thermal property	Temperature range (T) [ºC]	Property value	Reference
Density [kg/m³]	$T \geq 20$	128	Morgan Advanced Materials [75]
Thermal conductivity [W/m·K]	$20 \leq T < 800$	0.05	Morgan Advanced Materials [75]
	$200 \leq T < 400$	$0.00015 \cdot T + 0.02$	
	$400 \leq T < 600$	$0.0002 \cdot T$	
	$600 \leq T < 800$	$0.0003 \cdot T - 0.06$	
	$800 \leq T < 1000$	$0.00035 \cdot T - 0.1$	
	$1000 \leq T \leq 1200$	$0.00025 \cdot T$	

C.3 Gypsum Plasterboards

Table C.3 – Gypsum plasterboard thermal properties for the relevant temperature range.

Type of gypsum plasterboard	Thermal property	Temperature range (T) [ºC]	Property value	Reference
Type X	Specific heat [J/kg·K]	$20 \leq T < 78$	$6.146 \cdot T + 1377$	Sultan (1996) [40]
		$78 \leq T < 85$	$150 \cdot T - 9858$	
		$85 \leq T < 97$	$262 \cdot T - 19501$	
		$97 \leq T < 124$	$476 \cdot T - 40311$	
		$124 \leq T < 139$	$154507 - 1097 \cdot T$	
		$139 \leq T < 148$	$16601 - 105 \cdot T$	
		$148 \leq T < 373$	$1189 - 1.27 \cdot T$	
		$373 \leq T < 430$	714	
		$430 \leq T < 571$	$1151 - 1.014 \cdot T$	
		$571 \leq T < 609$	$1.877 \cdot T - 501$	
		$609 \leq T < 662$	$44.2 \cdot T - 26300$	
		$662 \leq T < 670$	3000	
		$670 \leq T < 685$	$103570 - 150 \cdot T$	
		$T \geq 685$	571	

Continues next page

Table C.3 – Gypsum plasterboard thermal properties for the relevant temperature range (continued).

Type of gypsum plasterboard	Thermal property	Temperature range (T) [ºC]	Property value	Reference
Type X	Density [kg/m³]	20 ≤ T < 80	698	Sultan (1996) [40]
		T ≥ 80	576	
Type X	Thermal conductivity [W/m·K]	20 ≤ T < 100	0.25	Sultan (1996) [40]
		100 < T < 400	0.12	
		400 ≤ T < 800	0.00035·T - 0.01	
		T ≥ 800	0.0013·T - 0.77	
Type F	Specific heat [J/kg·K]	Same as Type X	Same as Type X	Current research
Type F	Density [kg/m³] *	T = 20	770	Manufacturer
		20 ≤ T < 80	770	Current research
		T ≥ 80	619	Current research
Type F	Thermal conductivity [W/m·K]	Same as Type X	Same as Type X	Current research

* Adapted according to a shift factor expressed as 576/698 = 0.825, based on the values adopted by Sultan (1996) [40], in a way that the density of the Type F gypsum plasterboard for T ≥ 80 is 0.825·770 = 619 kg/m³.

C.4 Air

Table C.4 – Air thermal properties for the relevant temperature range.

Temperature [ºC]	Specific heat [J/kg·K]	Density [kg/m³]	Thermal conductivity [W/m·K]	Reference
20	1007	1.2040	0.02514	Çengel and Ghajar [76]
30	1007	1.1640	0.02588	
60	1007	1.0590	0.02808	
100	1009	0.9458	0.03095	
200	1023	0.7459	0.03779	
300	1044	0.6158	0.04418	
400	1069	0.5243	0.05015	
500	1093	0.4565	0.05572	

Continues next page

Table C.4 – Air thermal properties for the relevant temperature range (continued).

Temperature [ºC]	Specific heat [J/kg·K]	Density [kg/m³]	Thermal conductivity [W/m·K]	Reference
600	1115	0.4042	0.06093	Çengel and Ghajar [76]
700	1135	0.3627	0.06581	
800	1153	0.3289	0.07037	
900	1169	0.3008	0.07465	
1000	1184	0.2772	0.07868	
1500	1234	0.1990	0.09599	

D Technical Files – Validation Models

D.1 Model Specimen 1

Model Specimen 1 – Non-load-bearing Double-stud LSF Wall	**Thermal Insulation Performance**	
Gypsum plasterboard: 12.5 mm thick Type F fire-resistant	Fire resistance (T_{ave}) [minutes]:	70
Gypsum plasterboards on the exposed side: 1	Fire resistance (T_{max}) [minutes]:	67
Gypsum plasterboards on the unexposed side: 1	Fire resistance rating (FRR):	I60
Cavity insulation: -		
Air boundary layer: 1 x 10 mm		

3D Finite Element Mesh

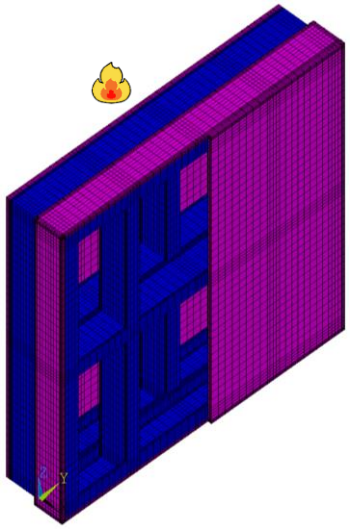

Labels:

- Gypsum plasterboard
- Steel frame
- Air layer

Steel Frame Description

- Stud/track section: C100 x 45 x 10 mm
- Steel thickness/grade: 1.0 mm / S280GD
- Connections: perfectly rigid

2D cross-section detail (z = 500 mm):

*measurements in millimetres

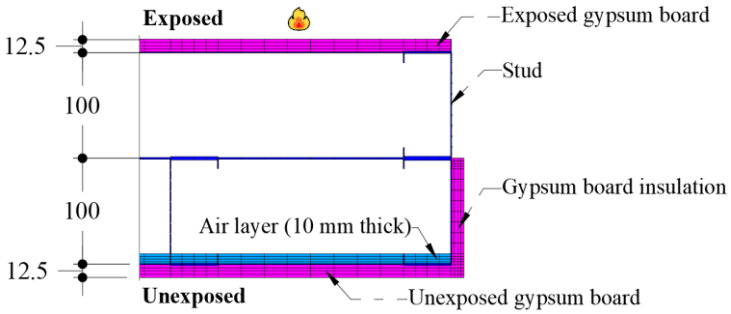

Mesh Details

Total number of nodes:	**Total number of elements:**
Steel frame – SHELL131 Finite Elements	*Gypsum plasterboard / Air layer – SOLID70 Finite Elements*

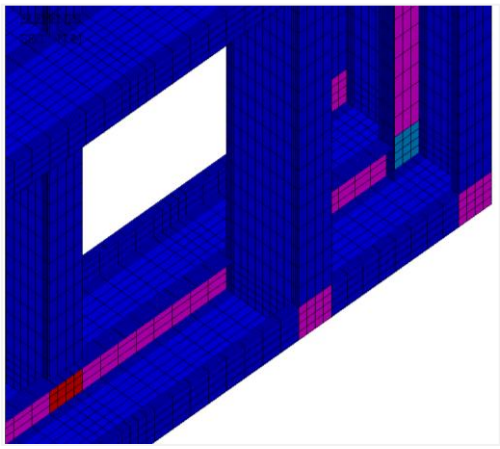

View from the unexposed side (right bottom corner)

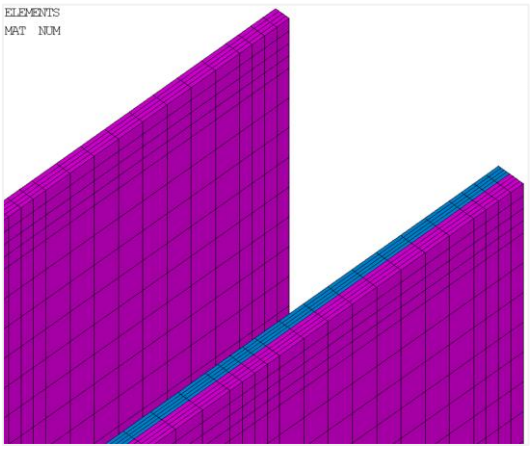

View from the unexposed side (right upper corner)

SHELL131 section thickness:

- 1 mm
- 2 mm
- 3 mm
- 4 mm

Boundary Conditions (z = 500 mm)

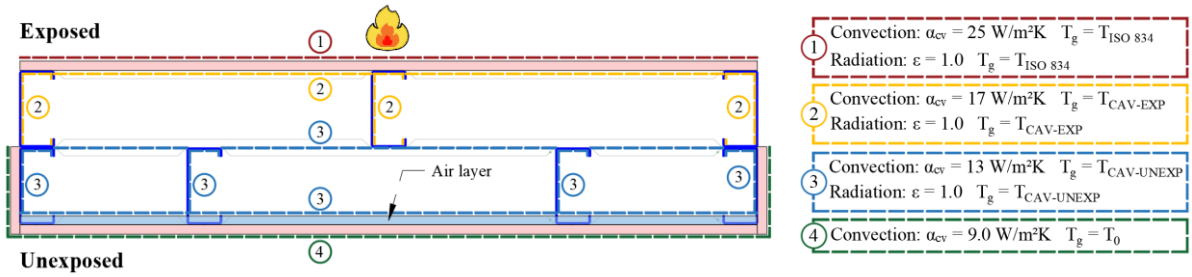

Nodal Temperatures *measurements in millimetres

Nodes:

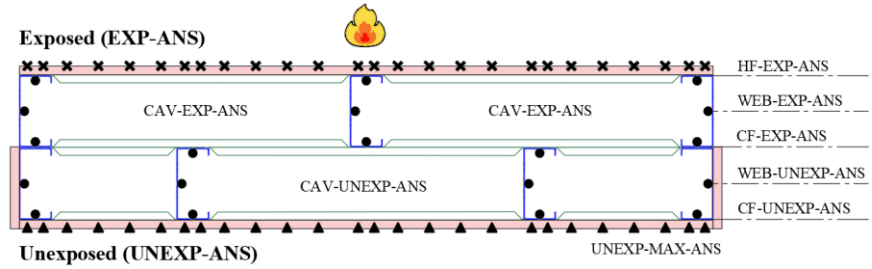

Labels:

- ✖ Nodes at 261.25 mm from the bottom of the wall
- ● Nodes at 500 mm from the bottom of the wall
- ▲ Nodes at 261.25 mm and 500 mm from the bottom of the wall

Numerical and Experimental Time-Temperature Profiles **Test duration:** 77 minutes

EXP-ANS / EXP

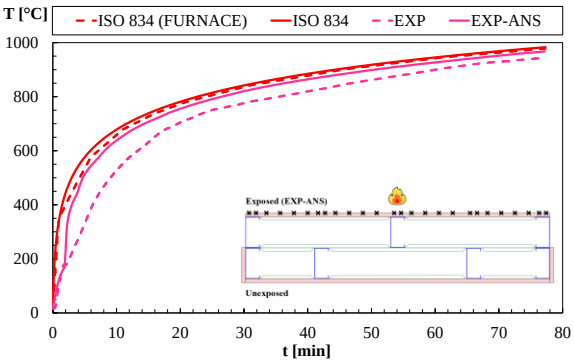

HF-EXP-ANS / HF-EXP

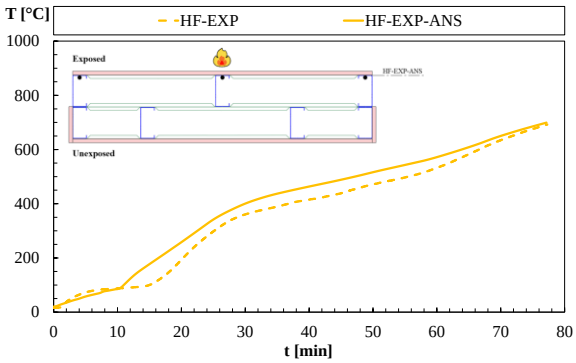

WEB-EXP-ANS / WEB-EXP

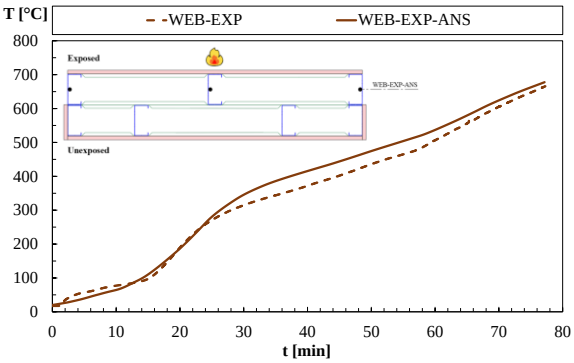

CF-EXP-ANS / CF-EXP

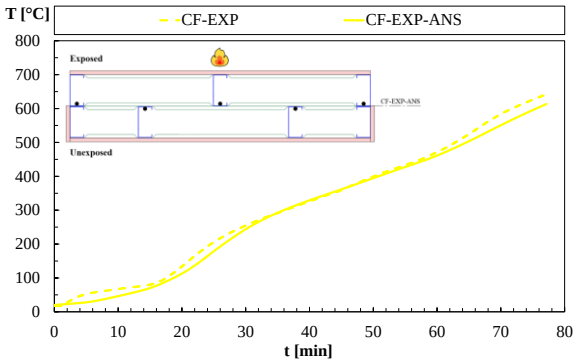

WEB-UNEXP-ANS / WEB-UNEXP

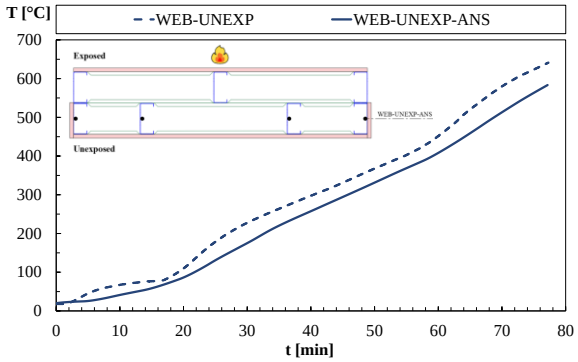

CF-UNEXP-ANS / CF-UNEXP

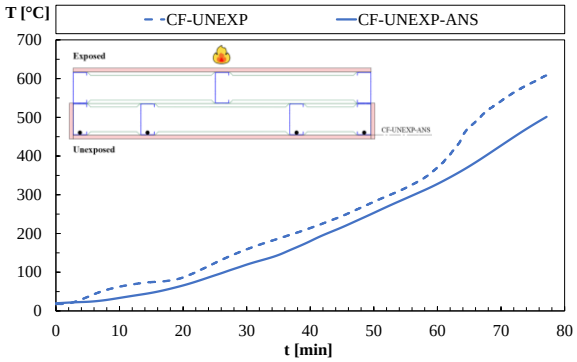

CAV-EXP-ANS / CAV-EXP

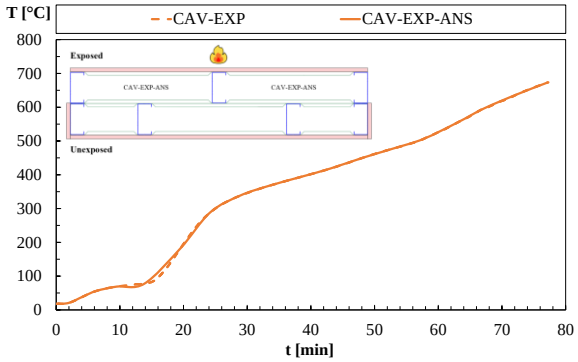

CAV-UNEXP-ANS / CAV-UNEXP

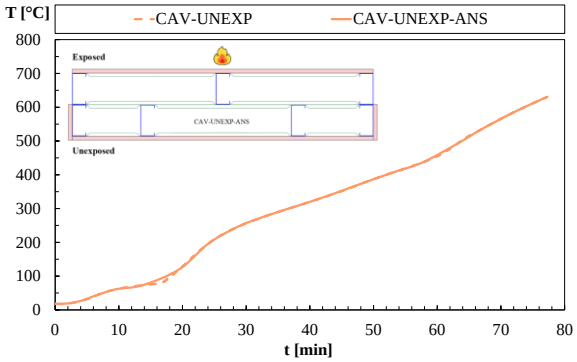

UNEXP / UNEXP-ANS

UNEXP-MAX / UNEXP-MAX-ANS

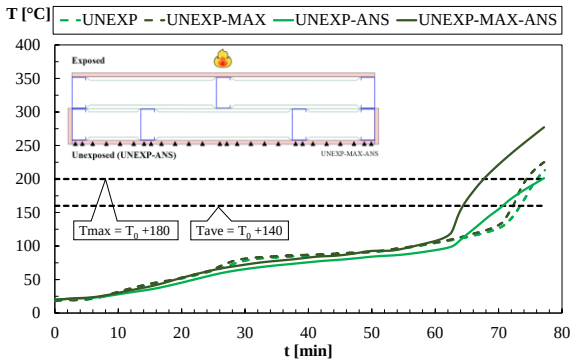

Temperatures on the Unexposed Plasterboard [°C] **Test duration:** 77 minutes

t = 10 minutes

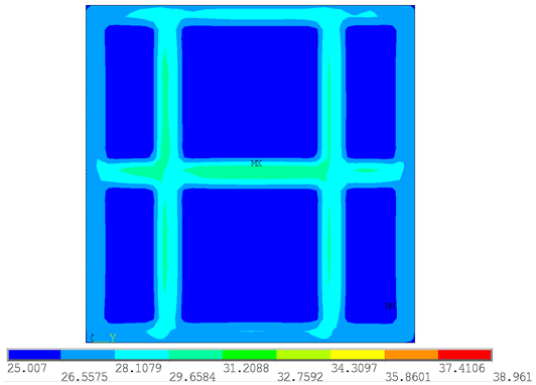

t = 20 minutes

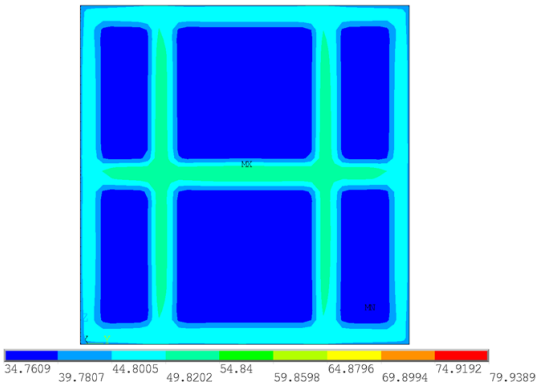

t = 30 minutes

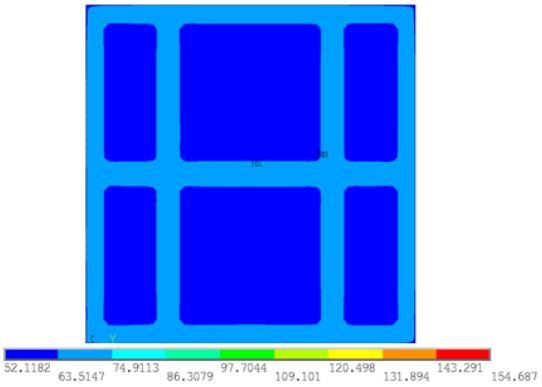

t = 40 minutes

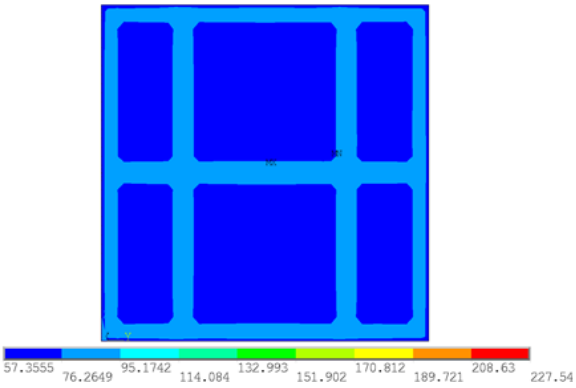

t = 50 minutes

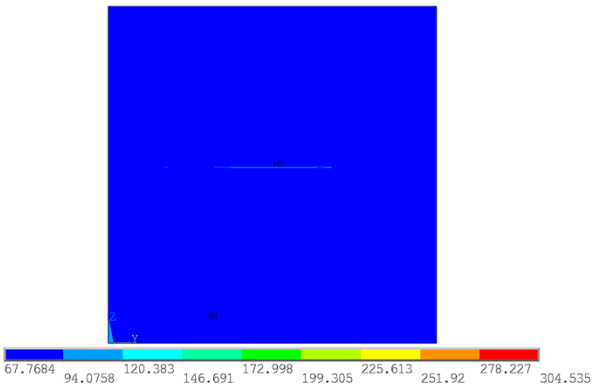

t = 60 minutes

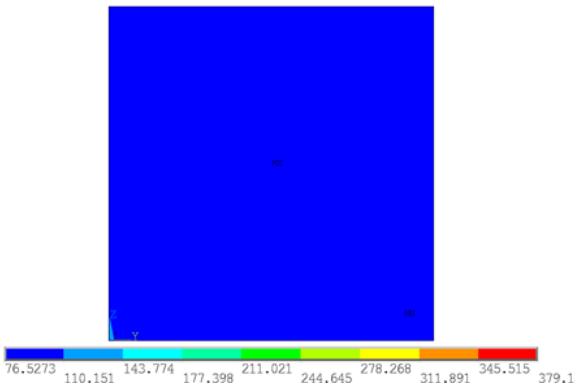

t = 67 minutes (at T_{max})

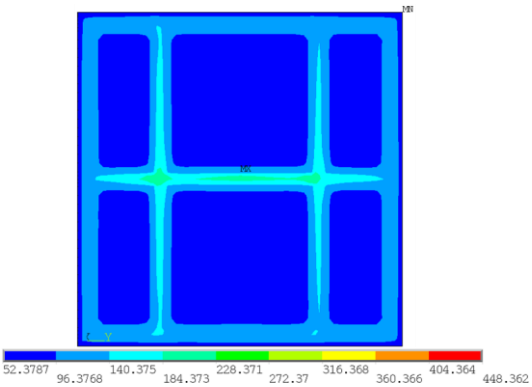

t = 70 minutes (at T_{ave})

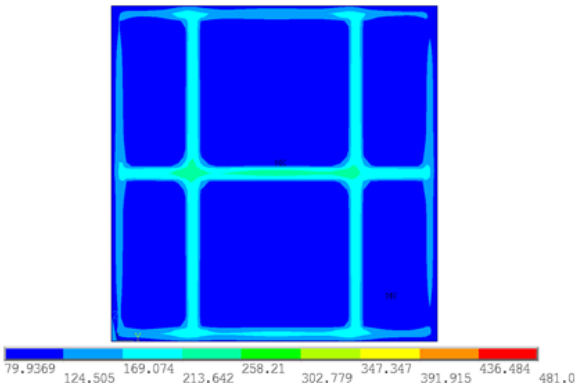

Temperatures on Steel Frame [ºC]		**Test duration:** 77 minutes
Critical temperature (T_{crit}) at T_{ave}:	524.17 ºC	(average)
Critical temperature (T_{crit}) at T_{max}:	496.54 ºC	(average)

t = 10 minutes

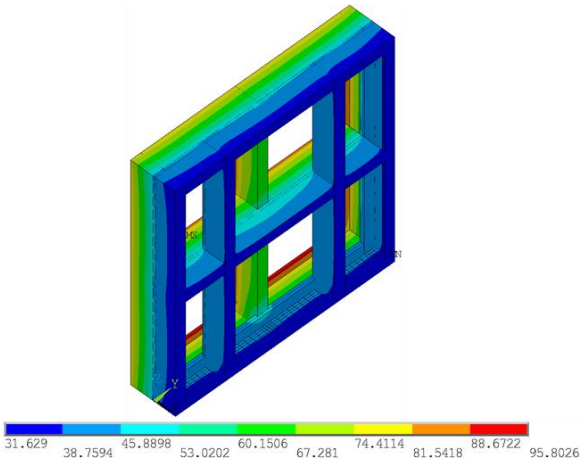

t = 20 minutes

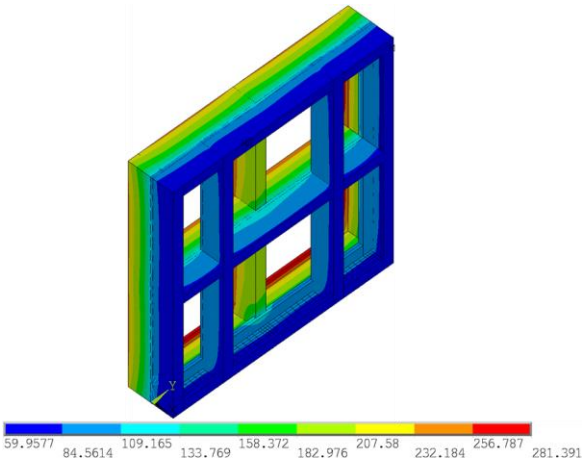

t = 30 minutes

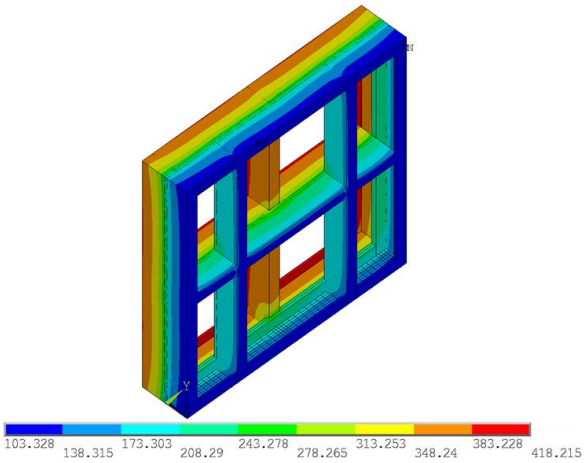

t = 40 minutes

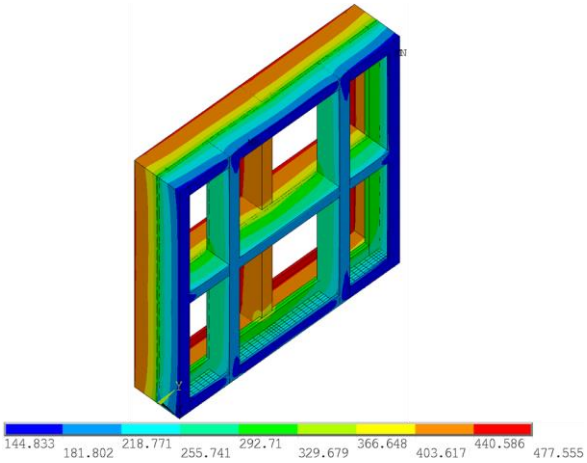

t = 50 minutes

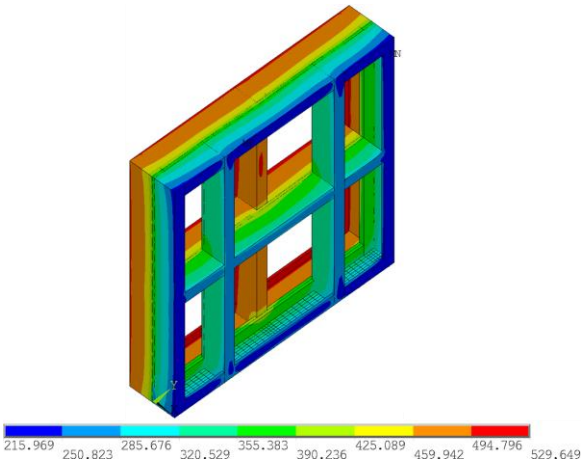

t = 60 minutes

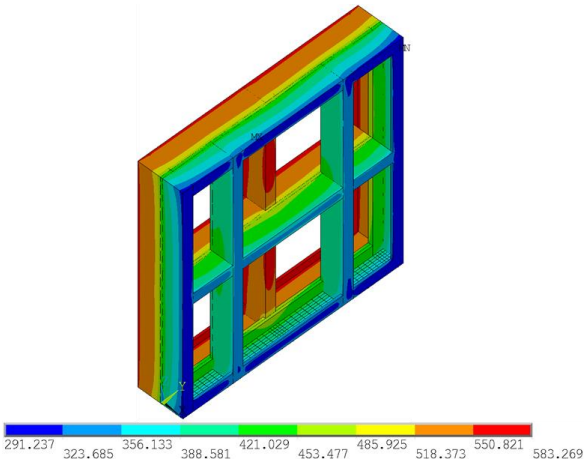

t = 67 minutes (at T_{max})

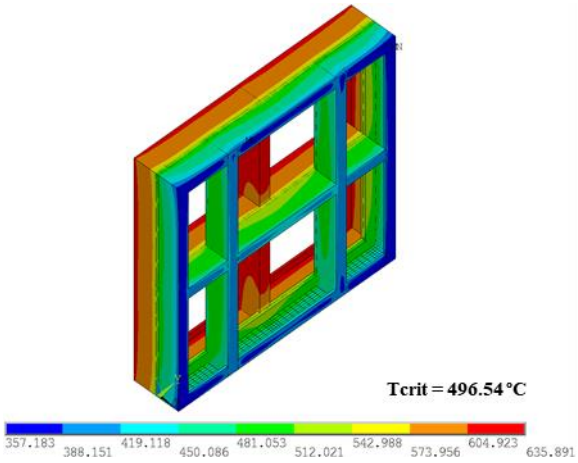

t = 70 minutes (at T_{ave})

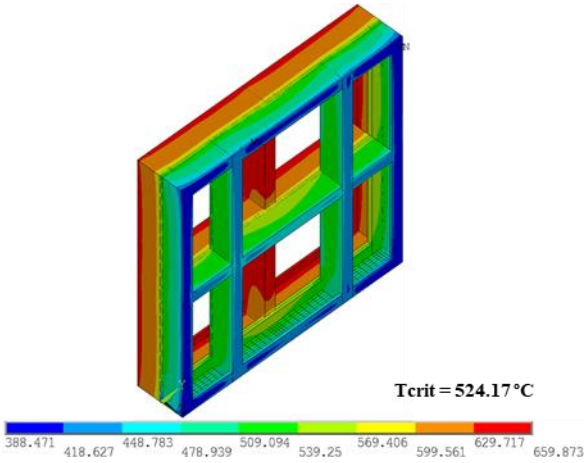

D.2 Model Specimen 2

Model Specimen 2 – Non-load-bearing Double-stud LSF Wall	**Thermal Insulation Performance**	
Gypsum plasterboard: 12.5 mm thick Type F fire-resistant	Fire resistance (T_{ave}) [minutes]:	118
Gypsum plasterboards on the exposed side: 2	Fire resistance (T_{max}) [minutes]:	115
Gypsum plasterboards on the unexposed side: 2	Fire resistance rating (FRR):	I90
Cavity insulation: -		
Air boundary layer: 1 x 10 mm		

3D Finite Element Mesh

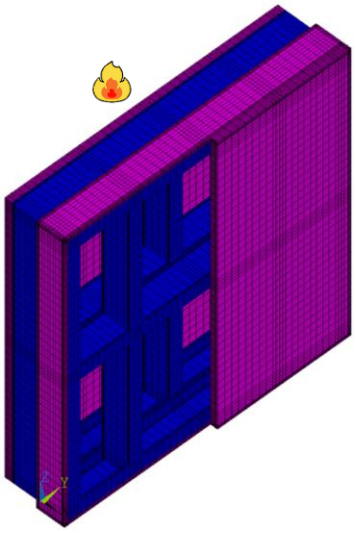

Labels:

- Gypsum plasterboard
- Steel frame
- Air layer

Steel Frame Description

- Stud/track section: C100 x 45 x 10 mm
- Steel thickness/grade: 1.0 mm / S280GD
- Connections: perfectly rigid

2D cross-section detail (z = 500 mm): *measurements in millimetres

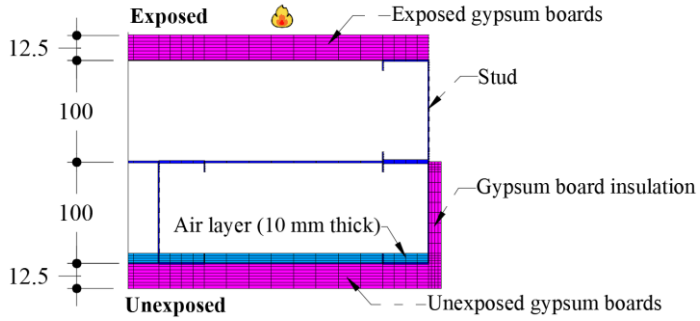

Mesh Details

Total number of nodes:	**Total number of elements:**
Steel frame – SHELL131 Finite Elements	*Gypsum plasterboard / Air layer – SOLID70 Finite Elements*

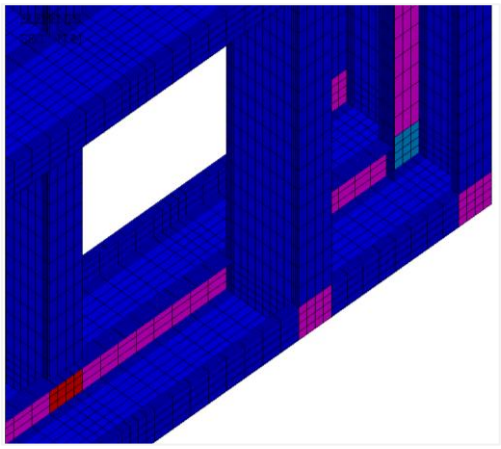

View from the unexposed side (right bottom corner)

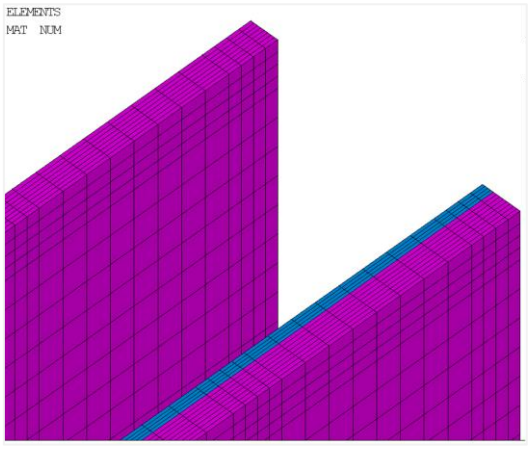

View from the unexposed side (right upper corner)

SHELL131 section thickness:

- 1 mm thick
- 2 mm thick
- 3 mm thick
- 4 mm thick

Boundary Conditions (z = 500 mm)

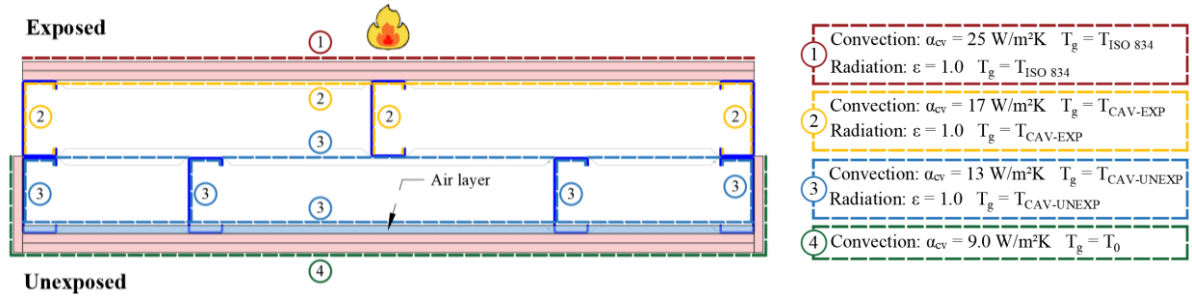

Nodal Temperatures *measurements in millimetres

Nodes:

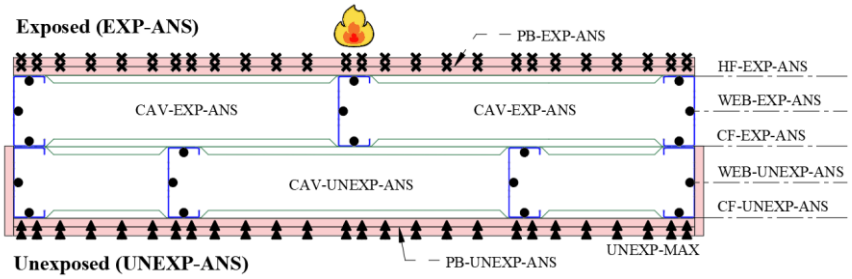

Labels:

- ✖ Nodes at 261.25 mm from the bottom of the wall
- ● Nodes at 500 mm from the bottom of the wall
- ▲ Nodes at 261.25 mm and 500 mm from the bottom of the wall

Numerical and Experimental Time-Temperature Profiles **Test duration:** 120 minutes

EXP / EXP-ANS

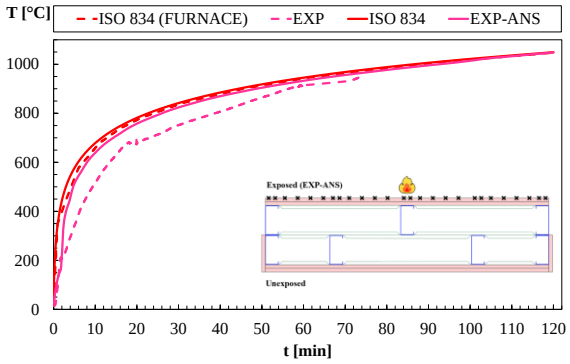

PB-EXP / PB-EXP-ANS

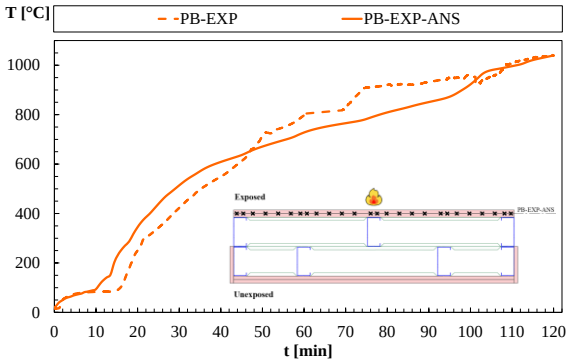

HF-EXP / HF-EXP-ANS

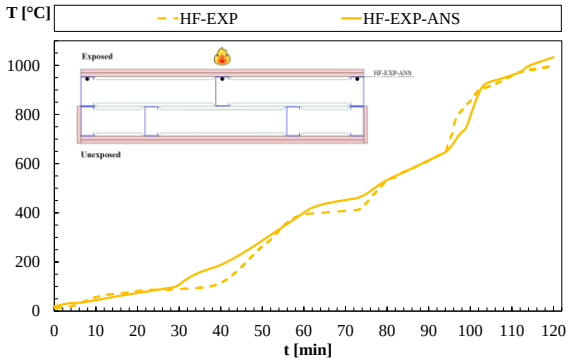

WEB-EXP / WEB-EXP-ANS

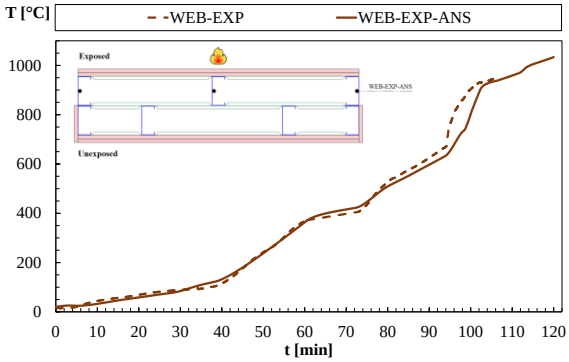

CF-EXP / CF-EXP-ANS

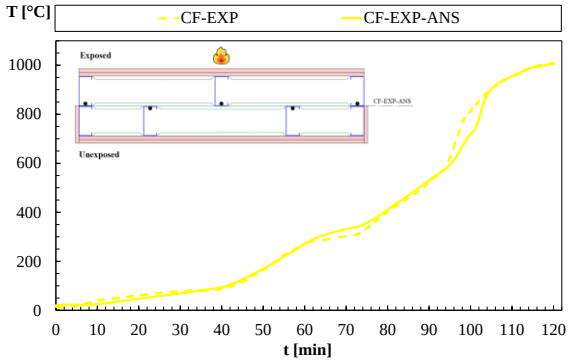

WEB-UNEXP / WEB-UNEXP-ANS

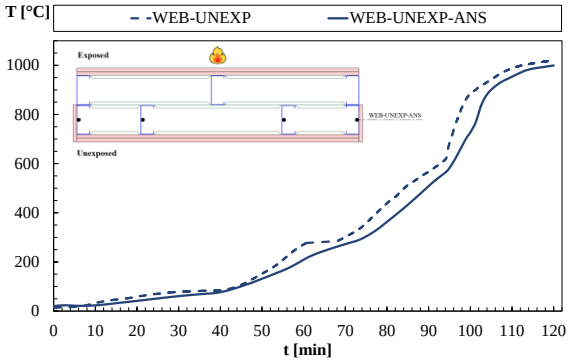

CF-UNEXP / CF-UNEXP-ANS

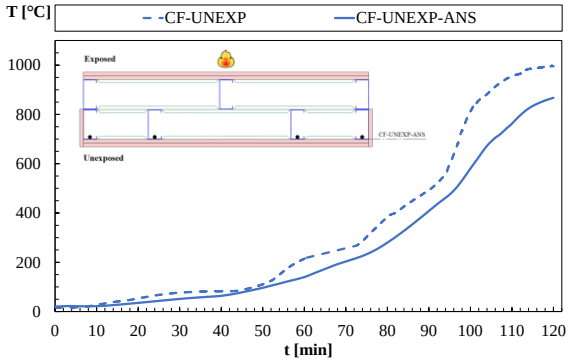

CAV-EXP / CAV-EXP-ANS

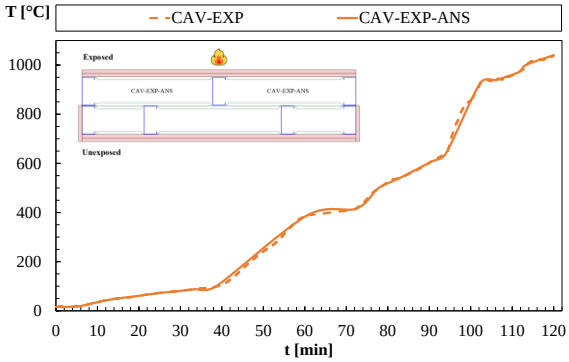

CAV-UNEXP / CAV-UNEXP-ANS

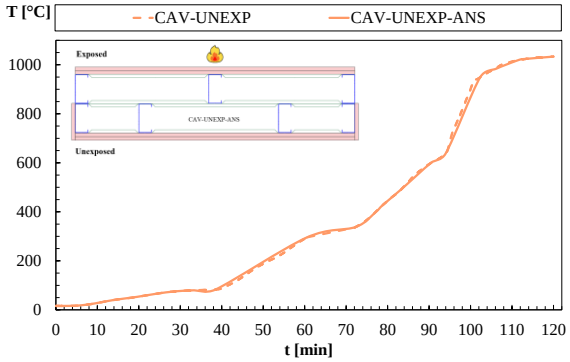

PB-UNEXP / PB-UNEXP-ANS

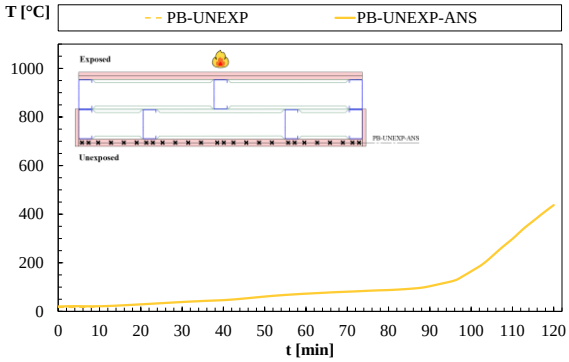

UNEXP / UNEXP-ANS

UNEXP-MAX / UNEXP-MAX-ANS

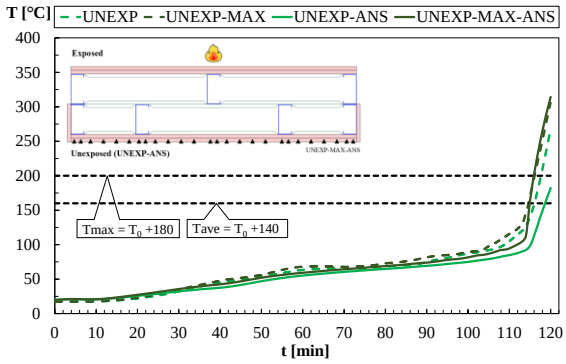

Temperatures on the Unexposed Plasterboard [ºC] **Test duration:** 120 minutes

t = 10 minutes

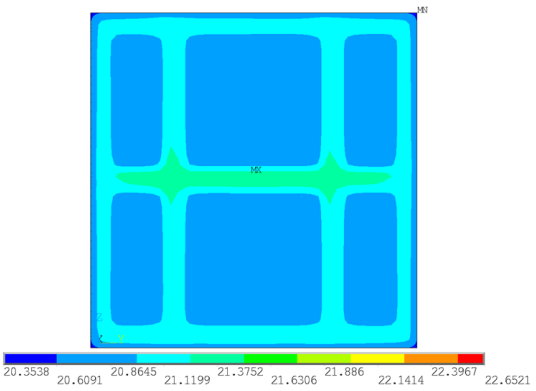

t = 20 minutes

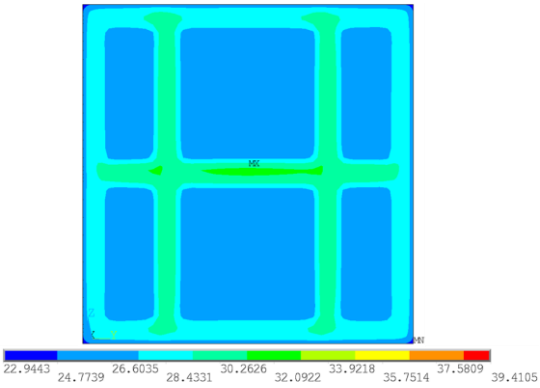

t = 30 minutes

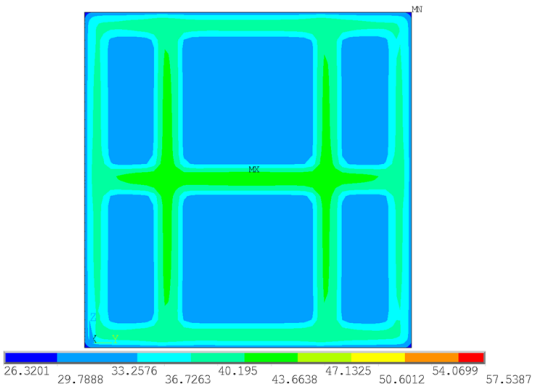

t = 40 minutes

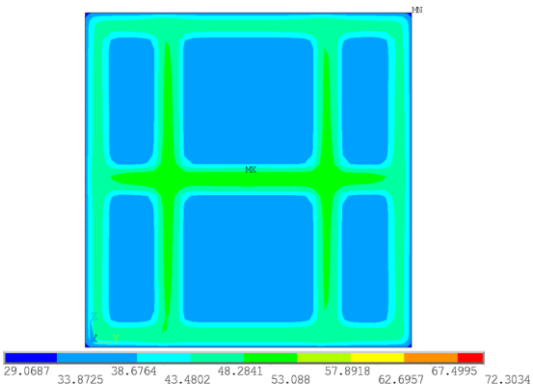

t = 50 minutes

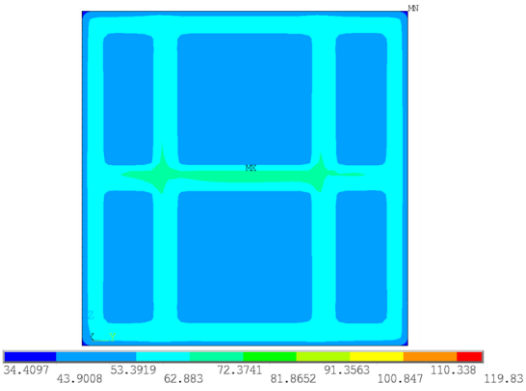

t = 60 minutes

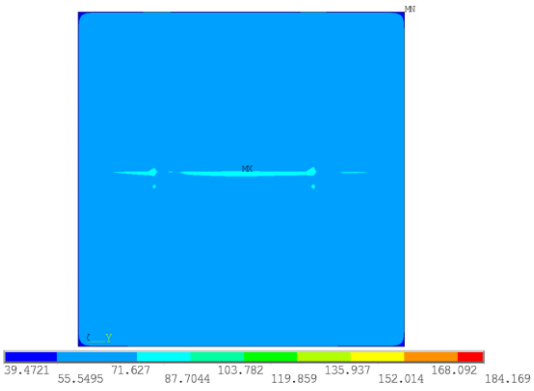

t = 70 minutes

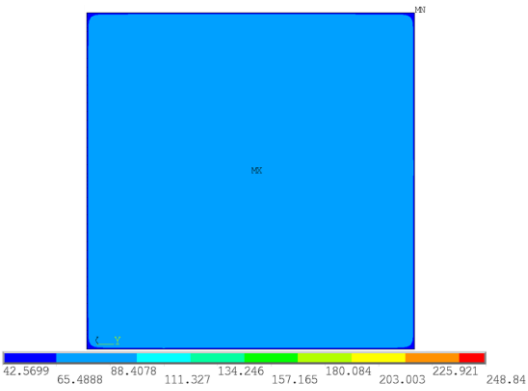

t = 80 minutes

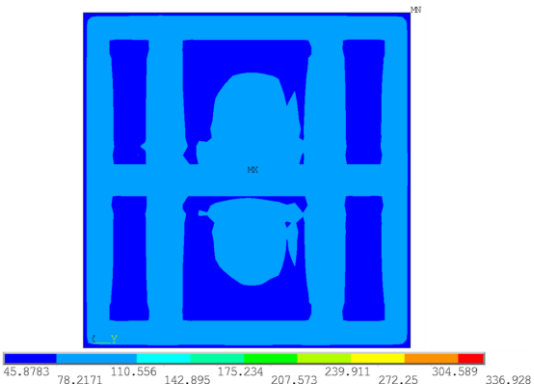

t = 90 minutes

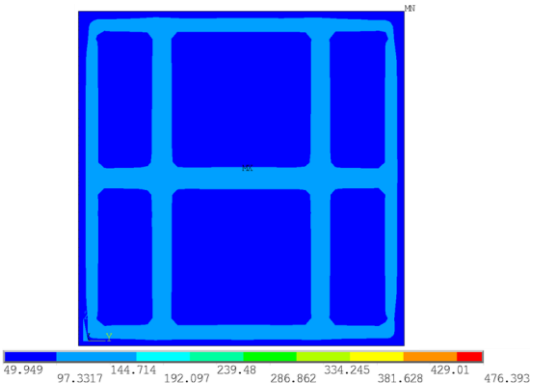

t = 100 minutes

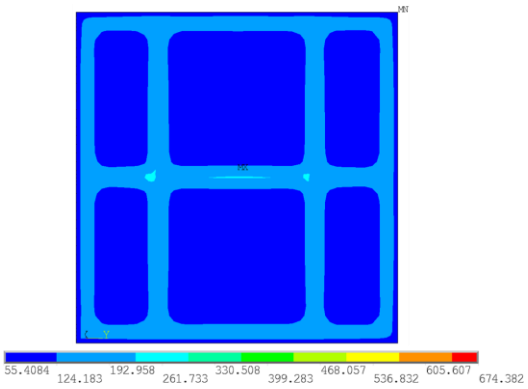

t = 110 minutes

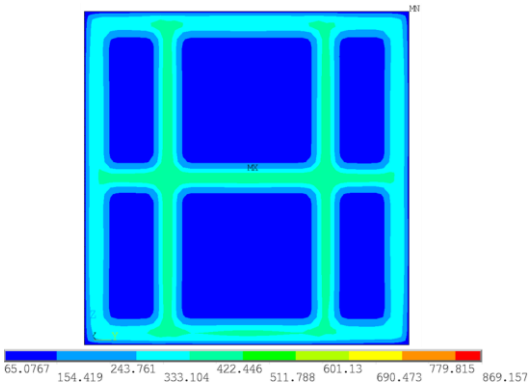

t = 115 minutes (at T_{max})

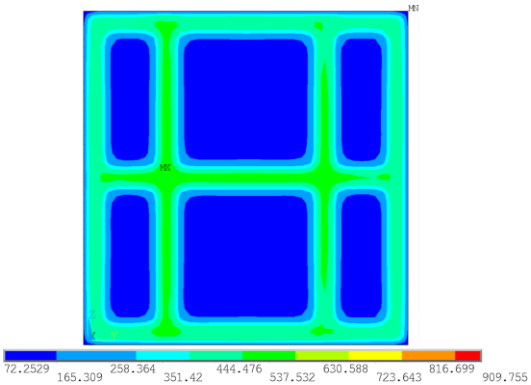

t = 118 minutes (at T_{ave})

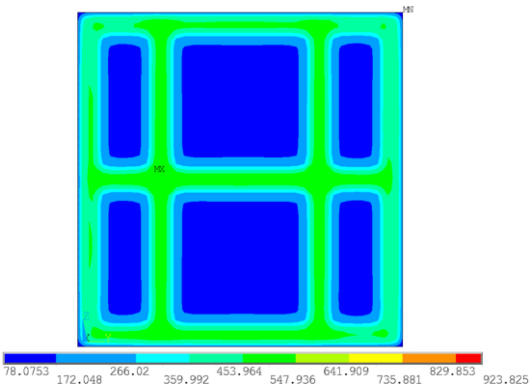

Temperatures on Steel Frame [ºC]		**Test duration:** 120 minutes
Critical temperature (T_{crit}) at T_{ave}:	917.92 ºC	(average)
Critical temperature (T_{crit}) at T_{max}:	895.32 ºC	(average)

t = 10 minutes

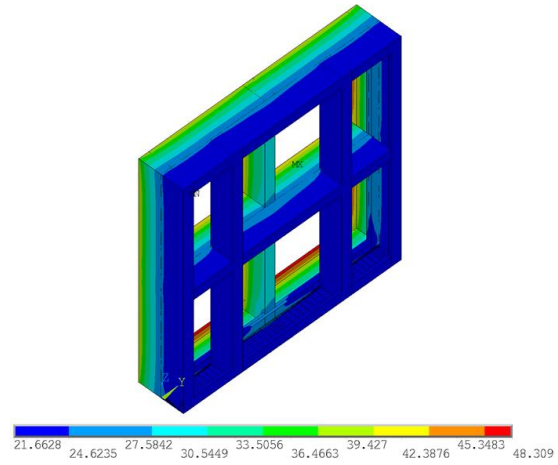

t = 20 minutes

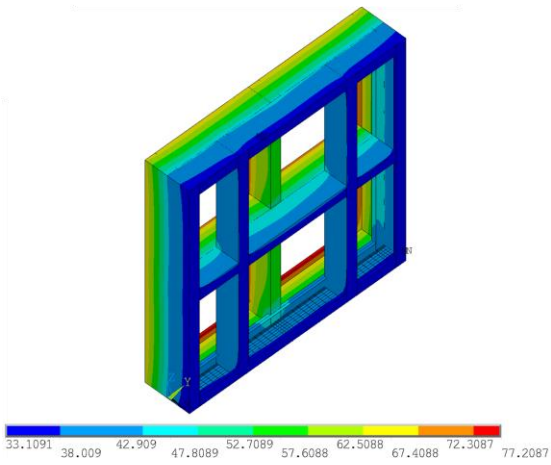

t = 30 minutes

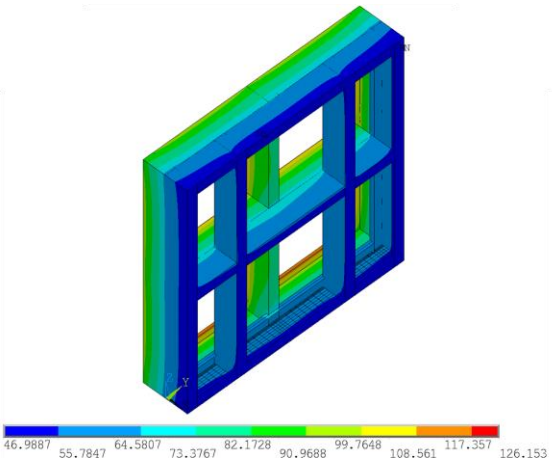

t = 40 minutes

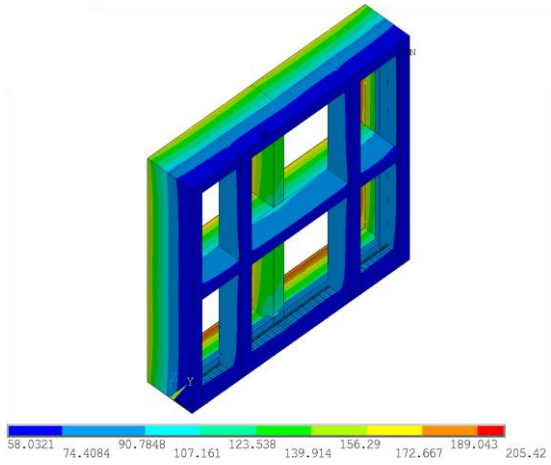

t = 50 minutes

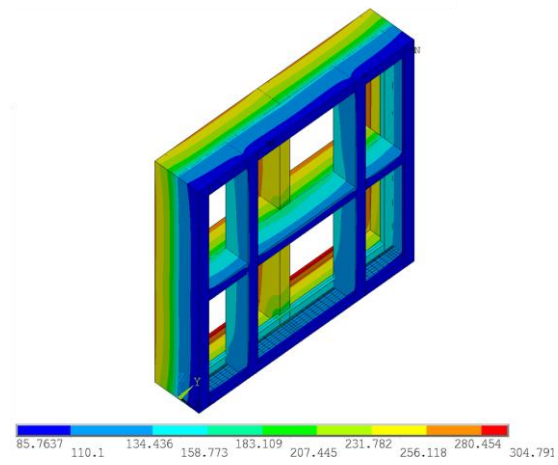

t = 60 minutes

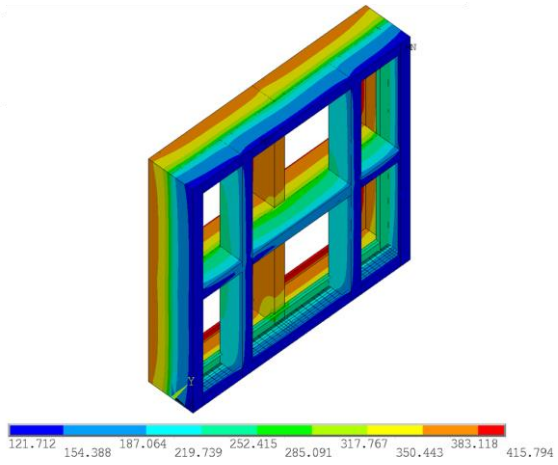

t = 70 minutes

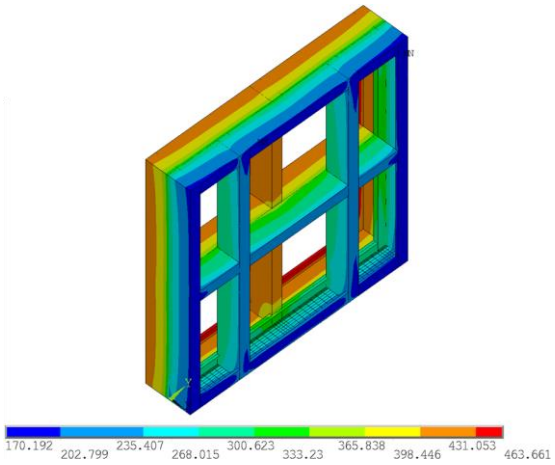

t = 80 minutes

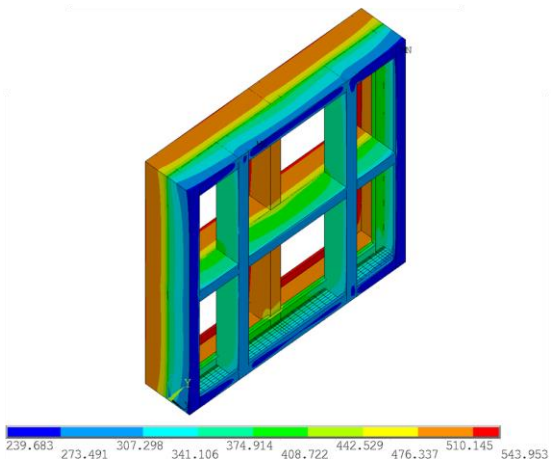

t = 90 minutes

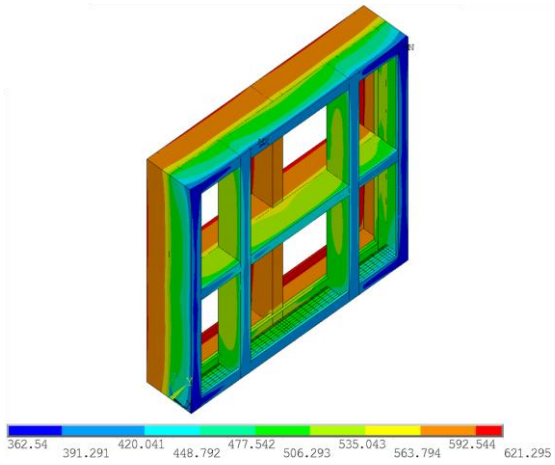

t = 100 minutes

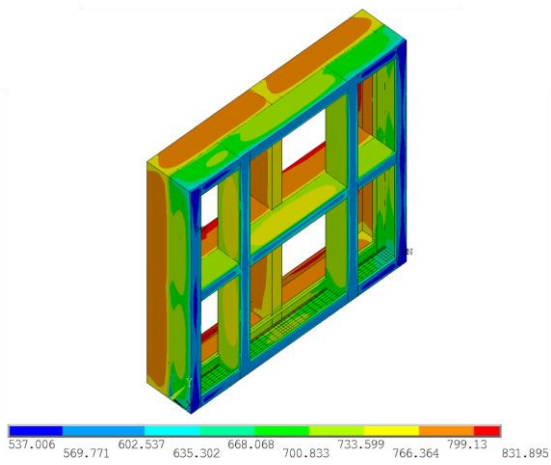

t = 110 minutes

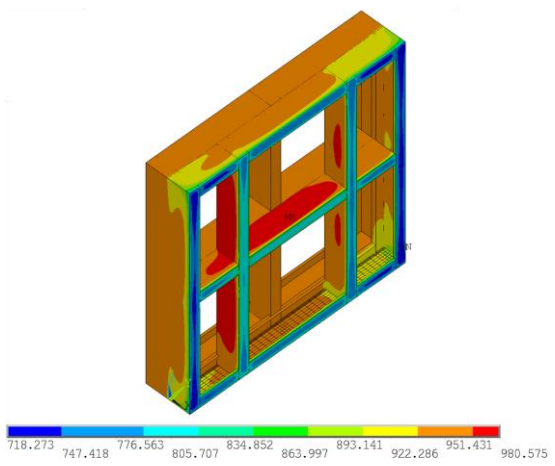

t = 115 minutes (at T_{max})

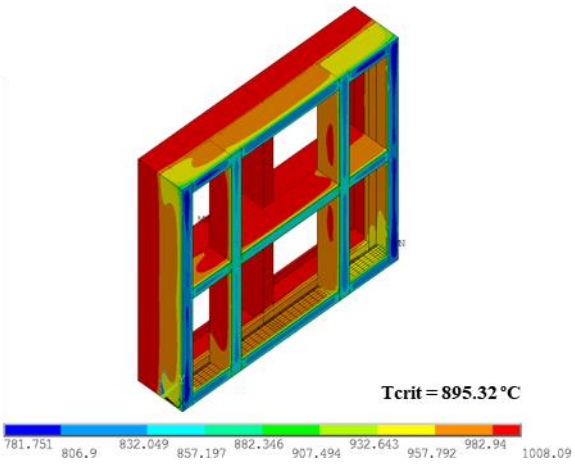

t = 118 minutes (at T_{ave})

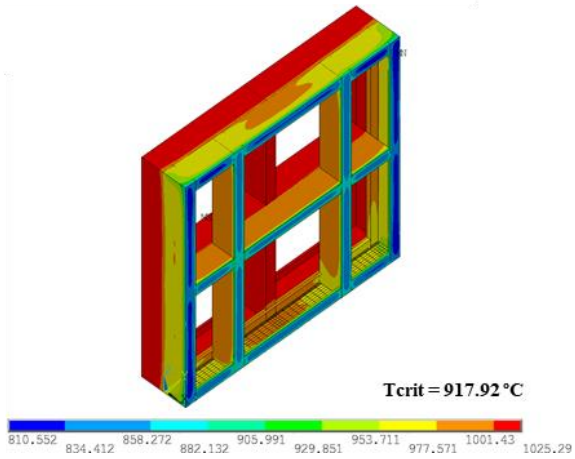

D.3 Model Specimen 3

Model Specimen 3 – Non-load-bearing Double-stud LSF Wall	**Thermal Insulation Performance**	
Gypsum plasterboard: 12.5 mm thick Type F fire-resistant	Fire resistance (T_{ave}) [minutes]:	181
Gypsum plasterboards on the exposed side: 1	Fire resistance (T_{max}) [minutes]:	172
Gypsum plasterboards on the unexposed side: 1	Fire resistance rating (FRR):	I120
Cavity insulation: 100 mm thick ceramic fibre		

3D Finite Element Mesh

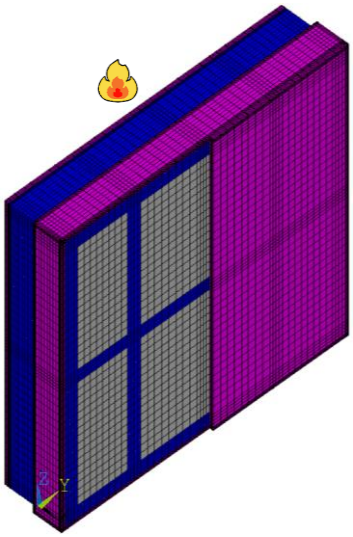

Labels:

- Gypsum plasterboard
- Steel frame
- Ceramic fibre

Steel Frame Description

- Stud/track section: C100 x 45 x 10 mm
- Steel thickness/grade: 1.0 mm / S280GD
- Connections: perfectly rigid

2D cross-section detail (z = 500 mm): *measurements in millimetres

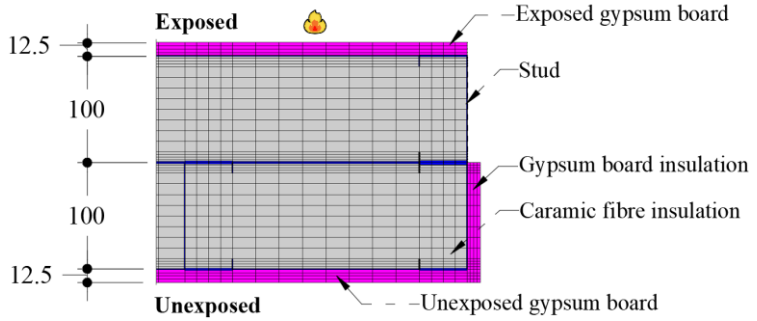

Mesh Details

Total number of nodes:	**Total number of elements:**
Steel frame – SHELL131 Finite Elements	*Gypsum plasterboard / Ceramic fibre insulation – SOLID70 Finite Elements*

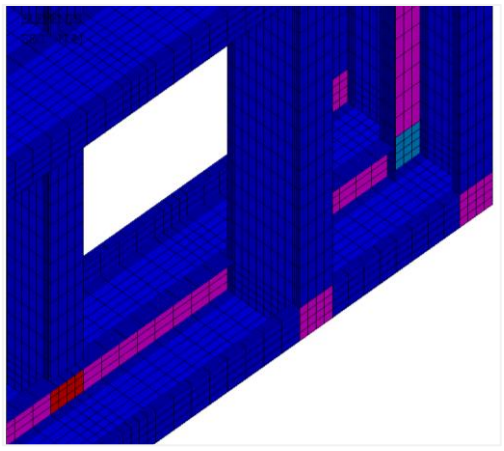

View from the unexposed side (right bottom corner)

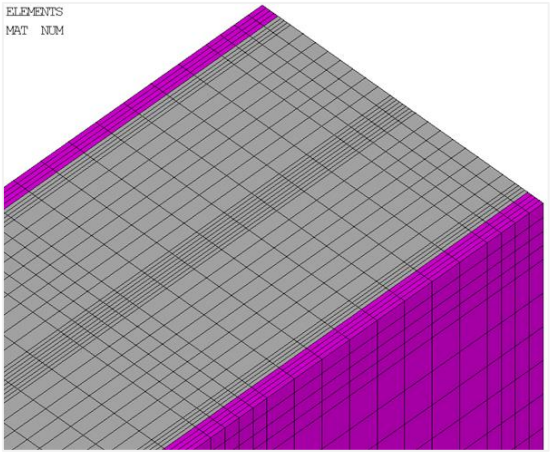

View from the unexposed side (right upper corner)

SHELL131 section thickness:

- 1 mm thick
- 2 mm thick
- 3 mm thick
- 4 mm thick

Boundary Conditions (z = 500 mm)

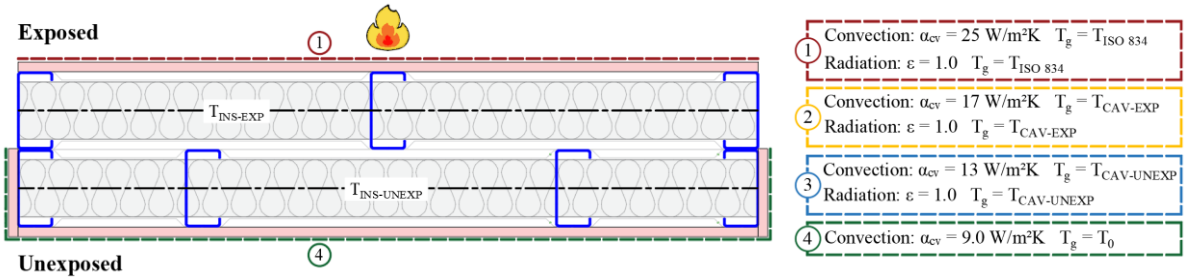

Nodal Temperatures *measurements in millimetres

Nodes:

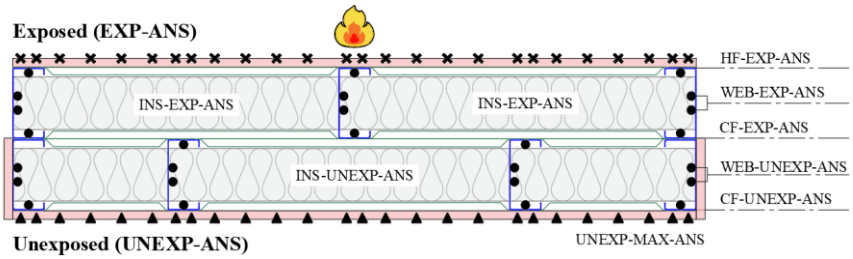

Labels:

- ✖ Nodes at 261.25 mm from the bottom of the wall
- ● Nodes at 500 mm from the bottom of the wall
- ▲ Nodes at 261.25 mm and 500 mm from the bottom of the wall

Numerical and Experimental Time-Temperature Profiles **Test duration:** 200 minutes

EXP/EXP-ANS

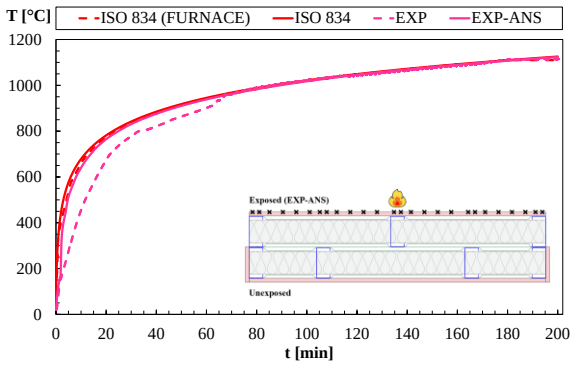

HF-EXP/HF-EXP-ANS

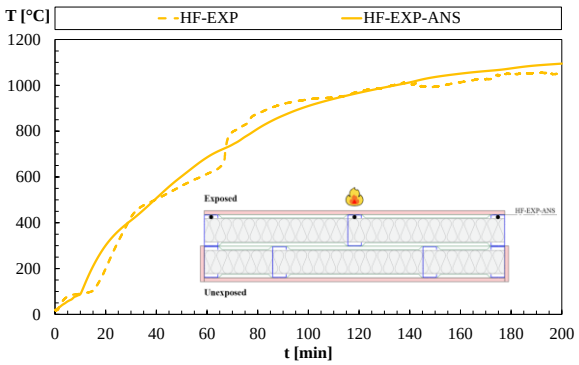

WEB-EXP/WEB-EXP-ANS

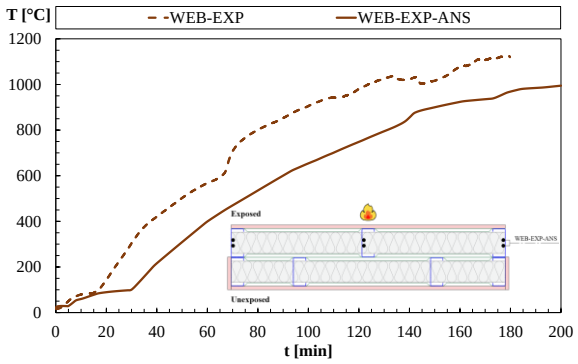

CF-EXP/CF-EXP-ANS

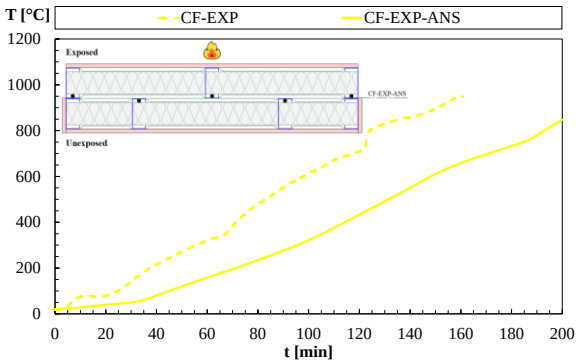

INS-EXP/INS-EXP-ANS

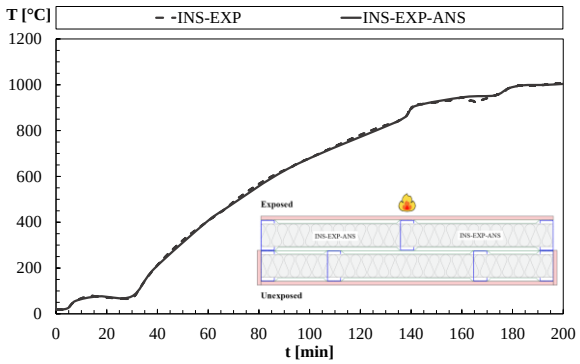

WEB-UNEXP/WEB-UNEXP-ANS

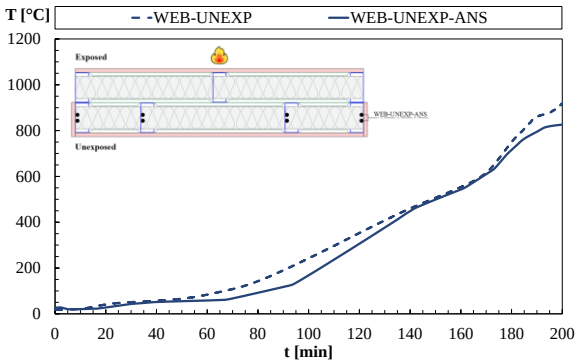

CF-UNEXP/CF-UNEXP-ANS

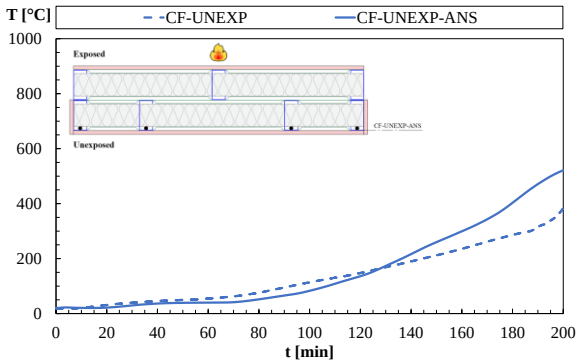

INS-UNEXP/INS-UNEXP-ANS

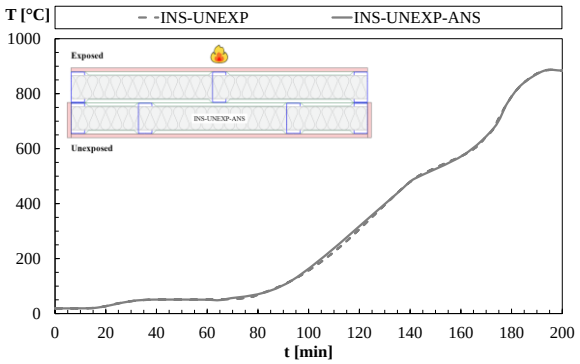

UNEXP / UNEXP-MAX

UNEXP-ANS/UNEXP-MAX-ANS

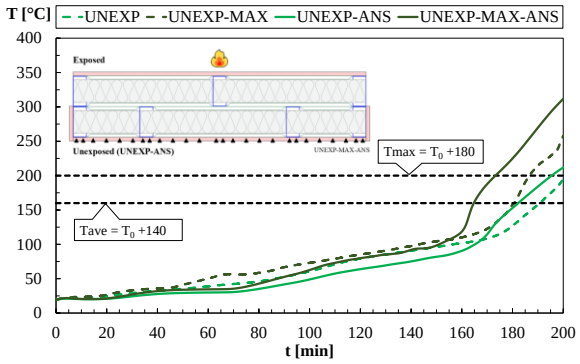

Temperatures on the Unexposed Plasterboard [ºC] **Test duration:** 200 minutes

t = 10 minutes

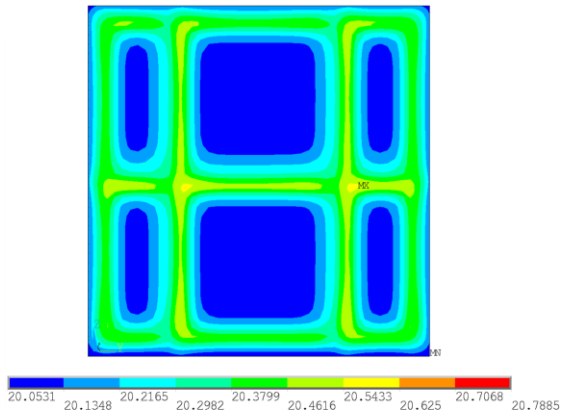

t = 20 minutes

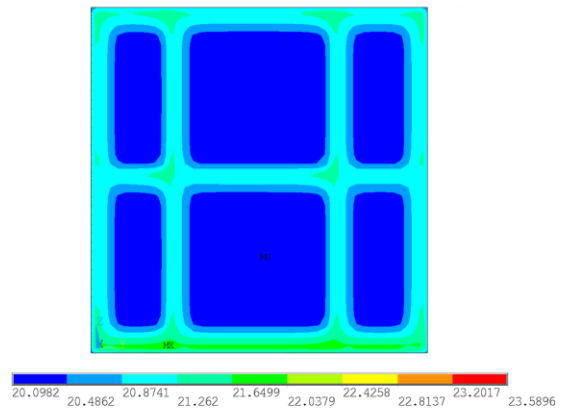

t = 30 minutes

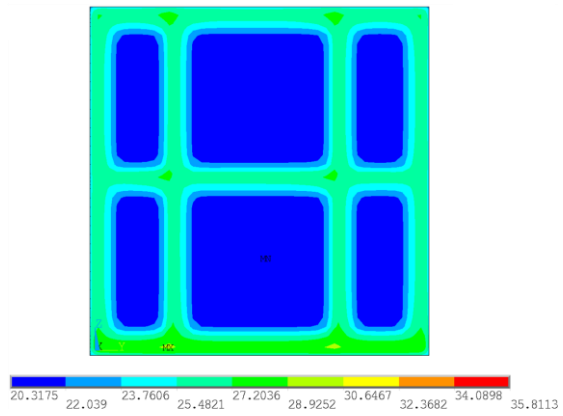

t = 40 minutes

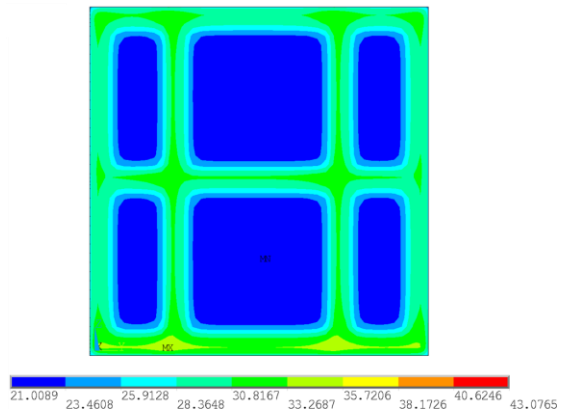

t = 50 minutes

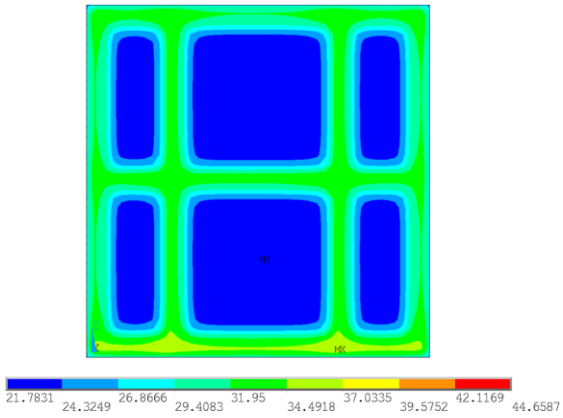

t = 60 minutes

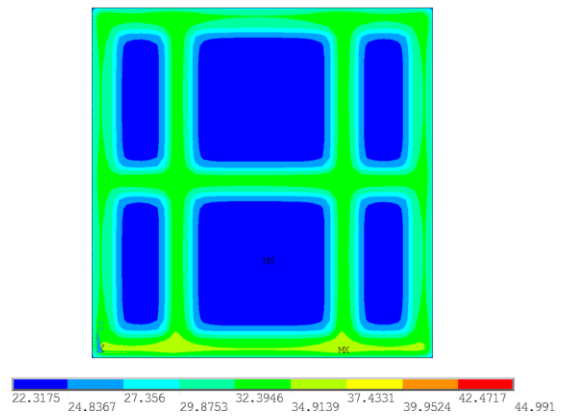

t = 70 minutes

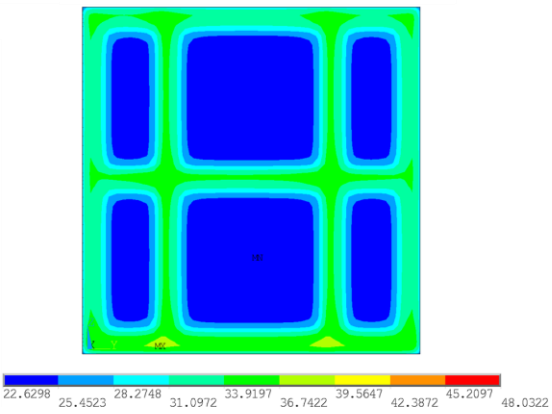

t = 80 minutes

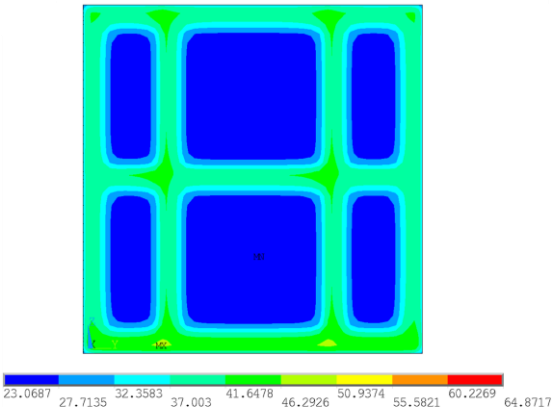

t = 90 minutes

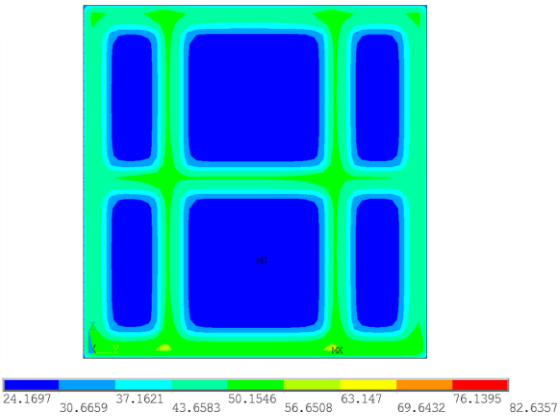

t = 100 minutes

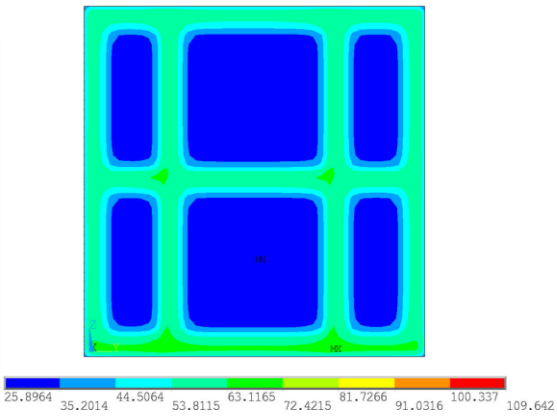

t = 110 minutes

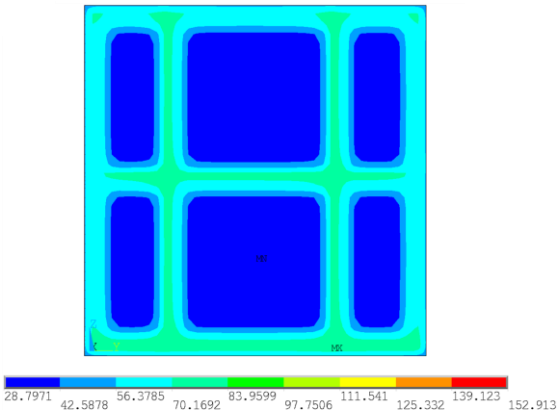

t = 120 minutes

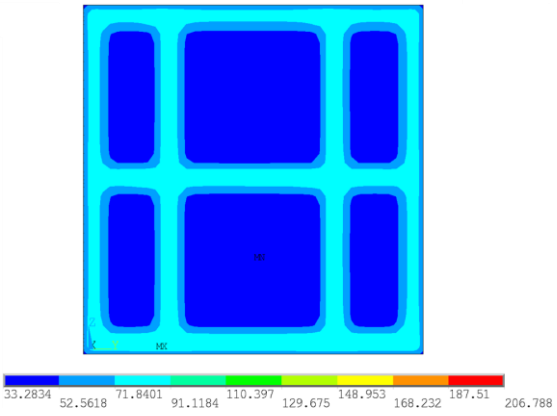

t = 130 minutes

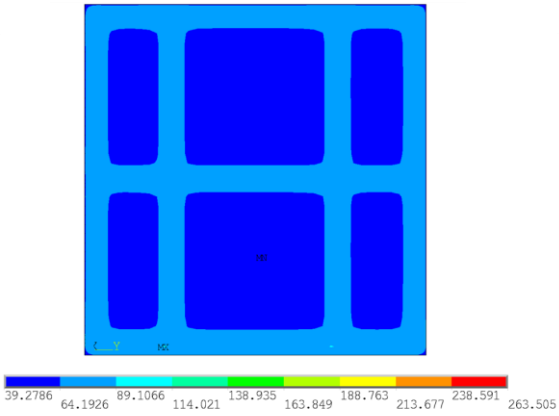

t = 140 minutes

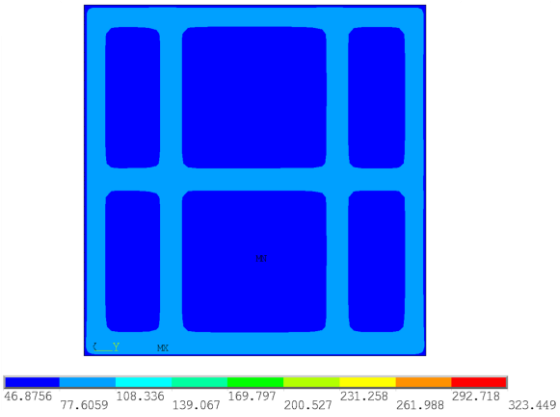

t = 150 minutes

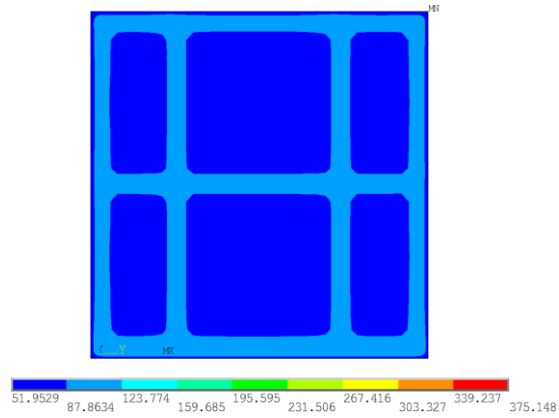

t = 160 minutes

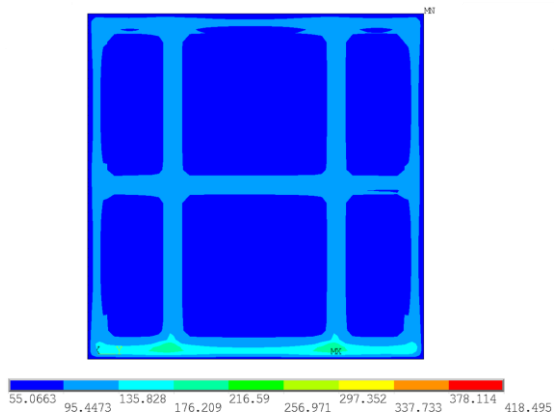

t = 170 minutes

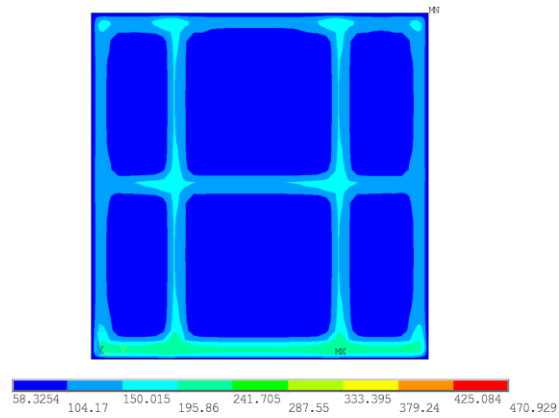

t = 172 minutes (at T_{max})

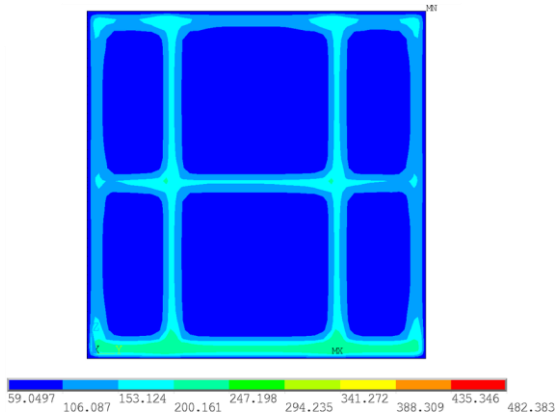

t = 180 minutes

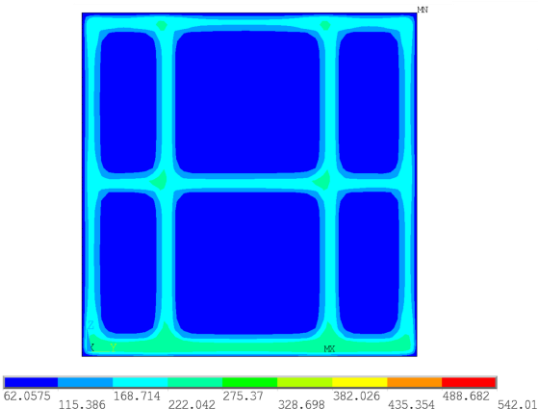

t = 181 minutes (at T_{ave})

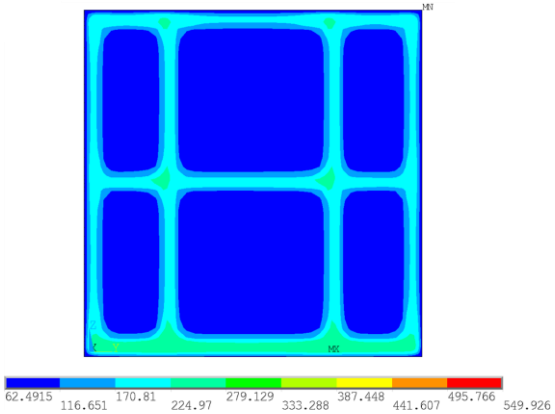

Temperatures on Steel Frame [ºC]		**Test duration:** 200 minutes
Critical temperature (T_{crit}) at T_{ave}:	707.92 ºC	(average)
Critical temperature (T_{crit}) at T_{max}:	679.00 ºC	(average)

t = 10 minutes

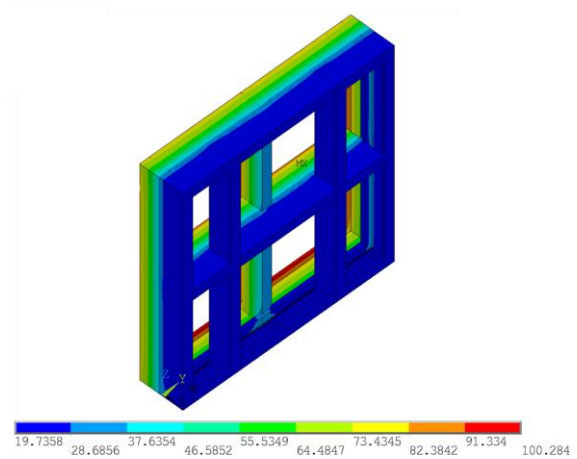

t = 20 minutes

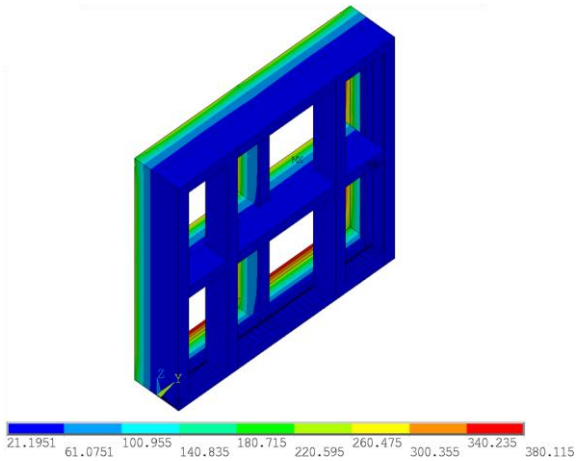

t = 30 minutes

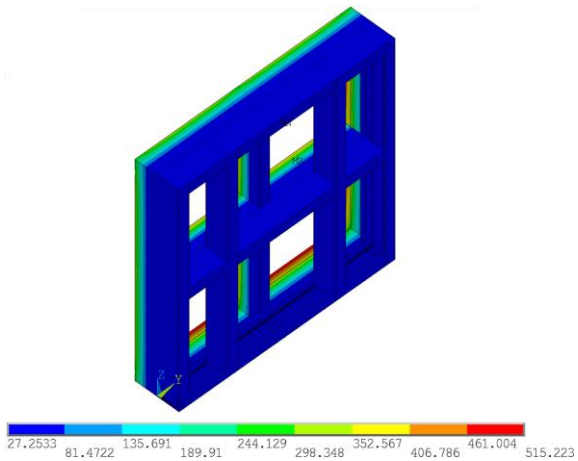

t = 40 minutes

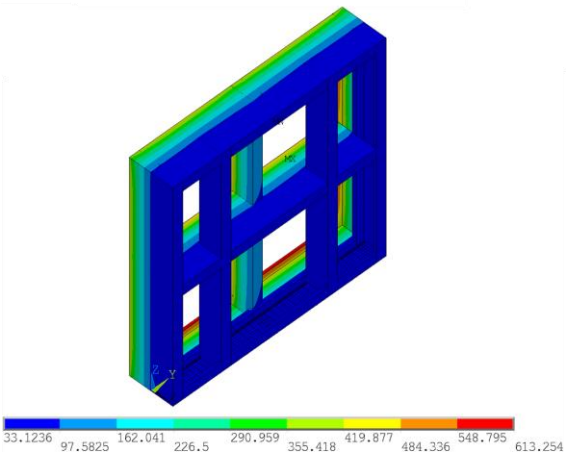

t = 50 minutes

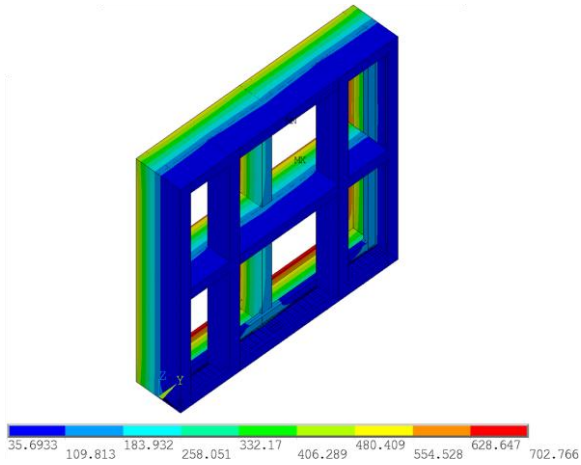

t = 60 minutes

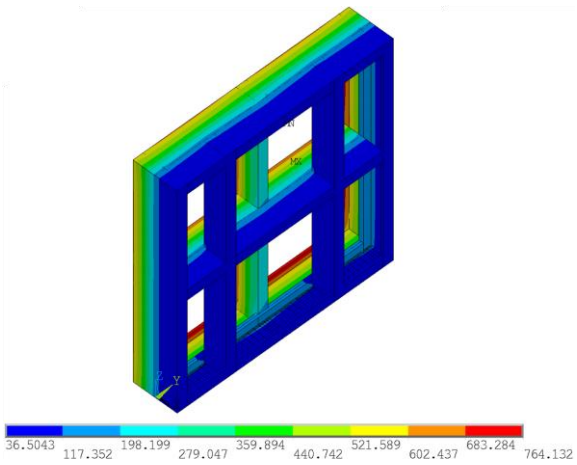

t = 70 minutes

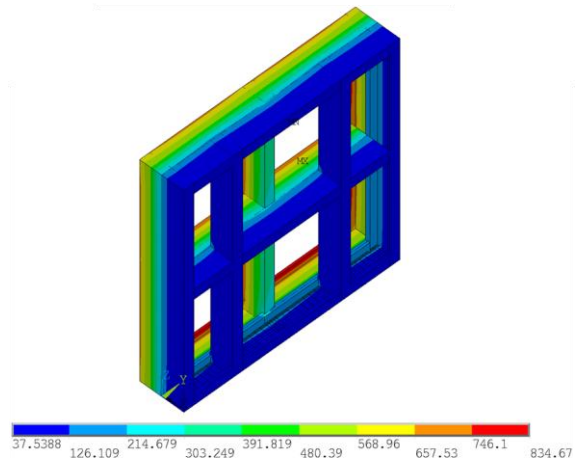

t = 80 minutes

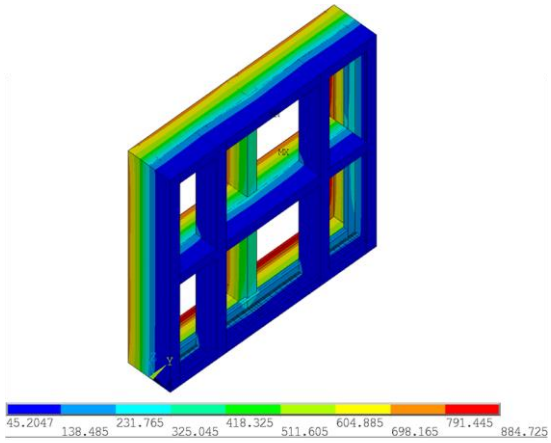

t = 90 minutes

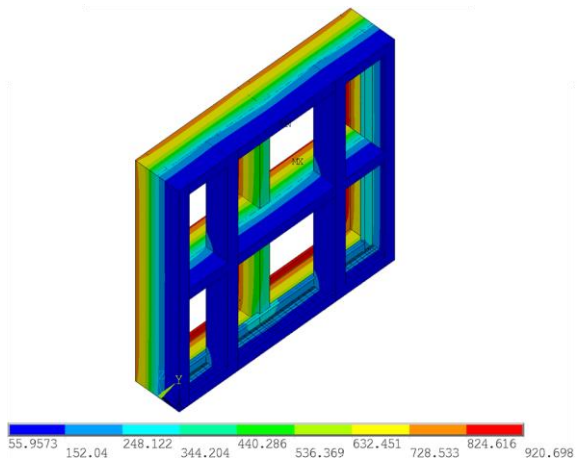

t = 100 minutes

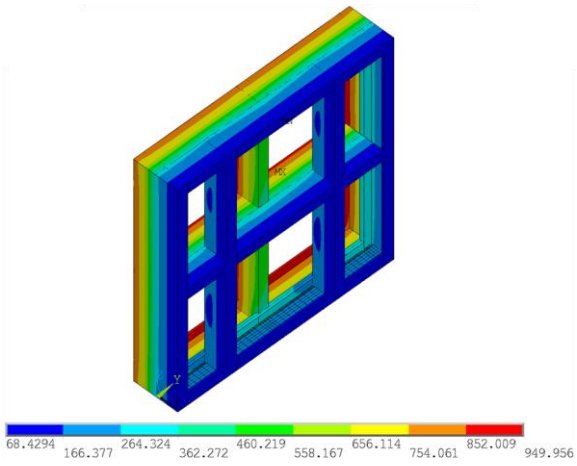

t = 110 minutes

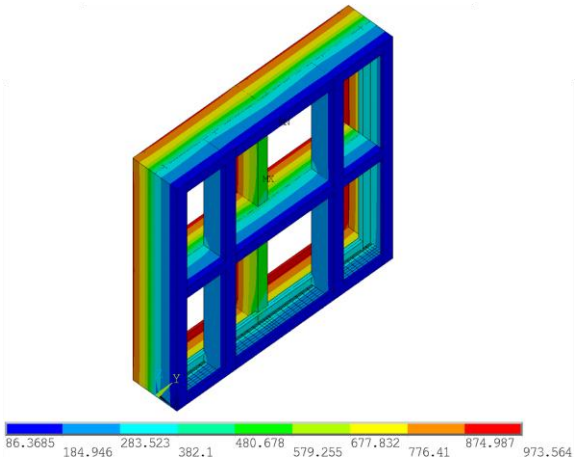

t = 120 minutes

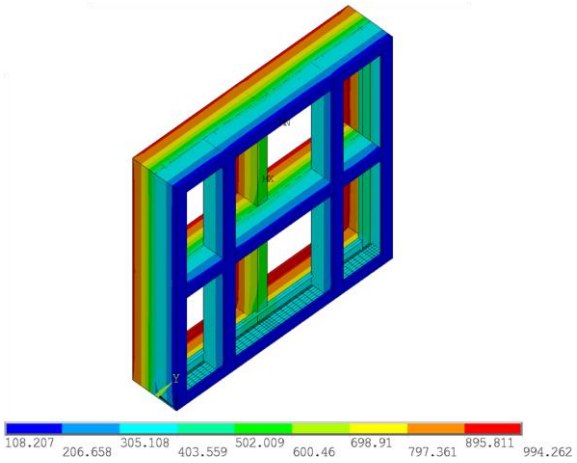

t = 130 minutes

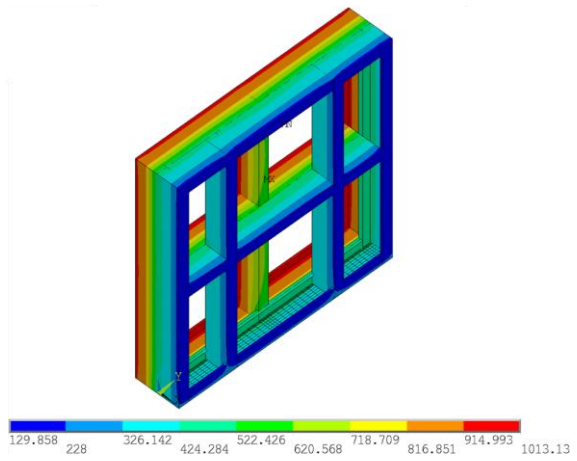

t = 140 minutes

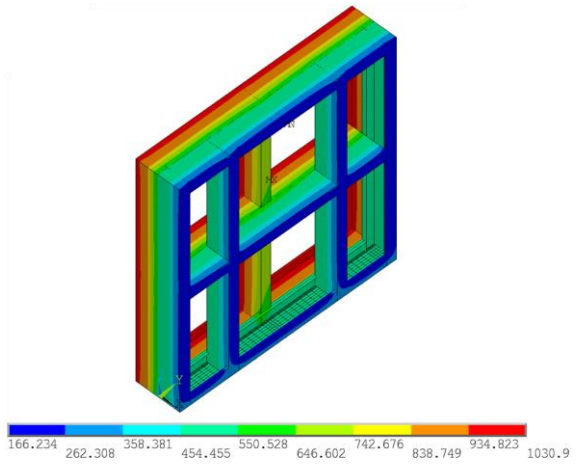

t = 150 minutes

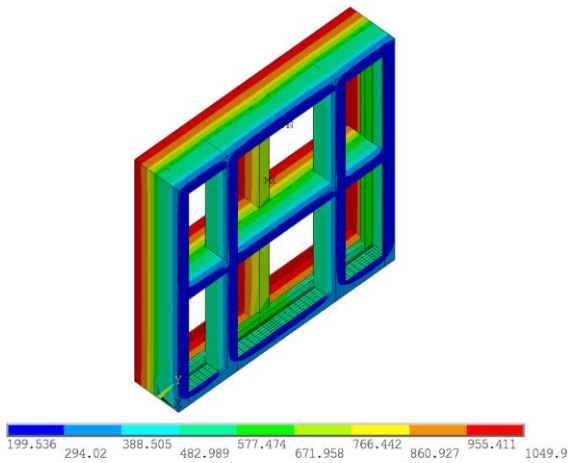

t = 160 minutes

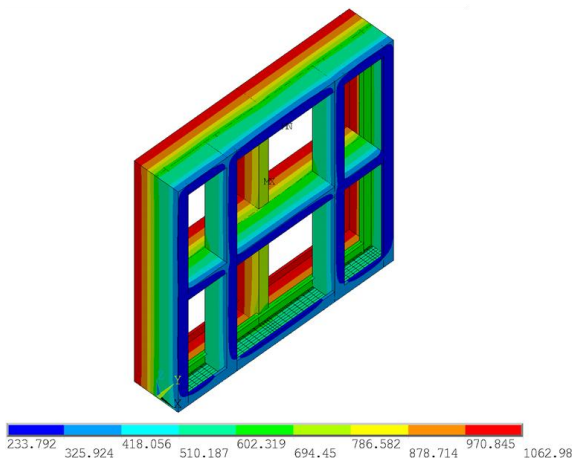

t = 170 minutes

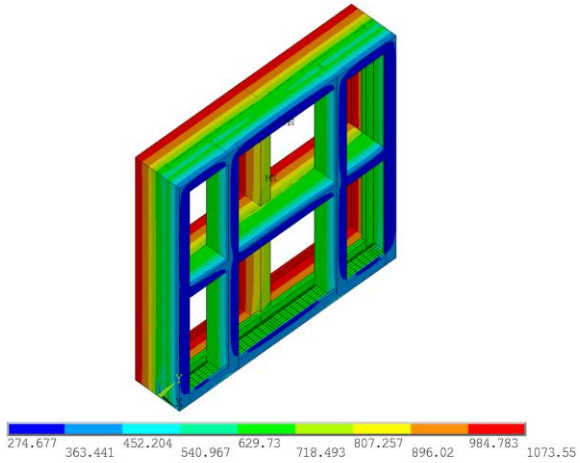

t = 172 minutes (at T_{max})

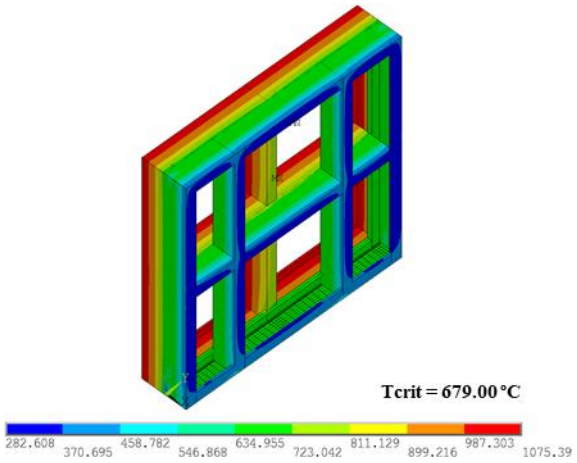

t = 180 minutes

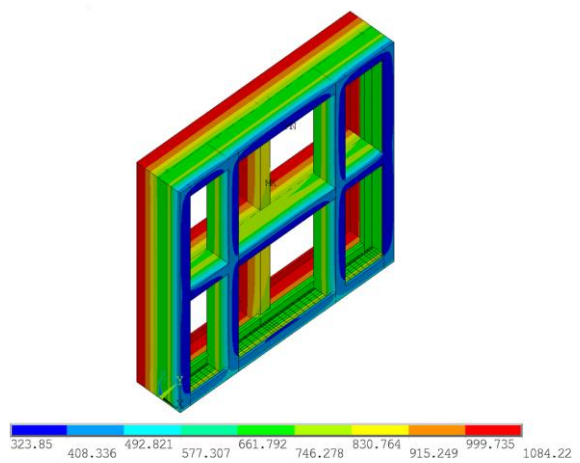

t = 181 minutes (at T_{ave})

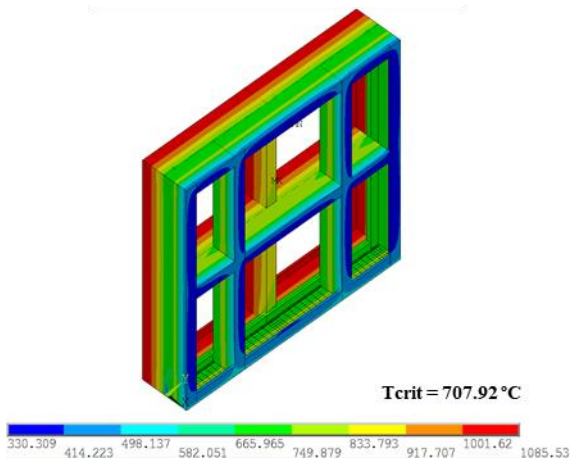

D.4 Model Specimen 4

Model Specimen 4 – Non-load-bearing Double-stud LSF Wall	**Thermal Insulation Performance**	
Gypsum plasterboard: 12.5 mm thick Type F fire-resistant	Fire resistance (T_{ave}) [min]:	122
Gypsum plasterboards on the exposed side: 1	Fire resistance (T_{max}) [min]:	112
Gypsum plasterboards on the unexposed side: 1	Fire resistance rating (FRR):	I90
Cavity insulation: 100 mm thick ceramic fibre		
Air boundary layer: 1 x 10 mm		

3D Finite Element Mesh

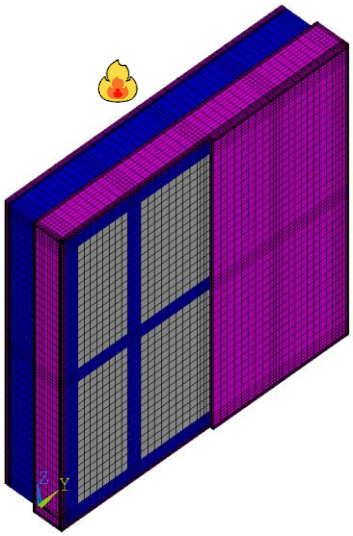

Labels:

- Gypsum plasterboard
- Steel frame
- Ceramic fibre
- Air layer

Steel Frame Description

Stud/track section: C100 x 45 x 10 mm

Steel thickness/grade: 1.0 mm / S280GD

Connections: perfectly rigid

2D cross-section details:

*measurements in millimetres

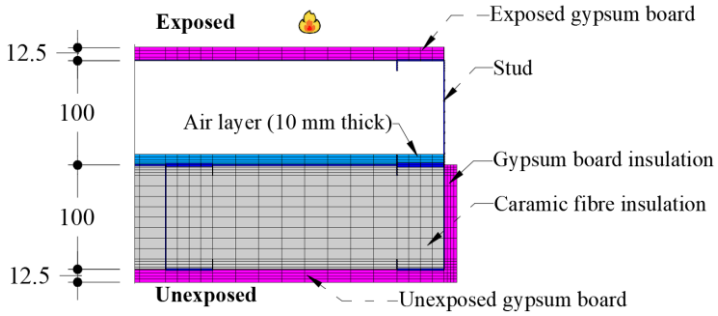

Mesh Details

Total number of nodes:	**Total number of elements:**
Steel frame – SHELL131 Finite Elements	*Gypsum plasterboard / Ceramic fibre insulation / Air layer – SOLID70 Finite Elements*

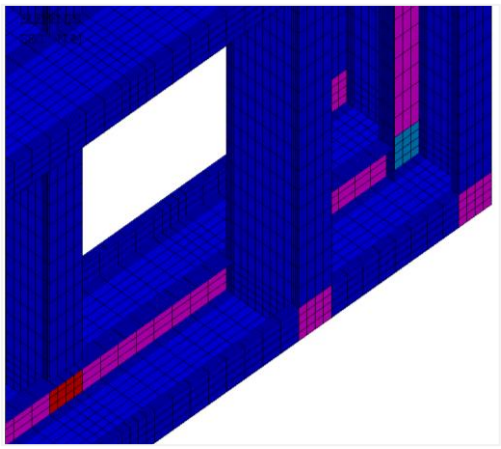

View from the unexposed side (right bottom corner)

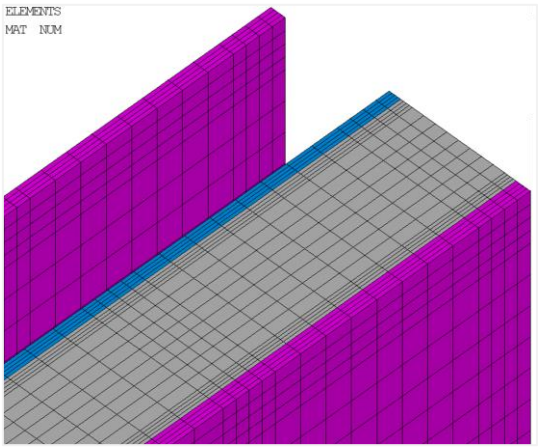

View from the unexposed side (right upper corner)

SHELL131 section thickness:

- 1 mm thick
- 2 mm thick
- 3 mm thick
- 4 mm thick

Boundary Conditions (z = 500 mm)

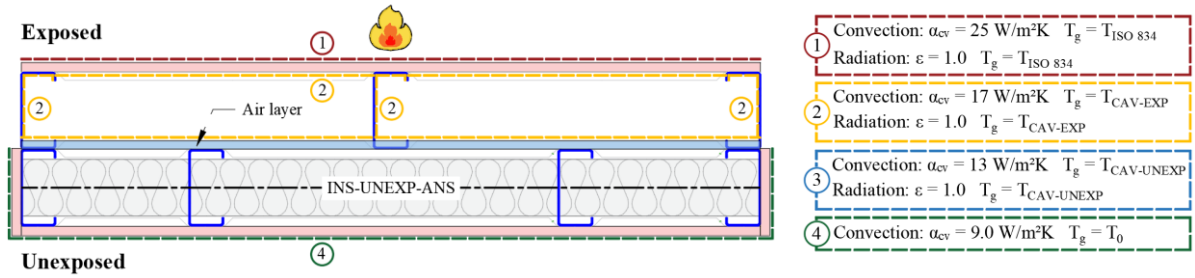

Nodal Temperatures *measurements in millimetres

Nodes:

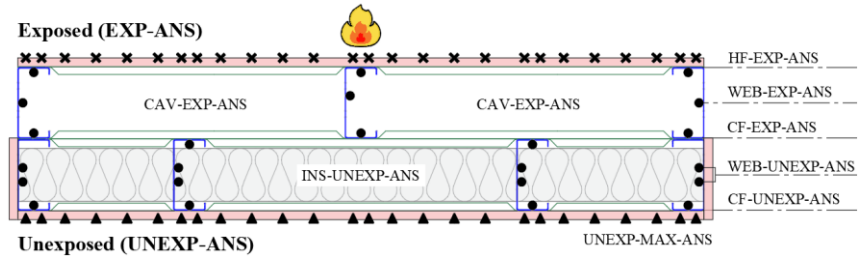

Labels:

- ✖ Nodes at 261.25 mm from the bottom of the wall
- ● Nodes at 500 mm from the bottom of the wall
- ▲ Nodes at 261.25 mm and 500 mm from the bottom of the wall

Numerical and Experimental Time-Temperature Profiles **Test length:** 150 minutes

EXP/EXP-ANS

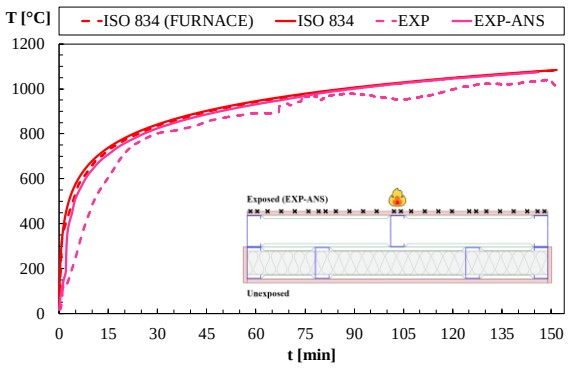

HF-EXP/HF-EXP-ANS

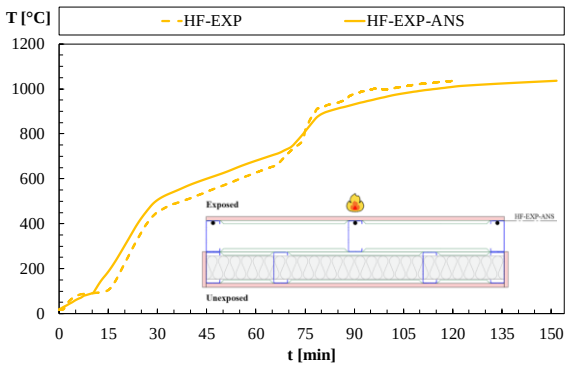

WEB-EXP/WEB-EXP-ANS

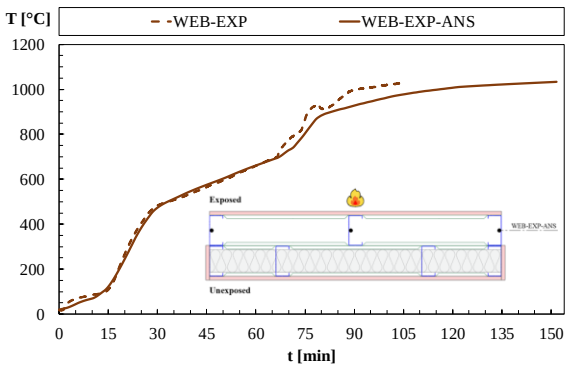

CF-EXP/CF-EXP-ANS

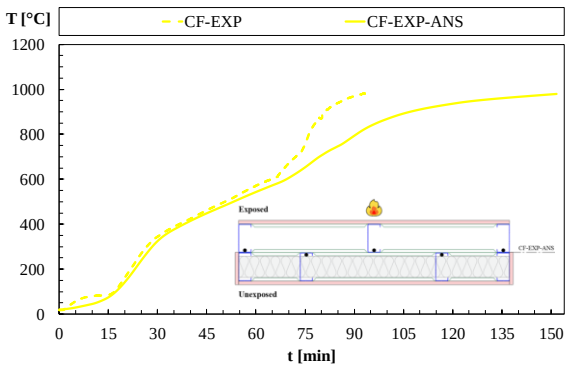

INS-UNEXP/INS-UNEXP-ANS

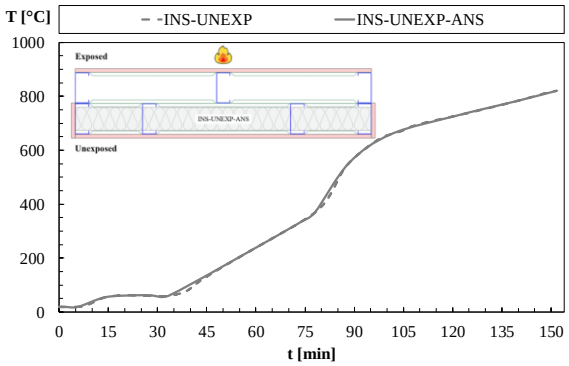

WEB-UNEXP/WEB-UNEXP-ANS

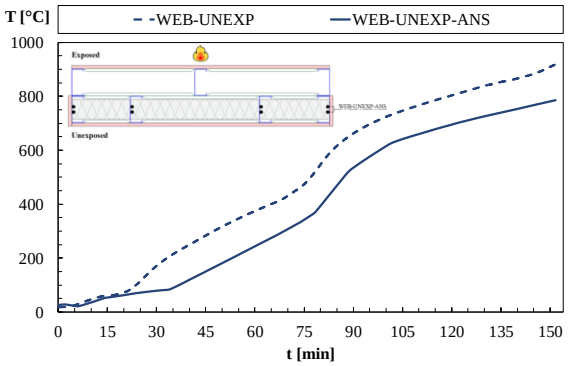

CF-UNEXP/CF-UNEXP-ANS

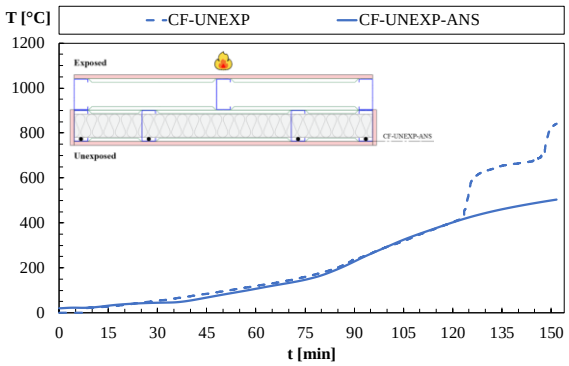

CAV-EXP/CAV-EXP-ANS

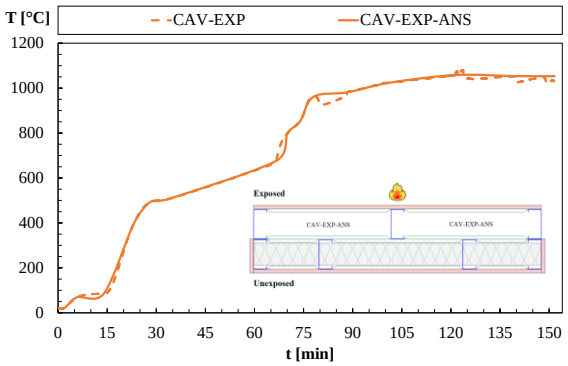

UNEXP / UNEXP-MAX

UNEXP-ANS/UNEXP-MAX-ANS

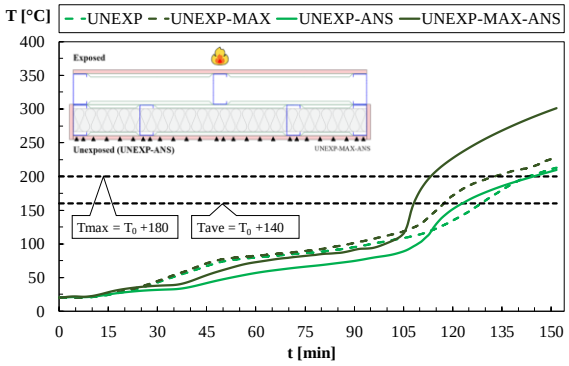

Temperatures on the Unexposed Plasterboard [ºC] **Test duration:** 150 minutes

t = 10 minutes

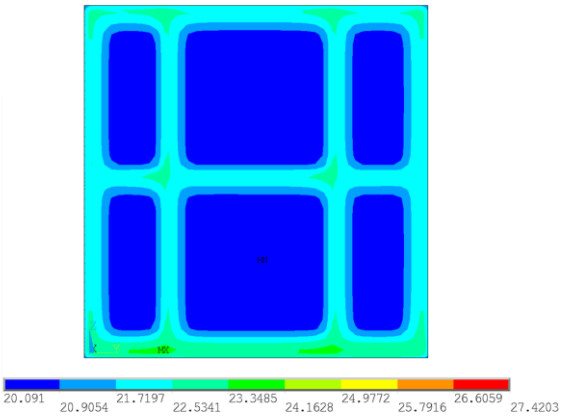

t = 20 minutes

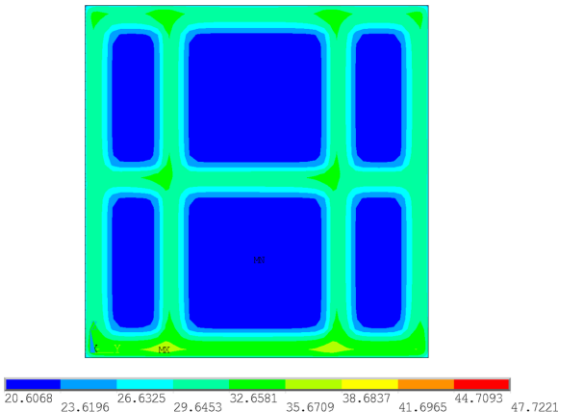

t = 30 minutes

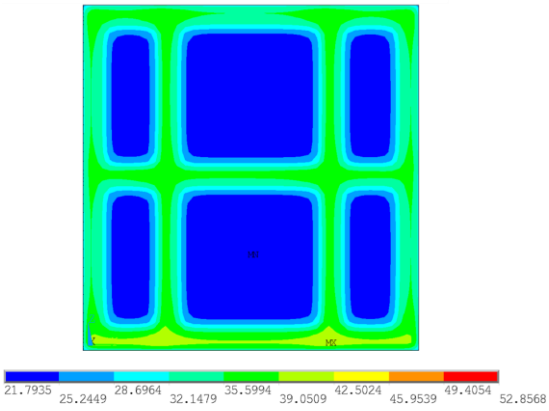

t = 40 minutes

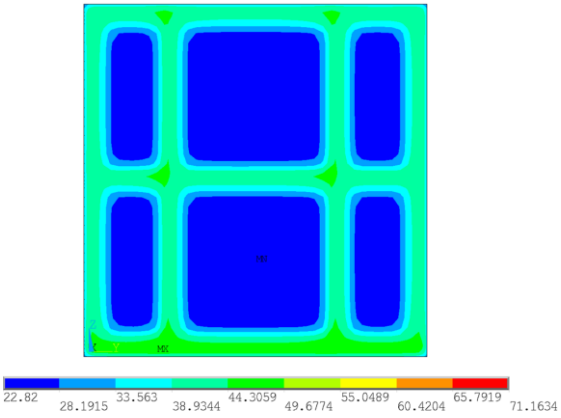

t = 50 minutes

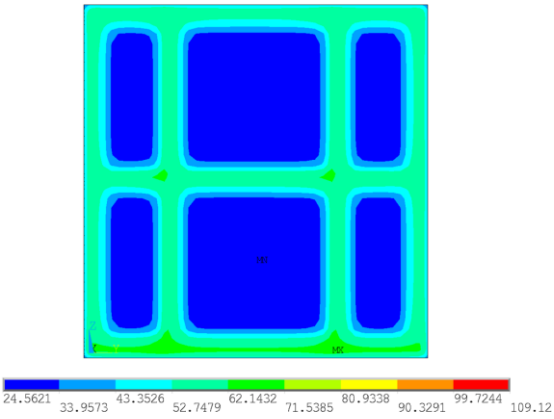

t = 60 minutes

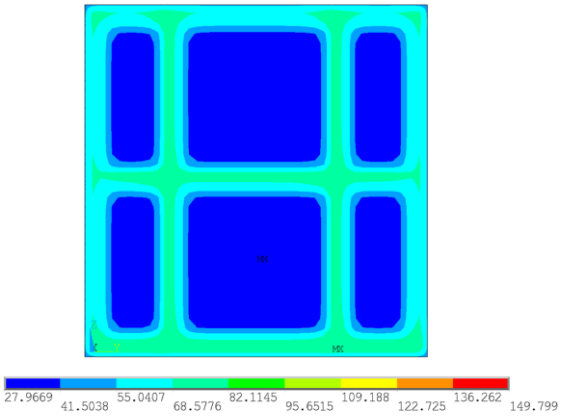

t = 70 minutes

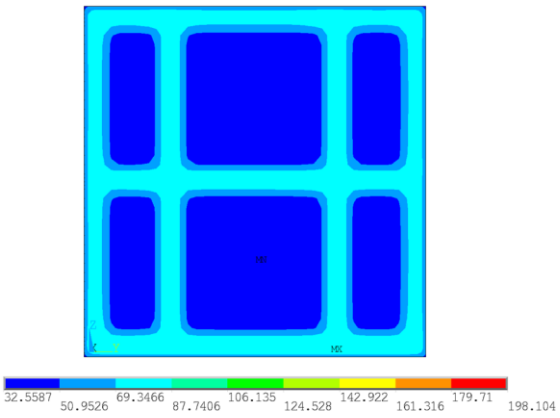

t = 80 minutes

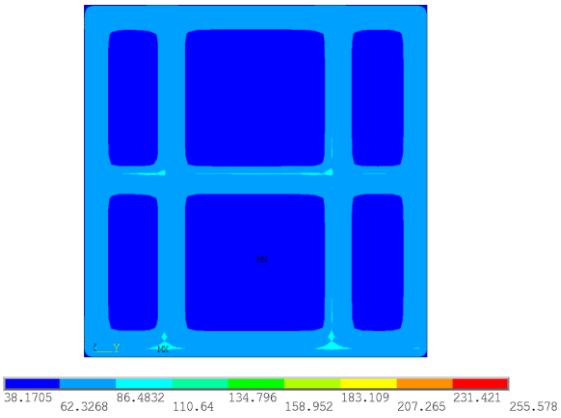

t = 90 minutes

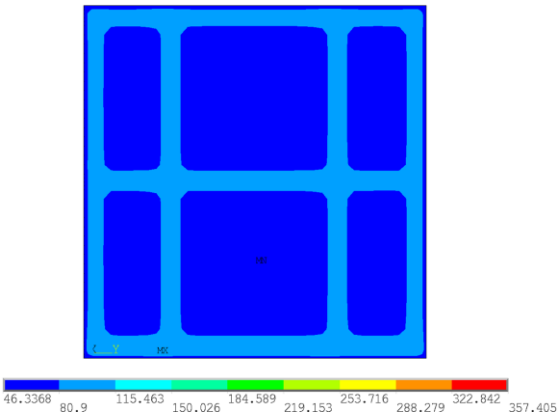

t = 100 minutes

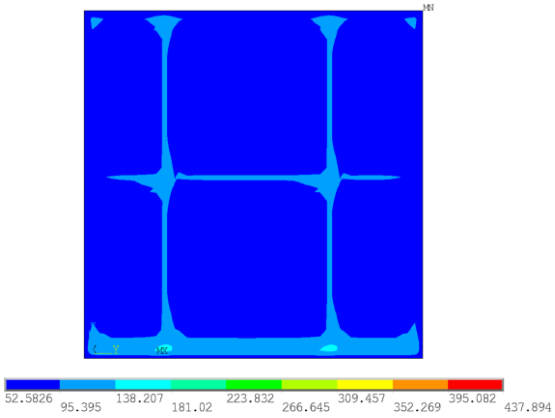

t = 110 minutes

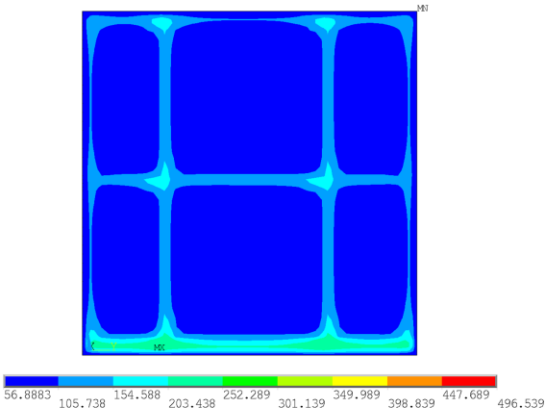

t = 112 minutes (at T_{max})

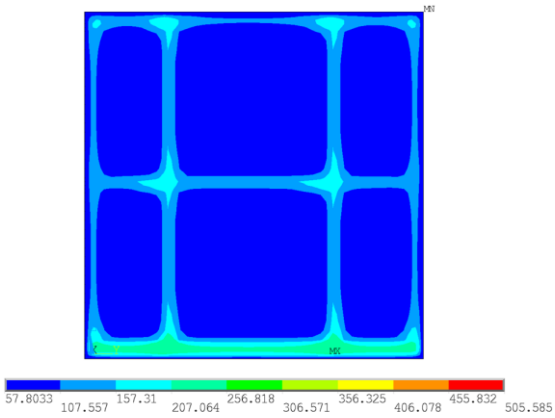

t = 120 minutes

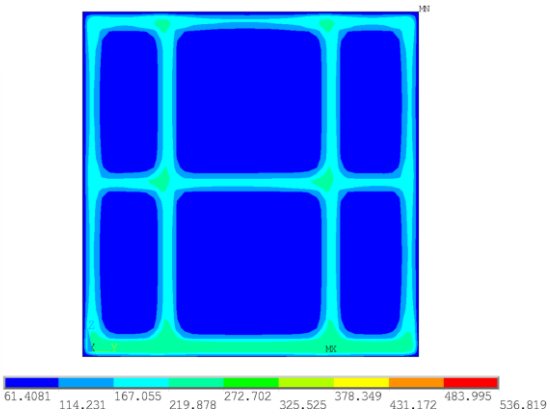

t = 122 minutes (at T_{ave})

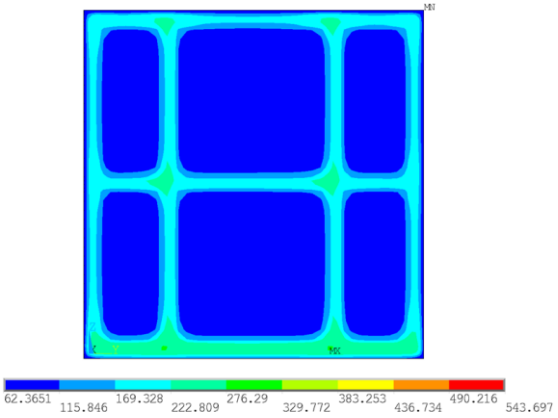

Temperatures on Steel Frame [ºC]		**Test duration:** 150 minutes
Critical temperature (T_{crit}) at T_{ave}:	675.04 ºC	(average)
Critical temperature (T_{crit}) at T_{max}:	644.16 ºC	(average)

t = 10 minutes

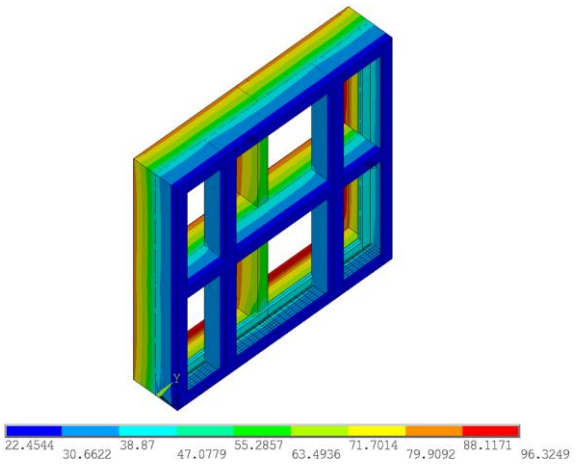

t = 20 minutes

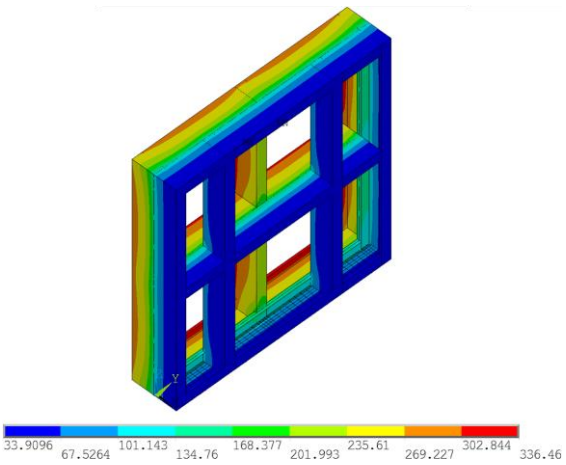

t = 30 minutes

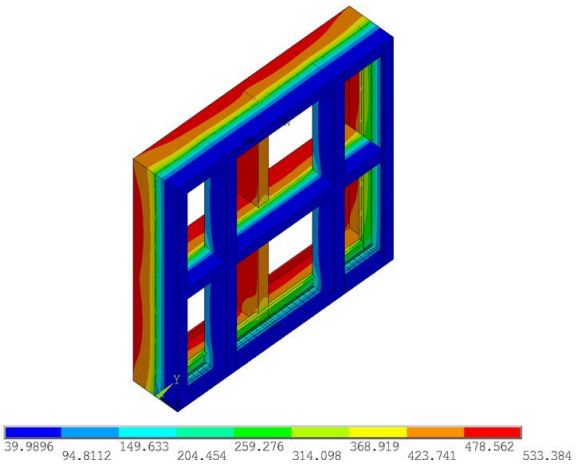

t = 40 minutes

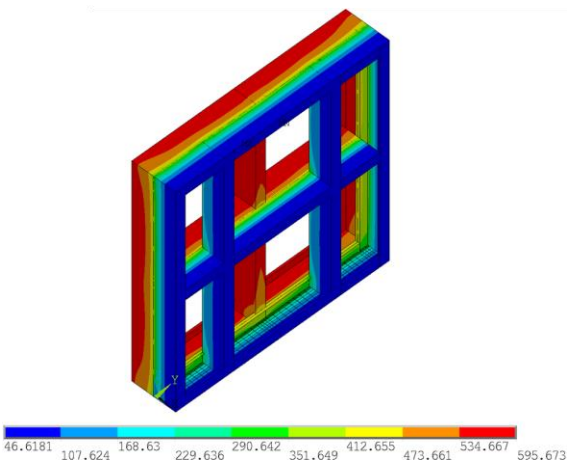

t = 50 minutes

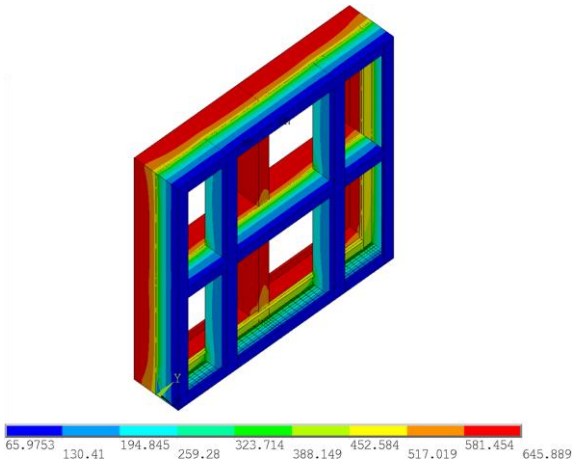

t = 60 minutes

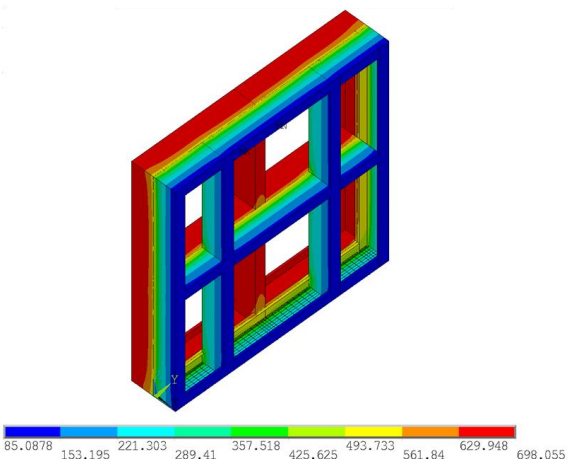

t = 70 minutes

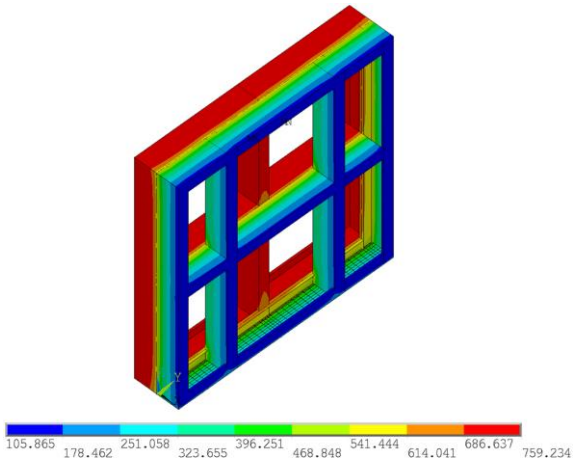

t = 80 minutes

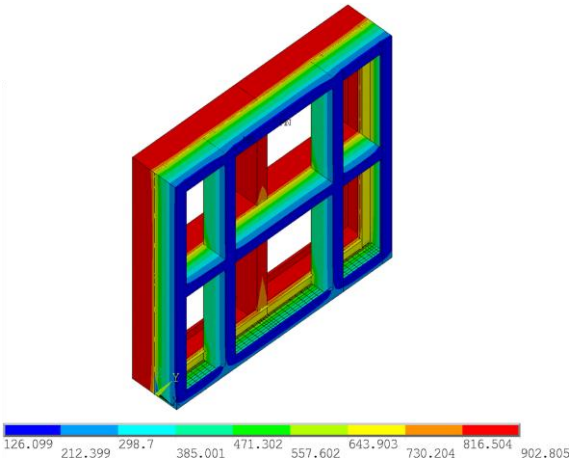

t = 90 minutes

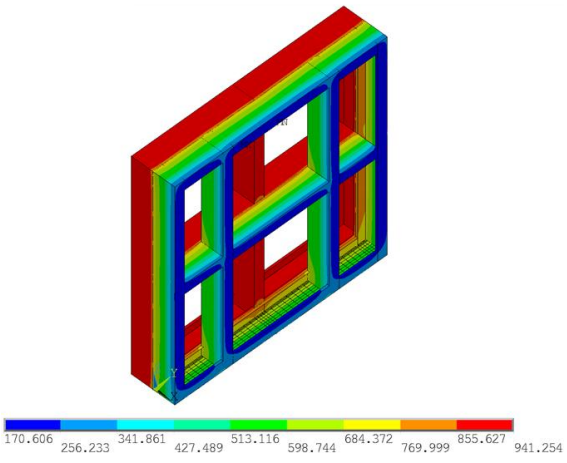

t = 100 minutes

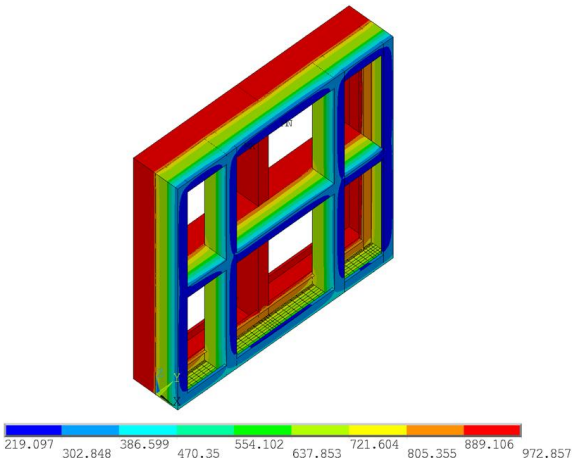

t = 110 minutes

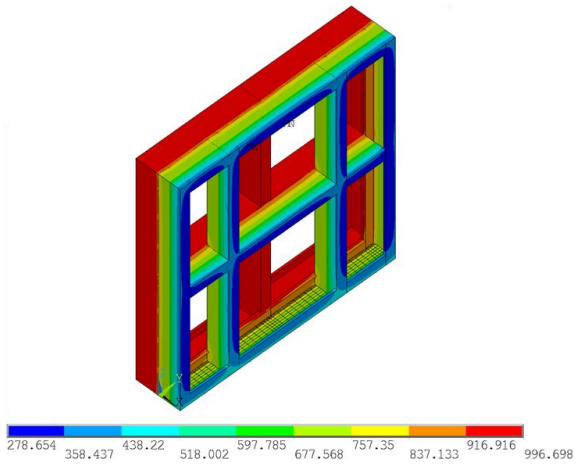

t = 112 minutes (at T_{max})

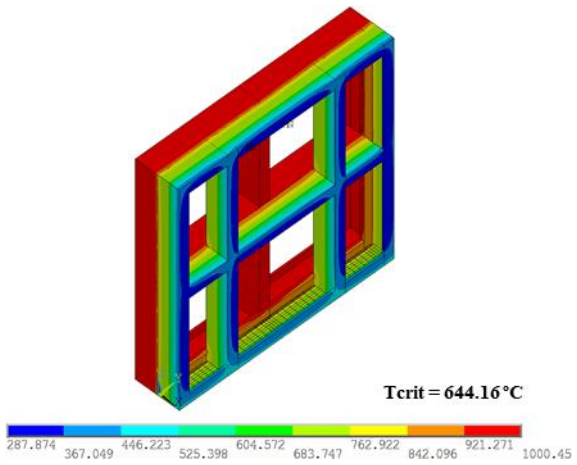

t = 120 minutes

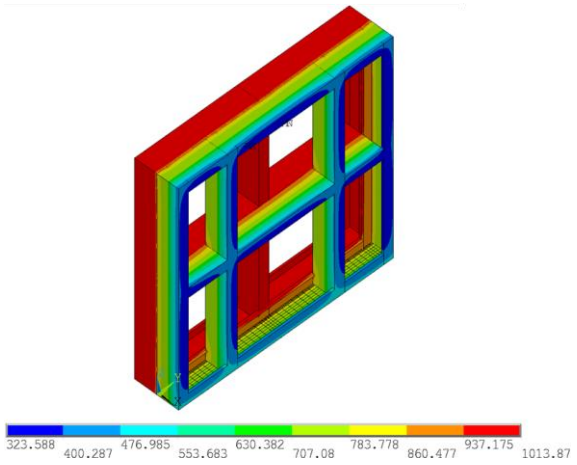

t = 122 minutes (at T_{ave})

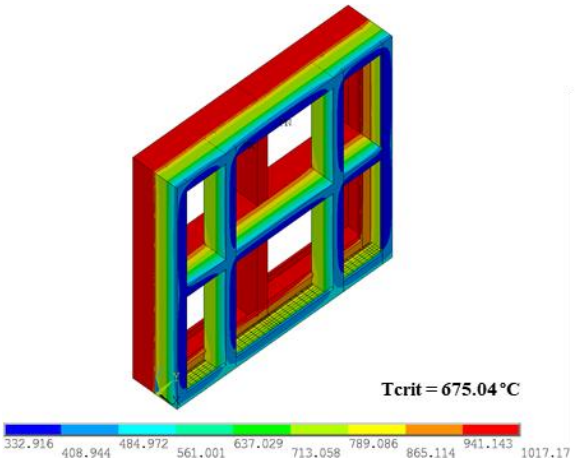

D.5 Model Specimen 5

Model Specimen 5 – Non-load-bearing Double-stud LSF Wall	**Thermal Insulation Performance**	
Gypsum plasterboard: 12.5 mm thick Type F fire-resistant	Fire resistance (T_{ave}) [min]:	176
Gypsum plasterboards on the exposed side: 1	Fire resistance (T_{max}) [min]:	170
Gypsum plasterboards on the unexposed side: 1	Fire resistance rating (FRR):	I120
Cavity insulation: 100 mm thick ceramic fibre		
Air boundary layer: 2 x 10 mm		

3D Finite Element Mesh

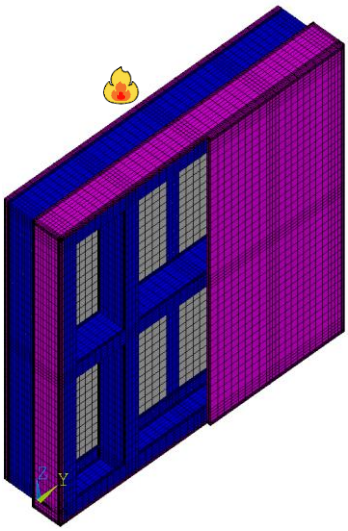

Labels:

- Gypsum plasterboard
- Steel frame
- Ceramic fibre
- Air layer

Steel Frame Description

Stud/track section: C100 x 45 x 10 mm

Steel thickness/grade: 1.0 mm / S280GD

Connections: perfectly rigid

2D cross-section:

*measurements in millimetres

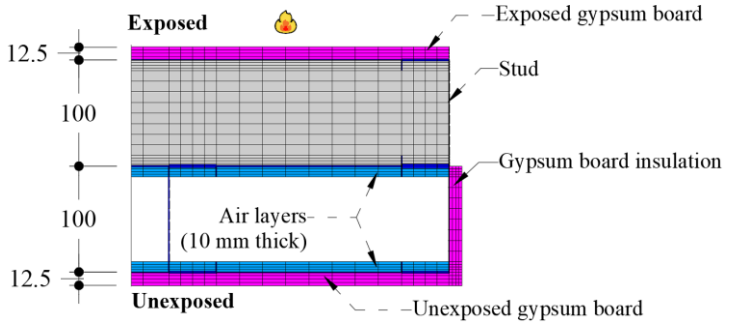

Mesh Details

Total number of nodes:	**Total number of elements:**
Steel frame – SHELL131 Finite Elements	*Gypsum plasterboard / Ceramic fibre insulation / Air layer – SOLID70 Finite Elements*

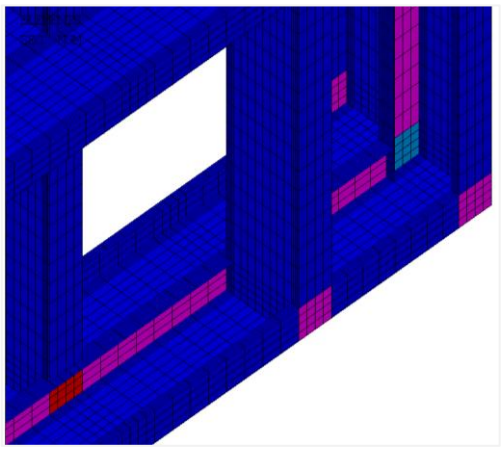

View from the unexposed side (right bottom corner)

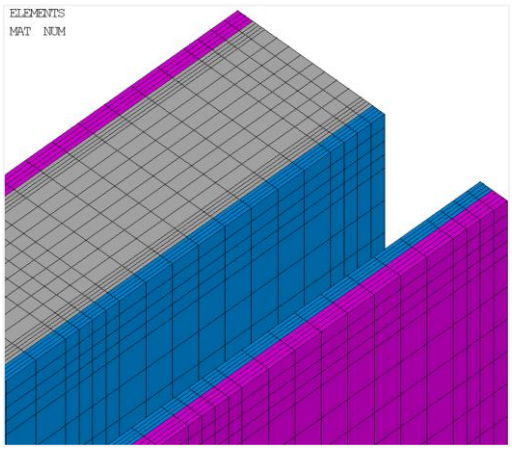

View from the unexposed side (right upper corner)

SHELL131 section thickness:

- 1 mm thick
- 2 mm thick
- 3 mm thick
- 4 mm thick

Boundary Conditions (z = 500 mm)

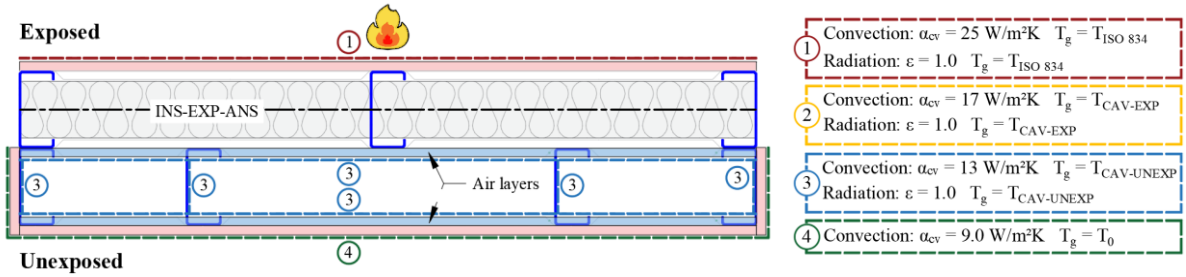

Nodal Temperatures *measurements in millimetres

Nodes:

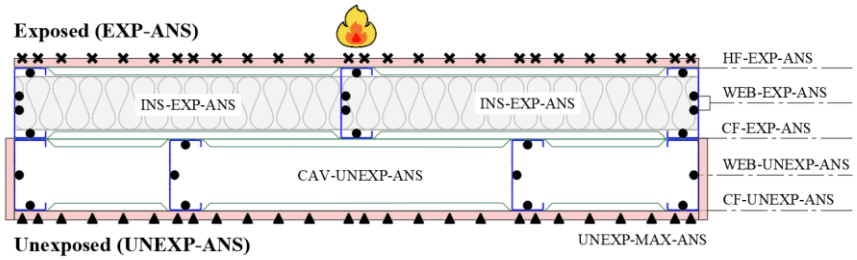

Labels:

- ✖ Nodes at 261.25 mm from the bottom of the wall
- ● Nodes at 500 mm from the bottom of the wall
- ▲ Nodes at 261.25 mm and 500 mm from the bottom of the wall

Numerical and Experimental Time-Temperature Profiles **Test duration:** 200 minutes

EXP/EXP-ANS

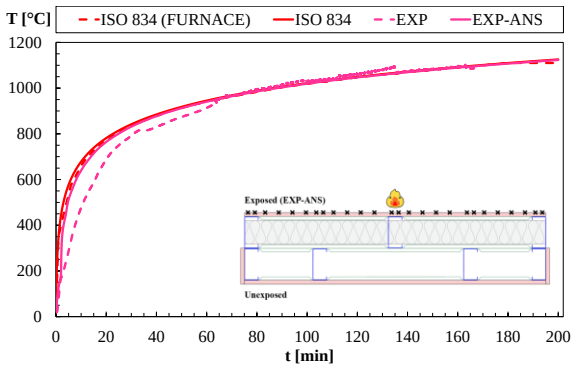

HF-EXP/HF-EXP-ANS

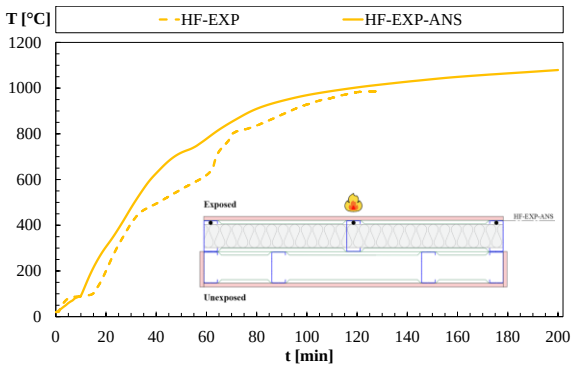

WEB-EXP/WEB-EXP-ANS

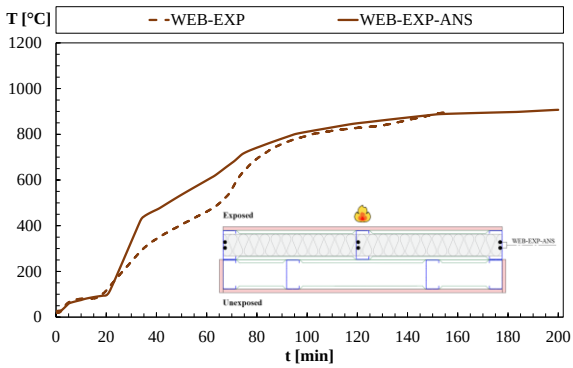

CF-EXP/CF-EXP-ANS

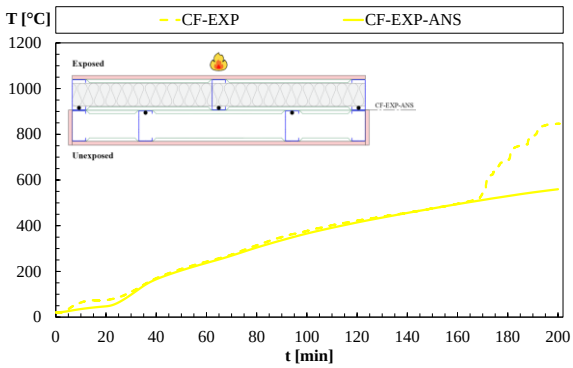

INS-EXP/INS-EXP-ANS

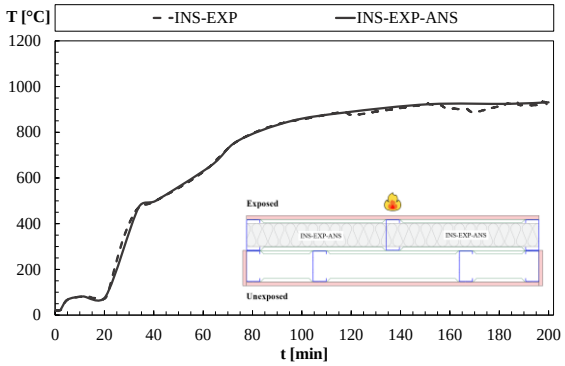

WEB-UNEXP/WEB-UNEXP-ANS

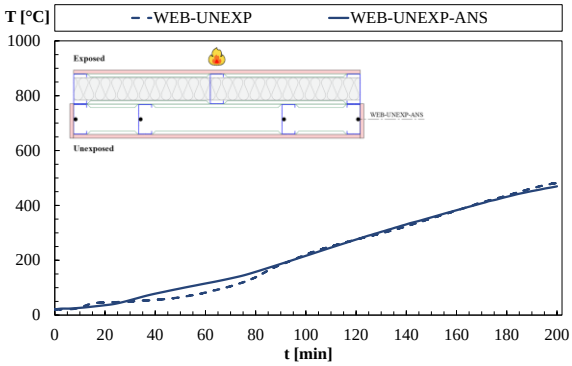

CF-UNEXP/CF-UNEXP-ANS

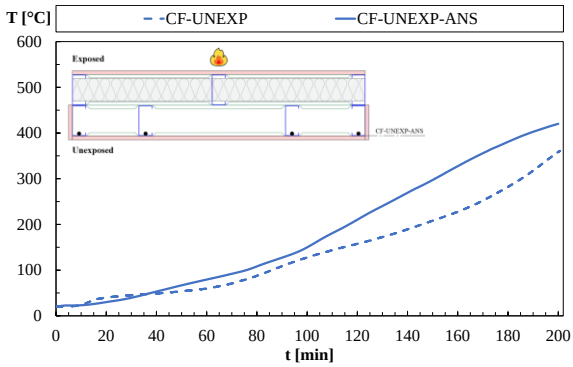

CAV-UNEXP/CAV-UNEXP-ANS

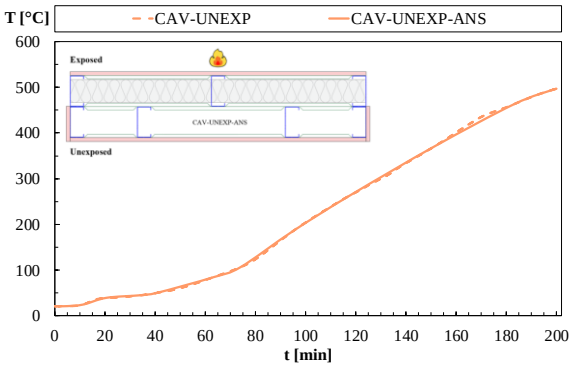

UNEXP / UNEXP-MAX

UNEXP-ANS/UNEXP-MAX-ANS

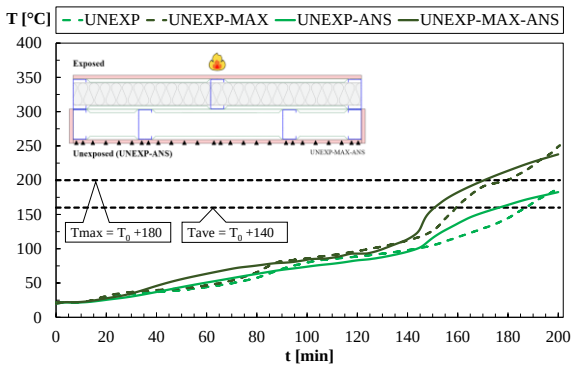

Temperatures on the Unexposed Plasterboard [ºC] **Test duration:** 150 minutes

t = 10 minutes

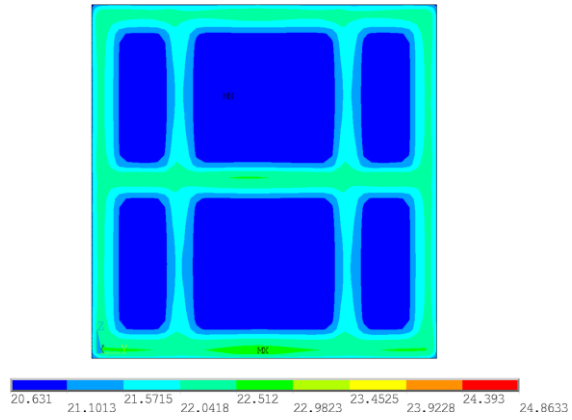

t = 20 minutes

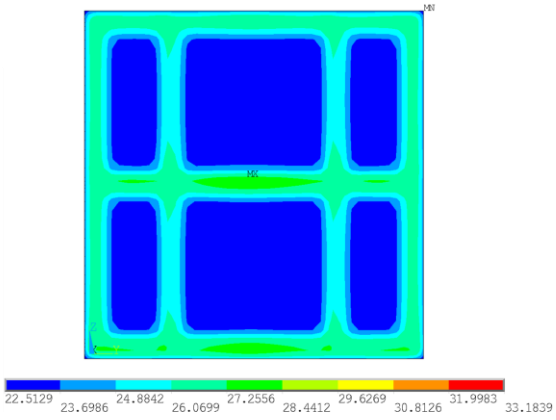

t = 30 minutes

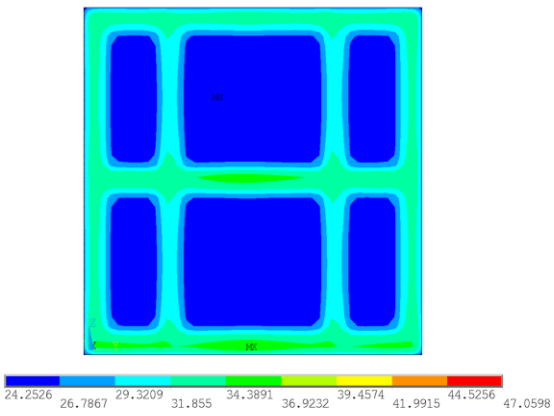

t = 40 minutes

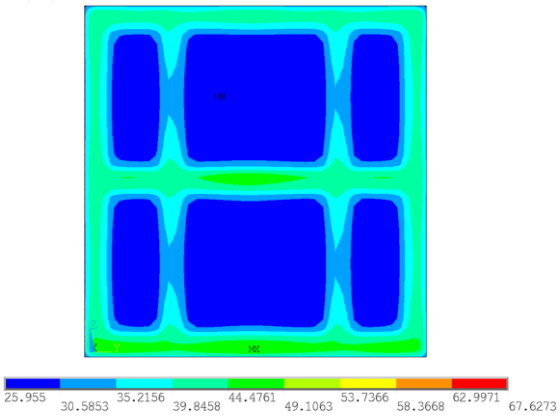

t = 50 minutes

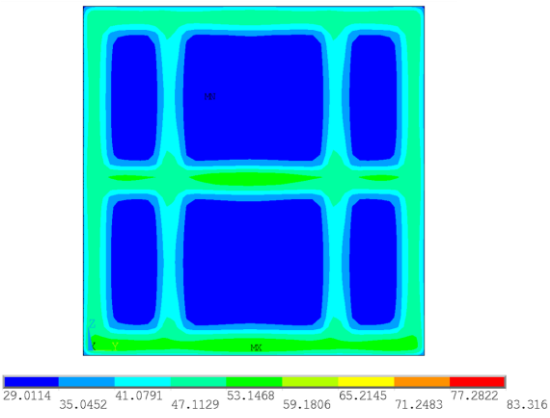

t = 60 minutes

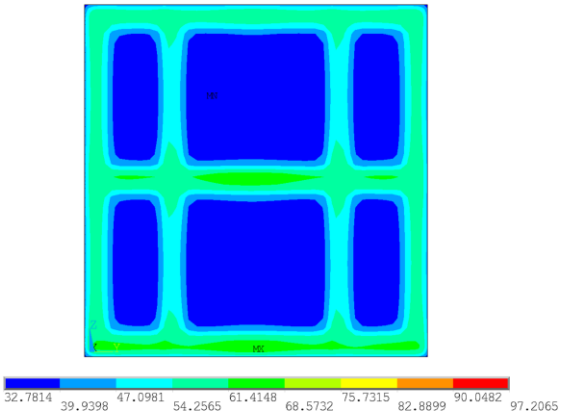

t = 70 minutes

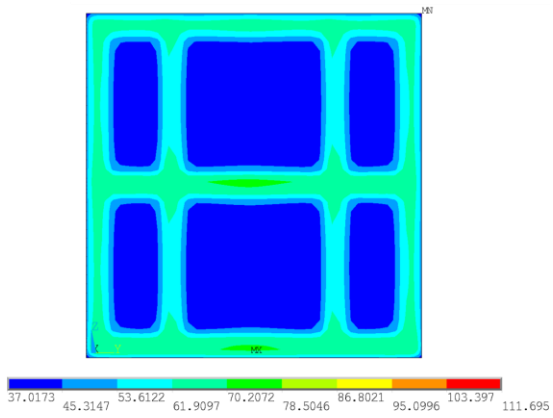

t = 80 minutes

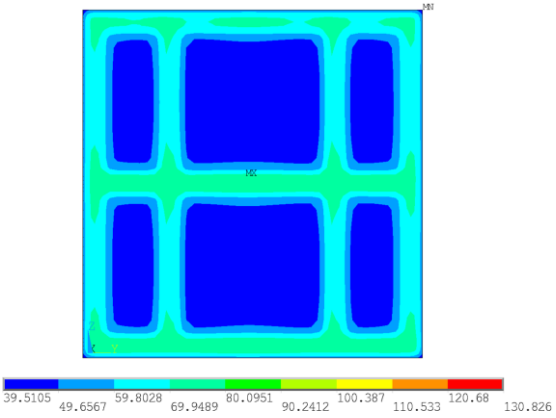

t = 90 minutes

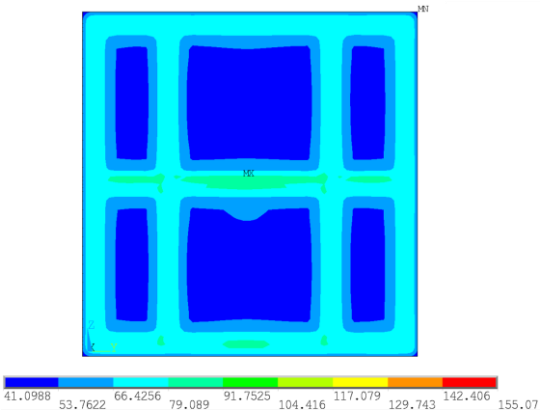

t = 100 minutes

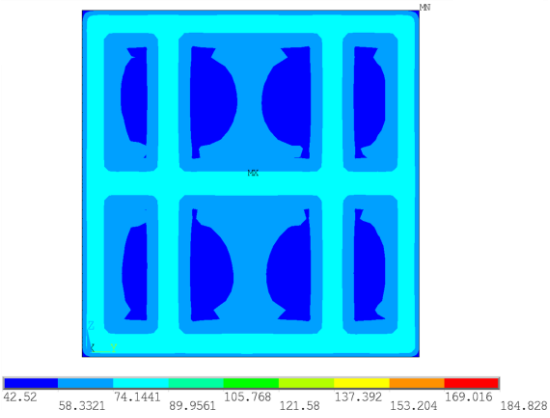

t = 110 minutes

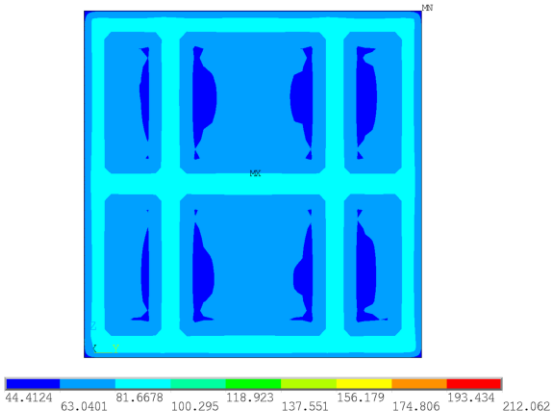

t = 120 minutes

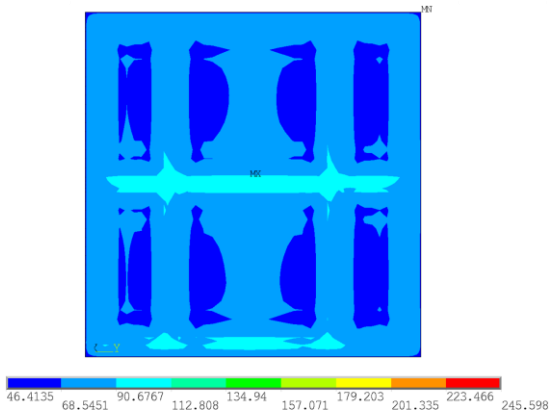

t = 130 minutes

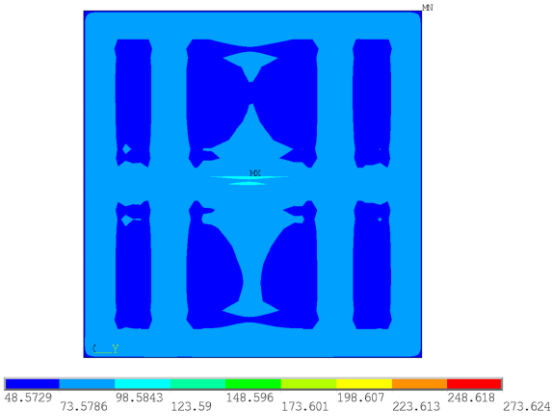

t = 140 minutes

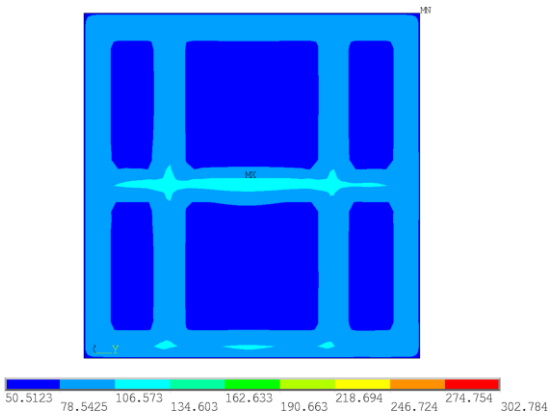

t = 150 minutes

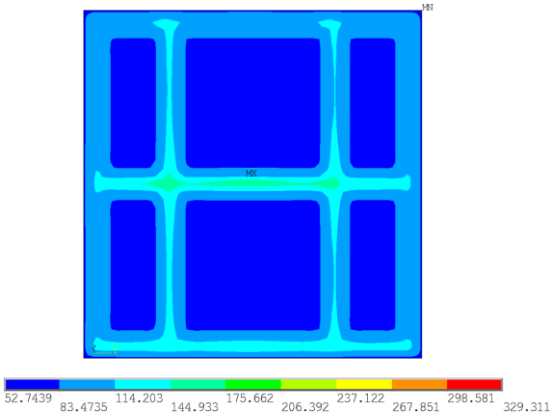

t = 160 minutes

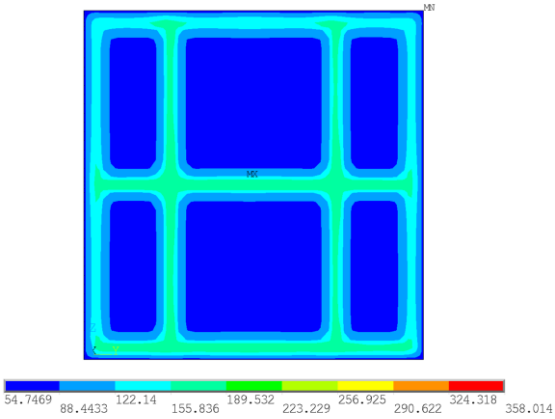

t = 170 minutes (at T_{max})

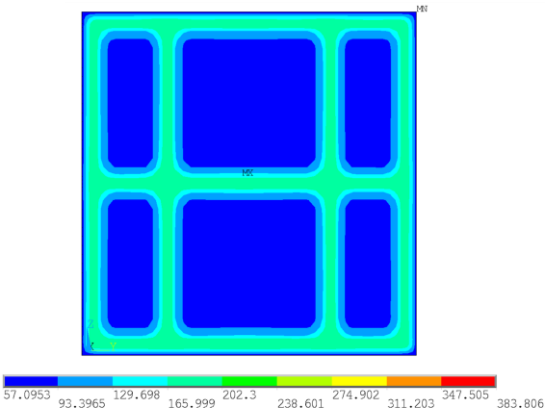

t = 176 minutes (at T_{ave})

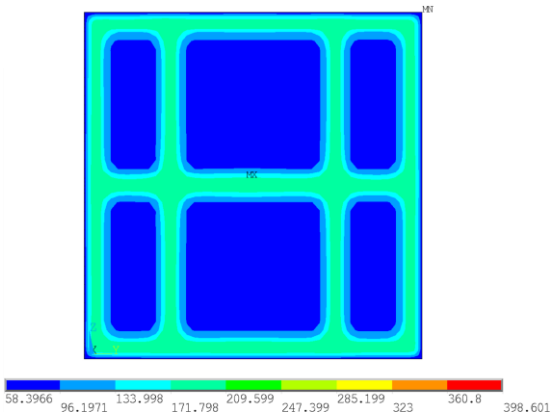

Temperatures on Steel Frame [ºC]			**Test duration:** 150 minutes
Critical temperature (T_{crit}) at T_{ave}:	710.16 ºC	(average)	
Critical temperature (T_{crit}) at T_{max}:	699.98 ºC	(average)	

t = 10 minutes

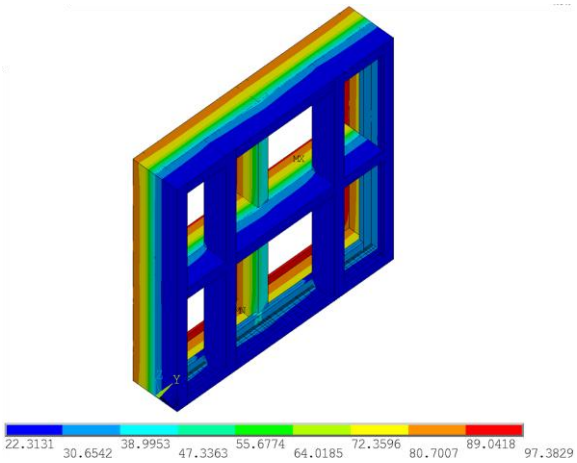

t = 20 minutes

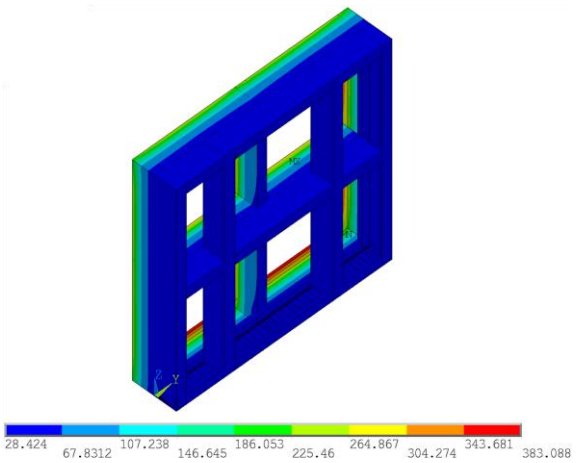

t = 30 minutes

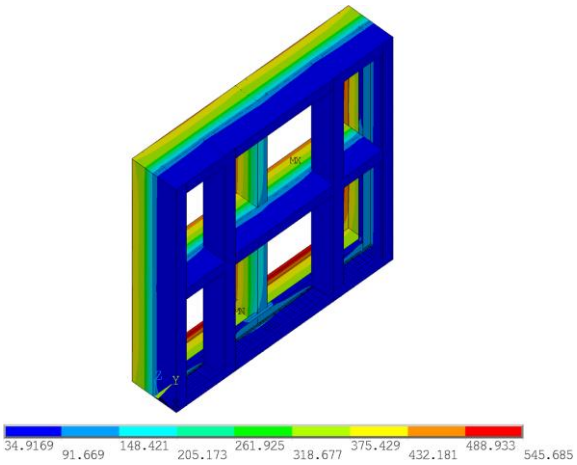

t = 40 minutes

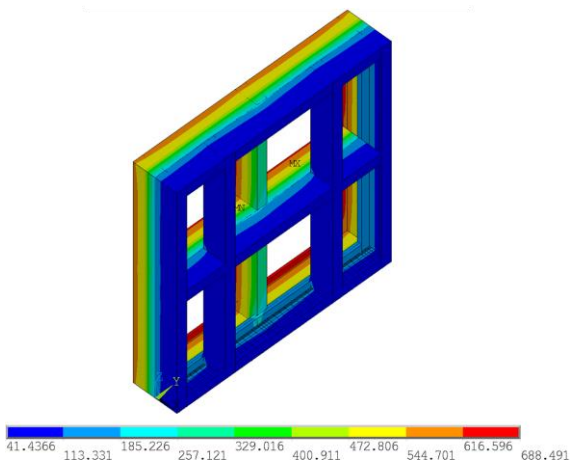

t = 50 minutes

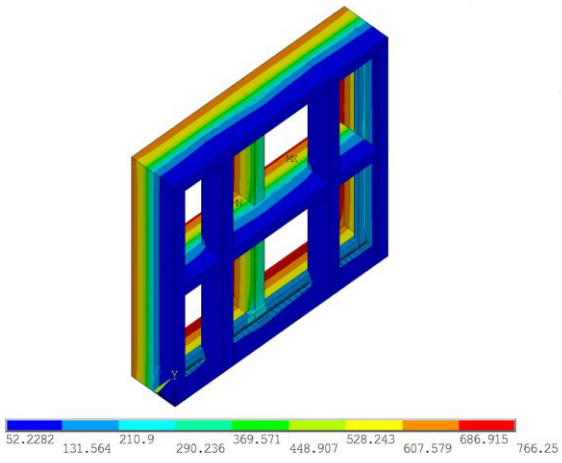

t = 60 minutes

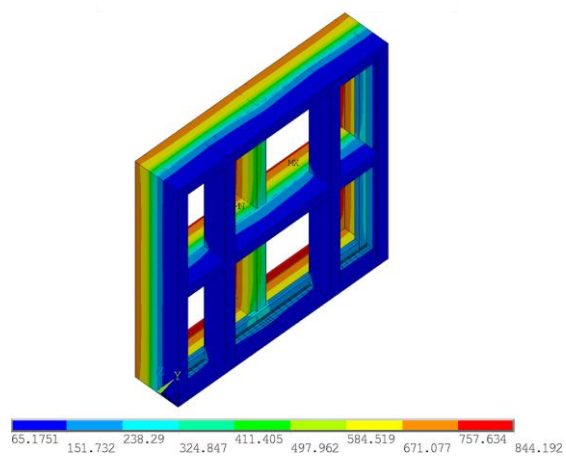

t = 70 minutes

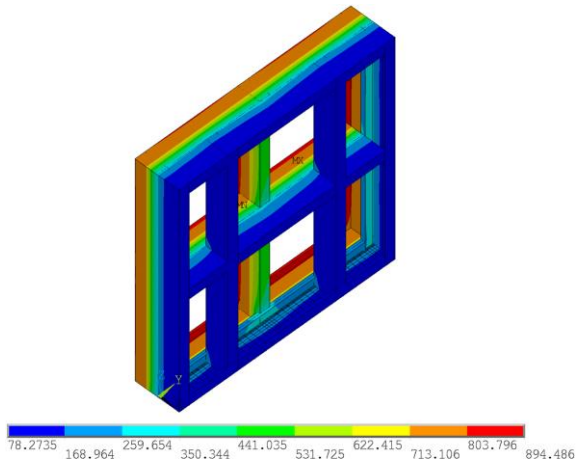

t = 80 minutes

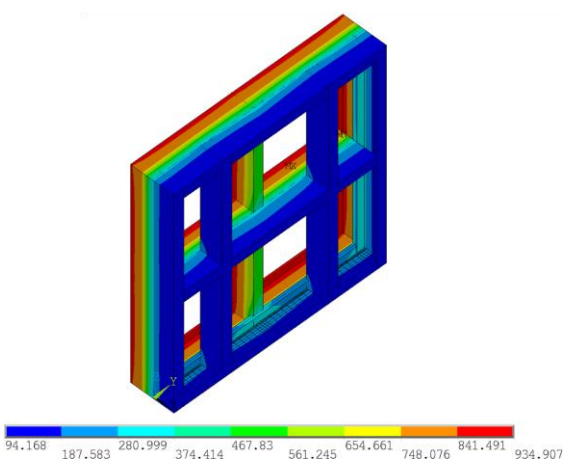

t = 90 minutes

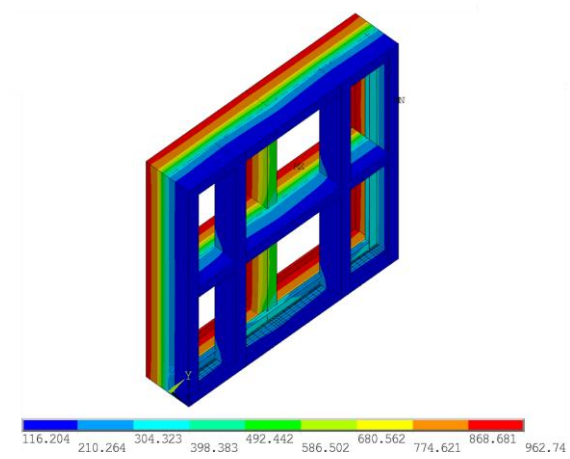

t = 100 minutes

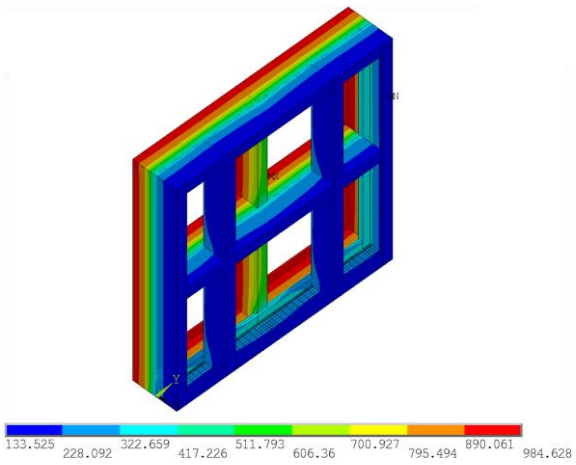

t = 110 minutes

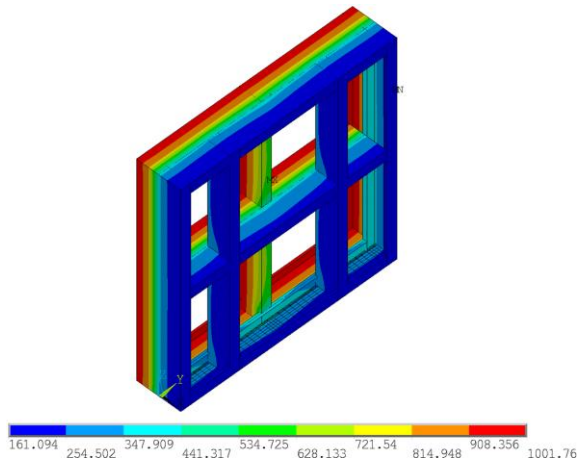

t = 120 minutes

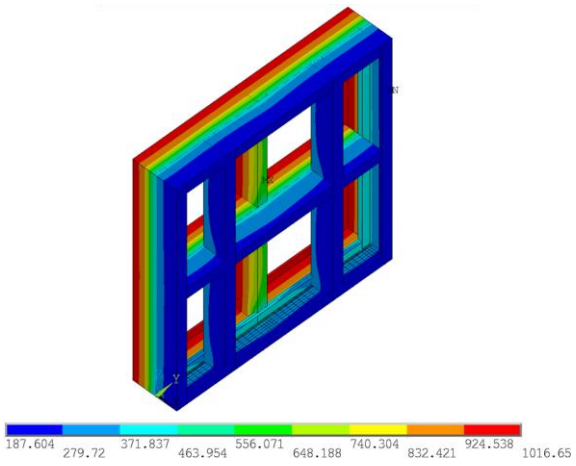

t = 130 minutes

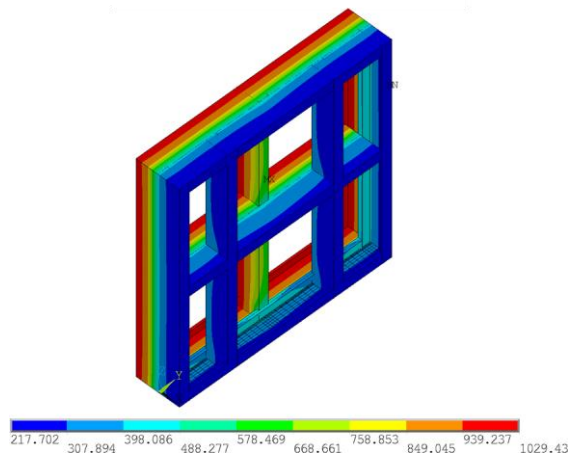

t = 140 minutes

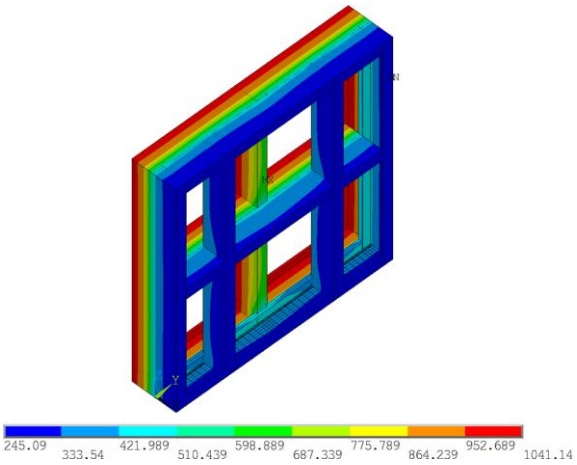

t = 150 minutes

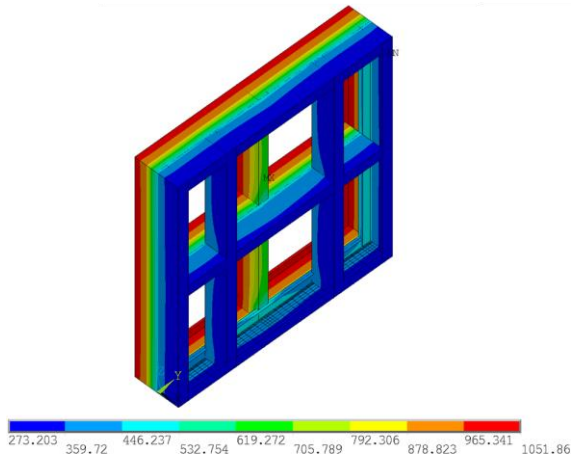

t = 160 minutes

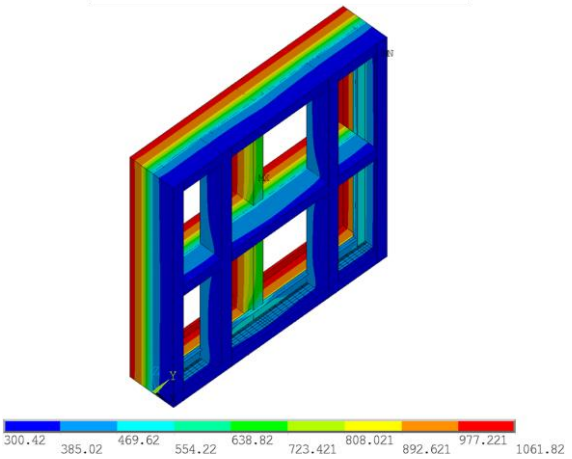

t = 170 minutes (at T_{max})

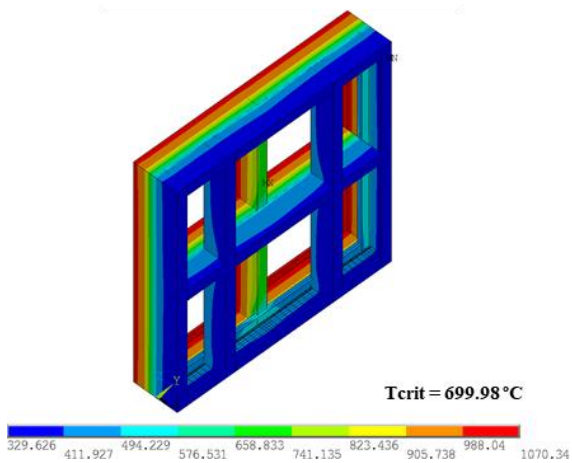

t = 176 minutes (at T_{ave})

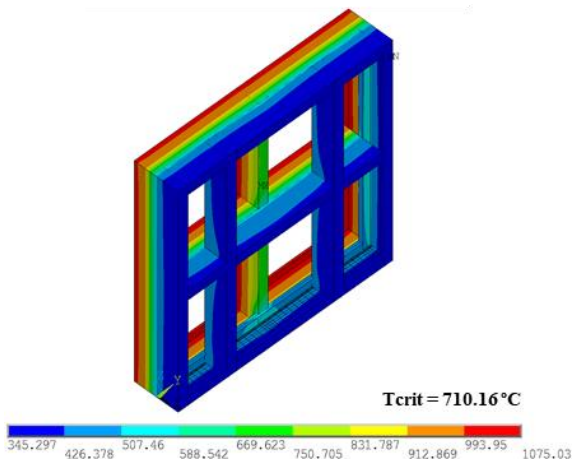

E Simplified Method – Design Tables

E.1 Basic Values

Table E.1 – Basic protection and insulation values for different materials.

Considered layer $(\mathbf{i}, \mathbf{n})$	Basic insulation value $(\mathbf{t_{ins,0,n}})$ [min]	Basic protection value $(\mathbf{t_{prot,0,i}})$ [min]	Reference
Gypsum plasterboard, gypsum fibreboard	$24\left(\frac{h_i}{15}\right)^{1.4}$	$30\left(\frac{h_i}{15}\right)^{1.2}$	Frangi [78]
Solid timber panel	$19\left(\frac{h_i}{20}\right)^{1.4}$	$30\left(\frac{h_i}{20}\right)^{1.1}$	Frangi [78]
Particleboard	$22\left(\frac{h_i}{20}\right)^{1.4}$	$33\left(\frac{h_i}{20}\right)^{1.1}$	Frangi [78]
OSB, plywood	$16\left(\frac{h_i}{20}\right)^{1.4}$	$23\left(\frac{h_i}{20}\right)^{1.1}$	Frangi [78]
Rock fibre	*	$0.3\ h_i^{(0.75\log(\rho_i)-\frac{\rho_i}{400})}$	Frangi [78]
Ceramic fibre	*	$0.3\ h_i^{(0.75\log(\rho_i)-\frac{\rho_i}{400})}$	Current research
Glass fibre	*	For $h_i < 40$ mm: 0 For $h_i \geq 40$ mm: $(0.0007\rho_i + 0.046)h_i + 13 \leq 20$	Frangi [78]

* Insulation materials as the last layer of the assembly are rarely used in construction practice;
h_i: thickness of the layer considered [mm];
ρ_i: density of the layer considered [kg/m³].

E.2 Position Coefficients

Table E.2 – Position coefficients of protection and insulation layers that contemplates the effects of the layers preceding the layer being considered.

Considered layer $(\mathbf{i}, \mathbf{n})$	Position coefficents $\mathbf{k_{pos,exp,i}}$ and $\mathbf{k_{pos,exp,n}}$		Reference
Cladding (gypsum, timber)	$\mathbf{k_{pos,exp,n}}$ **for** $\mathbf{t_{ins,n}}$		Frangi [78]
	$1 - 0.6\frac{\sum t_{prot,i-1}}{t_{ins,0,n}}$	For $\sum t_{prot,i-1} \leq \frac{t_{ins,0,n}}{2}$	
	$0.5\sqrt{\frac{t_{ins,0,n}}{\sum t_{prot,i-1}}}$	For $\sum t_{prot,i-1} > \frac{t_{ins,0,n}}{2}$	

Continues next page

Table E.2 – Position coefficients of protection and insulation layers that contemplates the effects of the layers preceding the layer being considered (continued).

Considered layer (**i**, **n**)	Position coefficents $k_{pos,exp,i}$ and $k_{pos,exp,n}$		Reference
Cladding (gypsum, timber)	$k_{pos,exp,i}$ **for** $t_{prot,i}$		Frangi [78]
	$1 - 0.6\frac{\sum t_{prot,i-1}}{t_{prot,0,i}}$	For $\sum t_{prot,i-1} \leq \frac{t_{prot,0,i}}{2}$	
	$0.5\sqrt{\frac{t_{prot,0,n}}{\sum t_{prot,i-1}}}$	For $\sum t_{prot,i-1} > \frac{t_{prot,0,i}}{2}$	
Rock fibre	$k_{pos,exp,i}$ **for** $t_{prot,i}$		Frangi [78]
	$1 - 0.6\frac{\sum t_{prot,i-1}}{t_{prot,0,i}}$	For $\sum t_{prot,i-1} \leq \frac{t_{prot,0,i}}{2}$	
	$0.5\sqrt{\frac{t_{prot,0,n}}{\sum t_{prot,i-1}}}$	For $\sum t_{prot,i-1} > \frac{t_{prot,0,i}}{2}$	
Ceramic fibre	$k_{pos,exp,i}$ **for** $t_{prot,i}$		Current research
	$1 - 0.6\frac{\sum t_{prot,i-1}}{t_{prot,0,i}}$	For $\sum t_{prot,i-1} \leq \frac{t_{prot,0,i}}{2}$	
	$0.5\sqrt{\frac{t_{prot,0,n}}{\sum t_{prot,i-1}}}$	For $\sum t_{prot,i-1} > \frac{t_{prot,0,i}}{2}$	
Glass fibre ($h_i \geq 40$ mm)	$k_{pos,exp,i}$ **for** $t_{prot,i}$		Frangi [78]
	$1 - 0.8\frac{\sum t_{prot,i-1}}{t_{prot,0,i}}$	For $\sum t_{prot,i-1} \leq \frac{t_{prot,0,i}}{4}$	
	$(0.001\,\rho_i + 0.27)\left[\frac{t_{prot,0,i}}{\sum t_{prot,i-1}}\right]^{(0.75-0.002\,\rho_i)}$	For $\sum t_{prot,i-1} > \frac{t_{prot,0,i}}{4}$	

ρ_i: density of the layer considered [kg/m³];

$\sum t_{prot,i-1}$: sum of the protection values of the layers preceding the layer being considered.

Table E.3 – Position coefficient of protection layers that contemplates the effects of the layer backing the layer being considered.

Considered layer (**i**, **n**)	$k_{pos,unexp,i}$ for layers backed by cladding made of gypsum or timber	$k_{pos,unexp,i}$ for layers backed by insulation	Reference
Gypsum plasterboard, gypsum fibreboard	1.0	$0.5\,h_i^{0.15}$	Frangi [78]

Continues next page

Table E.3 – Position coefficient of protection layers that contemplates the effects of the layer backing the layer being considered (continued).

Considered layer ($\mathbf{i}$, $\mathbf{n}$)	$\mathbf{k_{pos,unexp,i}}$ for layers backed by cladding made of gypsum or timber	$\mathbf{k_{pos,unexp,i}}$ for layers backed by insulation	Reference
Solid timber panel	1.0	$0.35\ h_i^{0.21}$	Frangi [78]
Particleboard	1.0	$0.41\ h_i^{0.18}$	Frangi [78]
OSB, plywood	1.0	$0.5\ h_i^{0.15}$	Frangi [78]
Rock fibre	1.0	$0.18\ h_i^{(0.001\ \rho_i+0.08)}$	Frangi [78]
Ceramic fibre	1.0	$0.18\ h_i^{(0.001\ \rho_i+0.08)}$	Current research
Glass fibre	1.0	$0.01\ h_i - \frac{h_i^2}{30000} + \rho_i^{0.009} - 1.3$	Frangi [78]

E.3 Correction Times

Table E.4 – Correction times of protection and insulation layers protected by Type F or Type X gypsum plasterboards and gypsum fibreboards.

Considered layer	Wall assemblies		Reference
Cladding (gypsum, timber)	$\mathbf{\Delta t_n}$ **for** $\mathbf{t_{ins,n}}$ **(min)***		Frangi [78]
	$0.03\ t_{prot,i-1} + 0.9\ t_{ins,0,n} - 2.3$	For $t_{ins,0,n} < 12$ min	
	$0.22\ t_{prot,i-1} - 0.1\ t_{ins,0,n} + 4.7$	For $t_{ins,0,n} \geq 12$ min	
	$\mathbf{\Delta t_i}$ **for** $\mathbf{t_{prot,i}}$ **(min)***		
	$0.03\ t_{prot,i-1} + 0.9\ t_{prot,0,i} - 2.3$	For $t_{prot,0,i} < 12$ min	
	$0.22\ t_{prot,i-1} - 0.1\ t_{prot,0,i} + 4.7$	For $t_{prot,0,i} \geq 12$ min	
Insulation (rock and glass fibre)	$\mathbf{\Delta t_i}$ **for** $\mathbf{t_{prot,i}}$ **(min)***		Frangi [78]
	$0.1\ t_{prot,i-1} + t_{prot,0,i} - 1.0$	For $t_{prot,0,i} < 6$ min	
	$0.22\ t_{prot,i-1} - 0.1\ t_{prot,0,i} + 3.5$	For $t_{prot,0,i} \geq 6$ min	

* $\Delta t_n > 0$, $\Delta t_i > 0$. Not stated in the original method.

E.4 Cavity Effect

Table E.5 – Correction factors of the position coefficients in the case of void cavities.

Considered layer	Layer on the fire-exposed side of the cavity	Layer on the fire-unexposed side of the cavity		Reference
Cladding	$k_{pos,unexp,i}$ according to Table E.4 , column 3	1.6 $k_{pos,exp,i}$ according to Table E.3	3 Δt_i according to Table E.5	Frangi [78]
Insulation	$k_{pos,unexp,i} = 1$		Δt_i according to Table E.5	Frangi [78]
Cladding	$k_{pos,unexp,i}$ according to Table E.4 , column 3	3.2 $k_{pos,exp,i}$ according to Table E.3*	3 Δt_i according to Table E.5	Current research
Insulation	$k_{pos,unexp,i} = 2.6$**		Δt_i according to Table E.5	Current research

* Only in the case of double-sized cavities. Otherwise, the correcion coefficient of 1.6 remains unchanged;
** Only in the case of ceramic fibre insulation placed on the fire-exposed side of the cavity.

F Simplified Method – Step by Step Solutions

F.1 Simplified Model Specimen 1

I. Description of the assembly

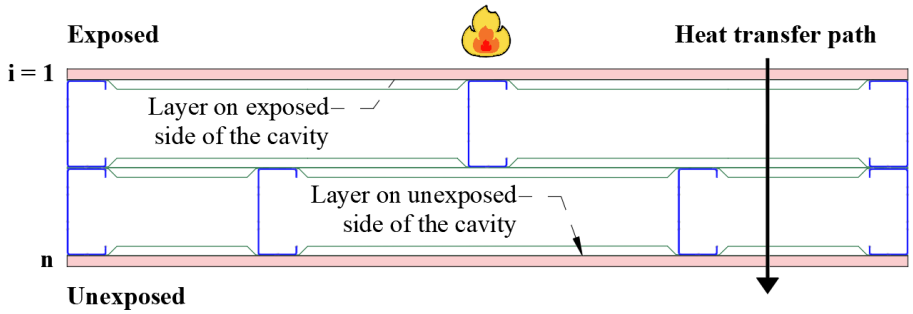

Layer	Material	Function	Thickness [mm]
1	Type F gypsum plasterboard	Protection	12.5
n	Type F gypsum plasterboard	Insulation	12.5
Cavity	-	-	200

II. Basic values

The first and only layer with protective function is a Type F gypsum plasterboard with $h_i = 12.5$ mm. Therefore, as presented in Table E.1:

$$t_{prot,0,i} = t_{prot,0,1} = 30\left(\frac{h_i}{15}\right)^{1.2} = 30\left(\frac{12.5}{15}\right)^{1.2} = 24.1 \text{ minutes} \qquad \textbf{Table E.1}$$

The last layer of the assembly is also a Type F gypsum plasterboard with an insulation function and $h_i = 12.5$ mm. Therefore, as shown in Table E.1:

$$t_{ins,0,n} = 24\left(\frac{h_i}{15}\right)^{1.4} = 24\left(\frac{12.5}{15}\right)^{1.4} = 18.6 \text{ minutes} \qquad \textbf{Table E.1}$$

III. Protection values

a. Layer i = 1

According to Table E.2:

$$\sum t_{prot,i-1} = 0 \leq \frac{t_{prot,0,1}}{2} \leq \frac{24.1}{2} \qquad \textbf{Table E.2}$$

$$k_{pos,exp,1} = 1 - 0.6\frac{\sum t_{prot,i-1}}{t_{prot,0,1}} = 1 - 0.6\left(\frac{0}{24.1}\right) = 1 \qquad \textbf{Table E.2}$$

According to the improved design model, the gypsum plasterboard on the exposed side of the cavity is being backed by the void cavity, which acts as an insulation layer. Consequently, in this case, the position coefficient that considers the effect of the backing layer $k_{pos,unexp,i}$ (Table E.3, column 3) is given by Table E.5, as follows:

$$k_{pos,unexp,1} = 0.5\, h_i^{0.15} = 0.5 * 12.5^{\,0.15} = 0.73 \qquad \textbf{Table E.3}$$

In this specimen, there is only one layer with a protective function and its protection value is now calculated as:

$$t_{prot,i} = t_{prot,1} = \left(t_{prot,0,1}\, k_{pos,exp,1}\, k_{pos,unexp,1} + \Delta t_1\right)$$

Note that $\Delta t_1 = 0$ since there is no preceding layer made of Type F gypsum plasterboard, which leads to:

$$t_{prot,1} = 24.1 * 1 * 0.73 \; + 0 = 17.6 \text{ minutes}$$

IV. Insulation value

a. Layer n

According to Table E.2:

$$\sum t_{prot,i-1} = t_{prot,1} = 17.6 > \frac{t_{ins,0,n}}{2} > \frac{18.6}{2} \quad \textbf{Table E.2}$$

$$k_{pos,exp,n} = 0.5 \sqrt{\frac{t_{ins,0,n}}{\sum t_{prot,i-1}}} = 0.5 \sqrt{\frac{18.6}{17.6}} = 0.51 \quad \textbf{Table E.2}$$

Nevertheless, $k_{pos,exp,n}$ must be modified to consider the effects of the void cavity, as presented in Table E.5.

$$k_{pos,exp,n} = 3.2\, k_{pos,exp,n} = 3.2 * 0.51 = 1.6 \quad \textbf{Table E.5}$$

The last layer is protected by a Type F gypsum plasterboard (layer $i = 1$) and the correction time presented in Table E.4 must be found.

$$t_{ins,0,n} = 18.6 \geq 12 \text{ minutes} \quad \textbf{Table E.4}$$

$$\Delta t_n = 0.22\, t_{prot,i-1} - 0.1\, t_{ins,0,n} + 4.7 \quad \textbf{Table E.4}$$

$$\Delta t_n = 0.22 * 17.6 - 0.1 * 18.6 + 4.7 = 6.7 \text{ minutes} \quad \textbf{Table E.4}$$

To consider the effects of the void cavity and since the insulation layer is a Type F gypsum plasterboard (cladding), the correction time is modified to

$$\Delta t_n = 3 * 6.7 = 20.1 \text{ minutes} \quad \textbf{Table E.5}$$

The insulation value of the last layer is given by

$$t_{ins,n} = \left(t_{ins,0,i}\, k_{pos,exp,n} + \Delta t_n\right)$$

$$t_{ins,n} = 18.6 * 1.6 + 20.1 = 49.9 \text{ minutes}$$

V. Fire resistance of the assembly

The expression that gives the fire resistance of the assembly in terms of insulation requirements is

$$t_{ins} = \sum_{i=1}^{i=n-1} t_{prot,i} + t_{ins,n}$$

Thus

$$t_{ins} = t_{prot,1} + t_{ins,n} = 17.6 + 49.9 = 67 \text{ minutes}$$

F.2 Simplified Model Specimen 2

I. Description of the assembly

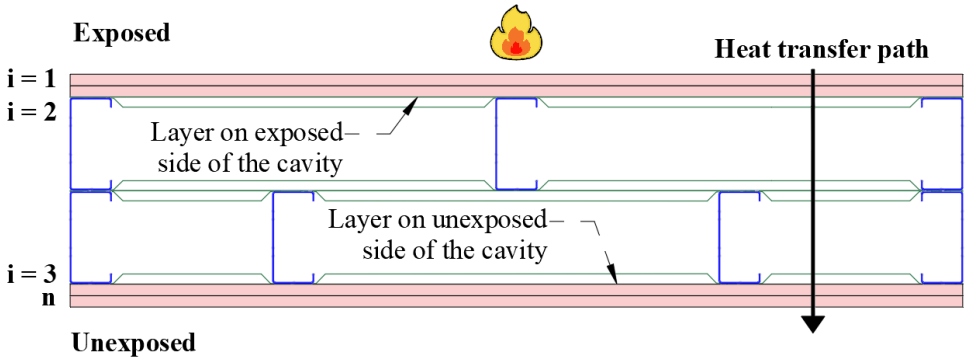

Layer	Material	Function	Thickness [mm]
1	Type F gypsum plasterboard	Protection	12.5
2	Type F gypsum plasterboard	Protection	12.5
3	Type F gypsum plasterboard	Protection	12.5
n	Type F gypsum plasterboard	Insulation	12.5
Cavity	-	-	200

II. Basic values

The first three layers with protective function are Type F gypsum plasterboards with $h_i = 12.5$ mm each. Therefore, as presented in Table E.1:

$$t_{prot,0,i} = t_{prot,0,1} = t_{prot,0,2} = t_{prot,0,3} \qquad \textbf{Table E.1}$$

$$t_{prot,0,i} = 30 \left(\frac{12.5}{15}\right)^{1.2} = 24.1 \text{ minutes} \qquad \textbf{Table E.1}$$

The last layer of the assembly is also a Type F gypsum plasterboard with an insulation function and $h_i = 12.5$ mm. Therefore, as shown in Table E.1:

$$t_{ins,0,n} = 24\left(\frac{h_i}{15}\right)^{1.4} = 24\left(\frac{12.5}{15}\right)^{1.4} = 18.6 \text{ minutes}$$ **Table E.1**

III. Protection values

a. Layer i = 1

According to Table E.2:

$$\sum t_{prot,i-1} = 0 \leq \frac{t_{prot,0,1}}{2} \leq \frac{24.1}{2}$$ **Table E.2**

$$k_{pos,exp,1} = 1 - 0.6\frac{\sum t_{prot,i-1}}{t_{prot,0,1}} = 1 - 0.6\left(\frac{0}{24.1}\right) = 1$$ **Table E.2**

The layer i = 1 is backed by a Type F gypsum plasterboard and according to Table E.3:

$$k_{pos,unexp,i} = k_{pos,unexp,1} = 1.0$$ **Table E.3**

The protection value is now calculated as

$$t_{prot,i} = t_{prot,1} = \left(t_{prot,0,1}\, k_{pos,exp,1}\, k_{pos,unexp,1} + \Delta t_1\right)$$

Note that $\Delta t_1 = 0$ since there is no preceding layer made of Type F gypsum plasterboard, which leads to:

$$t_{prot,1} = 24.1 * 1 * 1 \; + 0 = 24.1 \text{ minutes}$$

b. Layer i = 2

$$\sum t_{prot,i-1} > \frac{t_{prot,0,2}}{2} > \frac{24.1}{2} \quad \textbf{Table E.2}$$

$$k_{pos,exp,2} = 0.5\sqrt{\frac{t_{prot,0,2}}{\sum t_{prot,i-1}}} = 0.5\sqrt{\frac{24.1}{24.1}} = 0.5 \quad \textbf{Table E.2}$$

The layer i = 2 is protected by a Type F gypsum plasterboard (layer i = 1) and the correction time presented in Table E.4 must be found.

$$t_{prot,0,2} = 24.1 \geq 12 \text{ minutes} \quad \textbf{Table E.4}$$

$$\Delta t_i = 0.22\, t_{prot,i-1} - 0.1\, t_{prot,0,i} + 4.7 \quad \textbf{Table E.4}$$

$$\Delta t_2 = 0.22 * 24.1 - 0.1 * 24.1 + 4.7 = 7.6 \text{ minutes} \quad \textbf{Table E.4}$$

To consider the effects of the void cavity (Table E.3, column 3):

$$k_{pos,unexp,2} = 0.5\, h_i^{0.15} = 0.5 * 12.5^{\,0.15} = 0.73 \quad \textbf{Table E.3}$$

The protection value is now calculated as

$$t_{prot,i} = t_{prot,2} = \left(t_{prot,0,2}\, k_{pos,exp,2}\, k_{pos,unexp,2} + \Delta t_2\right)$$

$$t_{prot,2} = 24.1 * 0.5 * 0.73 + 7.6 = 16.4 \text{ minutes}$$

a. Layer i = 3

$$\sum t_{prot,i-1} = 24.1 + 16.4 = 40.5 > \frac{t_{prot,0,3}}{2} > \frac{24.1}{2} \quad \textbf{Table E.2}$$

$$k_{pos,exp,3} = 0.5\sqrt{\frac{t_{prot,0,2}}{\sum t_{prot,i-1}}} = 0.5\sqrt{\frac{24.1}{40.5}} = 0.39 \qquad \textbf{Table E.2}$$

The layer $i = 3$ is positioned on the unexposed side of the cavity. Thus, $k_{pos,exp,i}$ must be modified to consider the effects of the void cavity, as presented in Table E.5.

$$k_{pos,exp,3} = 3.2 * 0.39 = 1.2 \qquad \textbf{Table E.5}$$

The layer $i = 3$ is being backed by a Type F gypsum plasterboard and according to Table E.3:

$$k_{pos,unexp,i} = k_{pos,unexp,3} = 1.0 \qquad \textbf{Table E.3}$$

Also, layer $i = 3$ is protected by a Type F gypsum plasterboard (layer $i = 2$) and the correction time presented in Table E.4 must be found.

$$t_{prot,0,3} = 24.1 \geq 12 \text{ minutes} \qquad \textbf{Table E.4}$$

$$\Delta t_i = 0.22\, t_{prot,i-1} - 0.1\, t_{prot,0,i} + 4.7 \qquad \textbf{Table E.4}$$

$$\Delta t_2 = 0.22 * 16.4 - 0.1 * 24.1 + 4.7 = 5.9 \text{ minutes} \qquad \textbf{Table E.4}$$

To consider the effects of the void cavity:

$$\Delta t_3 = 3 * 5.9 = 17.7 \text{ minutes} \qquad \textbf{Table E.5}$$

The protection value is now calculated as

$$t_{prot,i} = t_{prot,3} = \left(t_{prot,0,3}\ k_{pos,exp,3}\ k_{pos,unexp,3} + \Delta t_3\right)$$

$$t_{prot,2} = 24.1 * 1.2 * 1 + 17.7 = \ 46.6 \text{ minutes}$$

IV. Insulation value

a. Layer n

According to Table E.2:

$$\sum t_{prot,i-1} = 87.1 > \frac{t_{ins,0,n}}{2} > \frac{18.6}{2} \qquad \textbf{Table E.2}$$

$$k_{pos,exp,n} = 0.5 \sqrt{\frac{t_{ins,0,n}}{\sum t_{prot,i-1}}} = 0.5 \sqrt{\frac{18.6}{87.1}} = 0.23 \qquad \textbf{Table E.2}$$

The last layer is protected by a Type F gypsum plasterboard (layer i = 3) and the correction time presented in Table E.4 must be found.

$$t_{ins,0,n} = 18.6 \ \geq \ 12 \text{ minutes} \qquad \textbf{Table E.4}$$

$$\Delta t_n = 0.22\ t_{prot,i-1} - 0.1\ t_{ins,0,n} + 4.7 \qquad \textbf{Table E.4}$$

$$\Delta t_n = 0.22 * 46.6 - 0.1 * 18.6 + 4.7 = 13.1 \text{ minutes} \qquad \textbf{Table E.4}$$

The insulation value of the last layer is given by

$$t_{ins,n} = \left(t_{ins,0,i}\ k_{pos,exp,n}\ + \Delta t_n\right)$$

$$t_{ins,n} = 18.6 * 0.23 + 13.1 = 17.4 \text{ minutes}$$

V. Fire resistance of the assembly

$$t_{ins} = \sum_{i=1}^{i=n-1} t_{prot,i} + t_{ins,n}$$

$$t_{ins} = t_{prot,1} + t_{prot,2} + t_{prot,3} + t_{ins,n}$$

$$t_{ins} = 24.1 + 16.4 + 46.6 + 17.4 = \ 104 \text{ minutes}$$

F.3 Simplified Model Specimen 3

I. Description of the assembly

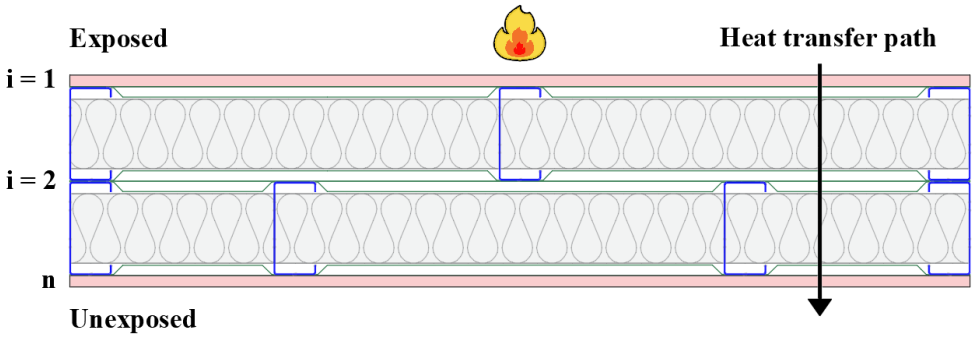

Layer	Material	Function	Thickness [mm]
1	Type F gypsum plasterboard	Protection	12.5
2	Ceramic fibre	Protection	150
n	Type F gypsum plasterboard	Insulation	12.5

II. Basic values

The first layer with protective function is a Type F gypsum plasterboard with h_i = 12.5 mm each. Therefore, as presented in Table E.1:

$$t_{prot,0,1} = 30 \left(\frac{12.5}{15}\right)^{1.2} = 24.1 \text{ minutes}$$ **Table E.1**

The second layer is a ceramic fibre batt with an effective thickness of $h_i = 150$ mm. The same expressions used in the original method are being applied for the ceramic fibre used in this study**.** Thus, the basic protection value of the ceramic fibre is given by Table E.1 as follows:

$$t_{prot,0,2} = 0.3\, h_i^{(0.75\, log(\rho_i) - \frac{\rho_i}{400})}$$ **Table E.1**

Note that in this study, $\rho_i = 128\ kg/m^3$, that is:

$$t_{prot,0,2} = 0.3 * 150^{(0.75\,log(128) - \frac{128}{400})} = 165.6 \text{ minutes} \qquad \textbf{Table E.1}$$

The last layer of the assembly is also a Type F gypsum plasterboard with an insulation function and $h_i = 12.5$ mm. Therefore, as shown in Table E.1:

$$t_{ins,0,n} = 24\left(\frac{h_i}{15}\right)^{1.4} = 24\left(\frac{12.5}{15}\right)^{1.4} = 18.6 \text{ minutes} \qquad \textbf{Table E.1}$$

III. Protection values

a. Layer i = 1

According to Table E.2:

$$\sum t_{prot,i-1} = 0 \leq \frac{t_{prot,0,1}}{2} \leq \frac{24.1}{2} \qquad \textbf{Table E.2}$$

$$k_{pos,exp,1} = 1 - 0.6\frac{\sum t_{prot,i-1}}{t_{prot,0,1}} = 1 - 0.6\left(\frac{0}{24.1}\right) = 1 \qquad \textbf{Table E.2}$$

The layer $i = 1$ is backed by a ceramic fibre blanket and according to Table E.3:

$$k_{pos,unexp,i} = k_{pos,unexp,1} = 0.5\,h_i^{0.15} = 0.5 * 12.5^{0.15} = 0.73 \qquad \textbf{Table E.3}$$

The protection value is now calculated as

$$t_{prot,i} = t_{prot,1} = \left(t_{prot,0,1}\,k_{pos,exp,1}\,k_{pos,unexp,1} + \Delta t_1\right)$$

Note that $\Delta t_1 = 0$ since there is no preceding layer made of Type F gypsum plasterboard, which leads to:

$$t_{prot,1} = 24.1 * 1 * 0.73 \ + 0 = 17.6 \text{ minutes}$$

b. Layer i = 2

$$\sum t_{prot,i-1} = 17.6 \leq \frac{t_{prot,0,2}}{2} \leq \frac{165.6}{2} \quad \textbf{Table E.2}$$

$$k_{pos,exp,2} = 1 - 0.6\frac{\sum t_{prot,i-1}}{t_{prot,0,2}} = 1 - 0.6\left(\frac{17.6}{165.6}\right) = 0.94 \quad \textbf{Table E.2}$$

The layer i = 2 is protected by a Type F gypsum plasterboard (layer i = 1) and the correction time presented in Table E.4 must be found.

$$t_{prot,0,2} = 165.6 \ \geq \ 6 \text{ minutes} \quad \textbf{Table E.4}$$

$$\Delta t_2 = 0.22\, t_{prot,i-1} - 0.1\, t_{prot,0,2} + 3.5 \quad \textbf{Table E.4}$$

$$\Delta t_2 = 0.22 * 24.1 - 0.1 * 165.6 + 3.5 = -7.8 \text{ minutes} \quad \textbf{Table E.4}$$

However, $\Delta t_2 \geq 0$, then $\Delta t_2 = 0$ is assumed for the following calculations.

The position coefficient that considers the effect of the backing layer is given by Table E.3. Since the ceramic fibre is backed by a Type F gypsum plasterboard:

$$k_{pos,unexp,i} = k_{pos,unexp,2} = 1 \quad \textbf{Table E.3}$$

The protection value is now calculated as

$$t_{prot,i} = t_{prot,2} = \left(t_{prot,0,2}\, k_{pos,exp,2}\, k_{pos,unexp,2} + \Delta t_2\right)$$

$$t_{prot,2} = 165.6 * 0.93 * 1 + 0 = \ 154 \text{ minutes}$$

IV. Insulation value

a. Layer n

According to Table E.2:

$$\sum t_{prot,i-1} = 171.6 > \frac{t_{ins,0,n}}{2} > \frac{18.6}{2} \quad \textbf{Table E.2}$$

$$k_{pos,exp,n} = 0.5 \sqrt{\frac{t_{ins,0,n}}{\sum t_{prot,i-1}}} = 0.5 \sqrt{\frac{18.6}{171.6}} = 0.16 \quad \textbf{Table E.2}$$

The insulation value of the last layer is given by

$$t_{ins,n} = \left(t_{ins,0,i}\, k_{pos,exp,n} \ + \Delta t_n\right)$$

$$t_{ins,n} = 18.6 * 0.16 + 0 = 3 \text{ minutes}$$

V. Fire resistance of the assembly

$$t_{ins} = \sum_{i=1}^{i=n-1} t_{prot,i} + t_{ins,n}$$

$$t_{ins} = t_{prot,1} + t_{prot,2} + t_{ins,n}$$

$$t_{ins} = 17.6 + 154 + 3 = 174 \text{ minutes}$$

F.4 Simplified Model Specimen 4

I. Description of the assembly

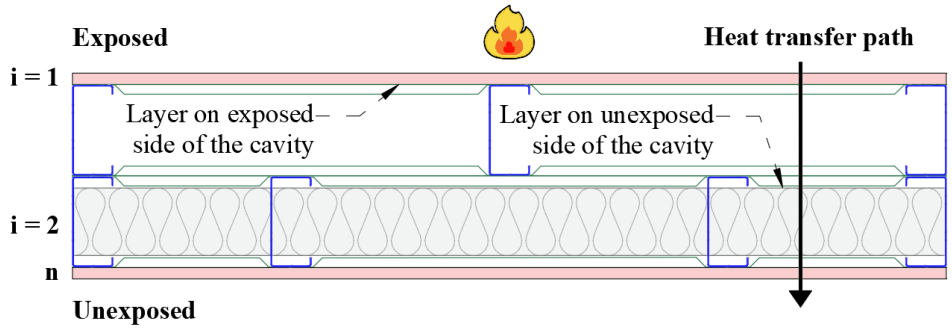

Layer	Material	Function	Thickness [mm]
1	Type F gypsum plasterboard	Protection	12.5
2	Ceramic fibre	Protection	75
n	Type F gypsum plasterboard	Insulation	12.5
Cavity	-	-	100

II. Basic values

The first layer with protective function is a Type F gypsum plasterboard with h_i = 12.5 mm each. Therefore, as presented in Table E.1:

$$t_{prot,0,1} = 30 \left(\frac{12.5}{15}\right)^{1.2} = 24.1 \text{ minutes} \qquad \textbf{Table E.1}$$

The second layer is a ceramic fibre batt with an effective thickness of h_i = 75 mm. Thus, the basic protection value of the ceramic fibre is given by Table E.1 as follows:

$$t_{prot,0,2} = 0.3\, h_i^{\left(0.75\, log(\rho_i) - \frac{\rho_i}{400}\right)} \qquad \textbf{Table E.1}$$

Note that in this study, $\rho_i = 128$ kg/m^3, that is:

$$t_{prot,0,2} = 0.3 * 75^{(0.75\,log(128)-\frac{128}{400})} = 69.1 \text{ minutes}$$ **Table E.1**

The last layer of the assembly is also a Type F gypsum plasterboard with an insulation function and $h_i = 12.5$ mm. Therefore, as shown in Table E.1:

$$t_{ins,0,n} = 24\left(\frac{h_i}{15}\right)^{1.4} = 24\left(\frac{12.5}{15}\right)^{1.4} = 18.6 \text{ minutes}$$ **Table E.1**

III. Protection values

a. Layer i = 1

According to Table E.2:

$$\sum t_{prot,i-1} = 0 \leq \frac{t_{prot,0,1}}{2} \leq \frac{24.1}{2}$$ **Table E.2**

$$k_{pos,exp,1} = 1 - 0.6\frac{\sum t_{prot,i-1}}{t_{prot,0,1}} = 1 - 0.6\left(\frac{0}{24.1}\right) = 1$$ **Table E.2**

Since layer $i = 1$ is positioned on the exposed side of the cavity. the position coefficient that considers the effect of the backing layer $k_{pos,unexp,i}$ (Table E.3, column 3) is given by Table E.5, as follows:

$$k_{pos,unexp,1} = 0.5\, h_i^{0.15} = 0.5 * 12.5^{\,0.15} = 0.73$$ **Table E.3**

The protection value is now calculated as

$$t_{prot,i} = t_{prot,1} = \left(t_{prot,0,1}\, k_{pos,exp,1}\, k_{pos,unexp,1} + \Delta t_1\right)$$

Note that $\Delta t_1 = 0$ since there is no preceding layer made of Type F gypsum plasterboard, which leads to:

$$t_{prot,1} = 24.1 * 1 * 0.73 \ + 0 = 17.6 \text{ minutes}$$

b. Layer i = 2

$$\sum t_{prot,i-1} = 17.6 \leq \frac{t_{prot,0,2}}{2} \leq \frac{69.1}{2} \quad \textbf{Table E.2}$$

$$k_{pos,exp,2} = 1 - 0.6\frac{\sum t_{prot,i-1}}{t_{prot,0,2}} = 1 - 0.6\left(\frac{17.6}{69.1}\right) = 0.85 \quad \textbf{Table E.2}$$

The layer $i = 2$ is positioned on the unexposed side of the cavity. Thus, $k_{pos,exp,i}$ must be modified to consider the effects of the void cavity, as presented in Table E.5.

$$k_{pos,exp,2} = 1.6 * 0.85 = 1.4 \quad \textbf{Table E.5}$$

The layer $i = 2$ is protected by a Type F gypsum plasterboard (layer $i = 1$) and the correction time presented in Table E.4 must be found.

$$t_{prot,0,2} = 69.1 \ \geq \ 6 \text{ minutes} \quad \textbf{Table E.4}$$

$$\Delta t_2 = 0.22\, t_{prot,i-1} - 0.1\, t_{prot,0,2} + 3.5 \quad \textbf{Table E.4}$$

$$\Delta t_2 = 0.22 * 24.1 - 0.1 * 69.1 + 3.5 = 0.46 \text{ minutes} \quad \textbf{Table E.4}$$

To consider the effects of the cavity void (Table E.5), the value calculated previously for Δt_2 remains unchanged. Hence, the protection value is now calculated as:

$$t_{prot,i} = t_{prot,2} = \left(t_{prot,0,2}\ k_{pos,exp,2}\ k_{pos,unexp,2} + \Delta t_2\right)$$

$$t_{prot,2} = 69.1 * 1.4 * 1 + 0.46 = \ 97.2 \text{ minutes}$$

IV. Insulation value

a. Layer n

According to Table E.2:

$$\sum t_{prot,i-1} = 114.8 > \frac{t_{ins,0,n}}{2} > \frac{18.6}{2} \qquad \textbf{Table E.2}$$

$$k_{pos,exp,n} = 0.5\sqrt{\frac{t_{ins,0,n}}{\sum t_{prot,i-1}}} = 0.5\sqrt{\frac{18.6}{114.8}} = 0.20 \qquad \textbf{Table E.2}$$

The insulation value of the last layer is given by

$$t_{ins,n} = \left(t_{ins,0,i}\ k_{pos,exp,n}\ + \Delta t_n\right)$$

$$t_{ins,n} = 18.6 * 0.2 + 0 = 3.7 \text{ minutes}$$

V. Fire resistance of the assembly

$$t_{ins} = \sum_{i=1}^{i=n-1} t_{prot,i} + t_{ins,n}$$

$$t_{ins} = t_{prot,1} + t_{prot,2} + t_{ins,n}$$

$$t_{ins} = 17.6 + 97.2 + 3.7 = 118 \text{ minutes}$$

F.5 Simplified Model Specimen 5

I. Description of the assembly

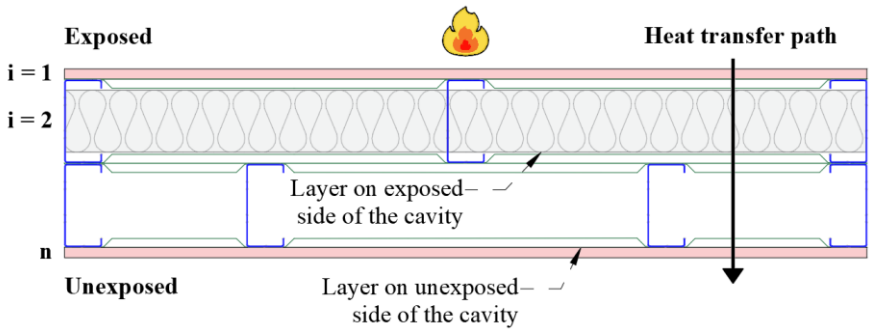

Layer	Material	Function	Thickness [mm]
1	Type F gypsum plasterboard	Protection	12.5
2	Ceramic fibre	Protection	75
n	Type F gypsum plasterboard	Insulation	12.5
Cavity	-	-	100

II. Basic values

The first layer with protective function is a Type F gypsum plasterboard with h_i = 12.5 mm each. Therefore, as presented in Table E.1:

$$t_{prot,0,1} = 30 \left(\frac{12.5}{15}\right)^{1.2} = 24.1 \text{ minutes} \qquad \textbf{Table E.1}$$

The second layer is a ceramic fibre batt with an effective thickness of h_i = 75 mm. Thus, the basic protection value of the ceramic fibre is given by Table E.1 as follows:

$$t_{prot,0,2} = 0.3\, h_i^{\left(0.75\, log(\rho_i) - \frac{\rho_i}{400}\right)} \qquad \textbf{Table E.1}$$

Note that in this study, $\rho_i = 128$ kg/m^3, that is:

$$t_{prot,0,2} = 0.3 * 75^{(0.75\,log(128)-\frac{128}{400})} = 69.1 \text{ minutes} \qquad \textbf{Table E.1}$$

The last layer of the assembly is also a Type F gypsum plasterboard with an insulation function and $h_i = 12.5$ mm. Therefore, as shown in Table E.1:

$$t_{ins,0,n} = 24\left(\frac{h_i}{15}\right)^{1.4} = 24\left(\frac{12.5}{15}\right)^{1.4} = 18.6 \text{ minutes} \qquad \textbf{Table E.1}$$

III. Protection values

a. Layer i = 1

According to Table E.2:

$$\sum t_{prot,i-1} = 0 \leq \frac{t_{prot,0,1}}{2} \leq \frac{24.1}{2} \qquad \textbf{Table E.2}$$

$$k_{pos,exp,1} = 1 - 0.6\frac{\sum t_{prot,i-1}}{t_{prot,0,1}} = 1 - 0.6\left(\frac{0}{24.1}\right) = 1 \qquad \textbf{Table E.2}$$

Since layer $i = 1$ is backed by insulation, the position coefficient $k_{pos,unexp,i}$ (Table E.3, column 3) is given by Table E.5, as follows:

$$k_{pos,unexp,1} = 0.5\, h_i^{0.15} = 0.5 * 12.5^{\,0.15} = 0.73 \qquad \textbf{Table E.3}$$

The protection value is now calculated as

$$t_{prot,i} = t_{prot,1} = \left(t_{prot,0,1}\, k_{pos,exp,1}\, k_{pos,unexp,1} + \Delta t_1\right)$$

$$t_{prot,1} = 24.1 * 1 * 0.73 \; + 0 = 17.6 \text{ minutes}$$

b. Layer i = 2

$$\sum t_{prot,i-1} = 17.6 \leq \frac{t_{prot,0,2}}{2} \leq \frac{69.1}{2} \quad \textbf{Table E.2}$$

$$k_{pos,exp,2} = 1 - 0.6\frac{\sum t_{prot,i-1}}{t_{prot,0,2}} = 1 - 0.6\left(\frac{17.6}{69.1}\right) = 0.85 \quad \textbf{Table E.2}$$

The layer i = 2 is positioned on the exposed side of the cavity. Thus, $k_{pos,unexp,i}$ must be modified to consider the effects of the void cavity, as presented in Table E.5.

$$k_{pos,unexp,2} = 2.6 \quad \textbf{Table E.5}$$

The layer i = 2 is protected by a Type F gypsum plasterboard (layer i = 1) and the correction time presented in Table E.4 must be found.

$$t_{prot,0,2} = 69.1 \geq 6 \text{ minutes} \quad \textbf{Table E.4}$$

$$\Delta t_2 = 0.22\, t_{prot,i-1} - 0.1\, t_{prot,0,2} + 3.5 \quad \textbf{Table E.4}$$

$$\Delta t_2 = 0.22 * 24.1 - 0.1 * 69.1 + 3.5 = 0.46 \text{ minutes} \quad \textbf{Table E.4}$$

To consider the effects of the cavity void (Table E.5), the value calculated previously for Δt_2 remains unchanged. Hence, the protection value is now calculated as:

$$t_{prot,i} = t_{prot,2} = \left(t_{prot,0,2}\, k_{pos,exp,2}\, k_{pos,unexp,2} + \Delta t_2\right)$$

$$t_{prot,2} = 69.1 * 0.85 * 2.6 + 0.46 = 153.2 \text{ minutes}$$

IV. Insulation value

a. Layer n

According to Table E.2:

$$\sum t_{prot,i-1} = 164.9 > \frac{t_{ins,0,n}}{2} > \frac{18.6}{2} \quad \textbf{Table E.2}$$

$$k_{pos,exp,n} = 0.5\sqrt{\frac{t_{ins,0,n}}{\sum t_{prot,i-1}}} = 0.5\sqrt{\frac{18.6}{164.9}} = 0.17 \quad \textbf{Table E.2}$$

Since the insulation layer is placed on the unexposed side of the cavity, as per Table E.5:

$$k_{pos,exp,n} = 1.6 * 0.17 = 0.27 \quad \textbf{Table E.5}$$

The insulation value of the last layer is given by

$$t_{ins,n} = \left(t_{ins,0,i}\, k_{pos,exp,n} + \Delta t_n\right)$$

$$t_{ins,n} = 18.6 * 0.27 + 0 = 5 \text{ minutes}$$

V. Fire resistance of the assembly

$$t_{ins} = \sum_{i=1}^{i=n-1} t_{prot,i} + t_{ins,n}$$

$$t_{ins} = t_{prot,1} + t_{prot,2} + t_{ins,n}$$

$$t_{ins} = 17.6 + 153.2 + 5 = 175 \text{ min}$$